Coupled space-time discontinuous Galerkin method for dynamical modeling in porous media

Dissertation

zur Erlangung des Grades
des Doktors der Ingenieurwissenschaften
der Naturwissenschaftlich-Technischen Fakultät III
Chemie, Pharmazie, Bio- und Werkstoffwissenschaften
der Universität des Saarlandes

von

Zhiyun Chen

Saarbrücken Germany, 2007

Tag der Einreichtung: 31.10.2007
Tag der Promotion: 25.02.2008

Dekan: Prof. Dr. Uli Müller
Berichtstatter: Prof. Dr. Stefan Diebels
Prof. Dr. Detlef Kuhl

ABSTRACT

This thesis deals with coupled space-time discontinuous Galerkin methods for the modeling of dynamical phenomena in fluid saturated porous media. The numerical scheme consists of finite element discretizations in the spatial and in the temporal domain simultaneously. In particular, two major classes of approaches have been investigated.

The first one is the so-called time-discontinuous Galerkin (DGT) method, consisting of discontinuous polynomials in the temporal domain but continuous ones in space. A natural *upwind* flux treatment is introduced to enforce the continuity condition at discrete time levels. The proposed numerical approach is suitable for solving first-order time-dependend equations. For the second-order equations, an Embedded Velocity Integration (EVI) technique is developed to degenerate a second-order equation into a first-order one. The resulting first-order differential equation with the primary variable in rate term (velocity) can in turn be solved by the time-discontinuous Galerkin method efficiently. Applications concerning both the first- and second-order differential equations as well as wave propagation problems in porous materials are investigated.

The other one is the coupled space-time discontinuous Galerkin (DGST) method, in which neither the spatial nor the temporal approximations pocesses strong continuity. Spatial fluxes combined with flux-weighted constraints are employed to enforce the interelement consistency in space, while the consistency in the time domain is enforced by the temporal *upwind* flux investigated in the DGT method. As there exists no coupling between the spatial and temporal fluxes, various flux treatments in space and in time are employed independently. The resulting numerical scheme is able to capture the steep gradients or even discontinuities. Applications concerning the single-phase flow within the porous media are presented.

Keywords: space-time finite element method, time-discontinuous Galerkin method, Embedded Velocity Integration method, fluid saturated porous media, wave propagation.

ZUSAMMENFASSUNG

Im Rahmen dieser Arbeit werden gekoppelte Raum-Zeit Finite-Elemente-Methoden für die Simulation dynamischer Effekte in fluid-gesättigten porösen Materialien entwickelt und numerisch umgesetzt. Dazu wird eine gekoppelte Diskretisierung des räumlichen und zeitlichen Gebietes vorgenommen. Insbesondere werden zwei Klassen von Verfahren untersucht.
Die erste Methode ist ein sogenanntes zeitlich-diskontinuierliches Galerkin Verfahren (DGT-Methode). Hierbei werden diskontinuierliche Ansätze in der Zeit und kontinuierliche Ansätze im Raum verwendet. Die Kontinuitätsnebenbedingung in der Zeit wird durch einen *upwind*-Flussterm erzwungen. Der Flussterm unterliegt mathematischen Restriktionen und daher ist das resultierende Finite Element Verfahren nur für Gleichungen mit zeitlichen Ableitungen erster Ordnung geeignet. Um auch Gleichungen zweiter Ordnungen mit dem entwickelten DGT-Verfahren behandeln zu können, ist die EVI-Methode (Embedded Velocity Integration method) entwickelt worden. Im Rahmen der EVI-Technik wird die Geschwindigkeit als Primärvariable gewählt und im Bezug auf die gewählten zeitlichen Ansätze integriert. Die aud der Geschwindigkeit basierenden schwachen Formen können wiederum mit der DGT-Methode gelöst werden. Die entwickelten numerischen Raum-Zeit Finite-Element-Methoden werden sowohl für elastische Wellenausbreitungsprobleme als auch für gekoppelte Fragestellungen in porösen Medien angewendet.
Abschließend wird ein räumlich diskontinuierliches Finite-Element-Verfahren entwickelt und mit den bereits entwickelten zeitlich-diskontinuierlichen Methoden gekoppelt. Die räumliche Kontinuitätsbedingung wird durch die Entwicklung eines speziellen Flusstermes erzwungen. Es wird gezeigt, dass sich das Verfahren mit den bereits entwickelten Flusstermen für die zeitliche Kontinuität koppeln lässt. Dies wird durch die Entkopplung der räumlichen und zeitlichen Flussterme möglich. Das resultierende Raum-Zeit diskontinuierliche Finite-Elemente-Verfahren wird wiederum auf Strömungsprobleme mischbarer Fluide in porösen Medien angewendet und mit klassischen Methoden verglichen.

Stichworte: Raum-Zeit Finite Elemente Verfahren, zeitlich-diskontinuierisch Galkerin Methode, EVI Methode, fluid-gesättigte poröse Medien, Wellenausbreitung

LIST OF APPENDED PAPERS

This thesis consists of a summary and four appended papers:

Paper A Z. Chen, H. Steeb and S. Diebels, A time-discontinuous Galerkin method for the dynamical analysis of porous media, *International Journal for Numerical and Analytical Methods in Geomechanics* 2006; **30**:1113–1134

Paper B Z. Chen, H. Steeb and S. Diebels, A new hybrid velocity integration method applied to elastic wave propagation, *International Journal for Numerical Methods in Engineering* 2008; **74**:56–79

Paper C Z. Chen, H. Steeb and S. Diebels, A EVI-space-time Galerkin method for dynamics at finite deformation in porous media, *Computational Mechanics* 2008; submitted for publication

Paper D Z. Chen, H. Steeb and S. Diebels, A space-time discontinuous Galerkin method for single-phase flow in porous media, *Comp. Geoscience* 2008; submitted for publication

CONTRIBUTIONS TO CO-AUTHORED PAPERS

The papers were prepared in collaboration with co-authers. The author of this thesis was responsible for the major progress of work in all of the papers.

Paper A Took part in planning the paper.
Took part in developing the method.
Developed the numerical implementation.
Carried out the numerical simulations.

Paper B Took part in planning the paper.
Took part in developing the method.
Developed the numerical implementation.
Carried out the numerical simulations.

Paper C Took part in planning the paper.
Took part in developing the method.
Developed the numerical implementation.
Carried out the numerical simulations.

Paper D Took part in planning the paper.
Took part in developing the method.
Developed the numerical implementation.
Carried out the numerical simulations.

Contents

ABBREVIATION

DG	Discontinuous Galerkin
DGS	Spatial Discontinuous Galerkin
DGST	Space-time discontinuous Galerkin method
DGT	Time-discontinuous Galerkin method
EVI	Embedded Velocity Integration
FEM	Finite Element Method
LDG	Local Discontinuous Galerkin method
MOL	Method of Lines
NIPG	Non-Symmetric Interior Penalty Galerkin method
ODE	Ordinary Differential Equations
PDE	Partial Differential Equation
PDG	Penalty Discontinuous Galerkin
REV	Representative Elementary Volume
RKDG	Runge-Kutta Discontinuous Galerkin method
SIPG	Symmetric Interior Penalty Galerkin method
TPM	Theory of Porous Media

PREFACE

The work presented here has been carried out during the years 2003 – 2007 at the Chair of Applied Mechanics, Saarland University, Germany. The research project has been funded by the Deutsche Forschungsgemeinschaft (DFG).

First of all, I would like to express my sincere gratitude and appreciation to Professor Stefan Diebels, head of the Chair of Applied Mechanics, for providing me the unique opportunity to work in the research area of numerical modeling, for his expert guidance and mentorship, for his encouragement and support at all levels.

I am extremely grateful to Dr. Holger Steeb for his constant support and instructive discussions at all times. His ideas and the way of dealing with problems has always been a source of inspiration for me.

Also, I am grateful to all the members of at Chair of Applied Mechanics, for their assistance, friendship and for many enjoyable times, in particular Tobias Ebinger, Michael Johlitz and Ralf Jänicke. It was an great pleasure to work with them. Thanks also my friends and people I met in the Saarland University during my time in Saarbrücken.

Finally, I take this opportunity to express my gratitude to my parents for their love and unfailing support. My special thanks go to my husband Pengfei for reminding me of what is truely important in life.

Zhiyun Chen

Saarbrücken, Germany

REVIEW AND SUMMARY OF THE THESIS

Space-time Galerkin methods are natural extensions of the classical Finite Element Method. They are a powerful tool in solving partial differential equations. Such methods are developed, implemented and applied to different physical problems.
A review of the thesis is presented. The numerical methods are discussed and motivated. In the appended papers, we illustrate the derivation and behavior of the numerical methods. References are made to Paper A-D in the thesis.

1 Introduction and motivation

1.1 Numerical simulation for engineering computation

With the development of the computer technology, the scientific computing has become a third paradigm in combination with theory and experiment. Numerical simulation enables the study of complex systems and natural phenomena that would be too expensive or dangerous, or even impossible to study directly by experimentation. Moreover, computer simulation provides the capability to enter fields that are inaccessible to traditional experimentation and method of inquiry. The physical phenomena can be described by a mathematical model consisting of partial differential equations (PDE) equipped with associated boundary and initial conditions. Due to the fact that only in extremely simplified case, analytical solutions of PDEs are accessible. In practice, instead of seeking an exact solution of the boundary value problem under study, engineers and scientists perform numerical analysis in order to find an approximate solution of the PDE within reasonable bounds of error.
To date, the fast development in the hardware and software has significantly increased the importance of large scale computation in the numerical simulations. The quest for higher levels of details and realism in scientific simulations require always enormous computational capacity. This has provided the impetus for developing even faster computers and more efficient numerical algorithms. The most popular method for performing numerical analysis is the finite element method (FEM), also called the Galerkin method. Since the birth of FEM in the 1950s [14, 60], the efforts on developing new algorithms to meet the ever growing demand of the scientific simulations have never stopped. Despite the diversities of various techniques, according to the chosen function spaces, the modern FEM can be primarily divided into two classes, the Bubnov Galerkin method, employing the same trial and test function spaces, and the Petrov Galerkin method where different trial and test function spaces are employed. By employing different trial and test function spaces, the Petrov Galerkin formulation can be enhanced with stabilization mechanism, which is favorable in the modeling of phenomena including sharp gradients or discontinuities. According to the domain of the finite element discretization, there are spatial FEM (classical FEM) in which a finite element mesh covers the spatial domain and the space-time FEM in which a coupled discretization in the space as well as in the

time domain is constructed. The classical finite element treatment is based on a finite element discretization in space, rendering the PDE into an equivalent system of Ordinary Differential Equations (ODE) in time, which can then be solved by certain time-stepping method, i. e. finite difference techniques (Method of Lines, MOL). Since the pioneer work of introducing the finite element technique also to the temporal domain in 1969 [2, 37], the space-time FEM has gained more and more attention in the community. Nowadays, using the finite element method in the temporal domain as well as in the spatial domain (space-time Galerkin method) to model transient phenomena has become a promising competitor to the classical finite element approaches. Among the family of space-time FEMs, according to the art of discretization, we can further identify the decoupled space-time FEM, in which the spatial and temporal discretizations are constructed subsequently, and the coupled space-time FEM whereby a finite element mesh covers the space-time domain simultaneously.
The objective of this thesis is to study a new coupled space-time finite element method for the application of dynamic analysis in porous media. The resulting finite element formulation possesses the form of the Bubnov Galerkin method but with enhanced stability properties, and it is able to capture sharp gradients and even discontinuities in the numerical solution. Moreover, the method provides a general approach for solving transient problems for a vast of engineering applications.

1.2 Modeling aspect within the Theory of Porous Media

The primary purpose of this thesis is to study an efficient space-time FEM method for applications in the Theory of Porous Media (TPM). In this section, we briefly review the main ideas of the TPM. The TPM is based on the axioms of the continuum theories of mixtures extended by the concept of volume fractions, cf. the textbooks [23, 30]. The physical model is based on a mixture consisting of immiscible constituents $\varphi^{\mathfrak{i}}$. The individual aggregate is considered as a statistically average value in the sense of a Representative Elementary Volume (REV) $\mathrm{d}v$. As a matter of course, the REV must be large enough to allow for a statistical statement. An individual constituent within the REV is identified according to its volume fracture defined by $n^{\mathfrak{i}} = \mathrm{d}v^{\mathfrak{i}}/\mathrm{d}v$, with $\mathrm{d}v^{\mathfrak{i}}$ denotes the volume of the constituent $\varphi^{\mathfrak{i}}$ in the REV. In the case that no empty void exists in the mixture, the mixture is called saturated, i. e. $\sum_{\mathfrak{i}} n^{\mathfrak{i}} = 1$. In this thesis, a binary mixture consisting of a solid phase $\varphi^{\mathfrak{s}}$ and a fluid phase $\varphi^{\mathfrak{f}}$ is studied, so that we have $\mathfrak{i} = \{\mathfrak{s}, \mathfrak{f}\}$ with $n^{\mathfrak{s}} + n^{\mathfrak{f}} = 1$, see Figure 1. Furthermore, by the use of the volume fraction, we can identify two density concepts, namely the partial density $\rho^{\mathfrak{i}} = \mathrm{d}m^{\mathfrak{i}}/\mathrm{d}v$ and the effective density $\rho^{\mathfrak{i}R} = \mathrm{d}m^{\mathfrak{i}}/\mathrm{d}v^{\mathfrak{i}}$. We denote that the effective density $\rho^{\mathfrak{i}R}$ represents the true density of the constituent $\varphi^{\mathfrak{i}}$, while the partial density $\rho^{\mathfrak{i}}$ stands for the density proportion of constituent $\varphi^{\mathfrak{i}}$ in the REV. These two densities are related via the volume fraction $n^{\mathfrak{i}}$, i. e. $\rho^{\mathfrak{i}} = n^{\mathfrak{i}}\,\rho^{\mathfrak{i}R}$. Regarding the total mass in the REV with respect to the total volume, the density of the mixture ρ equals the sum of the partial densities of its

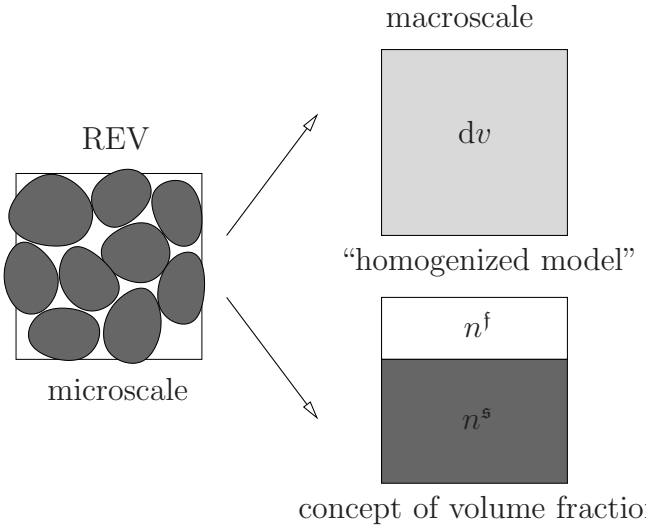

Figure 1: Illustration of the statistical distribution of a binary porous medium consisting of a granular solid phase $\varphi^{\mathfrak{s}}$ and a fluid phase $\varphi^{\mathfrak{f}}$.

components, i. e. $\rho = \sum_{\mathfrak{i}} \rho^{\mathfrak{i}}$. Obviously, even for a mixture with materially incompressible constituents $\rho^{\mathfrak{i}R} = \text{const.}$, the partial density $\rho^{\mathfrak{i}}$ varies with the change of volume fraction $n^{\mathfrak{i}}$.
In mixture theory [59], individual constituents of the mixture are completely smeared out through the considered domain in the sense of superimposed and interacting continua, see Figure 2. Herein, the spatial point $\mathbf{x}$ is occupied by both solid and fluid constituents simultaneously. Each constituent follows its own function of motion. The motion functions of these particles are given by

$$\mathbf{x} = \boldsymbol{\chi}_{\mathfrak{i}}(\mathbf{X}_{\mathfrak{i}}, t_0). \tag{1}$$

The motion function $\boldsymbol{\chi}_{\mathfrak{i}}$ of the constituent $\varphi^{\mathfrak{i}}$ is independent of the other. Usually, the motion of the solid is described with respect to the reference configuration (Lagrangian description), while the fluid motion is described with respect to the current configuration as relative motion to the solid (modified Eulerian description). The seepage velocity denoting the relative velocity between the solid and fluid constituents is given by

$$\mathbf{w}_{\mathfrak{f}} = \mathbf{x}'_{\mathfrak{f}} - \mathbf{x}'_{\mathfrak{s}}. \tag{2}$$

Herein, the operator $(\bullet)'_{\mathfrak{i}}$ represents the material time derivative following the motion of constituent $\varphi^{\mathfrak{i}}$, i. e. $(\bullet)'_{\mathfrak{i}} = \frac{\partial(\bullet)}{\partial t} + \operatorname{grad}(\bullet)\,(\mathbf{x})'_{\mathfrak{i}}$.
The model statement of the binary mixture was illustrated in detail in e. g. [23, 30]. A survey on the historical development of the TPM can be found in the monograph work of de Boer [24]. For a state of art introduction and applications, the interested readers are referred to [29].

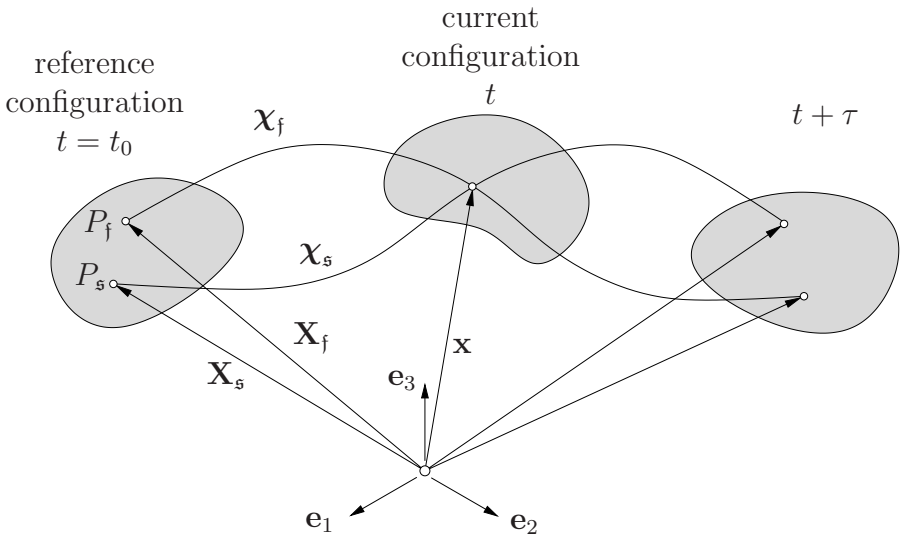

Figure 2: Illustration of the motion of a solid $P_{\mathfrak{s}}$ and a fluid particle $P_{\mathfrak{f}}$ in a fluid-saturated porous solid

Among the community of the TPM, most of the works done so far have been devoted to applications with respect to quasi-static investigations, e. g. [25, 32, 34]. Only few investigations based on the TPM have been done to analyze dynamic effects [10, 26, 27]. To date, the dynamic analysis is often performed by the use of Biot's theory [8, 9, 56]. Biot was the first person who systematically studied the interaction within a two-phase porous mixture. The significant contribution of him was to predict the existence of two compressional and one shear wave in a two-phase porous mixture. His innovative studies were later confirmed repeatedly in laboratory experiments [7, 50]. However, the essential drawback of Biot's model lies in the fact that the corresponding theory is not developed from the fundamental axioms and principles of mechanics and thermodynamics, but is constructed upon intuitive assumptions. Deficiencies of the Biot's theory have been shown in describing more complex physical situations [62], i. e. tri-phase porous material, nonlinear behavior of the pore fluid, etc. Moreover, it has been shown that if we exclude the most controversial "dynamic coupling" in Biot's model and restrict ourselves to the fully geometrically linear two-phase model, the TPM and the Biot's theory are equivalent and lead to same results [57]. Moreover, the main advantage of TPM is that it can be extended straight forwardly to describe more complex physical situations like multiphase flow in unsaturated porous media [31, 33, 58, 61].
In this thesis, we investigate the wave propagation within a simplified binary model using the TPM. In practice, the analysis of propagating waves in various porous materials (soil, rock, sediment, etc.) is important for the seismological engineering, geotechnical engineering, etc. In particular, in the petroleum exploration engineering, instead of drilling many test wells, the engineers use the technique of analyzing reflected signals of a sender to predict the location and capacity of the oil reservoir, see Figure 3. Since the earth ground is usually composed of several layers, a com-

plicated physical model as well as an accurate numerical algorithm are necessary for an extensive study of this topic. The technical details of this theme are beyond the scope of this thesis. However, the numerical method studied here provides a potential tool for the investigation of such complex physical situation.

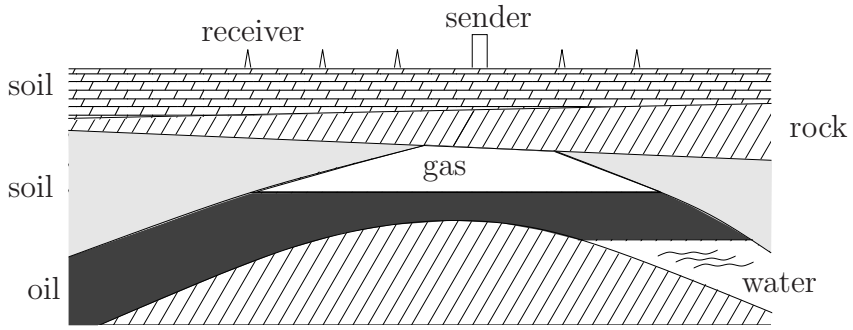

Figure 3: Illustration of oil exploration technique: Several receivers are located at various positions to collect the signals reflected by ground layers. By analyzing these signals, engineers intend to predict the location and capacity of the oil reservoir.

1.3 Classical approaches

In this section we discuss two popular strategies for solving PDE by the use of FEM, namely the Method of Lines (MOL) and a penalty type discontinuous Galerkin (PDG) method. Since in these approaches, the discretizations applied in space and in time are decoupled, these methods are characterized to semi-discrete methods.

1.3.1 Method of Lines

The Method of Lines (MOL) is a general technique for solving PDEs. The main strategy of the MOL is by using the finite element or finite difference strategy in space to produce a system of ODEs in time, which can in turn be solved by finite difference methods or other techniques which are appropriate for solving ODEs. According to the classical finite element MOLs, the spatial domain is discretisized using the FEM, rendering an ODE system that often has the form

$$\mathbf{M}\ddot{\mathbf{U}}(t) + \mathbf{D}\dot{\mathbf{U}}(t) + \mathbf{K}\mathbf{U}(t) = \mathbf{F}(t), \quad t \in [t_0, T] \tag{3}$$

in which $\mathbf{U}$ is the vector of model variables, i. e. the primary unknowns. Regarding the definitions in structural dynamics, $\mathbf{M}$ represents the mass matrix, $\mathbf{D}$ is the damping matrix of the system, and $\mathbf{K}$ is the stiffness matrix. $\mathbf{F}$ denotes the external force. Hereby, $\mathbf{U}$ represents the displacement vector. The dot operator $(\dot{\bullet})$ represents the first time derivative, and the double dots operator $(\ddot{\bullet})$ stands for the second time derivative. In this context, $\dot{\mathbf{U}}$ is the velocity and $\ddot{\mathbf{U}}$ corresponds to the acceleration.

After constructing the ODE system, a time-stepping strategy is applied to advance the solution in time. Among others, the most popular ones are the Euler method, the Newmark method, and the Runge-Kutta methods. Moreover, by using the order-reduction technique, such that a second-order time-dependent equation can be degenerated into an equation-system of two first-order equations, which can be solved by the finite difference methods that are designed for first-order problems, i. e. the Euler method, Runge-Kutta method. According to the order-reduction technique, eq. (3) can be rewritten into an equation-system consisting of two first-order equations like

$$\begin{bmatrix} \mathbf{I} & \mathbf{0} \\ \mathbf{0} & \mathbf{M} \end{bmatrix} \begin{bmatrix} \dot{\mathbf{U}} \\ \dot{\mathbf{V}} \end{bmatrix} + \begin{bmatrix} \mathbf{0} & -\mathbf{I} \\ \mathbf{K} & \mathbf{D} \end{bmatrix} \begin{bmatrix} \mathbf{U} \\ \mathbf{V} \end{bmatrix} = \begin{bmatrix} \mathbf{0} \\ \mathbf{F} \end{bmatrix}. \tag{4}$$

Here, both the displacement $\mathbf{U}$ and its velocity $\mathbf{V} = \dot{\mathbf{U}}$ are treated as primary unknowns and are solved within the system (4) simultaneously.
Although the mechanisms employed in the different MOLs are not all the same, a common property of these approaches is: the propagation of the numerical solutions in time depends on the projection of the velocity and the displacement at the current state to a future time. The MOL procedures have been successfully applied to solve various engineering problems. However, there are also some well known disadvantages of these methods, such as suffering from the strong numerical dispersion and dissipation, unphysical oscillations nearby sharp gradients and discontinuities, etc. We denote that the numerical dispersion inherent to the MOLs is closely related to the semi-discrete strategy. As long as the higher modes in the solution can not be resolved by the given spatial discretization, numerical dispersion occurs in the solution. Another disadvantage of the MOL procedures lies in the difficulty in designing algorithms that accurately capture discontinuities and sharp gradients in the solutions. In the region where high gradients or discontinuities exist, an extreme fine discretization or a stabilization algorithm has to be applied [11, 22] to prevent unphysical oscillations. A detailed discussion with respect to the applications and difficulties of the MOL can be found in [1, 35].

1.3.2 Penalty discontinuous Galerkin method

The idea of using the finite element approximation in the temporal domain as well as the spatial domain can be traced back to the work of Argyris & Scharpf [2], Fried [37] and Oden [48]. Employing discontinuous finite element approximations in time was first proposed by Hulbert & Hughes [39, 40, 41, 42]. A remarkable contribution of them is to introduce the Least Square approach as an additional penalty term to enforce the continuities between the time intervals. Due to the employment of the penalty term, this kind of method and similar ones were later classified to the penalty type Discontinuous Galerkin method (PDG).
The main procedure of PDG contains two steps. The first step is identical to the MOL, i. e. using the finite element method to produce an ODE system which is

similar to eq. (3). In the next step, discontinuous approximations in time for the primary variables $\mathbf{U}$ are employed. The inconsistent quantities, i. e. jumps, at the discrete time level t_n ($t_0 < \cdots < t_n < \cdots < T$) is denoted by

$$[\![\mathbf{U}(t_n)]\!] = \mathbf{U}^+(t_n) - \mathbf{U}^-(t_n), \quad \text{with} \quad \mathbf{U}^{\pm}(t_n) = \lim_{\epsilon \to 0^+} \mathbf{U}(t_n \pm \epsilon) \tag{5}$$

where ϵ represents a positive infinitely small number. Integrating the strong form on a piece of time-slab $Q^n = \Omega \times \mathcal{I}^n$ (detailed illustration will be given in Section 2.3), we obtain the finite element variational form like

$$\int_{\mathcal{I}^n} \left\{ \left(\mathbf{M}\ddot{\mathbf{U}} - \mathbf{D}\dot{\mathbf{U}} + \mathbf{K}\mathbf{U} \right) \cdot \delta\dot{\mathbf{U}} \right\} \mathrm{d}t + f([\![\mathbf{U}(t_n)]\!] \cdot \delta\mathbf{U}) = \int_{\mathcal{I}^n} \left(\mathbf{F} \cdot \delta\dot{\mathbf{U}} \right) \mathrm{d}t \tag{6}$$

where $\delta\mathbf{U}$ represents the test function and $f([\![\mathbf{U}(t_n)]\!] \cdot \delta\mathbf{U})$ is a penalty function depending on the amount of jumps $[\![\mathbf{U}(t_n)]\!]$. In structural dynamics, this function usually depends on the inner product of strain-energy [42]. Furthermore, in order to reduce or to eliminate the unphysical oscillation nearby the discontinuities, an additional stabilization operator, which has the Least Square form, was added to eq. (6). The Least Square operator can be derived by

$$\int_{\mathcal{I}^n} ([\![\mathbf{U}]\!] \cdot \delta\mathbf{U})^2 \rightsquigarrow \min \rightarrow 2 \int_{\mathcal{I}^n} ([\![\mathbf{U}]\!] \cdot \delta\mathbf{U}) = 0 \rightarrow \int_{\mathcal{I}^n} ([\![\mathbf{U}]\!] \cdot \delta\mathbf{U}) = 0. \tag{7}$$

The resulting finite element weak form reads

$$\int_{\mathcal{I}^n} \left\{ \left(\mathbf{M}\ddot{\mathbf{U}} - \mathbf{D}\dot{\mathbf{U}} + \mathbf{K}\mathbf{U} \right) \cdot \delta\dot{\mathbf{U}} \right\} \mathrm{d}t + f([\![\mathbf{U}(t_n)]\!] \cdot \delta\mathbf{U}) + \int_{\mathcal{I}^n} ([\![\mathbf{U}]\!] \cdot \delta\mathbf{U}) = \int_{\mathcal{I}^n} \left(\mathbf{F} \cdot \delta\dot{\mathbf{U}} \right) \mathrm{d}t. \tag{8}$$

More extensive studies of the PDG method with respect to the computational effort, stability and convergence properties were given in the work of Johnson [43] and French [36]. Li & Wiberg [45] proposed an adaptive space-time PDG method for the applications in the structural dynamics analysis. Huang & Costanzo [38] suggested a space-time discontinuous Galerkin method for elasto-dynamic problems depending on strain discontinuities. A hybrid discontinuous/interface Galerkin method was investigated by Mergheim *et al.* to model damage phenomena [46]. More recently, Kuhl & Meschke developed a discontinuous time-integration method and applied it to the non-linear dissolution processes [44].
Despite the great success of the PDG method in the applications of structural engineering, there are some drawbacks that can not be neglected:

- Semi-discrete formulations lead to strong numerical dispersion in case higher modes exist in the solution.
- The choice of the penalty function $f([\![\mathbf{U}, \delta\mathbf{U}]\!])$ depends on the statement of

the physical application, e. g. on the inner product of the strain-energy for the structural dynamics. No universal setting for the penalty function is available.

- The Least Square setting is often necessary to enforce the stability of the numerical solution nearby the discontinuities or sharp gradients. However, in regions where the solution is smooth, strong numerical dissipation is introduced by this term.

With respect to the above points, the objective of this thesis is to study a more general space-time Galerkin scheme, which enables coupled space-time integration and is independent of the artificial penalty functions. The resulting numerical scheme is able to capture the physical discontinuities and to resolve sharp gradients in the solution efficiently.

2 Space-time discontinuous Galerkin method

In this thesis we focus on the discontinuous Galerkin (DG) methods employing flux treatments to weakly fulfil the continuity condition. The DG method using numerical fluxes rather than penalty functions to enforce the interelement continuity has gain more and more attention in last decades. Since no more artificial penalty function is involved, this kind of approaches is applicable to a wide range of engineering problems. Furthermore, we abandon the semi-discrete formulation, but construct the finite element problem on a coupled space-time domain. The resulting space-time DG method has advantages in less numerical damping and dispersion, and it is able to efficiently capture sharp gradients or even discontinuities in the solution. In the following, since the techniques of the spatial and temporal flux treatments are not all the same, we discuss the different treatments separately.

2.1 Discontinuous Galerkin method in time

With a discontinuous Galerkin method in time, we are seeking for the numerical solution on the temporal domain $\mathcal{I} = [t_0, T]$. To do this, we first discretisize the time domain $\mathcal{I}$ into a sequence of time intervals $\mathcal{I}^n = (t_n, t_{n+1}]$, with $t_0 < \cdots < t_n < t_{n+1} < \cdots < T$. Analog to conventional time-stepping approaches, the numerical solution is achieved subsequently on each time interval $\mathcal{I}^n$. The equations to be solved on each time interval $\mathcal{I}^n$ are decoupled from those of the others. For the initial step $n = 0$, the input information comes from the given initial condition while for the successive steps, the data obtained at the end of the previous time interval $\mathcal{I}^{n-1}$ is used as initial conditions for the current computation.
Analog to the PDG approaches, due to the employment of discontinuous approximations, inconsistent values at discrete time levels occur. Similarly, we define the jump of a variable ϕ at time t_n by

$$[\![\phi]\!](t_n) = \phi^+(t_n) - \phi^-(t_n), \quad \text{with} \quad \phi^\pm(t_n) = \lim_{\epsilon \to 0^+} \phi(t_n \pm \epsilon), \tag{9}$$

in which ϵ denotes a positive infinitely small number. As have mentioned before, the continuity between the time intervals is enforced weakly by the flux terms. In the following, we will discuss in detail the flux treatment applied in the time domain.

2.1.1 *Upwind* flux for the first-order system

Using *upwind* flux to enforce the interelement continuity was originally a technique used in the finite volume method. It was introduced to the DG method by Reed & Hill [51] in 1970s. This technique has been widely used to solve first-order differential equations in space. Among others, Bassi & Rebay [4] developed a high-order accurate spatial DG method for solving the compressible Navier-Stokes equation. Cockburn and co-workers investigated the Local Discontinuous Galerkin (LDG) method for solving convection-diffusion equations [20]. By employing the Runge-Kutta scheme as an appropriate time-stepping algorithm, they developed a more general Runge-Kutta Discontinuous Galerkin (RKDG) method [16, 17, 18, 19, 21]. Further studies concerning error estimates were done by Castillo *et al.* [12, 13]. So far, applications of the *upwind* flux are mostly restricted to the spatial domain. Only few studies concerning the extension of this flux in the temporal domain have been done. In Paper A, we applied the *upwind* flux treatment in the time domain to develop a coupled time-discontinuous Galerkin method (DGT). The DGT method has been successfully applied to the prototype equations as well as to the application of the dynamical analysis within the two-phase porous material.
Here we illustrate the main idea of this flux treatment with a simple ODE example like

$$\dot{u} = f(t)\, u(t), \quad t \in \mathcal{I} = [t_0, T], \quad u(t_0) = u_0. \tag{10}$$

We are seeking for an approximation u_h to u with the discontinuous Galerkin method, i. e. $u_h \in \mathcal{V}$, where $\mathcal{V}$ denotes the function space consisting of discontinuous polynomials in time. According to a Bubnov Galerkin approach, we obtain the weak form of the above equation by multiplying eq. (10) with a test function $\delta u_h \in \mathcal{V}$ and then integrating over a piece of time interval $\mathcal{I}^n$

$$\int_{\mathcal{I}^n} \left\{ \dot{u}_h\, \delta u_h - f(t)\, u_h\, \delta u_h \right\} \mathrm{d}t = 0. \tag{11}$$

Moreover, applying integration by parts in time, the above equation yields

$$\int_{\mathcal{I}^n} \left\{ -u_h\, \delta \dot{u}_h - f(t)\, u_h\, \delta u_h \right\} \mathrm{d}t + \left(\breve{u}_h\, \delta u_h \right)\big|_{t_n}^{t_{n+1}} = 0. \tag{12}$$

We denote that for a continuous approximation of u_h, $\breve{u}_h$ represents the quantity of u_h at time t_n (or t_{n+1}). However, according to a discontinuous approximation over adjacent time intervals, inconsistent values of u_h occur at the discrete time level t_n.

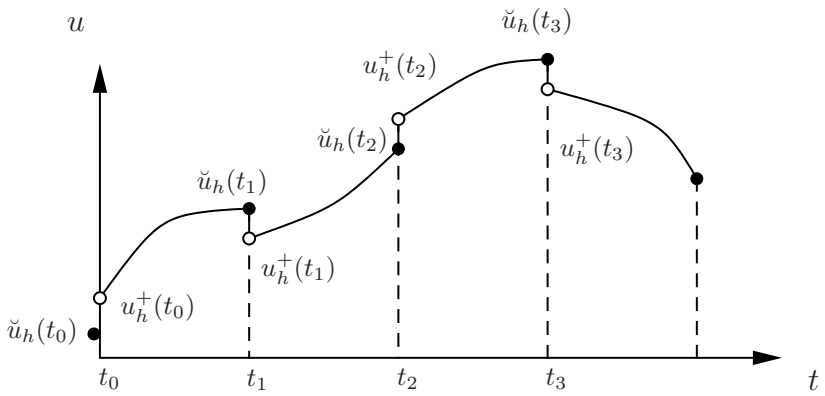

Figure 4: Distribution of the displacement u_h in time, due to the employment of discontinuous approximations, inconsistent values at each time level t_n occur, $\breve{u}(t_n)$ represents the *upwind* flux of u_h at time t_n.

Here, $\breve{u}_h$ represents the numerical flux of u_h on the border of time interval $\mathcal{I}^n$. We employ here the *upwind* flux for describing $\breve{u}_h$, so that

$$\breve{u}_h(t_n) = \begin{cases} u_0, & \text{if} \quad n = 0, \\ u_h^-(t_n) & \text{otherwise} \end{cases} \tag{13}$$

with

$$u_h^{\pm}(t_n) = \lim_{\epsilon \to 0^+} u_h(t_n \pm \epsilon). \tag{14}$$

Obviously, such definition makes sense, since for the ODE, the information travels "from the past into future". For the initial time step, $\breve{u}_h(t_0)$ equals the given initial condition u_0, while for the successive steps $t_n > t_0$, $\breve{u}_h(t_n)$ equals $u_h^-(t_n)$ which is the numerical solution obtained at the end of previous time interval $\mathcal{I}^{n-1}$, see Figure 4.

Inserting the *upwind* definition of $\breve{u}_h$ into eq. (12), the weak form on the time interval $\mathcal{I}^n$ yields

$$\int_{\mathcal{I}^n} \Big\{ - u_h \, \delta \dot{u}_h - f(t) \, u_h \, \delta u_h \Big\} \mathrm{d}t + u_h^-(t_{n+1}) \, \delta u_h = \breve{u}_h(t_n) \, \delta u_h. \tag{15}$$

We remark that in the above expression, the quantity $\breve{u}_h(t_n)$ is always known and serves as input information for the computation on the current time interval $\mathcal{I}^n$. In eq. (15), $u_h^-(t_{n+1}) \, \delta u_h$ stands for the contribution on the upper bound of interval $\mathcal{I}^n$, which can be added up into the matrix system resulting from the integration over $\mathcal{I}^n$ accordingly. Obviously, higher order approaches can be achieved by employing higher order polynomials for the approximation of the primary unknown u_h, see Paper A.

Moreover, we denote that using the *upwind* flux for describing $\breve{u}_h$ leads to good numerical results. However, depending on the practical applications, other choices for the numerical flux $\breve{u}_h$ are possible and may also result in excellent solutions. More detail can be found in [15].
We denote, however, as for an ODE system, it does not make any difference to specify the spatial and temporal fluxes. A difference occurs only when we are dealing with a PDE system, in which we employ this *upwind* flux treatment in time to enforce the continuities between the adjacent time-slabs. More details concerning the space-time FEM will be discussed later in Section 2.3.

2.1.2 Flux treatment for the second-order system

Although the *upwind* flux discussed above gives rise to a very good method, its applications are strictly restricted to first-order equations. According to the knowledge of the author, there is no satisfactory second-order flux treatment available yet. The second-order equation is usually solved by means of an order-reduction approach, in which the displacement and its velocity are solved simultaneously within a matrix system, cf. eq. (7). In Paper A, we applied this order-reduction technique to rewrite the second-order time-dependent equation into an equation-system of two first-order equations, which was in turn solved by the DGT method. Although this order-reduction technique leads to good numerical results, it has to be mentioned that the computational effort for solving an equation-system of two governing equations is much greater than that of a single equation. In Paper B, we developed a novel Embedded Velocity Integration (EVI) technique, in that the direct solution of the displacement is circumvented via an embedded consistent integration of the rate term, i. e. velocity and solve the resulting first-order equation with the unknown velocity with the DGT method. The displacement is computed in a post-processing step via a consistent integration of the velocity. Since there is no further auxiliary equation involved, the size of the algebraic system remains the same as those of a single-field one, which makes the method very attractive.
Next, we illustrate the basic idea of the EVI approach with a simple second-order ODE like

$$\ddot{u}(t) - f(t)\,u(t) = 0, \quad t \in \mathcal{I}, \quad u(t_0) = u_0, \quad \dot{u}(t_0) = v_0, \tag{16}$$

with $\ddot{u}(t)$ and $\dot{u}(t)$ denote the acceleration and velocity of the displacement u, respectively. The kinematic relation for the given equation reads

$$\dot{u}(t) = v(t), \tag{17}$$

where $v(t)$ represents the velocity. For a conventional order-reduction method, this kinematic relation serves as an additional governing equation, leading to a first-order equation-system with the primary unknowns in both displacement u and its velocity

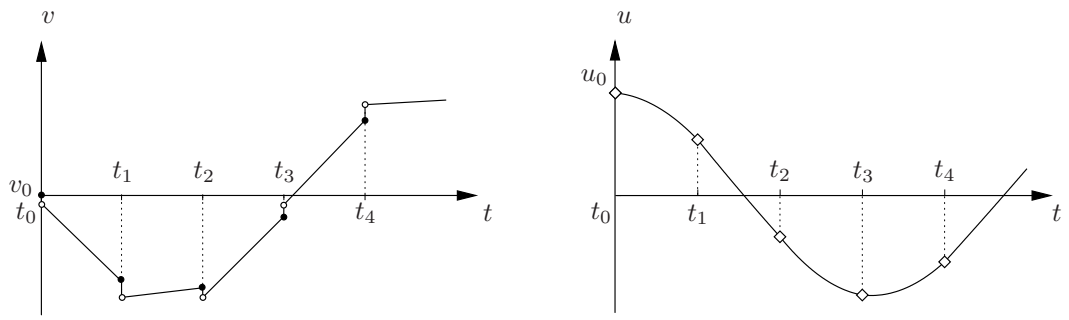

(a) velocity (b) displacement

Figure 5: Distribution of the displacement u and its velocity v: (a) Discontinuous approximations for v results in inconsistent values at each t_n; (b) Continuous distribution of displacement u according to the integral of velocity is achieved.

v, cf. eq. (4). However, according to the EVI technique, instead of introducing an additional governing equation, we embed this kinematic relation directly into eq. (16), which yields

$$\dot{v}(t) - f(t)\, u(t) = 0, \quad t \in \mathcal{I}, \quad u(t_0) = u_0, \quad v(t_0) = v_0. \tag{18}$$

Obviously, there are two primary unknowns u and v in the above equation. However, taken into consideration that for an arbitrary time t, $(t_n < t < t_{n+1})$, the displacement $u(t)$ can be expressed by integrating eq. (17) to an arbitrary time level t $(t_n < t < t_{n+1})$, such that

$$u(t) = \tilde{u}(t_n) + g_u(t), \quad \text{with} \quad g_u(t) = \int_{t_n}^{t} v(t)\, \mathrm{d}t \qquad (t_n < t < t_{n+1}). \tag{19}$$

Here $\tilde{u}(t_n)$ represents the quantity of u at the lower bound of the time interval $\mathcal{I}^n$, i. e. t_n, which is given by

$$\tilde{u}(t_n) = \begin{cases} u_0, & \text{if} \quad n = 0, \\ u(t_n) & \text{otherwise.} \end{cases} \tag{20}$$

Note that since the displacement is constructed as an integral of the velocity, independent of the approximation strategy of the velocity v, its distribution over the time domain is always continuous. Figure 5 shows exemplary the distributions of u according to a discontinuous linear approximation of velocity v. Therefore, for $n > 0$, the quantity of $\tilde{u}(t_n)$ is identical to the solution obtained at the end of previous time interval $\mathcal{I}^{n-1}$, while for the initial step, i. e. $n = 0$, $\tilde{u}_n$ equals the given initial condition u_0.
Inserting eq. (19) into eq. (18), we obtain an expression that contains only the un-

known velocity v as

$$\dot{v} - f(t)\Big(\tilde{u}(t_n) + g_u(t)\Big) = 0, \quad t_n < t < t_{n+1}. \tag{21}$$

So far we have accomplished an art of "order-reduction" in the sense that the second-order equation with the unknown displacement u is now transformed into a first-order equation with the unknown velocity v. In contrast to the conventional order-reduction technique, here, by embedding the kinematic relation implicitly into the governing equation, the resulting algebraic system retains the same dimension as a single field one, which makes the method numerically very efficient.
Next, we seek for a finite element solution $v_h \in \mathcal{V}$ to v on each time interval $\mathcal{I}^n$. Multiplying eq. (20) with the test function $\delta v_h \in \mathcal{V}$ and integrating over the time interval $\mathcal{I}^n$, we obtain the finite element weak form like

$$\int_{\mathcal{I}^n} \Big\{ \dot{v}_h \, \delta \, v_h - f(t) \, (\tilde{u}(t_n) + g_u(t)) \, \delta v_h \Big\} \, \mathrm{d}t = 0. \tag{22}$$

Obviously, as for the current time interval $\mathcal{I}^n$, the value $\tilde{u}(t_n)$ represents either the quantity obtained at the end of the previous time interval $\mathcal{I}^{n-1}$ or the given initial condition, cf. eq. (20), which serves as input information for the computation on the current time interval $\mathcal{I}^n$.
Solving eq. (22) with the DGT method mentioned in the previous Section 2.1.1, we further get

$$\begin{aligned} &\int_{\mathcal{I}^n} \Big\{ - v_h \, \delta \dot{v}_h - f(t) \, g_u(t) \, \delta v_h \Big\} \, \mathrm{d}t + v_h^-(t_{n+1}) \, \delta v_h \\ &= \breve{v}_h(t_n) \, \delta v_h + \tilde{u}_h(t_n) \int_{\mathcal{I}^n} f(t) \, \delta v_h \, \mathrm{d}t, \end{aligned} \tag{23}$$

where $\breve{v}_h(t_n)$ represents the *upwind* flux of the velocity v_h at time t_n, cf. eq. (13). Bear in mind that g_u itself denotes an integral of v_h over $[t_n, t]$ $(t_n < t < t_{n+1})$, see eq. (19). Therefore, in eq. (23) there exists a double integration of v_h. Obviously, a consistent integration scheme for the evaluation of g_u and the velocity v_h is essential for the accuracy and stability of the proposed method. According to the finite element strategy, the integrations are evaluated by means of the Gauss quadrature, in which only discrete quantities of the function at Gaussian points are considered. Such properties further simplified the integration strategy of g_u, where the integration upper bound t $(t_n < t < t_{n+1})$ can be replaced by the corresponding position of Gaussian point. A detailed discussion concerning the integration technique of g_u is given in Paper B.
Solving eq. (23) for v_h, the displacement $u_h(t_{n+1})$ is achieved in a post processing

step like

$$u_h(t_{n+1}) = \tilde{u}_h(t_n) + \int_{\mathcal{I}^n} v_h \, \mathrm{d}t. \tag{24}$$

Owning to the finite element approximation of the velocity v_h over time, such an operation can be easily performed within a conventional FE program.
Furthermore, it has to be mentioned, in the current work, we have used a DGT method as the solution strategy for eq. (22). However, the idea of replacing the displacement u_h with an integral of the velocity v_h is independent of the chosen time-stepping strategy, i. e. DGT method. Given a finite element approximation for the velocity v_h in time, it is always possible to evaluate the displacement u_h as a sum of the integral of the velocity v_h and the initial value $\tilde{u}_h(t_n)$. In other words, it is also possible to employ a continuous approximation for v_h in time. As long as the velocity v_h can be solved properly, so can be done for the displacement u_h.
So far we have discussed the main strategies of solving first- and second-order time-dependent problems with the DGT method. By the use of the EVI technique, the second-order equation is rewritten into a first-order one, which is in turn solved by the DGT method. Hereby, we briefly summarize the main properties of the DGT method:

- With the use of the *upwind* flux to enforce the continuity condition between adjacent time intervals, no artificial penalty term is involved.
- High order solutions may be achieved by employing high order polynomials in time.
- Jumps across adjacent time intervals can be used as a easy error indicator for the adaptive strategy.

The first two properties have been drawn in the above context. As for the third one, although using jumps as error indicator for an adaptive strategy is not new in the DG community, a strict proof of this property has not been properly discussed in most available literatures. In order to illustrate this point, we integrate eq. (12) by parts to get

$$\int_{\mathcal{I}^n} \left\{ \dot{u}_h \, \delta u_h - f(t) \, u_h \, \delta u_h \right\} \mathrm{d}t + (\breve{u}_h - u_h)|_{t_n}^{t_{n+1}} = 0. \tag{25}$$

Or, equivalently,

$$\int_{\mathcal{I}^n} \mathcal{R}(u_h) \, \delta u_h \, \mathrm{d}t = (u_h - \breve{u}_h)|_{t_n}^{t_{n+1}} \tag{26}$$

whereby $\mathcal{R}(u_h) = \dot{u}_h - f(t)u_h$ represents the residual. Moreover, bearing in mind the flux definition of $\breve{u}_h$ in eq. (13), we further get

$$\int_{\mathcal{I}^n} \mathcal{R}(u_h)\, \delta u_h \, \mathrm{d}t = [\![u_h]\!](t_n). \tag{27}$$

Here we can see that the jump $[\![u_h]\!](t_n)$ at t_n is nothing but the integral of the residual over the interval $\mathcal{I}^n$. This is a simple evidence to shown that the jumps can serve as a reliable error indicator for adaptive strategies, cf. [15].

2.2 Discontinuous Galerkin method in space

In the next, we discuss the flux treatments within a spatial discontinuous Galerkin (DGS) method. Hereby, the technique involved is slightly different to those used in the temporal domain. The convection term is handled by a similar *upwind* flux as discussed before, while the diffusion term is solved by the average flux treatment combined with flux-weighted constraints.

2.2.1 Spatial flux treatment

Given the convection-diffusion equation like

$$\dot{u} - \operatorname{div}\big(\mathbf{D} \cdot \operatorname{grad} u(\mathbf{x}, t) - \mathbf{q}\, u(\mathbf{x}, t)\big) = 0, \quad \mathbf{x} \in \Omega,\, t \in \mathcal{I}, \quad u(t_0) = u_0 \tag{28}$$

where $\mathbf{D}$ represents the diffusion tensor and $\mathbf{q}$ is the convection vector. The boundary of Ω consists of non-overlapping Neumann part Γ_{N} and Dirichlet part Γ_{D}, with $\partial\Omega = \Gamma_{\mathrm{N}} \cup \Gamma_{\mathrm{D}}$ and $\Gamma_{\mathrm{N}} \cap \Gamma_{\mathrm{D}} = \emptyset$. The associated boundary conditions are given as

$$\begin{aligned} (\mathbf{D} \cdot \operatorname{grad} u - \mathbf{q}\, u) \cdot \mathbf{n} &= \bar{f}, \qquad && \mathbf{x} \in \Gamma_{\mathrm{N}}, \\ u &= u_D, && \mathbf{x} \in \Gamma_{\mathrm{D}}, \end{aligned} \tag{29}$$

where $\mathbf{n}$ denotes the unit outward normal vector on the boundary $\partial\Omega$.
Before proceeding to illustrate the different flux treatments applied in space, we first declare some notations. Let us define $\mathcal{E}_h = \{E_1, E_2, \ldots, E_{N_{\mathrm{E}}}\}$ be regular subdivisions of the domain $\Omega_h \subset \Omega$. N_{E} is the total number of subdivisions. The edges of each subdivision E_i are denoted by ∂E_i. Moreover, we introduce the union of all edges in $\mathcal{E}_h$ as $\mathcal{K}_h = \{e_1, e_2, \ldots, e_{N_{\mathrm{K}}}\}$, in which N_{K} denotes the total number of edges. Therefore, the interior edges can be specified by

$$\Gamma_{\mathrm{int}} = \bigcup_{E_i, E_j \in \mathcal{E}_h}^{N_{\mathrm{int}}} (\partial E_i \cap \partial E_j), \quad (i \neq j). \tag{30}$$

Herein, N_{int} is the total number of the interior edges. The outward normal vector on the boundary of subdivision ∂E_i that coincides with the edge e_k is denoted by

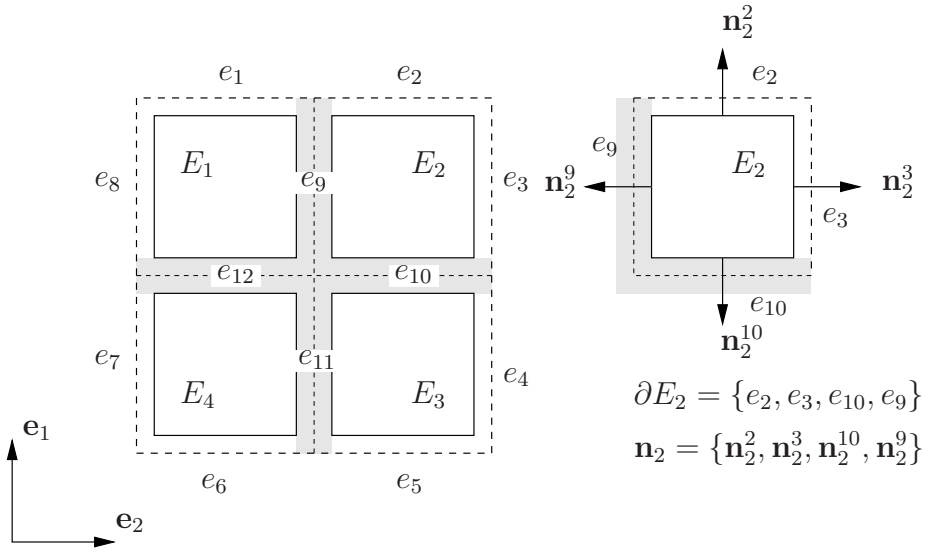

Figure 6: A finite element patch of four quadrilaterals $\mathcal{E}_h = \{E_1 \sim E_4\}$ with the boundaries $\mathcal{K}_h = \{e_1 \sim e_{12}\}$, among which the interior edges are $\{e_9 \sim e_{12}\}$

$\mathbf{n}_i^k$. The union of all outward vectors on ∂E_i is represented by $\mathbf{n}_i$. In Figure 6 we depicted examplarily one such finite element patch with four quadrilaterals.
In addition, according to the direction of the flow $\mathbf{q}$ over the element boundary, we can divide the edges $\mathcal{K}_h$ into the inflow part $e_k \in \mathcal{K}_h^+$ and the outflow part $\mathcal{K}_h^-$ by

$$\mathcal{K}_h^+ = \{\mathbf{x} \in (e_k \cap \partial E_j) : \mathbf{q} \cdot \mathbf{n}_j^k > 0, \quad j < N_E\}, \quad \mathcal{K}_h^- = \mathcal{K}_h \setminus \mathcal{K}_h^+. \tag{31}$$

Moreover, assume the normal vector $\mathbf{n}_j^k = n_\alpha \, \mathbf{e}_\alpha$[1], we defined the operator $\{\mathbf{n}_j^k\}$ of the vector $\mathbf{n}_j^k$ as $\{\mathbf{n}_j^k\} = (n_\alpha \, \mathbf{e}_\alpha \cdot \mathbf{e}_\beta)$, where $\mathbf{e}_\alpha$ and $\mathbf{e}_\beta$ are the basis vectors. For each interior edge $e_k = \partial E_i \cap \partial E_j$, the direction of the positive operator ($\{\mathbf{n}_i^k\} > 0$ or $\{\mathbf{n}_j^k\} > 0$) defined uniquely the jump on this edges. For $\{\mathbf{n}_j^k\} > 0$, jumps of an arbitrary scalar quantity and a vector quantity on this edge e_k yields

$$[\![\psi(\mathbf{x})]\!]_{e_k} = \psi_i(\mathbf{x}) - \psi_j(\mathbf{x}), \tag{32}$$

$$[\![\Psi(\mathbf{x})]\!]_{e_k} = \Psi_i(\mathbf{x}) - \Psi_j(\mathbf{x}), \tag{33}$$

in which $\psi_l(\mathbf{x})/\Psi_l(\mathbf{x}) = \{\psi(\mathbf{x})/\Psi(\mathbf{x}), \mathbf{x} \in (e_k \cap \partial E_l)\}$. The average fluxes on this edge are given by

$$\langle \psi \, \mathbf{n} \rangle|_{e_k} = \frac{1}{2}\big(\psi_i \, \mathbf{n}_j^k + \psi_j \, \mathbf{n}_j^k\big), \quad \{\mathbf{n}_j^k\} > 0, \tag{34}$$

$$\langle \Psi \cdot \mathbf{n} \rangle|_{e_k} = \frac{1}{2}\big(\Psi_i \cdot \mathbf{n}_j^k + \Psi_j \cdot \mathbf{n}_j^k\big), \quad \{\mathbf{n}_j^k\} > 0. \tag{35}$$

[1]Here, $n_\alpha \, \mathbf{e}_\alpha$ is the summation over the basis vector $\mathbf{e}_\alpha$ with $\mathbf{n}_\alpha \, \mathbf{e}_\alpha = n_1 \, \mathbf{e}_1 + n_2 \, \mathbf{e}_2 + n_3 \, \mathbf{e}_3$.

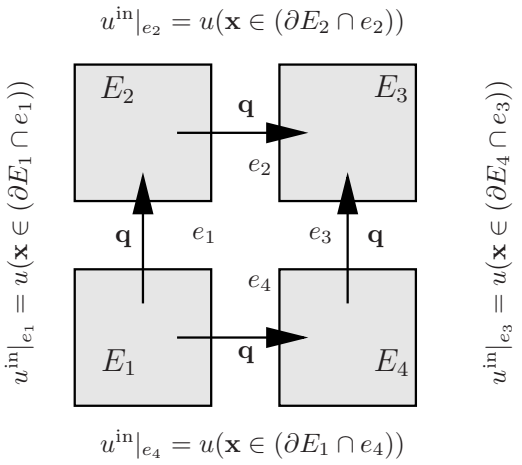

Figure 7: *Upwind* flux u^{in} in space, $\mathbf{q}$ represents the direction of the flow, the flux on each element interfaces equals its inflow part u^{in}.

Note that the average flux of a scalar quantity ψ is a vector, while the average flux of a vector Ψ is a scalar.
In analog to the *upwind* flux definition in time, the spatial *upwind* flux on edge e_k is defined by

$$\psi^{\text{in}}|_{e_k} = \psi\big(\mathbf{x} \in (e_k \in \mathcal{K}_h^+)\big), \tag{36}$$

$$\Psi^{\text{in}}|_{e_k} = \Psi\big(\mathbf{x} \in (e_k \in \mathcal{K}_h^+)\big). \tag{37}$$

The physical interpretation of the spatial *upwind* flux can be given as follows: the flux of ψ^{in} (Ψ^{in}) on the edge e_k always equals the flux on its inflow part $e_k \in \mathcal{K}_h^+$, cf. Figure 7. Such definition makes sense, since the fluxes can not be generated from nothing in the element interfaces.
After declaring some important notations, we proceed to the numerical treatments for the diffusion and convection term in detail.
The convection term is treated in a similar way as the first-order time derivative term in time, whereby the quantity on the element boundaries is substituted by its *upwind* flux u^{in}. For the sake of simple notations, we suppose at the moment that $\mathbf{D} = \mathbf{0}$ in eq. (28). Given the functional space $\mathcal{W}$ which is discontinuous over the element interfaces, the finite element approximation of $u_h \in \mathcal{W}$ to u can be obtained by solving the following weak form,

$$\begin{aligned}\sum_{i=1}^{N_{\text{E}}} \Big\{ \int_{E_i} \left\{ \dot{u}_h\, \delta u_h - u_h\, (\mathbf{q} \cdot \operatorname{grad} \delta u_h) \right\} \mathrm{d}v \\ + \int_{\partial E_i \setminus \Gamma_{\text{D}}} (\mathbf{q} \cdot \mathbf{n}_i)\, u_h^{\text{in}}\, \delta u_h \,\mathrm{d}a \Big\} = \sum_{e_k \in \Gamma_{\text{D}}} \int_{e_k} (\mathbf{q} \cdot \mathbf{n})\, u_D\, \delta u_h \,\mathrm{d}a\end{aligned} \tag{38}$$

whereby $\delta u_h \in \mathcal{W}$ represents the corresponding test function. Note that herein the Dirichlet boundary condition is assigned as the inflow flux on the boundary rather than a strict assignment, i. e. $\Gamma_{\mathrm{D}} \in \mathcal{K}_h^+$, cf. [5].
Next, we discuss about the numerical treatment of the diffusion term ($\mathbf{D} \neq \mathbf{0}$). The techniques of treating the second-order diffusion term can be divided into two major classes. One is the so-called Local Discontinuous Galerkin (LDG) method, developed mainly by Cockburn and his co-workers [16, 17, 18, 19, 21]. The essential strategy of the LDG method is to employ the order-reduction technique in space to produce an equation-system consisting of first-order differential equations. The resulting first-order equation-system is in turn handled by the *upwind* flux treatment in space. The other one, innovated by Nitsche [47], is to solve the second-order equation directly with the help of flux-weighted constraints. Obviously, the computational cost of using discontinuous Galerkin methods in space is higher than that of the continuous Galerkin method, in that a much larger algebraic system is resulted by the discontinuous approximations over the element interfaces. According to the LDG method, due to the employment of the order-reduction technique in space, which results in an equation-system of both the primary unknown and its gradient, an even larger algebraic system is resulted, which increases the computational effort further. However, a significant advantage of LDG is that by using the *upwind* flux treatment to enforce interelement consistency, no artificial penalty factor has to be involved. This was not the case in the original form of Nitsche's approach [47]. Although Nitsche's formulation intended to solve the diffusion equation directly without introducing additional governing equations. It was usually necessary to employ a penalty term to ensure the uniqueness of the solution. In the late last century, lots of efforts had been paid to identify the penalty term of this approach, see e. g. [3, 28, 55]. However, due to the complexity in determining the penalty factor for practical applications, investigations are restricted to academical examples. This situation has been changed by Baumann & Oden [5, 49] in the 1990s, when they developed Nitsche's approach to be independent of any kind of penalty terms. Their evolutionary contribution has invoked new attention on the flux-weighted DGS method, made it the most popular approach in the community.
Next, we illustrate the technique of Nitsche and Baumann & Oden in detail. For the sake of a simple illustration, we consider at the moment a domain Ω with only two adjacent subdivisions Ω_E and Ω_F, see Figure 8. u_E and u_F are the primary unknowns on the subdomains Ω_E and Ω_F, respectively. In order to make the expression as simple as possible, we assume now $\mathbf{q} = \mathbf{0}$ in eq. (28) and furthermore, we omit the time derivative term to consider only the solution procedure for the steady state problem. With δu_E and δu_F denoting the corresponding test functions, the

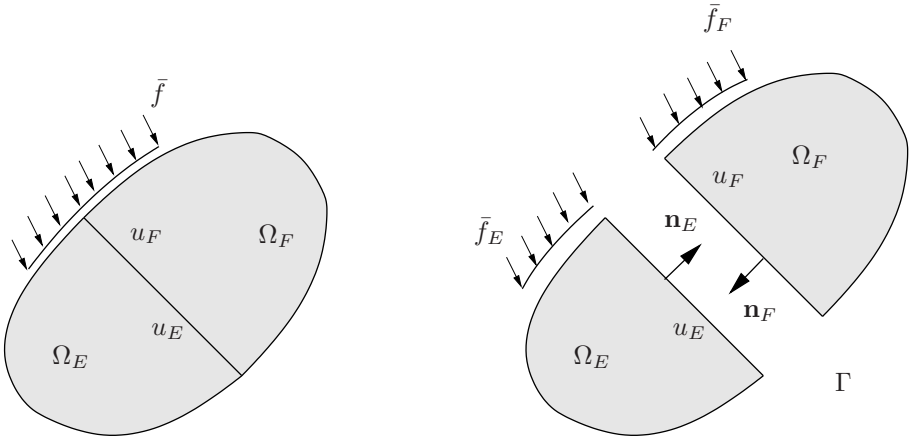

Figure 8: Two subdomains Ω_E and Ω_F as division of the domain Ω with an interior boundary Γ. $\mathbf{n}_E$ and $\mathbf{n}_F$ represent the unit outward normal vector on the interior boundary Γ shared with the subdomain Ω_E and Ω_F, respectively.

weak form on each subdomain can be written as

$$\Omega_E : \int_{\Omega_E} (\mathbf{D} \cdot \operatorname{grad} u_E) \cdot \operatorname{grad} \delta u_E \, \mathrm{d}v - \int_{\Gamma} \left(\mathbf{F}_E \cdot \mathbf{n}_E\right) \delta u_E \, \mathrm{d}a = \int_{\Gamma_{\mathrm{N}}^E} \bar{f}_E \, \delta u_E \, \mathrm{d}a \quad (39)$$

$$\Omega_F : \int_{\Omega_F} (\mathbf{D} \cdot \operatorname{grad} u_F) \cdot \operatorname{grad} \delta u_F \, \mathrm{d}v - \int_{\Gamma} \left(\mathbf{F}_F \cdot \mathbf{n}_F\right) \delta u_F \, \mathrm{d}a = \int_{\Gamma_{\mathrm{N}}^F} \bar{f}_F \, \delta u_F \, \mathrm{d}a \quad (40)$$

where $\mathbf{F}_E = \mathbf{D} \cdot \operatorname{grad} u_E$ and $\mathbf{F}_F = \mathbf{D} \cdot \operatorname{grad} u_F$ are the corresponding diffusion fluxes on the interior boundary Γ, see Figure 8. $\bar{f}_E$ ($\bar{f}_F$) represents the Neumann condition acting on the boundary Γ_{N}^E (Γ_{N}^F) of the subdomains Ω_E (Ω_F) and $\mathbf{n}_E$ ($\mathbf{n}_F$) denotes the unit outward normal vector on Γ, see Figure 8.
Next, we note that in the solution procedure, the following constraints must be fulfilled on the interior boundary Γ:

- The flux equilibrium requires that the sum of the diffusion fluxes on the boundary Γ must vanish, which yields

$$\mathbf{F}_E \cdot \mathbf{n}_E + \mathbf{F}_F \cdot \mathbf{n}_F = 0. \quad (41)$$

- The continuity constraint implies that the jump of the primary unknown has to disappear on the interior boundary,

$$u_F - u_E = 0. \quad (42)$$

Moreover, it is easy to identify that on the interior boundary Γ, there exists $\mathbf{n}_E = -\mathbf{n}_F$. For $\{\mathbf{n}_E\} > 0$, we introduce the Lagrange multiplier λ on this boundary Γ as

$$\lambda = \mathbf{F}_E \cdot \mathbf{n}_E = -\mathbf{F}_F \cdot \mathbf{n}_F, \quad \{\mathbf{n}_E\} > 0. \tag{43}$$

Inserting now the Lagrange multiplier λ into eq. (39) and eq. (40) and multiplying the continuity condition eq. (42) with $\delta\lambda$, we obtain a three fields formulation with the unknowns $\{u_E, u_F, \lambda\}$ like

$$\int_{\Omega_E} (\mathbf{D} \cdot \operatorname{grad} u_E) \cdot \operatorname{grad} \delta u_E \, \mathrm{d}v - \int_{\Gamma} \lambda \, \delta u_E \, \mathrm{d}a = \int_{\Gamma_N^E} \bar{f}_E \, \delta u_E \, \mathrm{d}a, \tag{44}$$

$$\int_{\Omega_F} (\mathbf{D} \cdot \operatorname{grad} u_F) \cdot \operatorname{grad} \delta u_F \, \mathrm{d}v + \int_{\Gamma} \lambda \, \delta u_F \, \mathrm{d}a = \int_{\Gamma_N^F} \bar{f}_F \, \delta u_F \, \mathrm{d}a, \tag{45}$$

$$\int_{\Gamma} (u_F - u_E) \, \delta\lambda \, \mathrm{d}a = 0. \tag{46}$$

Furthermore, we denote that the equation-system (44)-(46) is solvable, if certain criteria are fulfilled. Among others there is the counter condition, which says that the sum of the free parameters n_E (n_F) in u_E (u_F) must not be smaller than those of the λ

$$n_E + n_F \geq n_\lambda, \tag{47}$$

where n_λ denotes the number of free parameters in the approximation of λ. However, this is a necessary but not sufficient condition. Further details on additional conditions are given in [63].
Obviously, introducing the Lagrange multiplier λ as an auxiliary unknown leads to a larger algebraic system, which increases the computational effort. Moreover, the information of λ serves barely as an assistant variable to enforce the continuity constraints eq. (42). In face, only the solution of the primary unknown u_E (u_F) is of interest. Thus, it is desired to substitute the Lagrange parameter λ with an expression of the primary unknown u_E (and u_F) to diminish the computational effort. We observe that the Lagrange multiplier λ measures the diffusion flux on the interior boundary Γ, which can be replaced by the average flux as

$$\lambda = \frac{1}{2}(\mathbf{F}_E + \mathbf{F}_F) \cdot \mathbf{n}_E = \langle \mathbf{D} \cdot \operatorname{grad} u \cdot \mathbf{n} \rangle. \tag{48}$$

However, the equation-system constructed by inserting eq. (48) into eq. (44) and eq. (45) is often unsolvable. Hence, eq. (46) is included as an extra flux-weighted continuity constraint into the equation-system. Note that the continuity constraint eq. (46) works as a penalty term to enforce the continuity on the interface. Without

violating its function, we multiply eq. (46) with a non-zero parameter α ($\alpha = \pm 1$) and add it to eq. (44) and eq. (45), which yields

$$\begin{aligned}
&\int_{\Omega_E} (\mathbf{D} \cdot \operatorname{grad} u_E) \cdot \operatorname{grad} \delta u_E \,\mathrm{d}v - \int_{\Gamma} \langle \mathbf{D} \cdot \operatorname{grad} u \cdot \mathbf{n} \rangle \, \delta u_E \,\mathrm{d}a \\
&\qquad + \alpha \int_{\Gamma} (u_F - u_E) \, \langle \mathbf{D} \operatorname{grad} \delta u \cdot \mathbf{n} \rangle \,\mathrm{d}a = \int_{\Gamma_{\mathrm{N}}^E} \bar{f}_E \, \delta u_E \,\mathrm{d}a, \\
&\int_{\Omega_F} (\mathbf{D} \operatorname{grad} u_F) \cdot \operatorname{grad} \delta u_F \,\mathrm{d}v + \int_{\Gamma} \langle \mathbf{D} \operatorname{grad} u \cdot \mathbf{n} \rangle \, \delta u_F \,\mathrm{d}a \\
&\qquad + \alpha \int_{\Gamma} (u_F - u_E) \, \langle \mathbf{D} \operatorname{grad} \delta u \cdot \mathbf{n} \rangle \,\mathrm{d}a = \int_{\Gamma_{\mathrm{N}}^F} \bar{f}_F \, \delta u_F \,\mathrm{d}a.
\end{aligned} \tag{49}$$

The above weak form is constructed on a system of two subdomains with the primary unknown u (u_E, u_F). To make the above statement more general, for a system of N_{E} subdomains, the weak form can be written as

$$\begin{aligned}
&\sum_{i=1}^{N_{\mathrm{E}}} \int_{E_i} \left\{ (\mathbf{D} \cdot \operatorname{grad} u_h) \cdot \operatorname{grad} \delta u_h \right\} \mathrm{d}v \\
&+ \sum_{k=1}^{N_{\mathrm{int}}} \int_{e_k} \Big\{ \langle \mathbf{D} \cdot \operatorname{grad} u_h \cdot \mathbf{n} \rangle [\![\delta u_h]\!] + \alpha \, [\![u_h]\!] \langle \mathbf{D} \cdot \operatorname{grad} \delta u_h \cdot \mathbf{n} \rangle \Big\} \,\mathrm{d}a \\
&+ \sum_{e_k \in \Gamma_{\mathrm{D}}} \int_{e_k} \Big\{ (\mathbf{D} \cdot \operatorname{grad} u_h \cdot \mathbf{n}) \, \delta u_h + \alpha \, u_h \, (\mathbf{D} \cdot \operatorname{grad} \delta u_h \cdot \mathbf{n}) \Big\} \,\mathrm{d}a \\
&= \sum_{e_k \in \Gamma_{\mathrm{D}}} \int_{e_k} \alpha \, u_D \, (\mathbf{D} \operatorname{grad} \delta u_h \cdot \mathbf{n}) \,\mathrm{d}a + \sum_{e_k \in \Gamma_{\mathrm{N}}} \int_{e_k} \bar{f} \, \delta u_h \,\mathrm{d}a,
\end{aligned} \tag{50}$$

Note that different values of α represents different discontinuous methods. $\alpha = 1$ corresponds to the standard replacement of the flux-weighted constraint, which was first proposed by Nitsche [47]. However the formulation with $\alpha = 1$ is found to be less accurate and mostly instable, such that eq. (49) must be incorporated by an additional penalty term like

$$\int_{\Gamma} \tau [\![u_h \, \mathbf{n}]\!] \cdot [\![\delta u_h \, \mathbf{n}]\!] \,\mathrm{d}a, \tag{51}$$

where τ is a penalty factor. Since, the resulting algebraic system with $\alpha = 1$ is symmetric, this kind of approaches are called Symmetric Interior Penalty Galerkin

method (SIPG). The contribution of Baumann & Oden was to set $\alpha = -1$. Obviously, inverting the sign of the flux-weighted continuity conditions renders a non-symmetric algebraic system. The method was later given the name of Non-Symmetric Interior Penalty Galerkin method (NIPG). One of the significant benefit of setting α with inverse sign is the fact that no more auxiliary variables (i. e. penalty term like (51)) for the stabilization of the method are needed, which leads the method to be very practical. An extensive study concerning the mathematical foundation and the convergence study of the NIPG method is presented in the dissertation of Baumann [5].
Next, respecting both techniques for the diffusion and convection terms, the finite element weak form of eq. (28) reads

$$\begin{aligned}
&\sum_{i=1}^{N_{\mathrm{E}}} \Big\{ \int_{E_i} \left\{ \dot{u}_h \, \delta u_h + (\mathbf{D} \cdot \operatorname{grad} u) \cdot \operatorname{grad} \delta u_h - u_h \, (\mathbf{q} \cdot \operatorname{grad} \delta u_h) \right\} \mathrm{d}v \\
&\qquad + \int_{\partial E_i \setminus \Gamma_{\mathrm{D}}} (\mathbf{q} \cdot \mathbf{n}) \, u_h^{\mathrm{in}} \, \delta u_h \, \mathrm{d}a \Big\} \\
&+ \sum_{k=1}^{N(\Gamma_{\mathrm{int}})} \int_{e_k} \left\{ \langle \mathbf{D} \cdot \operatorname{grad} \delta u_h \cdot \mathbf{n} \rangle \, [\![u_h]\!] - \langle \mathbf{D} \cdot \operatorname{grad} u_h \cdot \mathbf{n} \rangle \, [\![\delta u_h]\!] \right\} \mathrm{d}a \\
&+ \sum_{e_k \in \Gamma_{\mathrm{D}}} \int_{e_k} \left\{ (\mathbf{D} \cdot \operatorname{grad} \delta u_h \cdot \mathbf{n}) \, u_h - (\mathbf{D} \cdot \operatorname{grad} u_h \cdot \mathbf{n}) \, \delta u_h \right\} \mathrm{d}a \\
&= \sum_{e_k \in \Gamma_{\mathrm{D}}} \int_{e_k} \left\{ (\mathbf{D} \cdot \operatorname{grad} \delta u_h \cdot \mathbf{n}) \, u_D + (\mathbf{q} \cdot \mathbf{n}) \, u_D \, \delta u_h \right\} \mathrm{d}a \\
&+ \sum_{e_k \in \Gamma_{\mathrm{N}}} \int_{e_k} \bar{f} \, \delta u_h \, \mathrm{d}a.
\end{aligned} \tag{52}$$

It is also necessary to mention, a very desirable feather of this Spatial Discontinuous Galerkin (DGS) method is that there exists no coupling between the rate term and the spatial fluxes. Hence, the transient problem can be solved in a similar way as those in the MOL, such that the DGS formulation is applied in space to produce the corresponding ODE system which can in turn be solved by finite difference methods, cf. [5, 49]. However, we denote that it is more attractive to solve the PDE with a coupled space-time Galerkin approach, in that finite element approximations in space and in time are employed simultaneously. We will discuss this kind of approaches in the Section 2.3.
The main properties of the DGS method based on the flux treatment can be summarized as below:

- By employing the fluxes on the element interface to enforce interelement con-

sistency, the physical discontinuity can be well resolved given that the interface of the elements coincides with this discontinuity.

- The flux treatment on the boundary provides a natural setting by imposing the inflow and outflow flux rather than a strict Dirichlet boundary condition.
- By setting $\alpha = -1$, no auxiliary penalty operator is necessary for the diffusion term.

Obviously by using discontinuous approximations on the element interfaces, the computational cost of DGS is higher than that the conventional Continuous Galerkin method. However, the simplicity of using parallel computation of the DGS method renders the method to be very attractive in realistic computations, see [55, 64]. The DGS method using flux-weighted constraints has been successfully applied to solving the Navier-Stokes equation [6] and to the modeling of single- and multi-phase flow problems in porous media [52, 53, 54], etc. However, its applications are mostly restricted to the semi-discrete formulations. In the next section, we will discuss a coupled space-time finite element formulation, which enables the finite element discretization in space and in time simultaneously.

2.3 Coupled space-time discontinuous Galerkin method

After declaring the flux treatments in space and in time separately, we focus on the construction of a coupled space-time discontinuous Galerkin method. Unlike the semi-discrete method, whereby the finite element mesh covers only the spatial domain, the proposed space-time Galerkin method is based on a coupled space-time discretization, in which finite element approximations are employed in the spatial and in the temporal domain simultaneously. The space-time domain is constructed by adding the time axis $\mathcal{I}$ orthogonal to the spatial domain Ω, which renders the space-time domain $Q = \Omega \times \mathcal{I}$. Figure 9 shows illustrative examples for the space-time domains constructed on the one-dimensional and two-dimensional spatial domains. Let $\mathcal{I}^n$ be a piece of time interval $\mathcal{I}^n = (t_n, t_{n+1}]$. The time-slab is constructed as $Q^n = \Omega \times \mathcal{I}^n$. According to a space-time finite element formulation, instead of solving the governing equation on the whole space-time domain Q at one time, we seek for numerical solutions on each time-slab Q^n subsequently. In this sense, the resulting numerical scheme is analogical to the MOL, i. e. Euler method, Newmark method, etc. For each time-slab Q^n $(n \geq 1)$ the numerical solution obtained at the end of the previous time-slab Q^{n-1} serves as input information for the current computation. For the first slab Q^0, the input information comes from the given initial condition. The advantage of seeking for the numerical solution on each time-slab subsequently instead of solving equations on the whole space-time domain at one time lies in the fact that smaller system of equations of a single time-slab can be handled much more efficiently than a very large system of the whole space-time domain. The computational effort and hardware requirement increase with the increase of the size of the algebraic system, which makes it inefficient to solve huge

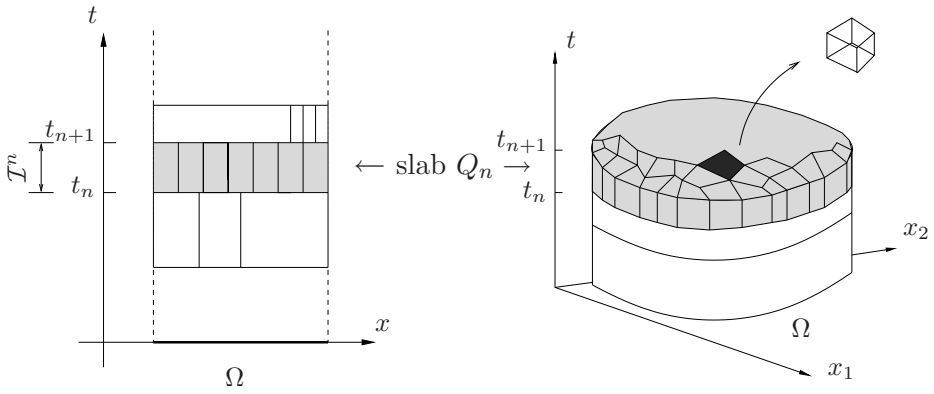

Figure 9: Space-time domain of a one-dimensional and two-dimensional spatial problem, respectively.

equation-systems. Nevertheless, it is possible to increase the size of the time steps without degrading the accuracy by employing higher order polynomials in time. In extreme case, the whole computational domain can be covered by a single time step if wanted.

With respect to the time-stepping strategy, in contrast to the MOL approach, in which time difference algorithm is applied to advance the solution in the time domain, in the space-time method, finite element approximations are employed in the time domain, leading to solutions that fulfils the weak integration form in time. To do this, on each time-slab, the conventional spatial finite element is enhanced with an extra dimension with respect to the approximations in time, leading to the so-called space-time finite element. Figure 10 shows examplarily the space-time finite elements constructed on a one-dimensional and a two-dimensional spatial element. The shape function of the proposed space-time element consists of the tensor product of polynomials in space and in time. One advantage of employing such space-time element is that we are now able to evaluate the spatial and temporal integration at one time

$$\int_{\Omega}\int_{\mathcal{I}^n} (\bullet)\,\mathrm{d}t\,\mathrm{d}v = \int_{Q^n} (\bullet)\,\mathrm{d}Q, \tag{53}$$

which leads to a so-called coupled formulation. This is an essential difference to semi-discrete formulations, i. e. MOL, whereby the evaluation of spatial and temporal integrations are decoupled and are evaluated subsequently. Such a coupled formulation provides the possibility to handle the numerical dispersion resulting from the semi-discrete approaches.

In the next, we illustrate the space-time Galerkin method in a synchronization example which involves all the possible components of a second-order equation (convection diffusion equation)

$$\dot{u} - \mathrm{div}(\mathbf{D}\cdot\mathrm{grad}\,u - \mathbf{q}\,u) = 0, \quad u \in Q = \Omega\times\mathcal{I}. \tag{54}$$

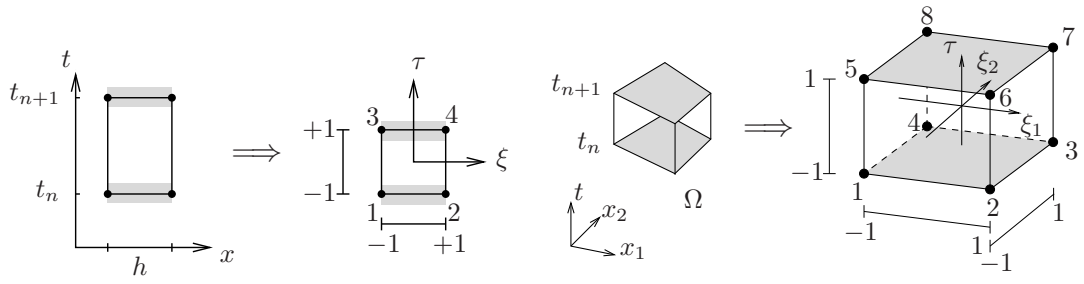

(a) 1-dim (b) 2-dim

Figure 10: Linear space-time finite elements

The associated initial condition is given by

$$u(\mathbf{x}, t_0) = u_0(\mathbf{x}), \quad \mathbf{x} \in \Omega. \tag{55}$$

The boundary condition is given for the non-overlapping Dirichlet part Γ_{D} and the Neumann part Γ_{N} ($\Gamma_{\mathrm{D}} \cup \Gamma_{\mathrm{N}} = \partial\Omega$, $\Gamma_{\mathrm{D}} \cap \Gamma_{\mathrm{N}} = \emptyset$)

$$\begin{aligned} (\mathbf{D} \cdot \operatorname{grad} u(t) - \mathbf{q}\, u(t)) \cdot \mathbf{n} = \bar{f}(t), \qquad & \mathbf{x} \in \Gamma_{\mathrm{N}}, \quad t \in \mathcal{I}, \\ u(t) = u_D(t), \qquad & \mathbf{x} \in \Gamma_{\mathrm{D}}, \quad t \in \mathcal{I}. \end{aligned} \tag{56}$$

In the following, we give the finite element variational form for a time-discontinuous Galerkin (DGT) method, in which discontinuous polynomials are applied in time while the spatial approximations are kept continuous, and the coupled space-time discontinuous Galerkin method (DGST), in which neither the spatial nor the temporal distribution process strong continuity.

2.3.1 Time-discontinuous Galerkin method

First, we solve eq. (54) with the DGT method. Let $\mathcal{P} = \{\mathcal{P}_h(Q^n)\}$ be a family of regular partitions of the time-slab Q^n composing of non-overlapping subdomains

$$Q^n = \bigcup_{i=1}^{N_{\mathrm{E}}} P_h^i, \quad P_h^i = E_i \times \mathcal{I}^n, \tag{57}$$

where E_i denotes the spatial subdomains that is identical to a standard finite element in space. N_{E} denotes the total number of subdomains. The functional space $\mathcal{V}(u_h)$ on the time-slab Q^n is given by

$$\mathcal{V}(u_h) = \left\{ \begin{array}{l} u_h(\mathbf{x}, \bullet) \in L^2(\Omega) \\ u_h(\bullet, t) \in L^2(\mathcal{I}^n) \end{array} \right\}. \tag{58}$$

Proceeding from the method discussed in Section 2.1, the variational form of a space-time method can be written as

Find $u_h \in \mathcal{V}(u_h)$, such that $\forall \delta u_h \in \mathcal{V}(\delta u_h)$, there exists

$$B_{\mathrm{DGT}}(u_h, \delta u_h) = L_{\mathrm{DGT}}(\delta u_h). \tag{59}$$

The bilinear form $B_{\mathrm{DGT}}(u_h, \delta u_h)$ and the linear form $L_{\mathrm{DGT}}(\delta u_h)$ are given by

$$\begin{aligned} B_{\mathrm{DGT}}(u_h, \delta u_h) = \sum_{i=1}^{N_{\mathrm{E}}} \Big\{ \int_{P_h^i} \big\{ & - u_h \, \delta \dot{u}_h + (\mathbf{D} \cdot \operatorname{grad} u_h) \cdot \operatorname{grad} \delta u_h \\ & - u_h \, (\mathbf{q} \cdot \operatorname{grad} \delta u_h) \big\} \, \mathrm{d}Q + \int_{E_i} u_h^-(t_{n+1}) \, \delta u_h \, \mathrm{d}v \Big\}, \end{aligned} \tag{60}$$

$$L_{\mathrm{DGT}}(\delta u_h) = \sum_{\partial e_k \in \Gamma_{\mathrm{N}}} \Big\{ \int_{\partial e_k \times \mathcal{I}^n} \bar{f}(t) \, \delta u_h \, \mathrm{d}a\mathrm{d}t \Big\} + \sum_{i=1}^{N_{\mathrm{E}}} \Big\{ \int_{E_i} \breve{u}_h(t_n) \, \delta u_h \, \mathrm{d}v \Big\}.$$

Note that in the above expression $\int_{E_i} (\bullet) \, \mathrm{d}v$ denotes a purely spatial integration performed on the border of the time-slab Q^n, i. e. t_n and t_{n+1}.
Moreover, we denote that although the chosen example eq. (54) processes only first-order derivatives in time, the second-order time-dependent equations can either be degenerated into first-order ones either by using order-reduction technique which produce a system of equations of two first-order ones, or by using the EVI technique to produce a first-order equation with the unknown velocities. Thus, we do not repeat the solution strategy of the second-order equation here. In Paper B and Paper C, a detailed discussion for the solution of second-order equations are presented with applications in elastic wave propagation problems and dynamic analysis in porous media. In particular, in Paper C, a generalized EVI method with enhanced stability properties is proposed.

2.3.2 Coupled space-time discontinuous Galerkin method

Next, we proceed to the coupled space-time discontinuous Galerkin (DGST) formulation. Hereby, we abandon both the strong continuities in space and in time, and enforce the consistency of the solution with various flux treatments. Since there exists no coupling between the spatial and temporal flux treatments, a coupled space-time discontinuous Galerkin formulation is developed straight forwardly by applying various flux treatments independently in the spatial and temporal domain.
For a coupled discontinuous Galerkin formulation, the function space is enriched to allow discontinuities in space as well as in time

$$\mathcal{V}(u_h) = \left\{ \begin{array}{l} u_h(\mathbf{x}, \bullet) \in L^2(E_j), (j < N_{\mathrm{E}}) \\ u_h(\bullet, t) \in L^2(\mathcal{I}^n) \end{array} \right\}. \tag{61}$$

Figure 11 shows examplarily one possible function space with both linear approxi-

mations in space and in time.
Taken into consideration that spatial and temporal fluxes are decoupled, additional spatial flux operators are added to the DGT formulation in eq. (59). Adopting the notations introduced in Section 2.2.1, the resultant formulation reads
Find $u_h \in \mathcal{V}(u_h)$*, such that* $\forall \delta u_h \in \mathcal{V}(\delta u_h)$*, there exists*

$$B_{\mathrm{DGST}}(u_h, \delta u_h) = L_{\mathrm{DGST}}(\delta u_h). \tag{62}$$

The bilinear form $B_{\mathrm{DGST}}(u_h, \delta u_h)$ and the linear form $L_{\mathrm{DGST}}(\delta u_h)$ are

$$\begin{aligned}
B_{\mathrm{DGST}}(u_h, \delta u_h) &= B_{\mathrm{DGT}}(u_h, \delta u_h) \\
&+ \sum_{i=1}^{N_{\mathrm{E}}} \Big\{ \int\limits_{(\partial E_i \setminus \Gamma_{\mathrm{D}}) \times \mathcal{I}^n} (\mathbf{q} \cdot \mathbf{n})\, u_h^{\mathrm{in}}\, \delta u_h \, \mathrm{d}a\mathrm{d}t \Big\} \\
&+ \sum_{k=1}^{N_{\mathrm{int}}} \Big\{ \int\limits_{e_k \times \mathcal{I}^n} \big\{ \langle (\mathbf{D} \cdot \operatorname{grad} \delta u_h) \cdot \mathbf{n} \rangle \, [\![u_h]\!] - \langle (\mathbf{D} \cdot \operatorname{grad} u_h) \cdot \mathbf{n} \rangle [\![\delta u_h]\!] \big\} \, \mathrm{d}a\mathrm{d}t \Big\} \\
&+ \sum_{e_k \in \Gamma_{\mathrm{D}}} \Big\{ \int\limits_{e_k \times \mathcal{I}^n} \big\{ (\mathbf{D} \cdot \operatorname{grad} \delta u_h \cdot \mathbf{n})\, u_h - (\mathbf{D} \cdot \operatorname{grad} u_h \cdot \mathbf{n})\, \delta u_h \big\} \, \mathrm{d}a\mathrm{d}t \Big\}, \\
L_{\mathrm{DGST}}(u_h, \delta u_h) &= L_{\mathrm{DGT}}(u_h, \delta u_h) \\
&+ \sum_{e_k \in \Gamma_{\mathrm{D}}} \Big\{ \int\limits_{e_k \times \mathcal{I}^n} \big\{ (\mathbf{D} \cdot \operatorname{grad} \delta u_h \cdot \mathbf{n})\, u_D + (\mathbf{q} \cdot \mathbf{n})\, u_D\, \delta u_h \big\} \, \mathrm{d}a\mathrm{d}t \Big\}
\end{aligned} \tag{63}$$

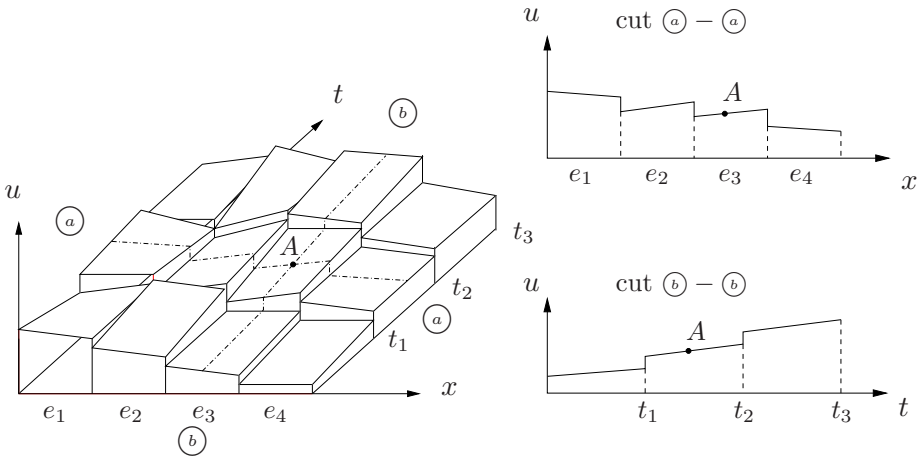

Figure 11: Coupled discontinuous space-time approximation of a one-dimensional spatial problem with four elements in space and three time-slabs in time, constructed by linear polynomials both in space and in time.

Due to the fact that discontinuous approximations are employed both in space and in time, this method results in large algebraic systems even for a mediate number of elements. It was often the case in the literature, that the DGS method is used in combination with an implicit time-stepping method, e. g. the backward Euler method [5, 54]. However, in the opinion of the author, although the DGS formulation turns out to be an appropriate tool to model discontinuous phenomena or sharp gradients in the quasi-static investigations [5, 64], in case of dynamic modeling, the error induced by the time-stepping method can be very dominant, so that after some steps, no significant improvement in the DGS results can be observed in comparison with those obtained by the classical continuous FE approach. In Paper D we employ the DGST method to model the single-phase transport problem in porous media, in which we show that the DGST method is superior to the semi-discrete DGS method, in that the steep concentration front can be captured more efficiently. We also observe that despite a great difference in the number of Degree Of Freedoms, the results computed by the DGS combined with the backward Euler scheme in time lead to smeared wave fronts which are similar to those achieved by the conforming FE method.
Another advantage of employing coupled discontinuous approximations lies in the fact that this formulation can be easily decomposed into several subdomains which simplify a parallel strategy. To date, the development of the computation power of single core processors has shown its limitation. The parallel computation enables the utilization of a large number of computers and has gain more and more attention for realistic computations. Furthermore, adaptive strategies, i. e. h- and/or p-refinement can be applied locally to the subdomain where refinement is necessary without reconstructing the whole computational domain.

3 Summaries of appended papers

In **Paper A**, *A time-discontinuous Galerkin method for the dynamical analysis of porous media*, we studied a new coupled time-discontinuous Galerkin method (DGT) for the dynamical analysis in porous media. The numerical scheme consists a finite element mesh that covers the spatial and temporal domain simultaneously. The finite element approximations are continuous in space but discontinuous in time. Inconsistent quantities of the primary unknowns occur at discrete time levels. Instead of using penalty term, which was widely applied in the DG community, we applied a natural *upwind* flux treatment to enforce the continuities between the adjacent time intervals. The advantage of using such coupled space-time formulation lies in the fact that no artificial penalty term is involved and the high gradients in time can be resolved efficiently. The proposed DGT method has been applied to both first- and second-order time-dependent problems, in that the second-order ones are solved by means of order-reduction technique. Applications of this method to the simple model equation and to the consolidation problem in porous media demonstrate the improved behavior in less numerical damping and

dispersion compared to the conventional FE approach.

In **Paper B**, *A new Hybrid Velocity Integration method applied to elastic wave propagation*, the current work is an extension of the previous investigated DGT method for second-order time-dependent problems. Due to the inherent restriction of the *upwind* flux treatment, the DGT method can only be applied to the first-order equations. In order to solve the second-order problems with the DGT method, we investigated an Hybrid Velocity Integration (HVI) technique to degenerate the second-order equation into a single first-order one. To do this, we rewrite the original second-order differential equation with the unknown displacement to a first-order one with the unknown in its rate term, i. e. velocity. The displacement field is substituted by a consistent integration of its velocity. The resultant first-order equation can be solved by the DGT method (proposed in A). The displacement field is achieved in a post-processing step according to a consistent integration of the velocities. Due to the employment of discontinuous approximation for the velocities, inconsistent quantities occur at discrete time levels. However, since the displacement quantities depends on the integral of the velocities, its quantities is always continuous and smooth. Convergence studies with respect to the velocity and displacement are presented. Numerical experiments concerning elastic wave propagations demonstrate the high order accuracy of the proposed method.

In **Paper C**, *A EVI-space-time Galerkin method for dynamics at finite deformation in porous media*[2], we studied a generalized EVI (see Paper B) integration scheme with enhanced stability property. The physical model is based on a materially incompressible solid skeleton saturated by a barotropic fluid. The deformation of the solid matrix is described by a compressible Neo-Hookean material law. The model equations are formulated in the Lagrangian description of the solid skeleton. Since the numerical scheme consists of a spatial continuous but temporal discontinuous Galerkin formulation, in the region where high gradient in space occurs, an extreme fine discretization in space must be employed to avoid unphysical oscillation. In the current work, however, by introducing more numerical dissipation in the time integration scheme of the displacement field, we are able to stabilize the numerical solution on the coarse spatial discretization accordingly. Herein, a stability factor α is introduced into the consistent integration scheme of the velocity. $\alpha = 0$ corresponds to the exact integration scheme presented in Paper B, in which the least numerical dissipation is inherent to the numerical approach. With an implicit integration scheme, i. e. $\alpha = 1$, we enforce the numerical stability of the overall solutions by introducing numerical dissipation in the temporal integration. However, too strong numerical dissipation affects the numerical accuracy. Thus, other value of α is allowed, leading to an approach that lies between the implicit

[2]Originally the method was named "Hybrid Velocity Integration (HVI)", but in the present work the term "Embedded Velocity Integration (EVI)" was used for convenience.

and exact one. Applications in the wave propagation problem within porous media shows the practical meaning of this parameter. Comparison with the conventional approaches demonstrated the improved behavior of the EVI(α) method in the accuracy and efficiency.

In **Paper D**, *A space-time discontinuous Galerkin method for single-phase flow in porous media*, we studied a coupled space-time discontinuous Galerkin formulation to model the flow problem in porous media. The numerical scheme consists of discontinuous finite element approximations in space and in time. Various flux treatments are applied to impose the continuity weakly. In the temporal domain, a similar *upwind* flux used in DGT method is applied to enforce the consistency between the adjacent time intervals. In the spatial domain, interelement consistency with respect to the convective term is enforced by a spatial *upwind* treatment, while the diffusion term is solved by the average flux combined with a flux-weighted constraint. The resulting space-time discontinuous Galerkin scheme has the advantage in less numerical dissipation and is able to capture the steep concentration front very efficiently. No extra stability term is necessary even for the convection dominant problems. Furthermore, the proposed the space-time discontinuous Galerkin method is superior to a spatial discontinuous Galerkin (DGS) method combined with backward Euler scheme in time, in that the less numerical dissipation in the temporal integration is involved. Computations have also shown that employing the DGS method alone does not ensure a more accurate solution in that the error deduced by the time-stepping method can be dominant. Numerical examples concerning the single-phase flow in a homogeneous and inhomogeneous domains demonstrates the behavior of the proposed method.

4 Concluding remarks and future work

In this thesis we have studied coupled space-time Galerkin methods. Instead of using penalty terms, the consistency of the solution is enforced weakly by various flux treatments. According to the art of discretization in space, the proposed approaches can be further subdivided into the time-discontinuous Galerkin method (DGT), where the finite approximations are continuous in space but discontinuous in time, and the coupled space-time discontinuous Galerkin (DGST) method, in which neither the spatial nor the temporal domain processes strong continuity. The mechanism of the DGT method is to employ the first-order *upwind* flux to enforce the continuity in time. Due to the restriction of the flux treatment, this approach is only applicable to first-order time-dependent problems. The second-order time-dependent problem can either be solved by means of order-reduction technique, leading to an equation system of two coupled first-order equations which can be in turn solved by the DGT method for both displacement and velocity simultaneously, or by using the Embedded Velocity Integration (EVI) technique to produce a sin-

gle first-order equation in the velocity field which can then be solved by the DGT method. In addition, the EVI technique provides a general approach for solving second-order time-dependent problems by means of finite element approximations in time. For the DGST method, discontinuous approximations in space and in time are applied. Herein, we employ the *upwind* flux for the treatment of the convection term, and the average flux treatment for the diffusion term. No penalty parameter is involved in the proposed methods. Moreover, since there exists no coupling between the spatial and temporal fluxes, various flux treatments in space and in time are employed independently.

The key issue of this thesis is to study the various flux treatments for the discontinuous Galerkin approaches. It has been shown that employing the fluxes on the element interface provides a natural treatment to enforce the interelement consistency, and is applicable to a vast of problem classes. In particular, the proposed DGT method has been applied to the dynamic analysis in the porous media. The dynamic consolidation procedure and the elastic wave propagation phenomena are investigated throughout the practices of the numerical schemes. In addition, transport of single-phase flow in porous media was studied with the DGST formulation. As for the future work, since the computational cost for DGST formulation is much higher than the conforming FE method, an adaptive strategy involving both the $p-$ and $h-$ refinement in space and in time have to be developed. Furthermore, discontinuities (jumps) occurring on the element interfaces provides a good choice for the error indicator. It has been shown that employing fluxes on the element interfaces to enforce the interelement consistency provides a good ride to construct the discontinuous Galerkin methods. Moreover, since the subdivisions are connected through the flux treatments on the element interfaces, it is possible to develop a local adaptive strategy, in which refinement applied in the subdomains where refinement are necessary without reconstructing the whole computational domain. Another challenge for the future is the parallelization of the proposed method. With the appearance of the multi-processor computers, the parallel computation will gain more and more attention in the near future. The spatial discontinuous discretization provides a good ride for the parallel strategy.

Bibliography

[1] W. F. Ames. *Numerical Methods for Partial Differential Equations,Second Edition*. Academic Press, Boston-New York, 1977.

[2] J. H. Argyris and D. W. Scharpf. Finite elements in space and time. *Nucl. Engrg. Des.*, 10:456–464, 1969.

[3] D. N. Arnold. *An interior penalty finite element method with discontinuous elements*. PhD thesis, The University of Chicago, Chicago, IL, 1979.

[4] F. Bassi and S. Rebay. A high-order accurate discontinuous finite element method for the numerical solution of the compressible Navier-Stokes equations. *J. Chem. Phys.*, 131:267–279, 1997.

[5] C. E. Baumann. *An hp-adaptive discontinuous finite element method for computational fluid dynamics*. PhD thesis, The University of Texas at Austin, 1997.

[6] C. E. Baumann and J. T. Oden. A discontinuous *hp* finite element method for the Euler and Navier-Stokes equations. *Int. J. Numer. Meth. Fluids*, 31:79–95, 1999.

[7] J. G. Berryman. Confirmation of Biot's theory. *Appl. Phys. Lett.*, 37(4):382–384, 1980.

[8] M. A. Biot. Theory of propagation of elastic waves in a fluid-saturated porous solid. I. Low-frequency range. *J. Acoust. Soc. Am.*, 29:168–178, 1956.

[9] M. A. Biot. Theory of propagation of elastic waves in a fluid-saturated porous solid. II. Higher frequency range. *J. Acoust. Soc. Am.*, 29:179–191, 1956.

[10] S. Breuer. Quasi-static and dynamic behavior of saturated porous media with incompressible constituents. *Transport Porous Med.*, 34:285–303, 1999.

[11] A. N. Brooks and T. J. R. Hughes. Streamline upwind/Petrov-Galerkin formulations for convection dominated flows with particular emphasis on the incompressible Navier-Stokes equations. *Comp. Meth. Appl. Mech. Eng.*, 32:199–259, 1982.

[12] P. Castillo. Performance of discontinuous Galerkin methods for elliptic PDEs. *SIAM Journal of Scientific Computation*, 24(2):524–547, 2002.

[13] P. Castillo, B. Cockburn, D. Schötzau, and C. Schwab. Optimal a priori error estimates for the *hp*-version of the local discontinuous Galerkin method for convection-diffusion problems. *Math. Comp.*, 71(238):455–478, 2001.

[14] R. W. Clough. The finite element method in plane stress analysis. *Proc. 2nd ASCE Conf. On Electronic Computation, Pitttsburg*, 1960.

[15] B. Cockburn. Discontinuous Galerkin methods. *Z. Angew. Math. Mech.*, 11:731–754, 2003.

[16] B. Cockburn, S. Hou, and C. W. Shu. TVB Runge-Kutta local projection discontinuous Galerkin finite element methods for conservation laws. IV: The multidimensional case. *Math. Comp.*, 54:545–581, 1990.

[17] B. Cockburn, S. Hou, and C. W. Shu. The Runge-Kutta discontinuous Galerkin finite element for conservation laws V: Multidimensional systems. *J. Comp. Phys.*, 141:199–224, 1999.

[18] B. Cockburn, S. Y. Lin, and C. W. Shu. TVB Runge-Kutta local projection discontinuous Galerkin finite element methods for conservation laws III: One dimensional systems. *J. Comp. Phys.*, 84:90–113, 1989.

[19] B. Cockburn and C. W. Shu. TVB Runge-Kutta local projection discontinuous Galerkin finite element methods for conservation laws. II: General framework. *Math. Comp.*, 52:411–435, 1989.

[20] B. Cockburn and C. W. Shu. The local discontinuous Galerkin finite element method for convection-diffusion systems. *SIAM J. Numer. Anal.*, 35:2440–2463, 1998.

[21] B. Cockburn and C. W. Shu. The Runge-Kutta discontinuous Galerkin method for conservation laws V. *J. Chem. Phys.*, 141:199–224, 1998.

[22] R. Codina, E. Oñate, and M. Cervera. The intrinsic time for the streamline upwind / Petrov-Galerkin formulation using quadratic elements. *Comp. Meth. Appl. Mech. Eng.*, 94:239–262, 1992.

[23] O. Coussy. *Mechanics of Porous Continua*. Wiley and Sons, New York, NY, 1995.

[24] R. de Boer. *Theory of porous media: Highlights in the historical development and current state*. Springer Verlag, Berlin, 2000.

[25] R. de Boer and W. Ehlers. Theorie der Mehrkomponentenkontinua mit Anwendung auf bodenmechanische Probleme. In *Forschungsberichte aus dem Fachbereich Bauwesen*, volume 40. Universität-GH-Essen, 1986.

[26] R. de Boer, W. Ehlers, and Z. Liu. One-dimensional transient wave propagation in fluid-saturated incompressible porous media. *Arch. Appl. Mech.*, 63:59–72, 1993.

[27] S. Diebels and W. Ehlers. Dynamic analysis of a fully saturated porous medium accounting for geometrical and material non-linearities. *Int. J. Numer. Meth. Eng.*, 39:81–97, 1996.

[28] J. Douglas, J. R., and T. Dupont. *Interior penalty procedures for elliptic and parabolic Galerkin methods, Lecture Notes in Phys. 58*. Springer-Verlag, Berlin, 1978.

[29] W. Ehlers. Foundations of multiphasic and porous materials. In W. Ehlers and J. Bluhm, editors, *Porous Media: Theory, Experiments and Numerical Applications*, pages 3–86. Springer-Verlag, Berlin, 2002.

[30] W. Ehlers and J. Bluhm, editors. *Porous Media*. Springer-Verlag, Berlin, 2002.

[31] W. Ehlers, S. Diebels, and P. Blome. Modelling of partially saturated soils by the Theory of Porous Media. In T. Schanz, editor, *3. Workshop Weimar 2001: Teilgesättigte Böden*, pages 91–112. Schriftenreihe Geotechnik, Heft 6, Bauhaus-Universität Weimar, 2002.

[32] W. Ehlers, S. Diebels, and W. Volk. Deformation and compatibility for elasto-plastic micropolar materials with applications to geomechanical problems. *J. Phys. IV France*, 8:127–134, 1998.

[33] W. Ehlers, T. Graf, and M. Ammann. Deformation and localization analysis of partially saturated soils. *Comp. Meth. Appl. Mech. Eng.*, 193:2885–2910, 2004.

[34] W. Ehlers and B. Markert. A linear viscoelastic biphasic model for soft tissues based on the theory of porous media. *J. Biomech. Eng.*, 123:418–424, 2001.

[35] K. Eriksson, D. Estep, P. Hansbo, and C. Johnson. *Computational Differential Equations*. Cambridge University Press, Cambridge, 1996.

[36] D. A. French. A space-time finite element method for the wave equation. *Comp. Meth. Appl. Mech. Eng.*, 107:145–157, 1993.

[37] I. Fried. Finite element analysis of time-dependent phenomena. *AIAA Journal*, J.:1170–1173, 1969.

[38] H. Huang and F. Costanzo. On the use of space-time finite elements in the solution of elasto-dynamic problems with strain discontinuities. *Comp. Meth. Appl. Mech. Eng.*, 191:5315–5343, 2002.

[39] T. J. R. Hughes and G. Hulbert. Space-time finite element methods for elastodynamics: formulations and error estimates. *Comp. Meth. Appl. Mech. Eng.*, 66:339–363, 1988.

[40] G. Hulbert. *Space-time finite element methods for second order hyperbolic equations*. PhD thesis, Department of Mechanical Engineering, Stanford University, Stanford, 1989.

[41] G. M. Hulbert. Time finite element methods for structural dynamics. *Int. J. Numer. Meth. Eng.*, 33:307–331, 1992.

[42] G. M. Hulbert and T. J. R. Hughes. Space-time finite element methods for second-order hyperbolic equations. *Comp. Meth. Appl. Mech. Eng.*, 84:327–348, 1990.

[43] C. Johnson. Discontinuous Galerkin finite element methods for second order hyperbolic problems. *Comp. Meth. Appl. Mech. Eng.*, 107:117–129, 1993.

[44] D. Kuhl and G. Meschke. Numerical analysis of dissolution processes in cementitious materials using discontinuous and continuous galerkin time integration schemes. *Int. J. Numer. Meth. Eng.*, 69(9):1775–1803, 2007.

[45] X. Li and N. E. Wiberg. Structural dynamics analysis by time-discontinuous Galerkin finite element method. *Int. J. Numer. Meth. Eng.*, 39:2131–2152, 1996.

[46] J. Mergheim, E. Kuhl, and P. Steinmann. A hybrid discontinuous Galerkin/interface method for the computational modelling of failure. *Commun. Numer. Meth. En.*, 20:511–519, 2004.

[47] J. Nitsche. Über ein Variationsprinzip zur Lösung von Dirichlet Problemen bei Verwendung von Teilräumen, die keinen Randbedingungen unterworfen sind. *Abh. Math. Sem. Univ. Hamburg*, 36:9–15, 1971.

[48] J. T. Oden. A general theory of finite elements. II. Applications. *Int. J. Numer. Meth. Eng.*, 1:247–259, 1969.

[49] J. T. Oden, I. Babuška, and C. E. Baumann. A discontinuous *hp* finite element method for diffusion problems. *J. Chem. Phys.*, 146:491–519, 1998.

[50] T. Plona. Observation of a second bulk compressional wave in a porous medium at ultrasonic frequencies. *Appl. Phys. Lett.*, 36:259–261, 1980.

[51] W. H. Reed and T. R. Hill. Triangular mesh methods for the neutron transport equation. *Los Alamos Scientific Laboratory Report LA-UR-73-479*, 1973.

[52] B. Rivière and V. Girault. Discontinuous finite element methods for incompressible flows on subdomains with non-matching interfaces. *Comp. Meth. Appl. Mech. Eng.*, 195:3274–3292, 2006.

[53] B. Rivière and M. F. Wheeler. Discontinuous Galerkin methods for flow and transport problems in porous media. *Commun. Numer. Meth. En.*, 79:157–174, 2002.

[54] B. Rivière, M. F. Wheeler, and K. Banaś. Part II: Discontinuous Galerkin methods applied to a single phase flow in porous media. *Comp. Geosciences*, 4:337–349, 2000.

[55] B. Rivière, M. F. Wheeler, and V. Girault. Improved energy estimates for interior penalty, constrained and discontinuous Galerkin methods for elliptic problems. Part I. *Comp. Geosciences*, 3:337–360, 1999.

[56] M. Schanz. *Wave propagation in viscoelastic and poroelastic continua*. Springer-Verlag, Berlin, 2001.

[57] M. Schanz and S. Diebels. A comperative study of Biot's theory and the linear Theory of Porous Media for wave propagation problems. *Acta Mech.*, 161:213–235, 2003.

[58] H. Steeb, S. Diebels, and I. Vardoulakis. Generalized multi-flow models for erosive mixtures. *Phil. Mag.*, 2004. submitted for publication.

[59] C. A. Truesdell and R. Toupin. *The classical field theories*. In S. Flügge (Herausgeber), Handbuch der Physik III/1, Springer-Verlag, Berlin, 1960.

[60] M. Turner, R. W. Clough, H. C. Martin, and L. J. Topp. Stiffness and deflection analysis of complex structures. *J. Aeronautical Science*, 23(9):805–824, 1956.

[61] I. Vardoulakis and H. Steeb. Sand production in gas-flown weak formations. In *Proceedings of '5$^{\text{th}}$ German-Greek-Polish Symposium on Advances in Mechanics', September 12-18, 2004, Bad Honnef, Germany*. 2004.

[62] K. Wilmański. A few remarks on Biot's model and linear acoustics of poroelastic saturated materials. *Soil Dyn. Earthq. Eng.*, 26:509–536, 2006.

[63] O. C. Zienkiewicz and R. L. Taylor. *The finite element method: the basis*, volume 1. Butterworth-Heinemann: Oxford, 5th edition, 2000.

[64] O. C. Zienkiewicz, R. L. Taylor, S. J. Sherwin, and J. Peiró. On discontinuous Galerkin methods. *Int. J. Numer. Meth. Eng.*, 58:1119–1148, 2003.

Paper A

A time-discontinuous Galerkin method for the dynamical analysis of porous media

published in *Int. J. Numer. Anal. Meth. Geomech.* 2006; **30**:1113–1134

INTERNATIONAL JOURNAL FOR NUMERICAL AND ANALYTICAL METHODS IN GEOMECHANICS
Int. J. Numer. Anal. Meth. Geomech. 2000; 00:1–6 Prepared using *nagauth.cls* [Version: 2002/09/18 v1.02]

A TIME-DISCONTINUOUS GALERKIN METHOD FOR THE DYNAMICAL ANALYSIS OF POROUS MEDIA

Zhiyun Chen, Holger Steeb, Stefan Diebels*

Saarland University, Chair of Applied Mechanics,
Postfach 15 11 50, D–66 041 Saarbrücken, Germany

SUMMARY

We present a time-discontinuous Galerkin method (DGT) for the dynamic analysis of fully-saturated porous media. The numerical method consists of a finite element discretization in space and time. The discrete basis functions are continuous in space and discontinuous in time. The continuity across the time interval is weakly enforced by a flux function. Two applications and several numerical investigations confirm the quality of the proposed space-time finite element scheme. Copyright © 2000 John Wiley & Sons, Ltd.

key words: Discontinuous Galerkin, space-time finite elements, porous media

1. INTRODUCTION

In recent years the Discontinuous Galerkin (DG) method has established itself as a viable method for solving partial differential equations and a wide variety of applications has been found. The name "Discontinuous Galerkin" method was first introduced by Reed & Hill [58] in 1973 while investigating hyperbolic partial differential equations. Mathematically, this method was extensively analyzed by LeSaint & Raviart [49], and successively by Johnson et al. [46] and Johnson & Pitkäranta [47]. In the 1970s several simultaneous but independent studies about DG methods for elliptic and parabolic problems were investigated, c. f. [4, 5, 10, 43, 66]. These methods were later briefly concluded as Interior Penalty methods (IP methods). In the last 10 years, due to the strong interaction of numerical flux, a technique traditionally used in upwind finite volume schemes, the DG methods have experienced a rigorous development. Cockburn and co-authers introduced the Runge-Kutta DG (RKDG) methods for the solution of first-order non-linear hyperbolic conservation laws [21, 22]. An *hp*-adaptive DG method was studied by Bey & Oden [15] and a more detailed analysis was presented by Houston [35]. Bassi & Rebay [11] expanded the method to a mixed formulation for solving the compressible Navier-Stokes equations. A strong influence on the DG methods was made by Baumann &

*Correspondence to: Saarland University, Chair of Applied Mechanics, Stefan Diebels, Postfach 15 11 50, D–66 041 Saarbrücken, Germany. email: s.diebels@mx.uni-saarland.de

Received February 6, 2006

Oden [12, 13, 14, 42] in solving the classical diffusion equation. Riviére et al. did further studies of these methods as well as error estimates, c. f. [8, 59, 60, 7]. Unlike the IP methods, the DG methods based on the numerical flux have been proved to show higher convergency rates.
A Galerkin formulation in space and time based on Hamilton's principle was first proposed by Argyris & Scharpf [3]. Hulbert & Hughes [39] studied the Discontinuous Galerkin time integration scheme in which they first introduced the Galerkin Least Square term to impose the inter-element consistency. In their following works they did further studies to such methods as well as appropriate error estimation techniques, c. f. [40, 41, 37]. Johnson [44] investigated reduced systems to solve second order hyperbolic problems with DG methods, for an overview we refer to [45]. Li & Wiberg (1998) [51] proposed an adaptive space-time DG method for applications in structural dynamics. In their work, they use an energetic argument (i. e. the internal and kinetic energy) to enforce the continuity between the elements. Steeb et al. (2002) [61, 62] studied adaptive DG method based on goal-oriented error estimation techniques. They applied these techniques to applications in structural dynamics and to consolidation problems. More recently, Palaniappan et al. (2004) [55] have introduced the flux treatment into the space-time finite element methods for scalar conservation laws.
In the following work, we studied a time-discontinuous Galerkin method (DGT) which is composed of a standard continuous Galerkin method in space coupled with a discontinuous Galerkin scheme in time. Hereby, we introduced a numerical technique based on the treatment of the flux term to enforce the temporal continuity conditions. Comparable techniques are quite common in spatial DG methods for convection-dominated problems, c. f. [20, 69].
In the present contribution, we apply this numerical method to a transient problem of a binary mixture consisting of a material incompressible pore fluid and an elastic incompressible solid skeleton in the framework of small deformations. The analyzed two-phase model is based on the thermodynamically consistent Theory of Porous Media (TPM), c. f. Bowen [17, 18], de Boer & Ehlers [24], Ehlers [28, 29] or the recently published book by Ehlers & Bluhm [30]. A historical overview of the TPM can be found in the textbook of de Boer [23].
The structure of this paper is as follows: In section 2 we introduce the basic terminology used in the contribution with respect to the space-time discretization. Afterwards, the continuous and discrete weak form of a 1-dim model problem is given. Section 3 devotes to the space-time finite element formulation of the transient problem of a binary mixture. The result is again a continuous and discrete set of coupled equations. In Section 4 we discuss some 1-dim and 2-dim numerical examples to demonstrate the improved behavior of the presented method. The contribution is closed by a final evaluation of the numerical method followed by a short discussion giving some final remarks and an outlook on possible future extensions.

2. PRELIMINARY

The space-time domain Q is constructed by intuitively adding an extra time domain $\mathcal{I} = [t_0, T)$ orthogonal to the spatial domain Ω in a way that a spatial one-dimension problem results in a two-dimensional finite element, and a spatial two-dimensional problem results in a three-dimensional one, i. e. $Q = \Omega \times \mathcal{I}$. Let $t_0 < t_1 < \cdots < t_n < \cdots < t_m = T$ be a sequence of discrete time level t_n, so that we are able to define the time interval $\mathcal{I}^n = [t_n, t_{n+1})$. The time-slab is defined as $Q^n := \Omega \times \mathcal{I}^n$, see Fig. 1 for one- and two-dimensional examples depicted

with a linear geometrical projection in space and time. The discrete solutions of the governing

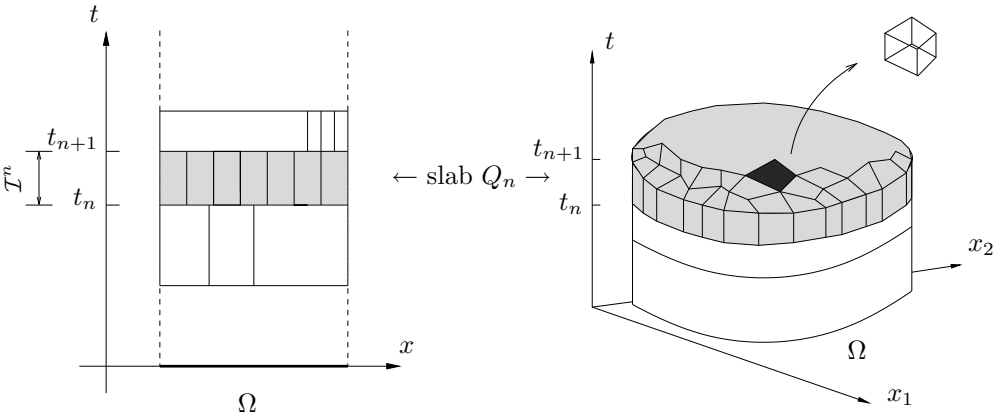

Figure 1. Space-time slab of a problem with one(left) or two(right) spatial dimensions

finite element problem are sequentially solved on every time-slab, so that the total degree of freedoms (DOFs) of the concerned algebraic problem is restricted to the DOFs on every single slab. Hence the overall numerical effort of the DGT is comparable to the classical method of lines (MOL). Each time-slab Q^n has private nodes on the time level t_n. The continuity condition on the discrete time level is weakly enforced by the flux term on the slab interface. In addition, the space-time finite elements are embedded on the time-slab as shown in Fig. 2. In the mentioned figure, we show examplarily a bilinear and trilinear space-time finite element for convenience. In contrast to standard semi-discrete methods, in which a spatial integration based on the finite element method is in turn solved by a certain finite difference method (e. g. a Euler method, a Runge-Kutta or Newmark method etc.) in time, a simultaneous, element-wise integration in space and time is evaluated by surface (1-dim) or volume (2-dim) integration within the present space-time finite element formulation, see Fig. 2. As we now restrict ourselves to discontinuous polynomials for the weighting- and test-functions, we

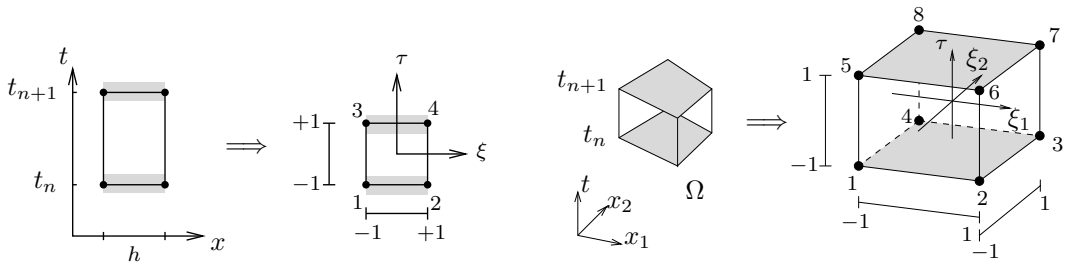

Figure 2. Linear space-time finite elements with one(left) or two(right) spatial dimensions

introduce the following integration scheme as

$$\int_{\mathcal{I}}\int_{\Omega} (\bullet)\,\mathrm{d}v\,\mathrm{d}t =: \int_{Q} (\bullet)\,\mathrm{d}Q = \sum_{n=0}^{m-1} \int_{Q^n} (\bullet)\,\mathrm{d}Q^n. \tag{1}$$

3. MODEL EQUATION

For the sake of a first brief numerical illustration, we restrict ourselves to a simple parabolic equation [†] like

$$\partial_t(\phi) - \operatorname{div}\mathbf{q} = f, \quad \text{in} \quad \Omega \times \mathcal{I}, \tag{2}$$

where Ω is an open-bounded Lipschitz domain in $\mathbb{R}^d$, and $\mathcal{I}$ is the temporal domain $\mathcal{I} = [t_0, T)$ again. Furthermore, we have introduced the corresponding flux $\mathbf{q} := \mathbf{A} \cdot \operatorname{grad}\phi$. $\mathbf{A}$ is a positive definite second-order tensor representing the diffusive character of the model. $\partial_t(\bullet)$ is the partial time derivative, $\operatorname{grad}(\bullet) := \partial_{\mathbf{x}}(\bullet)$ denotes the gradient operator and $\operatorname{div}(\bullet) := \partial_{\mathbf{x}}(\bullet) : \mathbf{I}$ is the corrsponding divergence operator, as $\mathbf{I}$ is the second-order tensor of unity. Sinks and sources are taken into account by the right hand side of (2), i. e. by f. The boundary $\partial\Omega$ of the domain Ω consists of disjoint parts, namely the Dirichlet boundary Γ_D and the Neumann boundary Γ_N with $\Gamma_N \bigcup \Gamma_D = \partial\Omega$ and $\Gamma_N \bigcap \Gamma_D = \emptyset$. The associated boundary conditions are

$$\begin{aligned} \phi &= \bar{\phi} \quad \text{on} \quad \Gamma_D, \\ \mathbf{q}\cdot\mathbf{n} &= \bar{q} \quad \text{on} \quad \Gamma_N, \end{aligned} \tag{3}$$

where $\mathbf{n}$ is the outward normal at the boundary. The initial boundary value problem (IBVP), c. f. Eqs. (2) and (3), is closed by an appropriate initial condition

$$\phi\,(\mathbf{x}, t_0) \quad = \quad \phi_0\,(\mathbf{x}) \quad \text{at} \quad \Omega \times t_0. \tag{4}$$

The underlying weak form of the IBVP is obtained by multiplying Eq. (2) with a test function $\delta\phi$ and by integrating over the time-slab Q^n. Hereby, we integrate by parts in space as well as in time. Applying first integration by parts in time leads to

$$\int_{Q^n} (\partial_t(\phi)\ \delta\phi)\ \mathrm{d}Q^n = -\int_{Q^n} (\phi\,\partial_t(\delta\phi))\ \mathrm{d}Q^n + \int_{\Omega} \Big[\breve{\phi}\,\delta\phi\Big]_{t_n}^{t_{n+1}}\ \mathrm{d}v, \tag{5}$$

in which we use $\breve{\phi}$ for the quantity at the discrete time level t_n or t_{n+1}. A detailed definition concerning its concrete value will be soon introduced in the following text. Taking Eqs. (1)

[†] In general, this model problem is known as the instationary heat equation; thus ϕ is identified as the temperature field. With respect to erosive fluid-flow through porous media, this instationary porosity diffusion equation models the sand erosion process in a rigid and material incompressible sandstone matrix ($\rho^{\mathfrak{s}^R} = \text{const}$). Such phenomena occur for instance during the first phase of petroleum production in the north-sea sandstone reservoir. Within such a suffosion process so-called fines, i. e. small particles are eroded away from the sandstone skeleton and transported away in direction of the borehole. Thus, the field quantity $\phi(\mathbf{x}, t)$ is identified as the porosity, i. e. $\phi := 1 - n^{\mathfrak{s}}$ while $n^{\mathfrak{s}} = \mathrm{d}v^{\mathfrak{s}}/\mathrm{d}v$ is the volume fraction of the matrix material, see e. g. Papamichos & Vardoulakis (2005) [56] or Steeb & Vardoulakis (2005) [63] for further theoretical details concerning the modeling of erosion phenomena. Furthermore, the flux $\mathbf{q}(\mathbf{x}, t)$ is nothing else but the total discharge of the eroded particles. A consequence of the porosity-diffusion model is the fact that the particles are enforced to exit from regions with increasing porosity.

and (5) into account, we obtain the governing continuous weak form in space and time of the corresponding IBVP in a natural way as

$$\sum_{n=1}^{m}\left[\int_{\Omega}\Big[\breve{\phi}\,\delta\phi\Big]_{t_n}^{t_{n+1}}\,\mathrm{d}v-\int_{Q^n}(\phi\,\partial_t(\delta\phi)-\mathbf{q}\cdot\operatorname{grad}\delta\phi)\,\mathrm{d}Q^n\right]=\sum_{n=1}^{m}\left[\int_{Q^n}f\,\delta\phi\,\mathrm{d}Q^n+\int_{\Gamma_N\times\mathcal{I}^n}\bar{q}\,\delta\phi\,\mathrm{d}a\,\mathrm{d}t\right]. \tag{6}$$

The analogy to the solution procedure of the MOL is obvious. Thus, for notational convenience, we disregard the overall space-time domain and restrict ourselves to the introduced time-slab. The resulting continuous space-time weak formulation is given as

$$\int_{\Omega}\Big[\breve{\phi}\,\delta\phi\Big]_{t_n}^{t_{n+1}}\,\mathrm{d}v-\int_{Q^n}(\phi\,\partial_t(\delta\phi)-\mathbf{q}\cdot\operatorname{grad}\delta\phi)\,\mathrm{d}Q^n=\int_{Q^n}f\,\delta\phi\,\mathrm{d}Q^n+\int_{\Gamma_N\times\mathcal{I}^n}\bar{q}\,\delta\phi\,\mathrm{d}a\,\mathrm{d}t. \tag{7}$$

As we have integrated the temporal derivative by parts, we obtain one term which has to be integrated only in the spatial domain (first term of Eq. (7)). Within the time-discontinuous Galerkin scheme, inconsistent values at the time level t_n or t_{n+1} appear, see Fig. 3. With the definition

$$\phi_n^{\pm}=\lim_{\epsilon\to 0^+}\phi(t_n\pm\epsilon) \tag{8}$$

where ϵ is an infinite small time range, the temporal jump quantity at $t=t_n$ yields

$$[\![\phi_n]\!]=|\phi_n^{+}-\phi_n^{-}|, \tag{9}$$

where the subscript $(\bullet)_n$ and $(\bullet)_{n+1}$ indicates the considered quantity in time t_n and t_{n+1}, respectively. Tracing back to Eqs. (6) and (7), we have introduced $\breve{\phi}$ at every discrete point in time t_n. The introduction of this quantity is motivated by the definition of the flux in spatially discontinuous Galerkin schemes [11, 20] concerning an upwind treatment

$$\breve{\phi}_n:=\begin{cases}\phi_0(\mathbf{x},t_0), & \text{if}\quad n=0,\\ \phi_n^{-}(\mathbf{x},t_n), & \text{otherwise,}\end{cases} \tag{10}$$

where ϕ_0 is the prescribed initial value and ϵ is introduced as a infinite small time range. Inserting the flux definition (10) into the weak form (7) we obtain

$$\begin{aligned}\int_{\Omega}\Big[\breve{\phi}\,\delta\phi\Big]_{t_0}^{t_1}\,\mathrm{d}v &= \int_{\Omega}\phi_1^{-}\,\delta\phi\,\mathrm{d}v-\int_{\Omega}\phi_0\,\delta\phi\,\mathrm{d}v, && \text{if}\quad n=0,\\ \int_{\Omega}\Big[\breve{\phi}\,\delta\phi\Big]_{t_n}^{t_{n+1}}\,\mathrm{d}v &= \int_{\Omega}\phi_{n+1}^{-}\delta\phi\,\mathrm{d}v-\int_{\Omega}\phi_n^{-}\delta\phi\,\mathrm{d}v, && \text{otherwise.}\end{aligned} \tag{11}$$

It is worth noticing that in the above equation ϕ_{n+1}^{-} is the unknown quantity which has to be calculated within the space-time finite element approach on the current time-slab Q^n at time $t=t_{n+1}^{-}$, while ϕ_n^{-} represents the already known numerical quantity obtained from the previous calculation of the time-slab Q^{n-1} at time $t=t_n^{-}$, c. f. Fig. 3. At this point, we are able to see again the similarities to the standard numerical solution technique of the MOL. Within the MOL, we also use the results of previous time-steps as known initial data for the current time-slab under consideration. The case $n=0$, which corresponds to the beginning of the

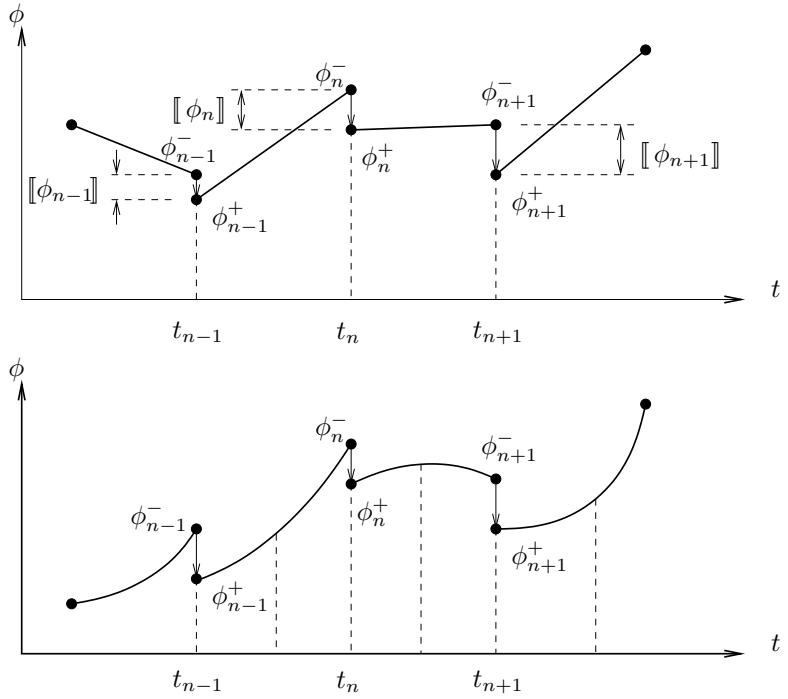

Figure 3. Discontinuous discretization with linear/quadratic approximation in the time

process according to the definition in Eq. (10), is naturally included in the presented scheme. Such concepts of numerical flux treatment stems from finite volume methods and has become an important member in the (space)-discontinuous Galerkin family in the recent 10 years, see [11, 20] and the literature therein. One simple reason for accepting such an assumption in a time-dependent problem is that the value at the time level t_n must be equal to the value of its immediate past $t_n - \epsilon$. Therefore, it is natural to start the numerical procedure at $t = t_0$ with the prescribed initial condition $\overset{\vee}{\phi} = \phi_0$, which is the initial value at t_0. It is obvious, that this idea can be transported to every following time-slab.

Applying integration by parts and transferring the space-time integration to a pure spatial integration at the time-slab borders, the continuity is weakly enforced by an upwind flux in the temporal direction. In addition to this, this numerical procedure differs from various other contributions [36, 39, 52, 53, 54] in applications of time-space finite elements as we do not introduce any penalty term (least-square term, etc.) weakly enforcing the continuity in the temporal direction. Thus, the investigated method does not contain any penalty parameters and, additionally, is more flexible and reliable than conventional numerical methods based on the MOL.

As the obtained weak forms are still of infinite dimensions, we introduce the associated finite element subspaces. Let the spatially-continuous time-slab $Q^n = \Omega \times \mathcal{I}^n$ be subject to a spatial

discretization, i. e. the finite element mesh

$$\mathcal{P}_h = \bigcup_N P_h^j, \quad \text{with} \quad 1 \le j \le N. \tag{12}$$

The mesh consists of N space-time finite elements $P_h^j = \Omega_h^j \times \mathcal{I}^n$. The spatial domain of the finite element P_h^j was introduced as Ω_h^j, while the temporal domain is again $\mathcal{I}^n$. We assume that the finite dimensional function space $\mathcal{U}_h \subset \mathcal{U}$ consists of the tensor products of spatial and temporal weighting- and test-functions. With the flux definition of (10) at the border of the time-slab, we formally define the underlying finite element problem:

$$\text{Find} \quad \phi_h \in \mathcal{U}_h, \quad \text{such that} \quad B(\phi_h, \delta\phi_h) = L(\delta\phi_h), \qquad \forall\, \delta\phi_h \in \mathcal{U}_h. \tag{13}$$

The bilinear form $B(\bullet\,,\bullet)$ and the linear form $L(\bullet)$ read

$$\begin{aligned} B(\phi_h, \delta\phi_h) \quad := \quad & -\sum_{j=1}^{N} \int_{P_h^j} \phi_h\, \partial_t(\delta\phi_h)\, \mathrm{d}Q^n + \sum_{j=1}^{N} \int_{\Omega_h^j} \phi_{h,n+1}^{-}\, \delta\phi_h\, \mathrm{d}v - \sum_{j=1}^{N} \int_{\Omega_h^j} \breve{\phi}_{h,n}\, \delta\phi_h\, \mathrm{d}v \\ & + \sum_{j=1}^{N} \int_{\mathcal{P}_h^j} (\mathbf{q} \cdot \operatorname{grad} \delta\phi_h)\, dQ^n, \\ L(\delta\phi_h) \quad := \quad & \sum_{j=1}^{N} \int_{\mathcal{P}_h^j} f\, \delta\phi_h\, \mathrm{d}Q^n + \sum_{k=1}^{M} \int_{\Gamma_{N,e} \times \mathcal{I}^n} \bar{q}\, \delta\phi_h\, \mathrm{d}a\, \mathrm{d}t. \end{aligned} \tag{14}$$

In addition to the previous definitions, we have introduced the number of edges (2-dim) M on the Neumann boundary Γ_N. Thus, the edge of a finite element lying on the discrete Neumann boundary of the partition is called $\Gamma_{N,h}^k$. Since the continuity condition along the time axis is weakly enforced in form of the upwind flux, inconsistent numerical values (jumps) at time level t_n can be obtained. It is well-known in the DG community, that the jumps between the finite element lead to stable and reliable numerical solutions. Furthermore it simplifies the approximations of physical discontinuities which are inherent in many applications. Additionally, the jump terms can be used to construct simple heuristical error indicators in the temporal domain leading to sophisticated space-time adaptive methods. According to the polynomial order (p) of the weighting- and test-functions in time, we denote in the following context this numerical method as a DGT(p) approach. In respect of the numerical effort, due to the extra DOFs at the discontinuous space-time slab borders in the DGT formulation, the size of the resulting system of algebraic equations which has to be solved at each time slab is $p+1$ times the number of DOFs of the ordinary methods (MOL). Thus, the lowest order of the present DGT method ($p = 1$) results in an algebraic equation at the time slab which has twice as much DOFs as the equivalent MOL. It's obvious, that by increasing the polynomial order of the weighting functions in time (p-refinement) the resulting system of equation is getting larger. However, a higher polynomial order of the weighting functions allows a much larger time step length! Therefore the number of total time steps can be reduced. This is not the case for the h-refinement technique, where the resulting system of algebraic equations is larger than that of an equivalent MOL, but smaller than that of the p-refinement technique. In practical applications a clever combination of h- and p-refinement is preferred leading to a method which has the lowest overall numerical effort. A simple expample concerning both h- and p-refinement is presented in Section 5.1.

4. APPLICATION TO POROUS MEDIA

In the present chapter we applied the DGT scheme to a more sophisticated, i. e. coupled problem. Thus, we investigate the dynamical behavior of fluid-flow through an elastic porous medium. The physical model is based on the well-studied thermodynamically consistent Theory of Porous Media (TPM), c. f. [17, 18, 24, 28, 29, 30] and the literature cited therein. For the sake of simplicity and goal-oriented illustration of the governing numerical method, we restrict ourselves to the geometrical linear case. However, the extension to nonlinear materials is possible. The mixture consists of two constituents φ^α with $\alpha \in \{\mathfrak{s}, \mathfrak{f}\}$, where the constituent $\varphi^\mathfrak{s}$ refers to the elastic solid matrix material and $\varphi^\mathfrak{f}$ identifies the viscous pore-fluid. Furthermore, as standard within the TPM, we introduce the volume fractions $n^\alpha := \mathrm{d}v^\alpha/\mathrm{d}v$ as additional field quantities. The porosity ϕ is related to the volume fraction as $\phi = 1 - n^\mathfrak{s} = n^\mathfrak{f}$. Here, $\mathrm{d}v^\alpha$ corresponds to the volume which is occupied by the constituent φ^α in a Representative Volume Element (RVE), while $\mathrm{d}v$ is the volume element of the mixture. We are interested in a fully-saturated mixture (i. e. a solid material totally filled with oil or water) thus the volume fractions sum up to one, i. e. $n^\mathfrak{s} + n^\mathfrak{f} \equiv 1$, which is also known as the saturation condition. Next, we have to distinguish between the partial densities $\rho^\alpha = \mathrm{d}m^\alpha/\mathrm{d}v$ and the effective or realistic densities $\rho^{\alpha R} = \mathrm{d}m^\alpha/\mathrm{d}v^\alpha$. Here, $\mathrm{d}m^\alpha$ is the mass of the constituent φ^α in the investigated RVE. A result of the introduced definition of the volume fractions and the densities is a relation between the partial and the effective densities, i. e. $\rho^\alpha = n^\alpha \rho^{\alpha R}$. Within this contribution, we restrict ourselves to the material incompressible case, which means that the effective densities $\rho^{\alpha R}$ are constant during the whole process. However, such a restriction does not lead to constant partial densities ρ^α since the field variable n^α varies during the process, see Diebels & Ehlers [25]. Another remark has to be given with respect to the appearing model-inherent wave forms. As the model is material incompressible we are just able to model the second compressional wave, the so-called Biot's slow wave [16]. The resulting IBVP of the four-field formulation of the concerned problem was proposed and numerically analyzed by Diebels & Ehlers [25] as follows

$$\mathbf{u}_\mathfrak{s}' - \mathbf{v}_\mathfrak{s} = 0 \qquad \text{in } \Omega \times \mathcal{I}, \quad (15)$$

$$(n^\mathfrak{s}\,\rho^{\mathfrak{s}R} + n^\mathfrak{f}\,\rho^{\mathfrak{f}R})\,\mathbf{v}_\mathfrak{s}' + n^\mathfrak{f}\,\rho^{\mathfrak{f}R}\,\mathbf{w}_\mathfrak{f}' - \operatorname{div}(\mathbf{T}_E^\mathfrak{s} - p\,\mathbf{I}) = \left(n^\mathfrak{s}\,\rho^{\mathfrak{s}R} + n^\mathfrak{f}\,\rho^{\mathfrak{f}R}\right)\mathbf{b} \quad \text{in } \Omega \times \mathcal{I}, \quad (16)$$

$$\rho^{\mathfrak{f}R}\,\mathbf{v}_\mathfrak{s}' + \rho^{\mathfrak{f}R}\,\mathbf{w}_\mathfrak{f}' + \frac{n^\mathfrak{f}\,\mu^{\mathfrak{f}R}}{k^\mathfrak{s}}\mathbf{w}_\mathfrak{f} + \operatorname{grad} p = \rho^{\mathfrak{f}R}\,\mathbf{b} \qquad \text{in } \Omega \times \mathcal{I}, \quad (17)$$

$$\operatorname{div}(\mathbf{v}_\mathfrak{s} + n^F\,\mathbf{w}_\mathfrak{f}) = 0 \qquad \text{in } \Omega \times \mathcal{I}. \quad (18)$$

The partial derivative with respect to time is given as $(\bullet)'$. Convective terms are neglected according to the assumption of a geometrically linear theory. The system of equations consists of the balance of volume of the mixture, i. e. the mixture's continuity equation (18). Eq. (17) is the balance of momentum of the fluid constituent. Here, we have to remark, that we neglect the fluid extra stresses ($\mathbf{T}_E^\mathfrak{f} \approx \mathbf{0}$) with respect to the momentum exchange, i. e. the interaction force between the solid and the fluid constituent [26]. This restricts the model to fluid-flow in the inner domain of a porous medium. Surface effects at the border of a saturated porous medium to a pure Newtonian fluid can not be investigated by this constitutive relation. In addition, we have assumed a proportionality between the non-equilibrium part $\hat{\mathbf{p}}_{neq}^\mathfrak{f}$ of the

momentum interaction of the fluid (also denoted as the effective drag force $\hat{\mathbf{p}}^{\mathfrak{f}}_E$, c. f. [30, §5.2]) and the seepage velocity $\mathbf{w}_{\mathfrak{f}} := \mathbf{v}_{\mathfrak{f}} - \mathbf{v}_{\mathfrak{s}}$, leading to $\hat{\mathbf{p}}^{\mathfrak{f}}_{neq} \propto \mathbf{w}_{\mathfrak{f}}$. This results in a transient Darcy-type equation (17). More realistic constitutive relations like e. g. Forchheimer-type equations for larger Reynolds numbers $Re > 1$ can be constructed in an analogous way adding higher-order terms of $\mathbf{w}_{\mathfrak{f}}$ on the right-hand side of the former relation. Material parameters are the intrinsic permability $k^{\mathfrak{s}}$ and the dynamic viscosity of the fluid $\mu^{\mathfrak{f}R}$. Notice, that the instrinsic permeability of the solid skeleton is linked to the Darcy permeability via $k^{\mathfrak{s}}\,(\rho^{\mathfrak{f}R}\,g) = k^{\mathfrak{f}}\,\mu^{\mathfrak{f}R}$, while g is the acceleration of gravity. We remark here, with respect to the principle of frame indifference it is natural to choose a relative velocity $\mathbf{w}_{\mathfrak{f}}$ (seepage velocity) or $n^{\mathfrak{f}}\mathbf{w}_{\mathfrak{f}}$ (filter velocity) as the appropriate process variable. In the considered model, the non-equilibrium part, i. e. the dissipation $\mathcal{D}$, depends on the relative quantity $\mathcal{D} = \hat{\mathbf{p}}_{neq} \propto \mathbf{w}_{\mathfrak{f}}$. Thus, it is guaranteed that in the corresponding equilibrium case the relative motion between the fluid and the skeleton vanishes, i. e. $\mathbf{w}_{\mathfrak{f}} \equiv 0$ and the equilibrium state is reached. For a detailed discussion concerning this point, we refer to the state of the art review of Wilmanski [67]. Furthermore, it is obvious, that Eq. (16) refers to the balance of momentum of the mixture, while the Lagrangian multiplier $p(\mathbf{x}, t)$ is identified as the pore-pressure of the fluid. $\mathbf{T}^{\mathfrak{s}}_E$ is the Cauchy extra stress tensor of the solid constituent. Hooke's law relates the Cauchy stresses to the symmetric part of the displacement gradients. $\mathbf{b}$ is the body force which is related to the gravity. Eq. (15) was introduced to reduce the order of temporal derivatives to one. Thus, the present system of equations is compatible to the implementation of the DGT scheme.
The primary variables of the proposed model are the displacement $\mathbf{u}_{\mathfrak{s}}$, the velocity $\mathbf{v}_{\mathfrak{s}} = (\mathbf{u}_{\mathfrak{s}})'_{\mathfrak{s}}$ of the solid phase, the seepage velocity $\mathbf{w}_{\mathfrak{f}}$ concerning the relative movement of the fluid phase with respect to the solid phase, as well as the pore pressure p of the fluid.
Due to the concept of superimposed constituents of the solid and fluid phases in the mixture the boundary conditions are described separately as follows

$$\begin{aligned}
\mathbf{u}_{\mathfrak{s}} &= \bar{\mathbf{u}}_{\mathfrak{s}} && \text{on} && \Gamma^{\mathfrak{s}}_D \times \mathcal{I}, \\
(\mathbf{T}^{\mathfrak{s}}_E - p\,\mathbf{I}) \cdot \mathbf{n} &= \bar{\mathbf{t}} && \text{on} && \Gamma^{\mathfrak{s}}_N \times \mathcal{I}, \\
\mathbf{w}_{\mathfrak{f}} &= \bar{\mathbf{w}}_{\mathfrak{f}} && \text{on} && \Gamma^{\mathfrak{f}}_{\mathbf{w}} \times \mathcal{I}, \\
p &= \bar{p} && \text{on} && \Gamma^{\mathfrak{f}}_p \times \mathcal{I},
\end{aligned} \tag{19}$$

where $\partial\Omega = \Gamma^{\mathfrak{s}}_D \bigcup \Gamma^{\mathfrak{s}}_N = \Gamma^{\mathfrak{f}}_p \bigcup \Gamma^{\mathfrak{f}}_{\mathbf{w}}$ with $\Gamma^{\mathfrak{s}}_D \bigcap \Gamma^{\mathfrak{s}}_N = \emptyset$ and $\Gamma^{\mathfrak{f}}_p \bigcap \Gamma^{\mathfrak{f}}_{\mathbf{w}} = \emptyset$. The initial conditions are prescribed for both constituents as

$$\begin{aligned}
\mathbf{u}_{\mathfrak{s}}(\mathbf{x}, t_0) &= \mathbf{u}_{\mathfrak{s},0}(\mathbf{x}) && \text{at} && \Omega \times t_0, \\
\mathbf{v}_{\mathfrak{s}}(\mathbf{x}, t_0) &= \mathbf{v}_{\mathfrak{s},0}(\mathbf{x}) && \text{at} && \Omega \times t_0, \\
\mathbf{w}_{\mathfrak{f}}(\mathbf{x}, t_0) &= \mathbf{w}_{\mathfrak{f},0}(\mathbf{x}) && \text{at} && \Omega \times t_0.
\end{aligned} \tag{20}$$

Since there exists no time derivative of the pore pressure p in the Eqs. (15-18), its value is solved in a consistent way within the system of differential algebraic equations. The weak form of the governing set of equations is obtained in analogy to the previous section. Thus we multiply the Eqs. (15-18) with certain test functions $\delta\mathbf{u} = \{\delta\mathbf{u}_{\mathfrak{s}}, \delta\mathbf{v}_{\mathfrak{s}}, \delta\mathbf{w}_{\mathfrak{f}}, \delta p\}$ and integrate over the space-time slab Q^n. Integration by parts for an artificial (here vectorial) time derivative $\boldsymbol{\Psi}'$ leads to

$$\int_{Q^n} \boldsymbol{\Psi}' \cdot \delta\boldsymbol{\Psi}\, \mathrm{d}Q^n = -\int_{Q^n} \boldsymbol{\Psi} \cdot \delta\boldsymbol{\Psi}'\, \mathrm{d}Q^n + \int_{\Omega} \Big[\breve{\boldsymbol{\Psi}} \cdot \delta\boldsymbol{\Psi}\Big]_{t_n}^{t_{n+1}}\, \mathrm{d}v. \tag{21}$$

Here, $\delta\boldsymbol{\Psi}$ is introduced as the corresponding vector-valued test-function. In analogy to the previous introduction in Eq. (10), we introduce the flux

$$\breve{\boldsymbol{\Psi}} := \begin{cases} \boldsymbol{\Psi}_0(\mathbf{x}, t_0), & \text{if} \quad n = 0, \\ \boldsymbol{\Psi}^-(\mathbf{x}, t_n), & \text{otherwise}, \end{cases} \qquad \text{where} \quad \boldsymbol{\Psi}^-(\mathbf{x}, t_n) = \lim_{\epsilon \to 0^+} \boldsymbol{\Psi}(\mathbf{x}, t_n - \epsilon), \tag{22}$$

in which $\boldsymbol{\Psi}_0$ is the prescribed initial value (e. g. the initial displacement of the solid constituent $\mathbf{u}_{\mathfrak{s},0}$). Let $\mathbf{u}_h = \{\mathbf{u}_{\mathfrak{s},h}, \mathbf{v}_{\mathfrak{s},h}, \mathbf{w}_{\mathfrak{f},h}, p_h\}$ denote the discrete weighting-functions and $\delta\mathbf{u}_h = \{\delta\mathbf{u}_{\mathfrak{s},h}, \delta\mathbf{v}_{\mathfrak{s},h}, \delta\mathbf{w}_{\mathfrak{f},h}, \delta p_h\}$ be the corresponding set of discrete test-functions. Again, we assume that the finite-dimensional function space $\mathcal{W}_h \subset \mathcal{W}$ consists of tensor products of spatial and temporal weighting- and test-functions. Thus, we can define the underlying finite element problem as:

$$\text{Find} \quad \mathbf{u}_h \in \mathcal{W}_h, \quad \text{such that} \quad B(\mathbf{u}_h, \delta\mathbf{u}_h) = L(\delta\mathbf{u}_h), \qquad \forall\, \delta\mathbf{u}_h \in \mathcal{W}_h. \tag{23}$$

For the sake of notational convenience, we suppress the subscript $(\bullet)_h$ on the right-hand-side of the following equations of the linear and bilinear form. Then, the bilinear form is given as:

$$\begin{aligned} B(\mathbf{u}_h, \delta\mathbf{u}_h) = \sum_{j=1}^{N} \Big\{ & \int_{P_h^j} -\mathbf{u}_{\mathfrak{s}} \cdot \delta\mathbf{u}'_{\mathfrak{s}} \,\mathrm{d}Q^n - \int_{P_h^j} \mathbf{v}_{\mathfrak{s}} \cdot \delta\mathbf{u}_{\mathfrak{s}} \,\mathrm{d}Q^n + \int_{\Omega_h^j} (\mathbf{u}^-_{\mathfrak{s},n+1} - \breve{\mathbf{u}}_{\mathfrak{s},n}) \cdot \delta\mathbf{u}_{\mathfrak{s}} \,\mathrm{d}v \\ & - \int_{P_h^j} \left\{ [(n^{\mathfrak{s}}\, \rho^{\mathfrak{s}R} + n^{\mathfrak{f}}\, \rho^{\mathfrak{f}R})\, \mathbf{v}_{\mathfrak{s}} + n^{\mathfrak{f}}\, \rho^{\mathfrak{f}R}\, \mathbf{w}_{\mathfrak{f}}] \cdot \delta\mathbf{v}'_{\mathfrak{s}} - (\mathbf{T}^{\mathfrak{s}}_E - p\,\mathbf{I}) : \operatorname{grad} \delta\mathbf{v}_{\mathfrak{s}} \right\} \mathrm{d}Q^n \\ & + \int_{\Omega_h^j} [(n^{\mathfrak{s}}\, \rho^{\mathfrak{s}R} + n^{\mathfrak{f}}\, \rho^{\mathfrak{f}R})(\mathbf{v}^-_{\mathfrak{s},n+1} - \breve{\mathbf{v}}_{\mathfrak{s},n}) + n^{\mathfrak{f}}\, \rho^{\mathfrak{f}R}(\mathbf{w}^-_{\mathfrak{f},n+1} - \breve{\mathbf{w}}_{\mathfrak{f},n})] \cdot \delta\mathbf{v}_{\mathfrak{s}} \,\mathrm{d}v \\ & - \int_{P_h^j} \{\rho^{\mathfrak{f}R}\, (\mathbf{v}_{\mathfrak{s}} + \mathbf{w}_{\mathfrak{f}}) \cdot \delta\mathbf{w}'_{\mathfrak{f}} - (\frac{n^{\mathfrak{f}} \mu^{\mathfrak{f}R}}{k^{\mathfrak{s}}} \mathbf{w}_{\mathfrak{f}} + \operatorname{grad} p) \cdot \delta\mathbf{w}_{\mathfrak{f}}\} \mathrm{d}Q^n \\ & + \int_{\Omega_h^j} \rho^{\mathfrak{f}R} (\mathbf{v}^-_{\mathfrak{s},n+1} + \mathbf{w}^-_{\mathfrak{f},n+1} - \breve{\mathbf{v}}_{\mathfrak{s},n} - \breve{\mathbf{w}}_{\mathfrak{f},n}) \cdot \delta\mathbf{w}_{\mathfrak{f}} \,\mathrm{d}v \\ & + \int_{P_h^j} \operatorname{div}(\mathbf{v}_{\mathfrak{s}} + n^{\mathfrak{f}}\, \mathbf{w}_{\mathfrak{f}})\, \delta p \,\mathrm{d}Q^n \Big\}. \end{aligned}$$

The linear form is given as

$$\begin{aligned} L(\delta\mathbf{u}) \;=\; & \sum_{k=1}^{M} \int_{\Gamma^{\mathfrak{s}}_{N,e} \times \mathcal{I}^n} \bar{\mathbf{t}} \cdot \delta\mathbf{v}_{\mathfrak{s}} \,\mathrm{d}a \,\mathrm{d}t \\ & + \sum_{j=1}^{N} \{ \int_{P_h^j} (n^{\mathfrak{s}}\, \rho^{\mathfrak{s}R} + n^{\mathfrak{f}}\, \rho^{\mathfrak{f}R})\, \mathbf{b} \cdot \delta\mathbf{v}_{\mathfrak{s}} + \rho^{\mathfrak{f}R}\, \mathbf{b} \cdot \delta\mathbf{w}_{\mathfrak{f}}) \mathrm{d}Q^n \}. \end{aligned}$$

Notice again, that we have integrated by parts all terms in the above equations containing partial derivatives with respect to time. Thus, we obtain the previously defined flux operator (22) at the border of the time-slab. It is worth noticing, that no temporal update through the flux operation is available for the pore pressure p. Its value is solved within the resulting system of algebraic equations in a consistent way on every time-slab Q^n.

5. NUMERICAL EXAMPLES

5.1. The one-dimensional erosion problem

The simplified erosion or suffosion problem of a fluid-saturated sample of polydisperse cohesionless granulates can be described by the classical parabolic model equation, for details we refer to [56]

$$\partial_t(\phi) - \operatorname{div} \mathbf{q} = 0, \quad \text{in} \quad \Omega \times \mathcal{I}$$

with $\Omega \in \mathbb{R}^1 = [0,1]$ m and $\mathcal{I} = [0, 2 \times 10^4]$ s. $A = 1 \times 10^{-4}$ m/s^2 represents the isotropic (scalar) porosity of the specimen that plays the role of a porosity diffusivity coefficient. A non-smooth initial distribution of the porosity ϕ is given as

$$\phi_0(x) = \begin{cases} 0.27, & 0.25 \text{ m} < x < 0.75 \text{ m}, \\ 0, & \text{otherwise} \end{cases}$$

and the given homogeneous Dirichlet boundary is prescribed for

$$\phi(0,t) = \phi(1,t) = 0 \, .$$

For this simple model example we employ standard Lagrangian polynomials in space and in time. In the spatial domain, we investigated linear weighting- and test-functions. In Fig. 4 we depict the numerical results of the IBVP obtained with the classical MOL and with the presented DGT method. First, Fig. 4(a) shows the result obtained by the trapezoidal rule [‡] (CD) with 20 spatial elements and 20 time-steps ($\Delta t = 1000$ s). In Fig. 4(b) we used refined the temporal discretization, i. e. 2000 time-steps $\Delta t = 10$ s while keeping the spatial discretization fixed. In Fig.4 (c) we depicted the CD result with refined spatial discretization $N = 200$. A CD result with both refined spatial and temporal discretization ($N = 200$ and $\Delta t = 10$ s) is shown in Fig. 4(d). From these diagrams, we observed that the spurious oscillations due to Fig. 4(e) is the result obtained with the backward-Euler method (BE) and Fig. 4(f) is those with DGT(1), both are calculated with a coarse discretization in space and time (20 spatial elements and $\Delta t = 10$ s). Both results are stable and of first order accuracy. As it is well-known for the Navier-Stokes equation, spurious oscillations in the numerical solution could be caused by insufficient mesh resolution in the boundary layer, [32, 34, 65]. Hereby, we have observed a similar effect in the space-time domain. The coarse temporal discretization is not able to reproduce the locally steep gradient in the initial phase, which consequently leads to spurious oscillations in the numerical results. As it is observed in the numerical results, these oscillations are transported within the temporal domain, see Fig. 4(a-d). We also observe, in Fig. 4(b), the spurious oscillation damps out in the pass of time which indicates that the oscillations could be avoided by a even finer temporal discretization. A likely parabolic problem was calculated by Quarteroni et al. [57, pp. 623], analyzing the heat equation in a uniaxial bar with non-smooth initial conditions. Under the same space and time discretization, the

[‡]The trapezoidal rule reads, c. f. Strang [64, p. 564]:

$$\partial_t(\bullet) = a\,(\bullet) \qquad \longrightarrow \qquad \frac{(\bullet)_{n+1} - (\bullet)_n}{\Delta t} = \frac{1}{2} a\, [(\bullet)_n + (\bullet)_{n+1}]$$

with $\Delta t = t_{n+1} - t_n$.

author showed that the Crank-Nicolson method (trapezoidal rule) leads to oscillating solutions while the backward-Euler method produces stable results. Owning to the strong numerical dissipation within the backward-Euler scheme, the numerical results are always stable even under rarely coarse discretizations, but nevertheless, from Fig. 5 which shows the temporal profile of porosity at $x = 0.25$ m, difference can be observed. Comparing to the less satisfying results of the backward-Euler method, the DGT(1) method under a relative coarse time step length agrees with the analytical result quite well. It is also observed that the largest jump appears at the initial state ($t = t_0$), where the gradient of the analytical solution is large. It is obvious, that the weak enforcement of the non-smooth initial condition ϕ_0 within the DGT method renders more accurate numerical solutions. Fig. 6 shows the spatial distribution of the gradient of the porosity ($\operatorname{grad}\phi = \mathbf{q}/A$). It has to be noticed that under the same space and time discretization, the gradient of the porosity obtained by the CD method shows large and unrealistic oscillations while the solution of the DGT(1) method is smooth and reliable. In Fig. 7 we depict the curves at $x = 0.25$ m obtained by various DGT(p). For the sake of a better illustration, we show just two time-steps with $\Delta t = 1000$ s. Hereby, the spatial discretization is fixed by 20 linear element in space. It can be observed that the amount of the weakly enforced discontinuity in the temporal domain diminishs with higher order of the temporal weighting functions. Furthermore, we note that the high gradient of the analytical solution at the beginning of the process is well reproduced with higher order (i. e. cubic) weighting functions.

5.2. Dynamic response of a soil column under a step loading

In the second numerical example we investigate the dynamic response of a soil column. The height of the concerned fully-saturated soil specimen is 10 m. A uniform step load $F(t) = 10h(t)$ kN is applied at the drained upper surface, where $h(t)$ is the Heaviside function. The remaining boundaries are treated as rigid and undrained, see Fig 8. The chosen material parameters are listed in Tab. I. The properties of the solid skeleton are prescribed with the

$E^{\mathfrak{s}} = 1.4516 \times 10^4$ kN/m^2	$k^{\mathfrak{s}} = 1 \times 10^{-12}$ m^2	$\rho^{\mathfrak{f}R} = 1000$ kg/m^3
$\nu^{\mathfrak{s}} = 0.3$	$\gamma^{\mathfrak{f}R} = 1 \times 10^4$ N/m^3	$\rho^{\mathfrak{s}R} = 2000$ kg/m^3
$n_0^{\mathfrak{f}} = 0.33$		

Table I. Material parameters

Youngs's modulus and Poisson's ratio $E^{\mathfrak{s}}$ and $\nu^{\mathfrak{s}}$ respectively, $k^{\mathfrak{s}}$ is the (scalar) intrinsic permeability and $\rho^{\mathfrak{s}R}$ is the effective density. For the fluid-phase, we give the effective weight $\gamma^{\mathfrak{f}R}$ and the effective density $\rho^{\mathfrak{f}R}$. The initial volume fraction of the fluid phase (porosity) $n_0^{\mathfrak{f}}$ is also given. Under the saturation condition, the corresponding initial volume fraction of the solid phase is $n_0^{\mathfrak{s}} = 1 - n_0^{\mathfrak{f}}$. The space-time discretization consists of a regular temporal discretization with a constant time-step $\Delta t = \text{const.}$ and an irregular discretization in space, see Fig. 8. Since we have not yet investigated an adaptive strategy neither in space nor in time, such a spatially-graded mesh takes into account the high pressure gradient near the upper surface. Due to the requirement of the Babuška-Brezzi condition [9, 19], we apply quadratic weighting functions for $\mathbf{u}_{\mathfrak{s}}$ and $\mathbf{v}_{\mathfrak{s}}$, and linear weighting functions for $\mathbf{w}_{\mathfrak{f}}$ and p in the spatial

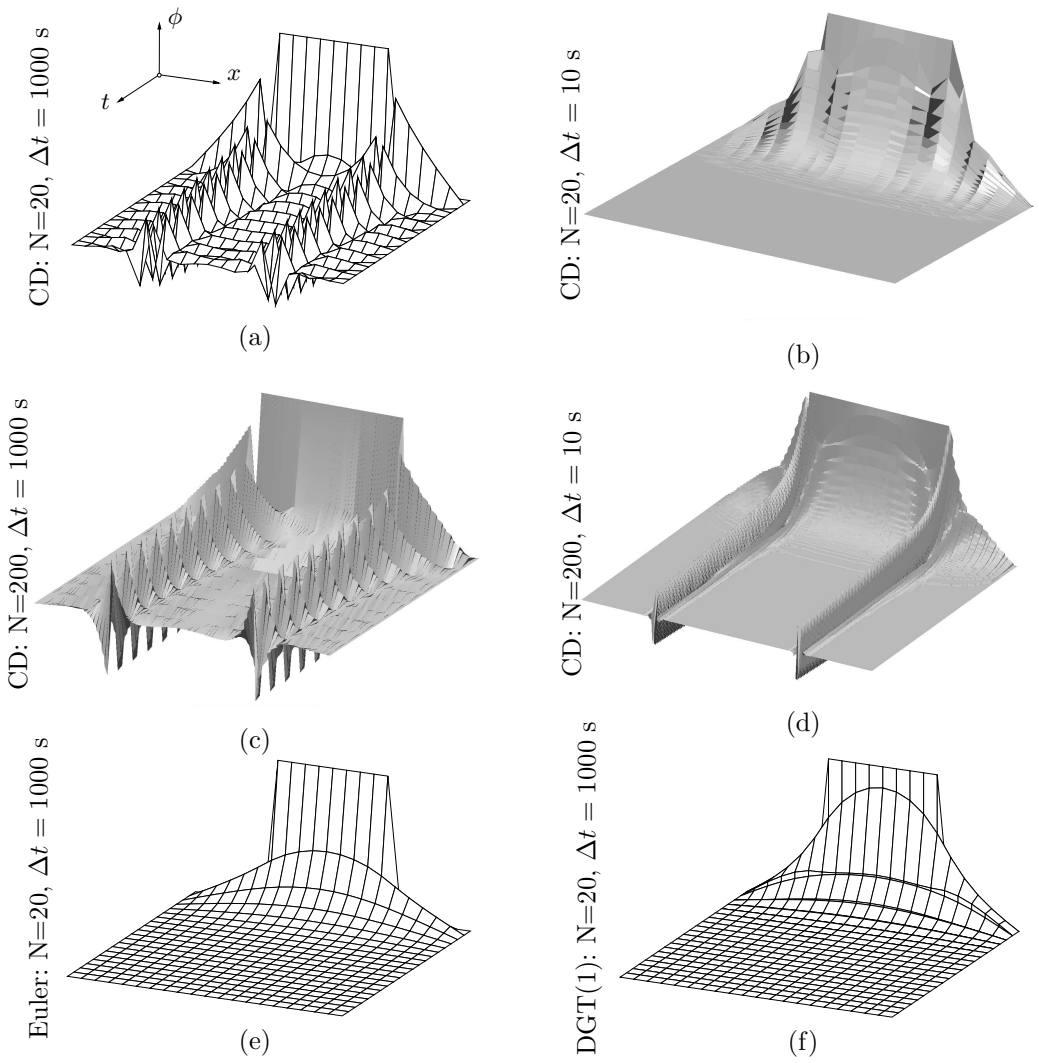

Figure 4. (a)CD: 20 spatial elements, $\Delta t = 1000$ s, (b)CD: 20 spatial elements, $\Delta t = 10$ s, (c)CD: 200 spatial elements, $\Delta t = 1000$ s, (d)CD: 200 spatial elements, $\Delta t = 10$ s, (e)Euler: 20 spatial elements, $\Delta t = 1000$ s, (f)DGT(1): 20 spatial elements, $\Delta t = 1000$ s

domain as depicted in Fig. 8. The chosen polynomials in the time domain are standard linear Lagrangian polynomials.

Concerning the present consolidation problem, the applied external load $F(t)$ on the drained boundary causes a discontinuity in the pore-pressure field $p(t)$. Within the first period of time, when the external load is applied suddenly, the deformation of the solid skeleton is neglectable, and therefore, the total external load is supported by the pore-pressure. Such an effect leads to jumps in the pressure field from zero at $t = t_0$ (initial state) to the certain value that

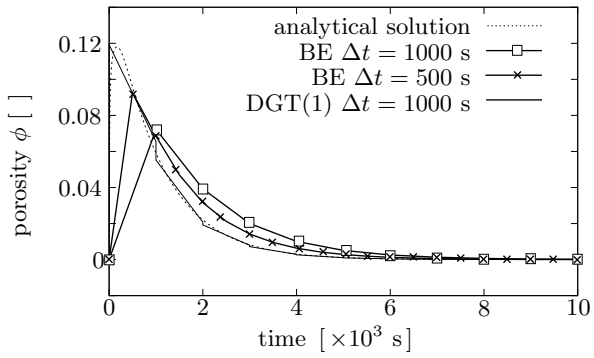

Figure 5. Temporal porosity profile at $x = 0.25$ m with 20 spatial elements

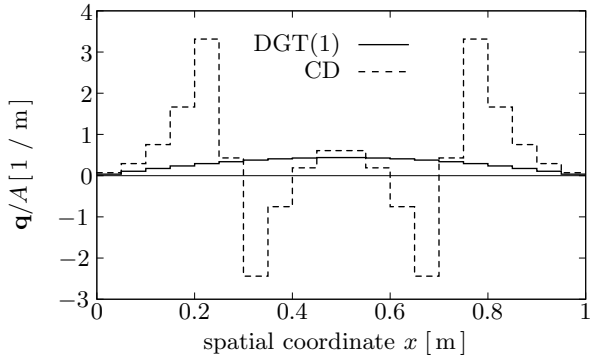

Figure 6. Flux distribution at $t = 3000$ s with $\Delta t = 1000$ s

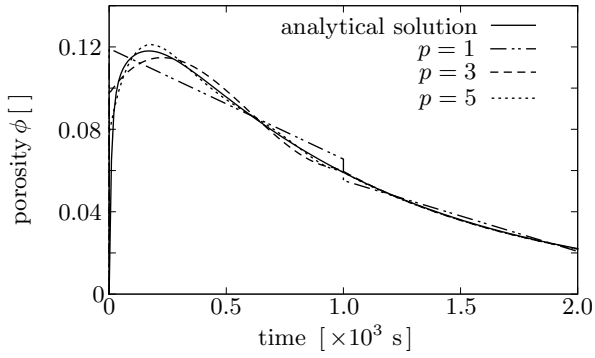

Figure 7. Temporal porosity profile at $x = 0.25$ m calculated with the DGT(p) method. N=20 spatial finite elements and $\Delta t = 1000$ s

withstands the external force at $t = t_0 + \epsilon$. Afterwards, as the fluid is squeezed out at the drained boundary and the deformation in the solid skeleton increases, the solid phase supports more external load. In the meantime, we observe that the pore-pressure decreases from the drained boundary to the depth. Problems arise if we apply the classical finite element method with continuous weighting- and test-functions combined with a finite difference method in time (MOL). This trouble stems in the fact that the standard MOLs are not able to reproduce the discontinuous phenomena, i. e. jumps in the pore pressure field. Thus, if the gradients of the pore-pressure field are increasing, spurious oscillations occur in the numerical solution, especially for extremely small time-steps Δt. Within the DGT however, the underlying weak form is fulfilled on the time-slab. Thus, any strong discontinuity of the analytical solution has not to be reproduced exactly as it is fulfilled only in a weak sense within the time-interval. Therefore, the described phenomena can be obtained efficiently. In Fig. 9, we depicted the space-time distribution of the pore pressure field $p(x, t)$ obtained by DGT(1) with a time-step size $\Delta t = 0.1$ s. As shown, the discontinuity in the pressure field caused by the suddenly applied external load $F(t)$ is very well reproduced. The displacement distribution of the solid skeleton is shown in Fig. 10. It is observed that the numerical results agree well with the well-known physical observations.

Next we observe the evolution of the seepage velocity $\mathbf{w}_{\mathfrak{f}}$ at the point P ($x = 2.5$ m) depicted in Fig 8. In order to demonstrate the improved behavior of DGT, we compare the numerical results with the results obtained by the implicit backward-Euler scheme in the temporal domain, as it is quite a common approach in the TPM [25, 31]. Compare the results under the same spatial discretization of the DGT and the MOL, we observed that the seepage velocity distribution $\mathbf{w}_{\mathfrak{f}}$ obtained with the DGT with a time-step length $\Delta t = 0.1$ s agrees already very well with the finest result $\Delta t = 0.0001$ s of the backward-Euler scheme. This impressively demonstrates the improved numerical behavior of the DGT compared to the backward-Euler method. Regarding the results of the backward-Euler method with varying time-step lengths in detail ($\Delta t = 1,\ 0.1,\ 0.01,\ 0.0001$ s), we observe further the effect of numerical dissipation,

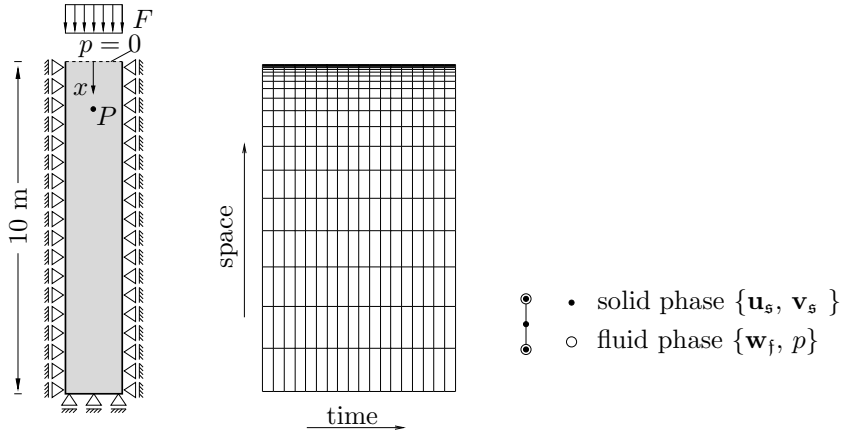

Figure 8. Initial boundary value problem, space-time discretization and spatially-mixed finite elements

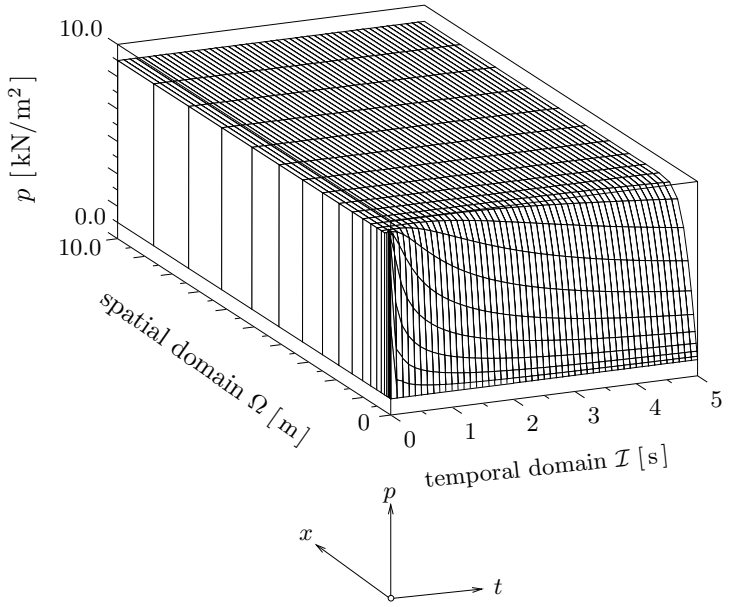

Figure 9. Space-time pore-pressure distribution $p(x,t)$ calculated by the DGT(1) with a time-step length $\Delta t = 0.1$ s

see Fig 11. With a large time-step ($\Delta t = 1$ s) the numerical dissipation is relatively large and the traveling seepage velocity wave (Biot's wave) is completely damped out. With a even finer temporal discretization ($\Delta t = 0.0001$ s) the result agrees well with the one of the DGT method (with $\Delta t = 0.1$ s). We denote here, in spite of increased DOFs due to discontinity on the discrete time level, the efficiency of the applied DGT(1) method is superior to the backward-Euler scheme.

Furthermore we want to remark within practical (e. g. inhomogeneous) applications it is more or less impossible to detect a priori an optimal time-step length within the MOL. Thus, it is very difficult to balance the time-step length as, on the one hand, we damp out the traveling waves applying a large time-step and, on the other hand, we get spurious oscillations at the drained boundary using very small time-steps. Therefore, adaptive a posteriori strategies based e. g. on embedded Runge-Kutta schemes are necessary within the MOL, c. f. [27]. Obviously we also can involve adaptive strategies into the present coupled space-time finite element scheme. Besides coupled space-time strategies based on duality techniques [6, 48, 61] simple temporal error indicators based on the jump terms [20, 68, 69] can be motivated. Within a system of Differential Algebraic Equation (DAE) there usually exits an optimal time step length. Further refinement exceeding such optimal time step length would even worsen the results [1, 33, 38]. In practical applications it is hard to detect this limit of refinement, therefore a jump based error indicator maybe more useful.

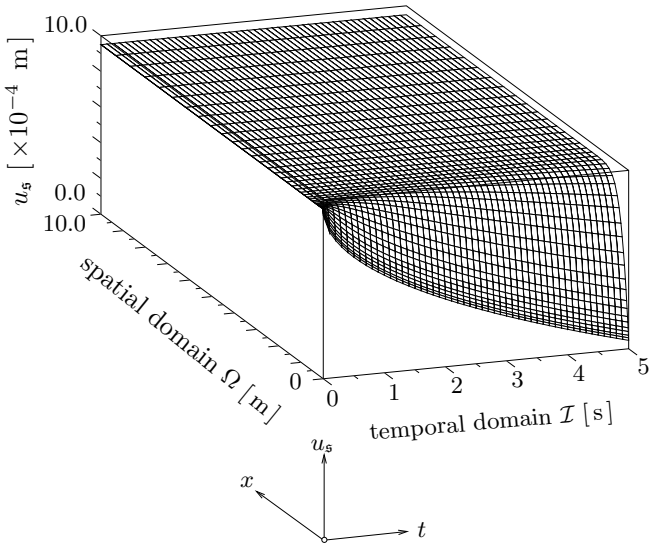

Figure 10. Space-time distribution of solid displacements $u_s(x,t)$ calculated by the DGT(1) with a time-step length $\Delta t = 0.1$ s

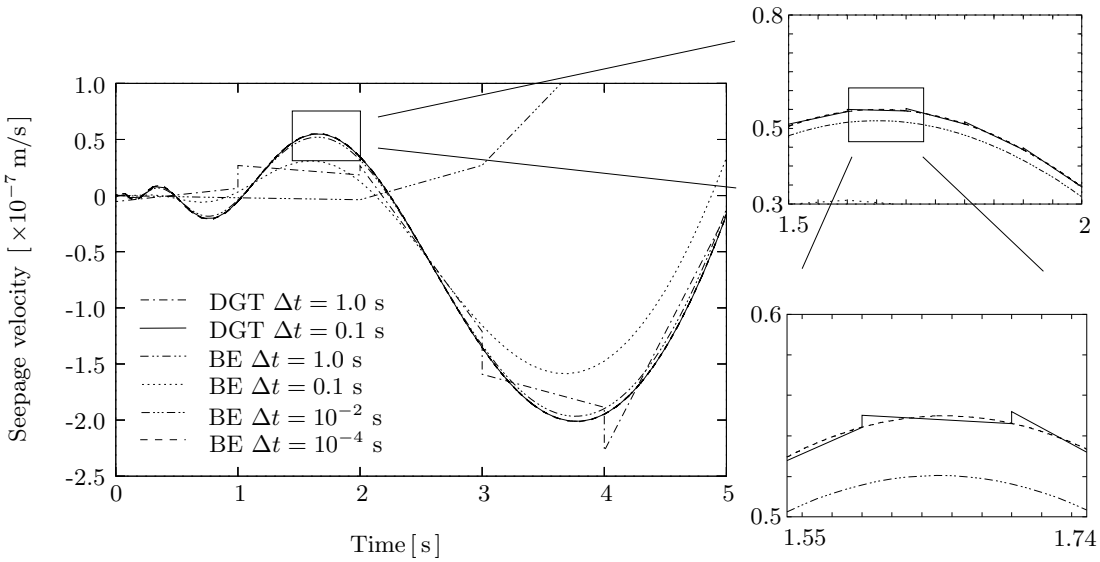

Figure 11. Seepage velocity at point P

5.3. Elastic response of a partially-loaded soil block

In this section, we consider a 2-dimensional partially loaded soil specimen as depicted in Fig. 12. In contrast to the previous investigation, we are now interested in calculating an inhomogeneous IBVP. The fully-saturated soil foundation of 10 m $\times$ 10 m is partially subjected to a constant external load $F = 15$ kN, see Fig 12. The free boundary at the upper-left part of the specimen is perfectly drained. Thus, a Dirichlet boundary condition is prescribed for the the pore-pressure, i. e. $p = 0$. The left and right walls and the bottom of the foundation are assumed to be rigid and undrained. The spatial discretization and the chosen spatially mixed finite element formulation is depicted in Fig. 12. Due to the reasons mentioned in the last examples, we choose biquadratic Lagrangian polynomials for the solid-phase quantities ($\mathbf{u}_{\mathfrak{s},h}$ and $\mathbf{v}_{\mathfrak{s},h}$) and bilinear ones for the quantities of the fluid phase ($\mathbf{w}_{\mathfrak{f},h}$ and p_h). Similar IBVPs have already been investigated in literature, c. f. [2, 25, 50], thus we are able to compare our results with the latter investigations. With respect to the material parameters we follow the work of [25] and [2], c. f. Tab. II. In the present investigation, we also analyze the movement of two corner points

$E^{\mathfrak{s}} = 1.4516 \times 10^4$ kN/m^2	$k^{\mathfrak{s}} = 1 \times 10^{-11}$ m^2	$\rho^{\mathfrak{f}R} = 1000$ kg/m^3
$\nu^{\mathfrak{s}} = 0.3$	$\gamma^{\mathfrak{f}R} = 1 \times 10^4$ N/m^3	$\rho^{\mathfrak{s}R} = 2000$ kg/m^3
$n_0^{\mathfrak{f}} = 0.33$		

Table II. Material parameters for the 2-dim problem

denoted as A and C, see Fig. 12. Since the horizontal movement of A and C is prevented by the rigid specimen walls only vertical movements are observable. Fig. 13 shows the numerical results obtained by backward-Euler schemes, again with different time-step lengths Δt. Since the applied external load F at the Neumann boundary is small, the observed motion of the nodes A and C have almost the same amount but opposite directions. We want to remark that our results obtained with a time-step-length $\Delta t = 0.01$ s is very similar to the one presented by Diebels & Ehlers [25]. However, refining again the time-step length ($\Delta t = 0.0001$ s), the previously numerically damped-out wave appears over the complete time interval. Due to the small Darcy permeability $k^{\mathfrak{f}} = 10^{-4}$ m/s (equivalent to the intrinsic permeability $k^{\mathfrak{s}} = 10^{-11}$ m^2), within such a short time interval ($\mathcal{I} = 2$ s), the total fluid-discharge is very small and, the consolidation process of the soil specimen is still at the very beginning, c. f. [50]. Therefore, we conclude that the fast attentuation of the oscillations in the displacement field is unphysical and can be completely assigned to the numerical dissipation of the chosen backward-Euler scheme, c. f. [25]. Fig. 14 shows the history of the solid displacement $\mathbf{u}_{\mathfrak{s}}$ at the same nodes obtained by the DGT(1) method with a varying temporal discretization. We observe, that even with a relativly large temporal discretization ($\Delta t = 0.01$ s), the quality of the result obtained with the DGT method agrees with the one of the backward-Euler scheme with a very small time-step ($\Delta t = 0.0001$ s) very well. Again, it has to be remarked that temporal jumps occur in the results of the coarse discretization of the DGT approach ($\Delta t = 0.05$ s). This motivates again to formulate a simple error indicator and to refine the temporal discretization within the space-time finite element approach if jumps occur.

In Fig. 15 we depicted some numerical results in one chart. Due to numerical dissipation it is observed that with a coarse time step length, i. e. $\Delta t = 0.01$ s, the amplitude of the calculated

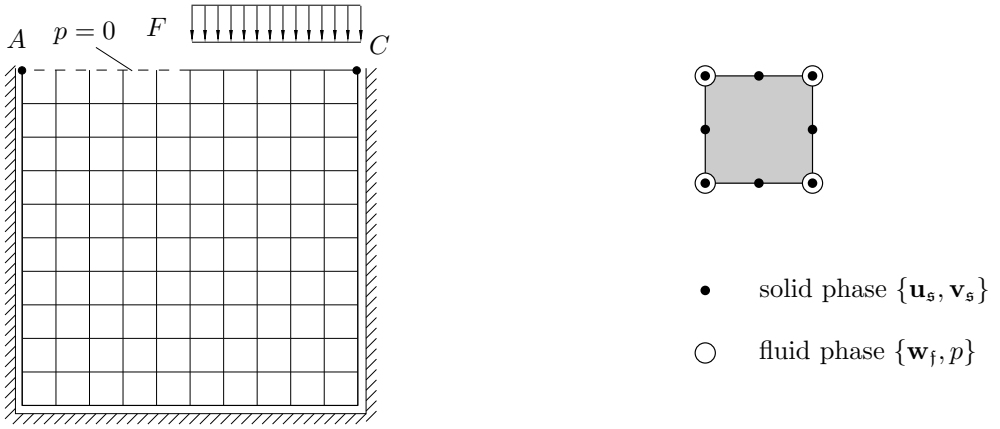

Figure 12. Spatial discretization and spatially mixed finite element formulation

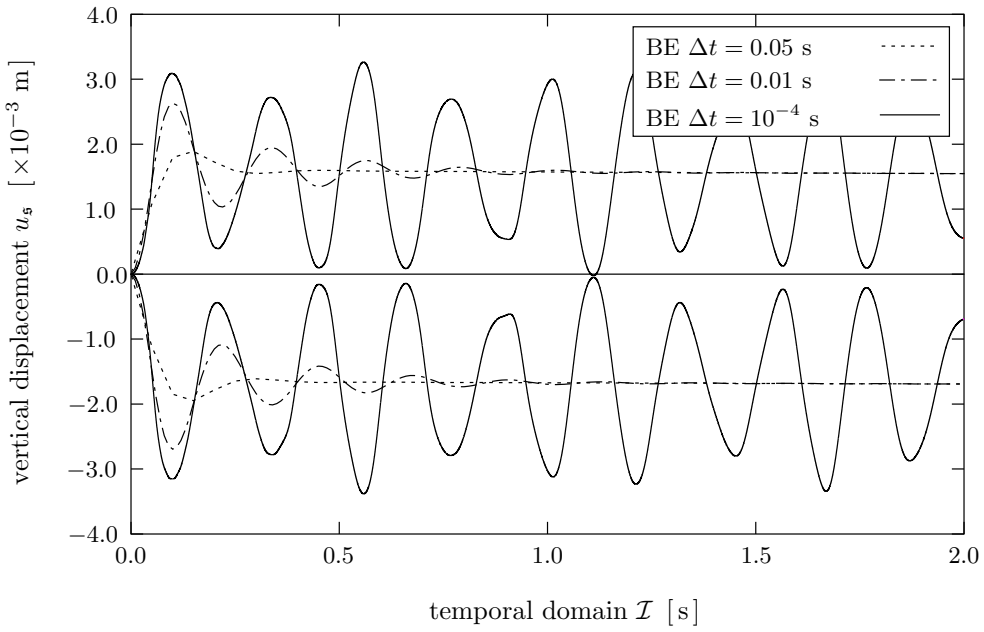

Figure 13. Solid displacements at the corners A and C of the specimen obtained by the backward-Euler scheme

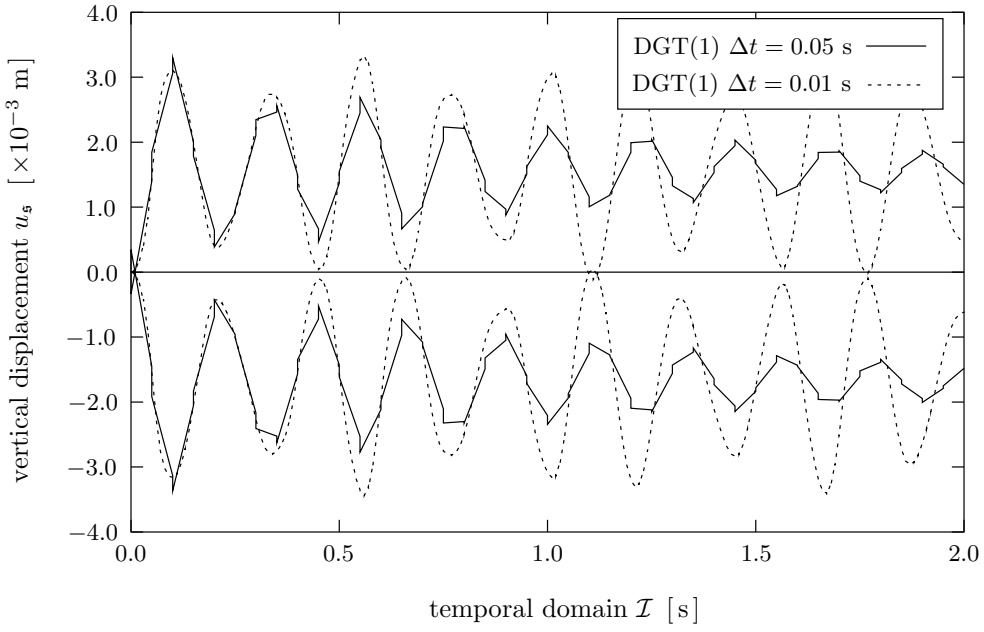

Figure 14. Solid displacements at the corners A and C of the specimen obtained by the DGT(1) approach

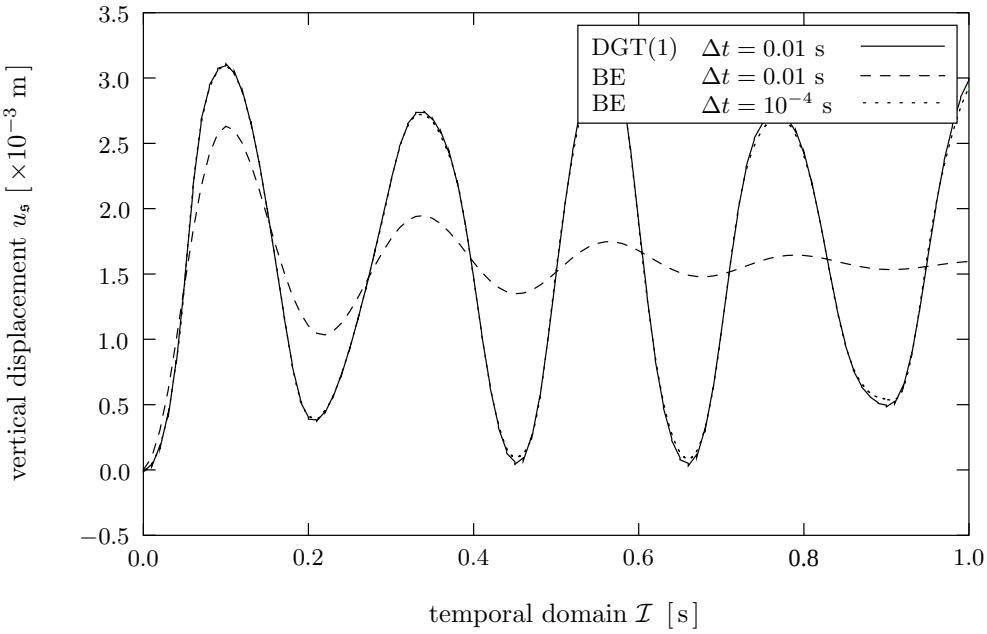

Figure 15. Solid displacement at the left corner A of the specimen

results of the backward-Euler schemes decrease dramatically. Nevertheless, the frequencies of the propagation wave is barely influenced. Moreover, we want to mention that this is in agreement with previous works of Diebels & Ehlers [25] and Arduino et al. [2]. On the other hand, we observe the excellent agreement of the results obtained with the DGT(1) with a large time step length ($\Delta t = 0.01$ s) and the one of the backward-Euler scheme with a small time step length ($\Delta t = 10^{-4}$ s). Thus, we conclude, that in spite of the increased number of DOFs at each time slab, the DGT method maybe much more efficient than the ordinary MOL approach.

6. CONCLUSION

In the present work, we studied a coupled space-time Galerkin method with discontinuous weighting- and test functions in the temporal domain. As it was shown within several numerical examples the developed finite element method is stable and efficient, and, which has to be emphasized, requires no auxiliary variable as it is needed in so-called DG-Penalty methods. The underlying weak form of the finite element approach is fulfilled on each time-slab, which leads to a method that is more flexible than the classical MOL, and is able to reproduce physical discontinuous phenomena occurring in various applications of fluid-flow through porous media. Furthermore, the numerical method shows a wide potential to develop both coupled space-time adaptive strategies based on residual- and/or gradient-based error estimation techniques and simple decoupled adaptive methods based on an error indicator of the temporal jump terms. In the present work, the possibility in both h and p-refinements in time is shown. It has to be concluded, that h-refinement leads to system matrices which can be compared to ordinary techniques (MOL) with respect to their sizes. On the other hand, the p-refinement technique with higher order weighting functions in the time domain enables larger time step lengths, i. e less time steps. However, a blow-up in the resulting system of algebraic equations at the time slab level must be taken into account.

Acknowledgment

The authors are grateful to the DFG (German Science Foundation – Deutsche Forschungsgemeinschaft) for their financial support through grant number Di 430/4-1.

REFERENCES

1. W. F. Ames. Numerical Methods for Partial Differential Equations,Second Edition. Academic Press, Boston-New York, 1977.
2. P. Arduino, E. Macari, and ASCE Members. Numerical analysis of geomaterials within theory of porous media. J. Eng. Meth., Feb.:167–175, 2001.
3. J.H. Argyris and D.W. Scharpf. Finite elements in space and time. Nucl. Engrg. Des., 10:456–464, 1969.
4. D.N. Arnold. An interior penalty finite element method with discontinuous elements. PhD thesis, The University of Chicago, Chicago, IL, 1979.
5. D.N. Arnold. An interior penalty finite element method with discontinuous elements. SIAM J. Numer. Anal., 19:742–760, 1982.
6. D. Aubry, D. Lucas, and B. Tie. Adaptive strategy for transient/coupled problems. Applications to thermoelasticity and elastodynamics. Comp. Meth. Appl. Mech. Eng., 176, 1999.
7. M. F. Wheeler B. Rivière and V. Girault. A priori error estiamates for finite methods based on discontinuous approximation spaces for elliptic problems. SIAM J. Numer. Anal., 39:902–931, 2001.
8. S. Shaw B. Rivière and M. F. Wheeler. Discontinuous galerkin finite element methods for linear elasticity and quasistatic linear viscoelasticity. Numer. Math., 95:347–376, 2003.
9. I. Babuška. Errors bounds for finite element method. Numer. Math., 16:322–333, 1971.
10. G.A. Baker. Finite element methods for elliptic equations with nonconforming elements. Math. Comp., 31:45–59, 1977.
11. F. Bassi and S. Rebay. A high-order accurate discontinuous finite element method for the numerical solution of the compressible Navier-Stokes equations. J. Chem. Phys., 131:267–279, 1997.
12. C.E. Baumann. An *hp*-adaptive discontinuous finite element method for computational fluid dynamics. PhD thesis, The University of Texas at Austin, 1997.
13. C.E. Baumann and J.T. Oden. A discontinuous *hp* finite element method for convection-diffusion problems. Comp. Meth. Appl. Mech. Eng., 175:311–341, 1999.
14. C.E. Baumann and J.T. Oden. A discontinuous *hp* finite element method for the Euler and Navier-Stokes equations. Int. J. Numer. Meth. Fluids, 31:79–95, 1999.
15. K.S. Bey and J.T. Oden. *hp*-Version discontinuous Gelerkin methods for hyperbolic conservation laws. Comp. Meth. Appl. Mech. Eng., 52:259–286, 1996.
16. M.A. Biot. Theory of propagation of elastic waves in a fluid-saturated porous solid. J.Acoust.Sco. Am., 29:168–191, 1956.
17. R.M. Bowen. Incompressible porous media models by use of the theory of mixtures. Int. J. Engng. Sci., 18:1129–1148, 1980.
18. R.M. Bowen. Compressible porous media models by use of the theory of mixtures. Int. J. Engng. Sci., 20:697–735, 1982.
19. F. Brezzi. On the existence, uniqueness and approximation of saddle point problems arising from lagrange multiplers. RAIRO, Ser. Rouge Anal. Numer., 8:R–2, 1976.
20. B. Cockburn. Discontinuous Galerkin methods. Z. Angew. Math. Mech., 11:731–754, 2003.
21. B. Cockburn, S.Y. Lin, and C.W. Shu. TVB Runge-Kutta local projection discontinuous Galerkin finite element methods for conservation laws III: One dimensional systems. J. Comp. Phys., 84:90–113, 1989.
22. B. Cockburn and C.W. Shu. TVB Runge-Kutta local projection discontinuous Galerkin finite element methods for conservation laws. II: General framework. Math. Comp., 52:411–435, 1989.
23. R. de Boer. Theory of porous media:Highlights in the historical development and current state. Springer Verlag, Berlin, 2000.
24. R. de Boer and W. Ehlers. On the problem of fluid- and gas-filled elasto-plastic solids. Int. J. Solids Structures, 22:1231–1242, 1986.
25. S. Diebels and W. Ehlers. Dynamic analysis of a fully saturated porous medium accounting for geometrical and material non-linearities. Int. J. Numer. Meth. Eng., 39:81–97, 1996.
26. S. Diebels, W. Ehlers, and B. Markert. Neglect of the fluid-extra stresses in volumetrically coupled soild-fluid problems. Z. Angew. Math. Mech., 81:S521–S522, 2001.
27. S. Diebels, P. Ellsiepen, and W. Ehlers. Error-controlled Runge-Kutta time integration of a viscoplastic hybrid two-phase model. Technische Mechanik, 19:19–29, 1999.
28. W. Ehlers. Poröse Medien - Ein kontinuumsmechanisches Modell auf der Basis der Mischungstheorie. Technical report, Berichte aus dem Fachbereich Bauwesen, Universit"at GH-Essen, 1989.
29. W. Ehlers. Grundlegende Konzepte in der Theorie Poröser Medien. Technische Mechanik, 16:63–76, 1996.
30. W. Ehlers. Foundations of multiphasic and porous materials. In W. Ehlers and J. Bluhm, editors, Porous Media: Theory, Experiments and Numerical Applications, pages 3–86. Springer-Verlag, Berlin, 2002.
31. W. Ehlers, T. Graf, and M. Ammann. Deformation and localization analysis of partially saturated soils. Comp. Meth. Appl. Mech. Eng., 193:2885–2910, 2004.

32. K. Eriksson, D. Estep, P. Hansbo, and C. Johnson. Computational Differential Equations. Cambridge University Press, Cmbridge, 1996.
33. K. Eriksson, D. Estep, P. Hansbo, and C. Johnson. Computational Differential Equations. Cambridge University Press, Cmbridge, 1996.
34. C. Gresho and R.L. Lee. Don't suppress the wiggles-they're telling you something. Finite Element Methods in Convection dominated Flows, ASME AME, 34:27–61, 1979.
35. P. Houson, C. Schwab, and E. Suli. Stabilized *hp*-finite element methods for first-order hyperbolic problems. Technical report, Oxford University computing Laboratory, Oxford, England, 1998.
36. H. Huang and F. Costanzo. On the use of space-time finite elements in the solution of elasto-dynamic problems with strain discontinuities. Comp. Meth. Appl. Mech. Eng., 191:5315–5343, 2002.
37. G.M. Hulbert T.J.R. Hughes. Space-time finite element methods for second-order hyperbolic equations. Comp. Meth. Appl. Mech. Eng., 84:327–348, 1990.
38. T. J. R. Hughes. The Finite Element Method. Prentice-Hall, Englewood Cliffs, New York, 1987.
39. T.J.R. Hughes and G.M. Hulbert. Space-time finite element methods for elastodynamics: Formulations and error estimates. Comp. Meth. Appl. Mech. Eng., 66:339–363, 1988.
40. G. Hulbert. Space-time finite element methods for second order hyperbolic equations. PhD thesis, Department of Mechanical Engineering, Stanford University, Stanford, 1989.
41. G.M. Hulbert. Time finite element methods for structural dynamics. Int. J. Numer. Meth. Eng., 33:307–331, 1992.
42. I.Babuška, C.E. Baumann, and J.T. Oden. A discontinuous *hp* finite element method for diffusion problems: 1-d analysis. Comp. Math. Appl., 37:103–122, 1999.
43. JR. J. Douglas and T. Dupont. Interior penalty procedures for elliptic and parabolic Galerkin methods, Lecture Notes in Phys. 58. Springer-Verlag, Berlin, 1978.
44. C. Johnson. Disontinuous Galerkin finite element methods for second order hyperbolic problems. Comp. Meth. Appl. Mech. Eng., 107:117–129, 1993.
45. C. Johnson. Adaptive FEM for conservation laws, Advanced numerical approximation of nonlinear hyperbolic equations (Springer lecture notes in mathematics). Springer Verlag, 1998.
46. C. Johnson, U. Nävert, and J. Pitkäranta. Finite element methods for linear hyperbolic problems. Comp. Meth. Appl. Mech. Eng., 45:285–312, 1984.
47. C. Johnson and J. Pitkäranta. An analysis of the discontinuous Galerkin method for a scalar hyperbolic equation. Math. Comp., 46:1–26, 1986.
48. F. Larsson, P. Hansbo, and K. Runesson. Space-time finite elements and adaptive strategy for the coupled thermoelasticity problem. Int. J. Numer. Meth. Eng., 56:261–293, 2003.
49. P. Lesaint and P.-A. Raviart. On a finite element method for solving the neutron transport equation, in: C. de Boor (Ed), Mathematical Aspects of Finite Elements in Partial Differential Equations. Academic Press, New York, 1974.
50. C. Li, R. Borja, and R. Regueiro. Dynamics of porous media at finite strain. Comp. Meth. Appl. Mech. Eng., 193:3837–3870, 2004.
51. X.D. Li and N.-E. Wiberg. Implementation and adaptivity of a space-time finite element method for structural dynamics. Comp. Meth. Appl. Mech. Eng., 156:211–229, 1998.
52. A. Masud and T.J.R. Hughes. A space-time Galerkin/least-squares finite element formulation of the navier-stokes equations for moving domain problems. Comp. Meth. Appl. Mech. Eng., 146:91–126, 1997.
53. J. Mergheim, E. Kuhl, and P. Steinmann. A hybrid discontinuous Galerkin/interface method for the computational modelling of failure. Commun. Numer. Meth. En., 20:511–519, 2004.
54. J. Liou O. Pironneau and T. Tezduyar. Characteristic-Galerkin and Galerkin/least-squares space-time formulations for the advection-diffusion equation with time-dependent domains. Comp. Meth. Appl. Mech. Eng., 100:117–141, 1992.
55. J. Palaniappan, R.B. Haber, and R.L. Jerrard. A spacetime discontinuous Galerkin method for scalar conservation laws. Comp. Meth. Appl. Mech. Eng., 193:3607–3631, 2004.
56. E. Papamichos and I. Vardoulakis. Sand erosion with a porosity diffusion law. Computers and Geotechnics, 32:47–58, 2005.
57. A. Quarteroni, R. Sacco, and F. Saleri. Numerical Mathematics. Number 37 in Texts in Applied Mathematics. Springer-Verlag, Berlin, 2000.
58. W.H. Reed and T.R. Hill. Triangular mesh methods for the neutron transport equation. Los Alamos Scientific Laboratory Report LA-UR-73-479, 1973.
59. B. Rivière and M. F. Wheeler. Discontinuous galerkin methods for flow and transport problems in porous media. Commun. Numer. Meth. En., 79:157–174, 2002.
60. B. Rivière, M. F. Wheeler, and K. Banaś. Part II: Discontinuous galerkin methods applied to a single phase flow in porous media. Comp. Geosciences, 4:337–349, 2000.
61. H. Steeb, S. Diebels, and W. Ehlers. Galerkin-type space-time finite elements for volumetrically coupled problems. Proc. Appl. Math. Mech., 2:264–265, 2003.

62. H. Steeb, A. Maute, and E. Ramm. Goal-oriented error estimation in solid mechanics. In E. Stein, editor, Error-controlled Adaptive Finite Elements in Solid Mechanics. John Wiley & Sons, Chichester, 2002.
63. H. Steeb and I. Vardoulakis. Sand production in gas-flown weak conditions. Arch. Appl. Mech., 2005. submitted for publication.
64. G. Strang and G.J. Fix. An Analysis of the Finite Element Method. Prentice-Hall, Englewood Cliffs, New York, 1973.
65. Wolfgang A. Wall. Fluid-Struktur-Interaktion mit stabilisierten Finiten Elementen. Bericht Nr. 31 (1999), Institut f"ur Baustatik der Universit"at Stuttgart, 1999.
66. M. F. Wheeler. An elliptic collocation-finite element method with interior penalties. SIAM J. Numer. Anal., 15:152–161, 1978.
67. K. Wilmański. Some questions on material objectivity arising in models of porous materials. In P. Podio-Guidugli and M. Brocato, editors, Rational continua, classical and new, pages 149–161. Springer-Verlag, Berlin, 2001.
68. M. Zhang and C. W. Shu. An analysis of three different formulations of the discontinuous Galerkin method for diffusion equations. Math. Mod. Meth. Appl. S., 13:395–413, 2003.
69. O. C. Zienkiewicz, R. L. Taylor, S. J. Sherwin, and J. Peiró. On discontinuous Galerkin methods. Int. J. Numer. Meth. Eng., 58:1119–1148, 2003.

Paper B

A new hybrid velocity integration method applied to elastic wave propagation

published in *Int. J. Numer. Meth. Engrg* 2008; **74**:56–79

INTERNATIONAL JOURNAL FOR NUMERICAL METHODS IN ENGINEERING
Int. J. Numer. Meth. Engng 2000; **00**:1–6 *Prepared using* nmeauth.cls *[Version: 2002/09/18 v2.02]*

A new hybrid velocity integration method applied to elastic wave propagation

Zhiyun Chen, Holger Steeb & Stefan Diebels*

Saarland University, Chair of Applied Mechanics,
Postfach 15 11 50, D-66 041, Saarbrücken, Germany

SUMMARY

We present a novel space-time Galerkin method for solutions of second order time-dependent problems. By introducing the displacement-velocity relation implicitly, the governing set of equations is reformulated into a first-order single field problem with the unknowns in the velocity field. The resulting equation is in turn solved by a time-discontinuous Galerkin (DGT) approach [9], in which the continuity between the time intervals is weakly enforced by a special *upwind* flux treatment. After solving the equation for the unknown velocities, the displacement field quantities are computed *a posteriori* in a post-processing step. Various numerical examples demonstrate the efficiency and reliability of the proposed method. Convergence studies with respected to the h- and p-refinement and different discretization techniques are given. Copyright © 2000 John Wiley & Sons, Ltd.

KEY WORDS: space-time FE, time-discontinuous Galerkin methods, elasto-dynamics

1. INTRODUCTION

The idea of applying the Finite Element Method (FEM) in the temporal domain can be traced back to the work of Argyris & Scharpf [1] and Fried [17]. Remarkable development has been done by Hughes & Hulbert [20], who introduced the Galerkin Least Square term into the FEM formulation to enforce the inter-element consistency. These methods have also been applied to second-order hyperbolic equations [20, 21, 22, 23], whereby the second-order equation is first degenerated into an equation system of two first order equations.
Apart from the Least Square treatment, the *upwind* treatment, first introduced by Reed & Hill [28], has been commonly accepted in the Discontinuous Galerkin (DG) community. The mathematical foundation of this method was analyzed by Lesaint & Raviart [25] and Johnson & Pitkäranta [24], among others. Cockburn and Shu [12, 13, 14] developed the Runge-Kutta Discontinuous Galerkin method (RKDG) to solve space-time coupled problems. These semi-discrete methods essentially

*Correspondence to: s.diebels@mx.uni-saarland.de

Contract/grant sponsor: German Science Foundation – Deutsche Forschungsgemeinschaft (DFG); contract/grant number: Di 430/4-2

Received 28.07.2006
Revised 18 September 2002

employ a FEM mesh in space and advance the solution via the Runge-Kutta scheme in time. By rewriting the second-order equation as a degenerated first order equation system, the method is also capable of solving time-dependent scalar advection-diffusion equations [15]. Bassi & Rebay [4] extended the spatial DG method to solve the compressible Navier-Stokes equation, in which the second-order equation was treated in a similar manner so that both the solution and its gradient were approximated in the same function space. Remarkable development in solving second-order diffusion equations was made by Baumann & Oden [5, 6, 7], who developed the Nitsche's approach to solve the convective-diffusion problems efficiently. Further studies concerning the error estimation of Baumann's method were achieved by Riviére *et al.* [3, 2, 29]. A good overview of the historical perspective and various applications of the DG method can be found in [10]. More recently, various efforts have been made in developing the methods composed of a semi-discretization mesh in space and advancing the solution with a discontinuity-eliminating-operator in time, see [26, 27]. In the present work a new space-time discontinuous Galerkin scheme is developed for the solution of classical wave propagation problems in elastic media. We circumvent the standard technique of solving a second-order time-dependent problem by means of an equation system composed of two first-order equations. The method is somewhat analogical to the Nyström methods [18], in which we embedded the derivative of the primary unknowns in the governing equation. The Hybrid Velocity Integration (HVI) scheme presented in this work is designed to solve second-order problems directly. To do this, the displacement-velocity relation is embedded implicitly by means of a consistent integration of the velocity. The resulting first-order equation is solved via the the time-discontinuous Galerkin (DGT) method [9] on a space-time finite element mesh. After solving the equation for the velocity field, the displacement field is updated subsequently within a post-processing step.
The structure of the present work is as follows: In the following section, we present the HVI formulation for an Ordinary Differential Equation (ODE). Next, a generalized HVI method for a simple space-time coupled problem is given in Section 3. Section 4 is devoted to various numerical examples in which the convergence study of the HVI method is presented. The paper is closed with a short conclusion and discussion about future works.

2. HYBRID VELOCITY INTEGRATION (HVI)

2.1. Continuous weak form of a simple model equation

The HVI method can be introduced by a simple model equation resulting from rigid body dynamics. For the sake of simplicity, the prototype equation (ODE) is given by

$$M\,\ddot{u} + D\,\dot{u} + C\,u = F, \quad \text{with} \quad t \in \mathcal{I} = [\,t_0, T\,], \tag{1}$$

where $u(t)$ is the displacement, $\dot{u}(t)$ and $\ddot{u}(t)$ are the velocity and the acceleration, respectively. M,D and C are mass, viscosity and stiffness coefficients, respectively. The right hand side term $F(t)$ denotes the external force. In order to solve equation (1) uniquely, associated initial conditions are given for the displacement and the velocity as

$$u(t_0) = u_0 \quad \text{and} \quad \dot{u}(t_0) = v_0. \tag{2}$$

Introducing the velocity-displacement relation $v(t) \equiv \dot{u}(t)$, the model equation (1) can be written as a two-field displacement-velocity formulation like

$$M\,\dot{v} + D\,v + C\,u = F, \qquad t \in \mathcal{I} = [\,t_0, T\,]. \tag{3}$$

Furthermore, the weak form of Eq. (1) on an interval $\mathcal{I}^n = [\, t_n,\, t_{n+1}\,]$ is obtained by multiplying (3) with a proper test function δv,

$$\int_{\mathcal{I}^n} \Big\{ (D\, v + C\, u)\, \delta v \Big\}\, \mathrm{d}t - \int_{\mathcal{I}^n} M\, v\, \delta \dot{v}\, \mathrm{d}t + [M\, \breve{v}\, \delta v]_{t_n}^{t_{n+1}} = \int_{\mathcal{I}^n} F\, \delta v\, \mathrm{d}t. \tag{4}$$

Note that in the above expression, we have integrated the inertia term by parts in time. Next, we apply the *upwind* flux treatment to the $\breve{v}$. Applying the *upwind* flux treatment in time was introduced in [11] and has been successfully applied to the dynamical analysis of porous materials in [9]. The *upwind* flux of $\breve{v}$ reads

$$\breve{v}(t_n) = \begin{cases} v_0, & \text{for } n = 0, \\ v^-(t_n), & \text{otherwise,} \end{cases} \qquad \text{with} \quad v^{\pm}(t_n) = \lim_{\epsilon \to 0^+} v(t_n \pm \epsilon). \tag{5}$$

Hence, for an arbitrary interval $\mathcal{I}^n$ we have

$$[M\, \breve{v}\, \delta v]_{t_n}^{t_{n+1}} = \begin{cases} M\ (v^-(t_{n+1}) - v_0)\ \delta v, & \text{for } n = 0, \\ M\ (v^-(t_{n+1}) - v^-(t_n))\ \delta v, & \text{otherwise.} \end{cases} \tag{6}$$

According to the discontinuous approximation, inconsistent values of velocities $v(t_n)$ ("jump") at time t_n occur. The jump is introduced as $[\![v]\!] := |v^+(t_n) - v^-(t_n)|$, see Figure 1(a). The solution strategy with respect to the first order equation has been discussed extensively in [9], which will not be repeated here. Hence, we proceed to the treatment of the displacement field u in Eq. (4). Integrating the velocity-displacement relation $v(t) = \dot{u}(t)$ to an arbitrary time t ($t_n < t < t_{n+1}$), we obtain the expression for the unknown field u as

$$u(t) = \tilde{u}(t_n) + g_u(t), \tag{7}$$

with

$$\tilde{u}(t_n) = \begin{cases} u_0, & \text{for } n = 0, \\ u(t_n) & \text{otherwise,} \end{cases} \qquad \text{and} \quad g_u(t) = \int_{t_n}^{t} v\, \mathrm{d}\tau. \tag{8}$$

According to such a relation, we note that the displacement field $u(t)$ can be implicitly related to the integral of the velocity $g_u(t)$ and an integration constant $\tilde{u}(t_n)$. In contrast to the upwind treatment of $\breve{v}(t)$, cf. (5), there exist no jumps at the discrete time t_n, see Figure 1(b). Hence, we formally obtain

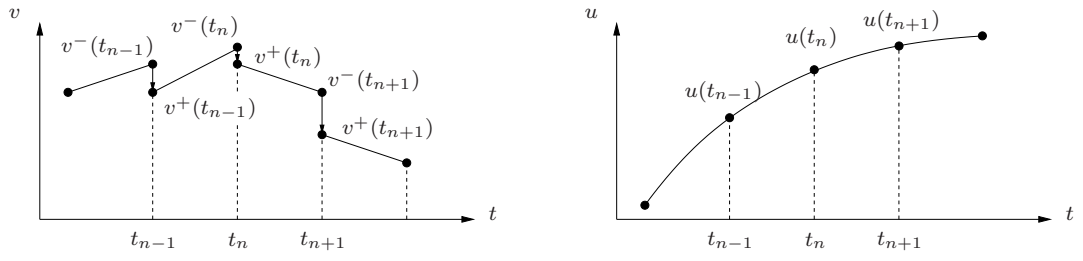

(a) velocity v (b) displacement u

Figure 1. Velocity and displacement distribution based on linear velocity approximation

the weak form as

$$\int_{\mathcal{I}^n} \Big\{ \big[D\, v + C\, \{\tilde{u}(t_n) + g_u(t)\}\big]\, \delta v \Big\}\, \mathrm{d}t - \int_{\mathcal{I}^n} M\, v\, \delta \dot{v}\, \mathrm{d}t + [M\, \breve{v}\, \delta v]_{t_n}^{t_{n+1}} = \int_{\mathcal{I}^n} F\, \delta v\, \mathrm{d}t. \tag{9}$$

Note that in the above weak form, the only unknown field is the velocity v.

2.2. Discrete weak form

Within our numerical approach discontinuous trial- and test functions v_h and δv_h are chosen. Let $\mathcal{V}_h$ denotes a finite-dimensional function space. The finite element problem can be formulated as: Find $v_h \in \mathcal{V}_h$ such that $\forall\ \delta v_h \in \mathcal{V}_h$ the following weak form holds,

$$\int_{\mathcal{I}^n} \Big\{ \big[D\, v_h + C\, g_{u_h}(t) \big]\, \delta v_h \Big\}\, \mathrm{d}t + C\, \tilde{u}_h(t_n)\, \Delta t - \int_{\mathcal{I}^n} M\, v_h\, \delta \dot{v}_h\, \mathrm{d}t + \big[M\, \breve{v}_h\, \delta v_h \big]_{t_n}^{t_{n+1}} = \int_{\mathcal{I}^n} F\, \delta v_h\, \mathrm{d}t. \tag{10}$$

The $\tilde{u}_h(t_n)$ and the g_{u_h} are the corresponding terms related to the discrete quantities u_h and v_h. Moreover, since the quantity of $\tilde{u}_h(t_n)$ is a constant with respect to the current interval $\mathcal{I}^n$, its integral in (9) is substituted by $[C\, \tilde{u}_{h,n}\, \Delta t]$ with $\Delta t = t_{n+1} - t_n$. Next, we discuss the contribution of the integral $\int_{\mathcal{I}^n} [C\, g_{u_h}(t)]\, \delta v_h\, \mathrm{d}t$ in detail. Obviously, this term can be integrated numerically by various numerical integration schemes. However, in order to guarantee an efficient and accurate numerical solution, a consistent integration scheme for both the displacement and the velocity field has to be employed. For the sake of simple notation, we introduce the term H as

$$H = \int_{\mathcal{I}^n} g_{u_h}(t)\, \delta v_h\, \mathrm{d}t = J \int_{-1}^{+1} g_{u_h}(\xi)\, \delta v_h\, \mathrm{d}\xi, = J \int_{-1}^{+1} \left(J_\xi \int_{-1}^{\xi} v_h\, \mathrm{d}\tau \right)\, \delta v_h\, \mathrm{d}\xi, \tag{11}$$

where J and J_ξ denotes the corresponding Jacobians, see (49) - (50). According to the Gauss quadrature, equation (11) can be evaluated by

$$H = J \sum_{GP} w_i\, g_{u_h}(\xi_i)\, \delta v_h(\xi_i). \tag{12}$$

Here GP is the number of Gauss integration points, ξ_i and w_i are the weights and local positions of Gauss points, respectively. Assume that the discrete trial- and test-functions are given as

$$v_h = \sum_{l=1}^{p+1} N_l\, \hat{v}_l \quad \text{and} \quad \delta v_h = \sum_{k=1}^{p+1} N_k\, \delta \hat{v}_k, \tag{13}$$

where N_l and N_k represent the Lagrangian polynomials of order p. The nodal values of the trial- and test-functions are introduced by $\hat{v}_l$ and $\delta \hat{v}_k$, respectively. The consistent integration scheme for H according to the Gauss quadrature can be written as

$$H = J \sum_{GP} w_i \left(J \sum_{l=1}^{p+1} N_l^{\xi_i}\, \hat{v}_l \right) \left(\sum_{k=1}^{p+1} N_k\, \delta\, \hat{v}_k \right) \tag{14}$$

with

$$N_l^{\xi_i} := J_{\xi_i} \sum_{GP} w_j\, N_l(\xi_i^j). \tag{15}$$

A detailed derivation is given in the Appendix.
From (14), we note that the integral $\int_{\mathcal{I}^n} [C\, g_{u_h}(t)]\, \delta v_h\, \mathrm{d}t$ can be evaluated within a standard FEM

procedure. Moreover, it has to be pointed out that $N_l^{\xi_i}$ can be considered as a new class of polynomials defined for each polynomial N_l at each Gauss point ξ_i. Note that the value of $N_l^{\xi_i}$ is independent of the nodal solution $\hat{v}_l$. According to a chosen polynomial N_l and the corresponding integration scheme, the evaluation of $N_l^{\xi_i}$ has to be carried out only once. Thus, we would like to point out that no extra numerical effort due to the calculation of $N_l^{\xi_i}$ is demanded within the computational process. After solving Eq. (10) for the unknown velocities v_h, the displacement field u_h is achieved in a post-precessing step like

$$u_{h,n+1} = \tilde{u}_{h,n} + \int_{t_n}^{t_{n+1}} v_h \, \mathrm{d}\, \tau. \tag{16}$$

So far, we have illustrated the solution strategy of the discrete weak form (10). It has to be mentioned that the integration of the displacement field u_h is carried out by a consistent Gauss integration scheme. Furthermore, depending on the polynomial order p, as long as sufficient integration points are employed, the integration can be carried out exactly.

3. SPACE-TIME COUPLED GALERKIN FORMULATION

After presenting the main idea of the HVI method by a simple ODE equation, we proceed now to generalize the HVI scheme to a coupled space-time Galerkin method. First of all, let us recall the definition of the space-time domain. The spatial domain is introduced as Ω with a position vector $\mathbf{x} \in \mathbb{R}^d, d = 1, 2, 3$. The space-time domain Q is constructed by adding the time axis orthogonal to the spatial domain Ω, so that we obtain $Q := \Omega \times \mathcal{I}$. According to the time discretization, the so-called time-slab Q^n is defined analogously by $Q^n := \Omega \times \mathcal{I}^n$. For further details concerning the notation and the space-time discretization we refer to [9].

3.1. Elastic wave-propagation

The governing equation of wave propagation in a linear elastic solid is described by the Lamé-Navier equation †

$$\rho\, \ddot{\mathbf{u}} - \mu \ \mathrm{div}\ \mathrm{grad}\, \mathbf{u} - (\mu + \lambda)\ \mathrm{grad}\ \mathrm{div}\, \mathbf{u} = \mathbf{0} \qquad \text{in} \quad \Omega \times \mathcal{I}, \tag{18}$$

with the boundary conditions on the Dirichlet boundary Γ_D and Neumann boundary Γ_N ($\partial\Omega = \Gamma_N \bigcup \Gamma_D$ and $\Gamma_N \bigcap \Gamma_D = \emptyset$)

$$\mathbf{u} = \bar{\mathbf{u}} \quad \text{on} \quad \Gamma_D \times \mathcal{I} \quad \text{and} \quad \mathbf{T} \cdot \mathbf{n} = (2\,\mu\ \mathrm{grad}^{sym}\, \mathbf{u} + \lambda\, (\mathrm{div}\, \mathbf{u})\, \mathbf{I}) \cdot \mathbf{n} = \bar{\mathbf{t}} \quad \text{on} \quad \Gamma_N \times \mathcal{I}, \tag{19}$$

---

†Splitting the vector field $\mathbf{u} = \mathbf{u}_1 + \mathbf{u}_2$ into an irrotational part ($\mathrm{rot}\, \mathbf{u}_1 = \mathbf{0}$) and into a solenoidal part ($\mathrm{div}\, \mathbf{u}_2 = 0$), respectively, we can divide equation (18) into a scalar equation describing the propagation of a compressional wave and into a vector-valued equation describing the propagation of the shear wave,

$$\rho\, \ddot{\phi} - (\lambda + 2\,\mu)\ \mathrm{div}\, \mathrm{grad}\, \phi = 0 \quad \text{and} \quad \rho\, \ddot{\mathbf{m}} - \mu \ \mathrm{div}\ \mathrm{grad}\, \mathbf{m} = \mathbf{0}. \tag{17}$$

In equation (17) we have introduced the scalar potential $\phi(\mathbf{x}, t)$ with $\mathbf{u}_1 = \mathrm{grad}\, \phi$ and the vector potential $\mathbf{m}(\mathbf{x}, t)$ with $\mathbf{u}_2 = \mathrm{rot}\, \mathbf{m}$.

where $\mathbf{n}$ denotes the outward normal vector on the Neumann boundary Γ_N. The initial conditions are given for both the displacement $\mathbf{u}$ and the velocities $\dot{\mathbf{u}}$ as

$$\mathbf{u} = \mathbf{u}_0, \quad \text{at} \quad \Omega \times t_0 \qquad \text{and} \qquad \dot{\mathbf{u}} = \mathbf{v}_0, \quad \text{at} \quad \Omega \times t_0. \tag{20}$$

The elastic parameters are given by the Lamé constants μ and λ. The density is denoted by ρ. Analogously, by introducing the displacement-velocity relation of the vector field quantities $\mathbf{v} = \dot{\mathbf{u}}$, Eq. (18) yields

$$\rho\, \dot{\mathbf{v}} - \mu\ \mathrm{div}\ \mathrm{grad}\, \mathbf{u} - (\mu + \lambda)\ \mathrm{grad}\, \mathrm{div}\, \mathbf{u} = \mathbf{0} \qquad \text{in} \quad \Omega \times \mathcal{I}. \tag{21}$$

The *upwind* flux of the vector quantity $\breve{\mathbf{v}}$ and the displacement $\tilde{\mathbf{u}}$ are given by

$$\breve{\mathbf{v}}(\mathbf{x},\, t_n) = \begin{cases} \mathbf{v}_0, & \text{for } n = 0, \\ \mathbf{v}^-(\mathbf{x},\, t_n), & \text{otherwise}, \end{cases} \qquad \text{and} \qquad \tilde{\mathbf{u}}(\mathbf{x}, t_n) = \begin{cases} \mathbf{u}_0, & \text{for } n = 0, \\ \mathbf{u}(\mathbf{x},\, t_n) & \text{otherwise}, \end{cases} \tag{22}$$

with $\mathbf{v}^{\pm}(\mathbf{x},\, t_n) = \lim\limits_{\epsilon \to 0^+} \mathbf{v}(\mathbf{x},\, t_n \pm \epsilon)$. The implicit expression of the displacement field $\mathbf{u}(\mathbf{x}, t)$ based on the integral of the velocity field $\mathbf{v}(\mathbf{x}, t)$ can be written as

$$\mathbf{u}(\mathbf{x}, t) = \tilde{\mathbf{u}}(\mathbf{x}, t_n) + \mathbf{g}_{\mathbf{u}}(\mathbf{x}, t) \quad \text{with} \quad \mathbf{g}_{\mathbf{u}}(\mathbf{x}, t) = \int_{t_n}^{t} \mathbf{v}(\mathbf{x}, \tau)\, \mathrm{d}\tau, \qquad t_n < t < t_{n+1}. \tag{23}$$

It is necessary to point out that the differential operators $\mathrm{grad}(\bullet)$ and $\mathrm{div}(\bullet)$ are pure spatial operators. Since integration over the time and differentiation in space are commutative, the following expressions hold

$$\begin{aligned} &\mathrm{grad}\, \mathbf{u}(\mathbf{x}, t) = \mathrm{grad}\, \tilde{\mathbf{u}}_n + \mathrm{grad}\, \mathbf{g}_{\mathbf{u}}(\mathbf{x}, t), \quad \text{with} \quad \mathrm{grad}\, \mathbf{g}_{\mathbf{u}}(\mathbf{x}, t) = \int_{t_n}^{t} \mathrm{grad}\, \mathbf{v}(\mathbf{x},\, \tau)\, \mathrm{d}\tau, \\ &\mathrm{div}\, \mathbf{u}(\mathbf{x}, t) = \mathrm{div}\, \tilde{\mathbf{u}}_n + \mathrm{div}\, \mathbf{g}_{\mathbf{u}}(\mathbf{x}, t), \qquad \text{with} \quad \mathrm{div}\, \mathbf{g}_{\mathbf{u}}(\mathbf{x}, t) = \int_{t_n}^{t} \mathrm{div}\, \mathbf{v}(\mathbf{x},\, \tau)\, \mathrm{d}\tau. \end{aligned} \tag{24}$$

Hereby, the subscript n denotes the quantity at time level t_n. The weak form is obtained by multiplying Eq. (21) with a proper test function $\delta\mathbf{v}$ and integrating over the time-slab Q^n. Bearing in mind that both differential operations $\mathrm{grad}\, \tilde{\mathbf{u}}_n$ and $\mathrm{div}\, \tilde{\mathbf{u}}_n$ are known with respect to the time slab Q^n, we obtain the following weak form

$$\begin{aligned} &\int_{Q^n} \Big\{ -\rho\, \mathbf{v} \cdot \delta\dot{\mathbf{v}} + \mu\ \mathrm{grad}\, \mathbf{g}_{\mathbf{u}} : \mathrm{grad}\, \delta\mathbf{v} + (\mu + \lambda)\, \mathrm{div}\, \mathbf{g}_{\mathbf{u}}\ \mathrm{div}\, \delta\mathbf{v} \Big\}\, \mathrm{d}Q \\ &+ \Delta t \int_{\Omega} \Big\{ \mu\ \mathrm{grad}\, \tilde{\mathbf{u}}_n : \mathrm{grad}\, \delta\mathbf{v} + (\mu + \lambda)\, \mathrm{div}\, \tilde{\mathbf{u}}_n\ \mathrm{div}\, \delta\mathbf{v} \Big\}\, \mathrm{d}v \\ &+ \int_{\Omega} \rho\, \left[\mathbf{v}^-_{n+1}\, \delta\mathbf{v} - \breve{\mathbf{v}}_n\, \delta\mathbf{v} \right]\, \mathrm{d}v = \int_{\Gamma_N \times \mathcal{I}^n} \bar{\mathbf{t}} \cdot \delta\mathbf{v}\, \mathrm{d}a\, \mathrm{d}t. \end{aligned} \tag{25}$$

Note that the second and the third lines in Eq. (25) are designated as pure spatial integrations occurring at the temporal borders of the time-slab Q^n. Moreover, both $\tilde{\mathbf{u}}_n$ and $\breve{\mathbf{v}}_n$ are known quantities, which

are either solutions from the previous time slab Q^{n-1} or the prescribed initial values.
So far we have obtained the weak form (25) formulated in the velocity field $\mathbf{v}$. The displacement field $\mathbf{u}$ is embedded implicitly as a function of the velocity $\mathbf{v}$, c. f. (23), more details concerning the FEM formulation are given in the Appendix.
Next, we have to reformulate the boundary conditions (19) given for the displacement field $\mathbf{u}$ to those prescribed in the velocity field $\mathbf{v}$. Nevertheless, we note that in Eq. (25) the Neumann assignment $\bar{\mathbf{t}}$ holds. Taking into account that (23) is valid also on the Dirichlet boundary Γ_D, we obtain

$$\mathbf{u}(\mathbf{x},t) = \tilde{\mathbf{u}}_n(\mathbf{x}) + \int_{t_n}^{t} \mathbf{v}(\mathbf{x},\tau)\,\mathrm{d}\tau \equiv \bar{\mathbf{u}} \quad \text{with} \quad \mathbf{x} \in \Gamma_D, \tag{26}$$

which leads to

$$\bar{\mathbf{v}} = \dot{\bar{\mathbf{u}}} - \dot{\tilde{\mathbf{u}}}_n, \quad \text{on} \quad \Gamma_D \times \mathcal{I} \qquad \text{and} \qquad \tilde{\mathbf{u}}_0 = \bar{\mathbf{u}}_0, \quad \text{on} \quad \Gamma_D \times t_0. \tag{27}$$

The second relation is derived by taking $t = t_n = t_0$ in (26). Similarly, by inserting Eq. (24) in the Neumann assignment in (19) at the initial time t_0, we obtain

$$\mathbf{T}\cdot\mathbf{n} = (2\,\mu\,\mathrm{grad}^{sym}\,\tilde{\mathbf{u}}_0 + \lambda\,\mathrm{div}\,\tilde{\mathbf{u}}_0\,\mathbf{I})\cdot\mathbf{n} = \bar{\mathbf{t}} \quad \text{on} \quad \Gamma_N \times t_0. \tag{28}$$

Thus, we note that the argument $\tilde{\mathbf{u}}_0 = \mathbf{u}_0$ is valid for $\mathbf{x} \in (\Omega\partial\Omega)$, the corresponding initial assignment on the Dirichlet Γ_D and Neumann Γ_N are given in (27) and (28), respectively.

3.2. HVI finite element scheme

Let $\mathcal{P} = \{\mathcal{P}_h(\Omega \times \mathcal{I}^n)\}$ be the set of all partitions of the time slab Q^n. Next, the spatial continuous time-slab $Q^n = \Omega \times \mathcal{I}^n$ is subjected to a spatial discretization, i.e. the finite element mesh $\mathcal{P}_h$

$$\mathcal{P}_h = \bigcup_{M} P_h^i \quad \text{with} \quad 1 \le i \le M. \tag{29}$$

The mesh consists of M space-time finite elements $P_h^i = \Omega_h^i \times \mathcal{I}^n$, where Ω_h^i $(1 \le i \le M)$ denotes the disjoint subdomains of Ω. Assume that the finite-dimensional function space $\mathcal{V}_h$ consists of the tensor products of spatial and temporal trial- and test-functions. With the continuous weak form given in (25) we are able to formulate the underlying finite element problem:

$$\text{Find } \mathbf{v}_h \in \mathcal{V}_h, \quad \text{such that} \quad \forall\,\delta\mathbf{v}_h \in \mathcal{V}_h, \text{there exists} \quad B(\mathbf{v}_h, \delta\mathbf{v}_h) = L(\delta\mathbf{v}_h). \tag{30}$$

The bilinear form $B(\mathbf{v}_h, \delta\mathbf{v}_h)$ and the linear form $L(\delta\mathbf{v}_h)$ read

$$\begin{aligned}
B(\mathbf{v}_h,\delta\mathbf{v}_h) \;&:=\; \sum_{i=1}^{M} \int_{P_h^i} \Big\{ -\rho\,\mathbf{v}_h\cdot\delta\dot{\mathbf{v}}_h + \mu\,\mathrm{grad}\,g_{\mathbf{u},h} : \mathrm{grad}\,\delta\mathbf{v}_h + (\lambda+\mu)\;\mathrm{div}\,g_{\mathbf{u},h}\,\mathrm{div}\,\delta\mathbf{v}_h \Big\}\,\mathrm{d}Q \\
&+\; \sum_{i=1}^{M} \int_{\Omega_h^i} \Big\{ \rho\,\mathbf{v}_{h,n+1}^{-}\cdot\delta\mathbf{v}_h \Big\}\,\mathrm{d}v, \\
L(\delta\mathbf{v}_h) \;&:=\; \sum_{k=1}^{E} \int_{\Gamma_{N,h}^k\times\mathcal{I}^n} \bar{\mathbf{t}}\cdot\delta\mathbf{v}_h\,\mathrm{d}a\,\mathrm{d}t + \sum_{i=1}^{M} \int_{\Omega_h^i} \Big\{ \rho\,\breve{\mathbf{v}}_{h,n}\cdot\delta\mathbf{v}_h \Big\}\,\mathrm{d}v \\
&-\; \Delta t \sum_{i=1}^{M} \int_{\Omega_h^i} \Big\{ \mu\;\mathrm{grad}\,\tilde{\mathbf{u}}_{h,n} : \mathrm{grad}\,\delta\mathbf{v}_h + (\lambda+\mu)\;\mathrm{div}\,\tilde{\mathbf{u}}_{h,n}\,\mathrm{div}\,\delta\mathbf{v}_h \Big\}\,\mathrm{d}v,
\end{aligned} \tag{31}$$

where E denotes the number of edges $\Gamma^i_{N,h}$ of the subdomain Ω^i_h that encounter the Neumann boundary Γ_N. Solving Eq. (26) for $\mathbf{v}_h$, the displacement field $\mathbf{u}_h$ is computed according to the integral

$$\mathbf{u}_{h,n+1} = \tilde{\mathbf{u}}_{h,n} + \int_{t_n}^{t_{n+1}} \mathbf{v}_h \mathrm{d}t. \tag{32}$$

So far we have accomplished the solution strategy of the HVI method for a coupled space-time problem. By embedding the displacement-velocity relation implicitly in the weak formulation, the set of unknowns is reduced to the velocity field. In this sense, we degenerate the second-order equation to a first-order one without expanding the dimension of the matrix system. Furthermore, by modifying the polynomials according to (15), the solution procedure is compatible to a standard time-discontinuous FEM code. Besides, as has already been discussed in [9], inconsistent quantities, i. e. "jumps", contribute to the stability and accuracy of the numerical solution. Such jumps can be served as a heuristical error indicator in the time domain leading to $hp-$refinement approach. Moreover, according to the consistent integration scheme given here, the displacement field $\mathbf{u}_h$ as well as its associated quantities $\mathrm{grad}\,\mathbf{u}_h$ and $\mathrm{div}\,\mathbf{u}_h$ can be integrated exactly.

4. NUMERICAL EXAMPLES

4.1. The simple model example

In the first example, we focus on a Single Degree of Freedom (SDOF) described by the motion equation like

$$M\,\ddot{u}(t) + C\,u(t) = 0 \quad \text{with} \quad t \in \mathcal{I} = [0, 4]\ \text{s} \tag{33}$$

with the stiffness $C = 100$ [Ns/m] and the unit mass $M = 1$ [kg]. The system is started from the static state with an initial displacement

$$u_0 = u(t = 0) = 10\ [\text{m}], \quad v_0 = v(t = 0) = 0. \tag{34}$$

For such a simple system, the exact solution reads

$$u(t) = 10\,\cos(10\,t), \qquad v(t) = -100\,\sin(10\,t). \tag{35}$$

Figure 2 shows the numerical results obtained by the HVI method with linear trial- and test functions in space and time and a uniform time step size $\Delta t = 0.1$ [s]. For comparison, results obtained by the standard Newmark method with the same time step size ($\Delta t = 0.1$ [s]) are depicted in the same figure, Figure 2. We observe that both methods lead to stable solutions. However, the HVI method provides a much more accurate solution than the Newmark method, in which less phase delay due to the numerical dispersion is observed. Moreover, since the displacement u_h depends on the integral of the velocity v_h, even with linear trial functions for v_h, we obtain a rather smooth numerical solution of u_h with the HVI method, see Figure 2(b). Also, despite the discontinuous approximations for v_h, no visuable jumps in the plot scale are observed.
Next, we define the error in the L_2 norm for both the velocity and the displacement field as

$$e_v = \sqrt{\frac{1}{N}\sum_{n=1}^{N}\Big[v(t_n) - v_h(t_n)\Big]^2} \quad \text{and} \quad e_u = \sqrt{\frac{1}{N}\sum_{n=1}^{N}\Big[u(t_n) - u_h(t_n)\Big]^2}, \tag{36}$$

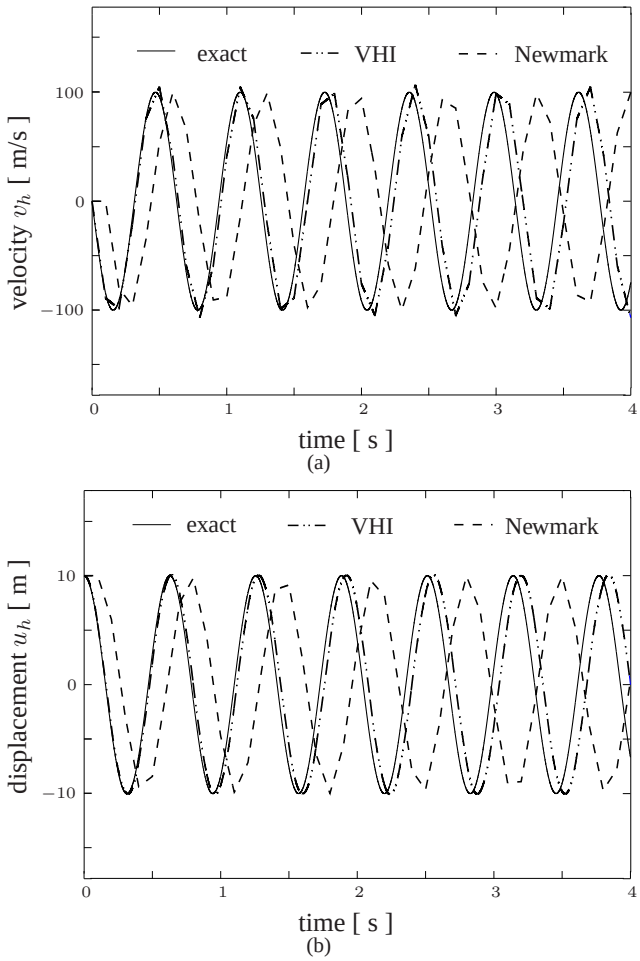

Figure 2. Numerical solutions of the velocity v_h and the displacement u_h with $\Delta t = 0.1$ s calculated with the HVI method and the classical Newmark scheme.

where $u(t_n), v(t_n)$ and $u_h(t_n), v_h(t_n)$ represent the exact and the finite element solutions at discrete time level t_n, respectively. N is the number of time steps. Figure 3 shows the convergence rate with respect to the velocity v_h as well as the displacement u_h fields, whereby p represents the order of the trial- and test functions. It can be observed that the convergence rate for the velocity is of $\mathcal{O}(p+1)$, and a slightly higher convergence rate in the displacement field u_h is achieved

As for the Galerkin finite element methods, the natural norm reflecting the quantity of the numerical solution scheme with respect to numerical accuracy and stability is the energy norm. Next, we study the energy conserving property of the HVI scheme for this simple model problem. The proposed SDOF system is an energy conservation system, for which the total energy E is given by the sum of the potential energy ($V = \frac{1}{2} C\, u^2$) and the kinetic energy ($K = \frac{1}{2} m\, v^2$), i. e. $E = V + K$. The error in the

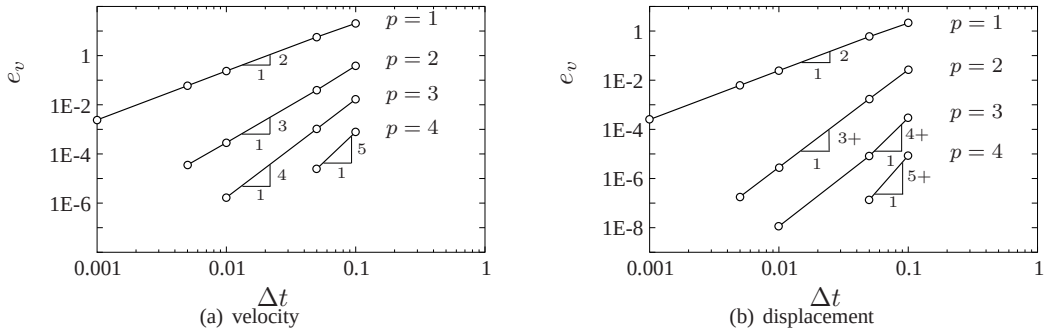

Figure 3. Convergence rates of velocities and displacements obtained by the HVI method with polynomials of order p.

total energy is defined as

$$e_E = \sqrt{\frac{1}{N}\sum_{n=1}^{N}\Big[E - E_h(t_n)\Big]^2}, \tag{37}$$

with E the exact total energy, and $E_h(t_n) = \dfrac{1}{2}(C\,u_{h,n}^2 + M\,v_{h,n}^2)$ represents total energy of the finite element solution at the time t_n. N denotes again the number of total time steps. Figure 4 shows the convergence rate of the energy norm obtained with the HVI method. We observe that the convergence rate of error e_E is of $\mathcal{O}(p+1)$ for the given problem.

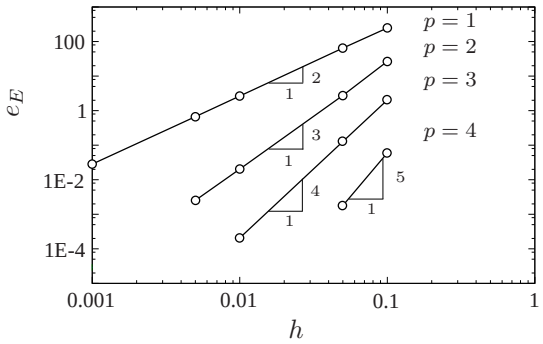

Figure 4. Convergence rate in the energy norm for the simple model example calculated by the HVI methods with polynomials of order p.

4.2. One-dimensional wave propagation in an elastic bar

In the second example, we investigate the wave propagation problem in a one-dimensional bar. The governing equation is a special form of Eq. (18) and the prototype of a second-order wave equation

$$\ddot{u}(x,t) - u''(x,t) = 0, \quad \text{with} \quad x \in L = 1 \ \text{[m]}, \quad \text{and} \quad t \in \mathcal{I} = [0,1] \ \text{[s]}, \tag{38}$$

where $(\bullet)''$ represents the second order derivative in space. In order to minimize the influence of numerical dispersion, a sinusoidal spatial distribution of the initial condition is chosen

$$u_0(x) = u(x, t = 0) = \sin\left(\frac{2\,\pi}{L}x\right), \quad v_0 = v(x, t = 0) = 0. \tag{39}$$

Both ends of the bar are fixed such that we have the Dirichlet boundary conditions for the displacements as

$$u(x = 0, t) = 0, \quad u(x = L, t) = 0, \quad \text{with} \quad t \in \mathcal{I}. \tag{40}$$

Owing to the simplicity of the given problem, the exact solution can be expressed in form of a Fourier series like

$$u(x,t) = \sum_{m=1}^{\infty} A_m \cos\left(\frac{m\pi t}{L}\right) \sin\left(\frac{m\pi x}{L}\right), \quad \text{with} \quad A_m = \frac{2}{L}\int_0^L u_0 \sin\left(\frac{m\pi x}{L}\right) \mathrm{d}x. \tag{41}$$

Figure 5 shows examplarily the exact solution for the displacement ($u(x,t)$) as well as for the velocity ($v(x,t) = \dot{u}(x,t)$).

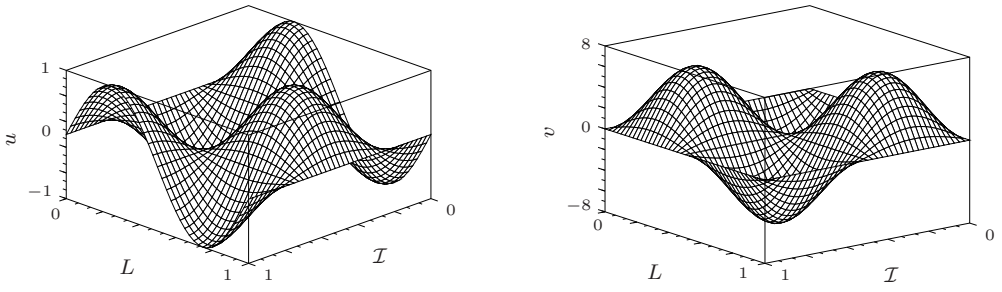

(a) displacement u (b) velocity v

Figure 5. exact solutions

The problem is now computed with 20 bilinear elements (linear trial/test functions both in space and in time) and with the temporal discretization size $\Delta t = 0.1$ [s]. Figure 6 shows the HVI solution recorded at point $x = 0.25$ [m]. Due to the employment of linear polynomials, we obtain a linear distribution of the velocity v_h. Inconsistent values (jumps) on time-slab interfaces are observed, see Figure 6(a). However, it has to be mentioned that the jumps don't spoil the numerical result but contribute to a more accurate solution. Since the displacement u_h relates to the integral of the velocity v_h, its distribution is nevertheless continuous and fits the exact solution very well, see Figure 6(b).

As is well known, such an initial boundary value problem can also be solved within the classical MOL (Method of Lines). Therein, the problem is first discretized with a spatial FEM mesh, and the resulting system of ODEs is in turn solved by a time difference scheme, e. g. the Newmark scheme. For comparison, in Figure 6 we depicted also the solutions obtained by the Newmark scheme with the same spatial (20 linear element in space) and temporal ($\Delta t = 0.1$ [s]) discretization. We observe, with such discretization, the solutions of this HVI method are much more accurate than those obtained by

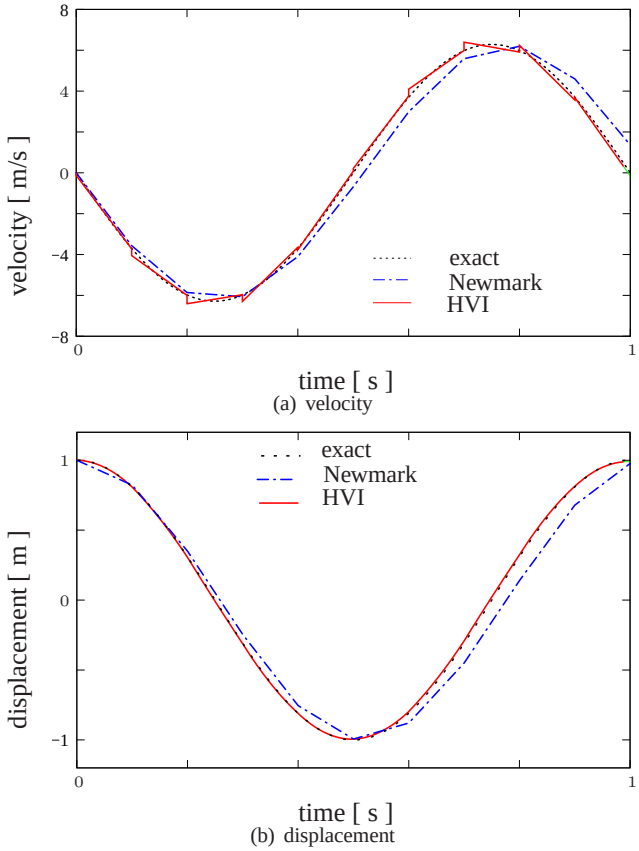

(a) velocity

(b) displacement

Figure 6. Newmark vs. HVI solution at $x = 0.25$

the Newmark scheme.

Next we study the property of the convergence rate of the space-time coupled HVI formulation. For such space-time coupled problems, the temporal and spatial refinement must be performed simultaneously (uniformly decreasing Δt and Δx), cf. [22]. Here, we introduce the space-time mesh parameter as

$$h = \max\{c\,\Delta t, \Delta x\}, \tag{42}$$

where c is the dilatational wave speed, i. e. $c = 1$ [m/s] for the given problem, and Δx and Δt are the size of the finite element discretization in space and in time, respectively. Moreover, same orders of polynomials in space and in time are chosen, which are denoted by p in the latter context.

For this space-time problem we define the error in the L_2 norm as

$$e_{\square} = \sqrt{\frac{1}{N\,L}\sum_{n=1}^{N}\int_{L}\Big[\square(x,t_n) - \square_h(x,t_n)\Big]^2\,\mathrm{d}x}, \quad \text{with} \quad \square \in u, v \tag{43}$$

in which N is the total number of time steps and L denotes the length of the bar. The quantities $v(x_i, t_n), u(x_i, t_n)$ represent the exact solutions at (x_i, t_n), while $v_h(x_i, t_n), u_h(x_i, t_n)$ are the discrete solutions obtained by the HVI method.
Figure 7 shows the convergence rate of the HVI solution in e_u and e_v. Here, we observe a similar convergence rate as for the simple SDOF problem. The convergence rate in the velocity field v_h turns out to be $\mathcal{O}(p+1)$, and a slightly higher convergence rate in the displacement field u_h than in the velocity field v_h is observed.

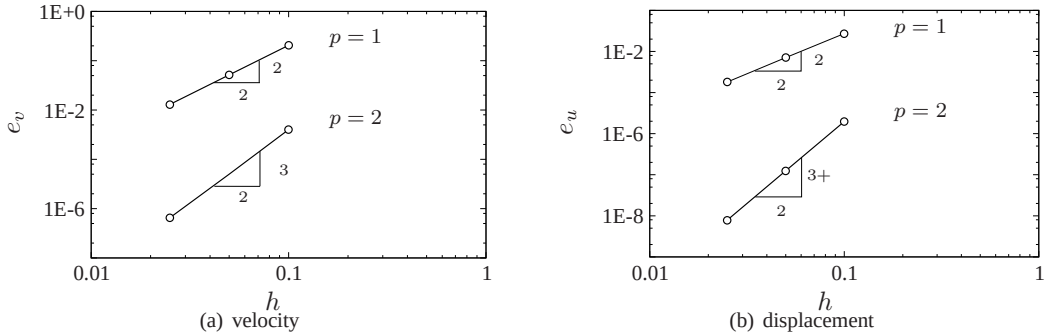

Figure 7. Convergence rate of velocities and displacements obtained by the HVI method with polynomials of order p in space and time.

Next, the propagation of a discontinuous wave form is investigated. Hereby, a rectangular spatial distribution of the initial displacement as

$$u_0(x) = \begin{cases} 10, & 0.49\,[\mathrm{m}] < x < 0.51\,[\mathrm{m}] \\ 0, & \text{otherwise} \end{cases} \quad \text{and} \quad v_0(x) = 0, \tag{44}$$

is chosen. For comparison, we solve the given problem with the Newmark method, the HVI method and the first order DGT method based on an equation system with two first-order equations, cf. [9]. The DGT method based on a system of two first order equations is abbreviated as the RDG method in the latter context. Respecting the space-time mesh parameter given in Eq. (42), as for the current case with $c = 1$ [m/s], uniform discretizations in space and time are chosen. Moreover, in order to minimize the numerical effort, linear polynomials in space for the Newmark method and bilinear polynomials in space and time for the HVI method as well as for the RDG method are employed. Figure 8 shows the numerical results computed with 20 finite element and $\Delta t = 0.05$ [s] by the three different methods, while Figure 9 show those results computed with 100 element and $\Delta t = 0.01$ [s]. Note that due to the coarse spatial discretization in the case of 20 elements, the initial assignment (Eq. (44)), can not be well resoluted. Thus the triangular form initial displacement is resulted in Figure 8. Only in the case of finer discretization (100 element), this initial assignment can be rather well resoluted, see Figure 9. In these diagrams, we observe that numerical dispersion spoils the solution of the Newmark method on the both discretizations (20 and 100 elements), while more stable results are achieved by the HVI and the RDG method. As is known, the conventional semi-discretization method (MOL) normally suffers from the numerical dispersion and spurious oscillation in modeling the wave solutions with sharp gradient and discontinuities, cf. [8]. As for the current problem, the Newmark method fails in reproducing the high modes inherenting in the discontinuous initial assignment whereby dramatically

numerical dispersion is observed. In contrast, more accurate results are obtained by the HVI and the RDG method. Moreover, as for the HVI method, weak numerical dispersion in the velocity field is observed, while the displacement field is less influenced. The best results are obtained by the RDG method. However, we denote that the numerical effort of solving the equation system of two first-order equations with the RDG method is almost twice as much as those of solving a single equation with the HVI method. Nevertheless, the results of the HVI method is much better compared to the solution obtained by the Newmark method under the same discretizations.

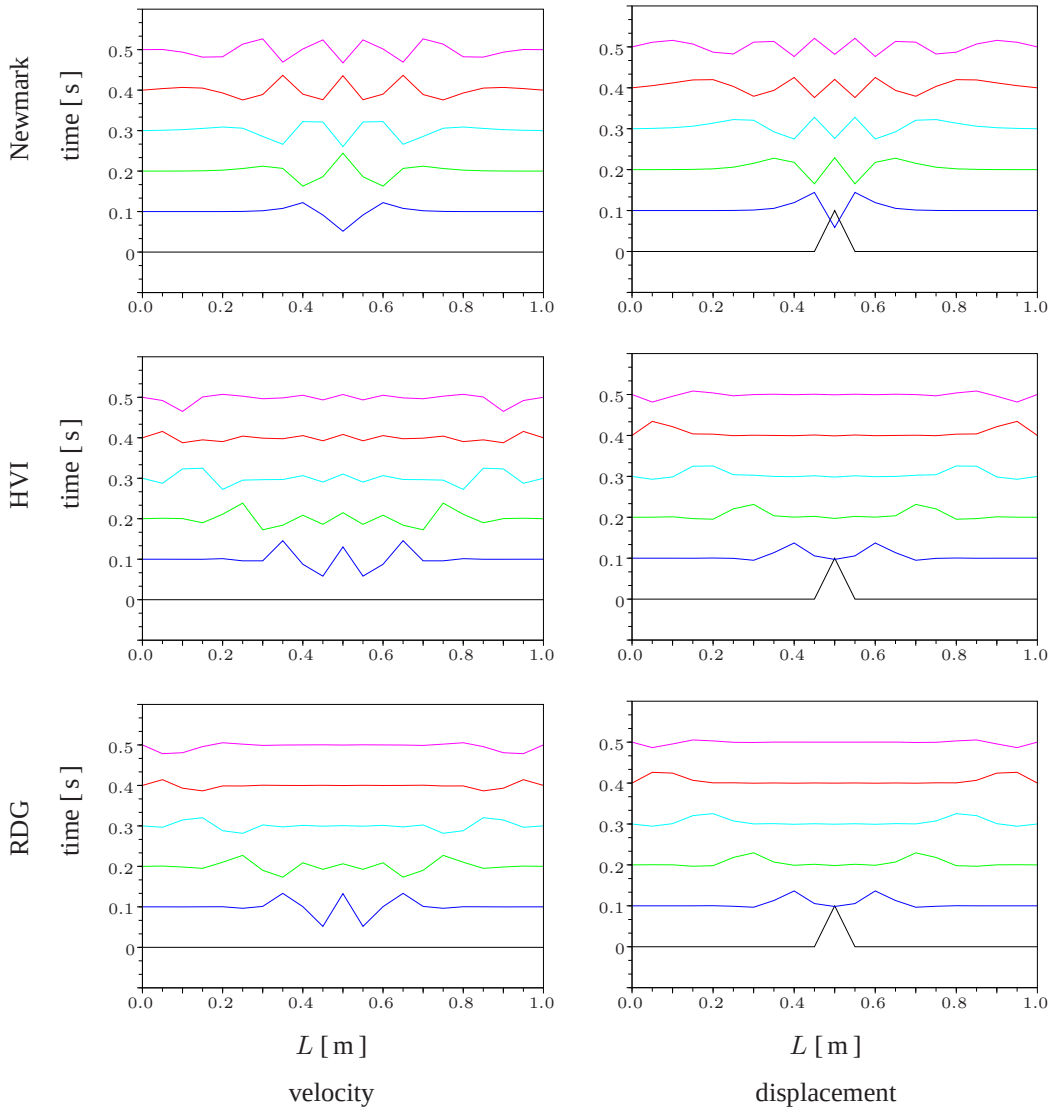

Figure 8. Propagation of discontinuous wave front computed with 20 element $\Delta t = 0.05$ [s] with Newmark method, HVI method and RDG method

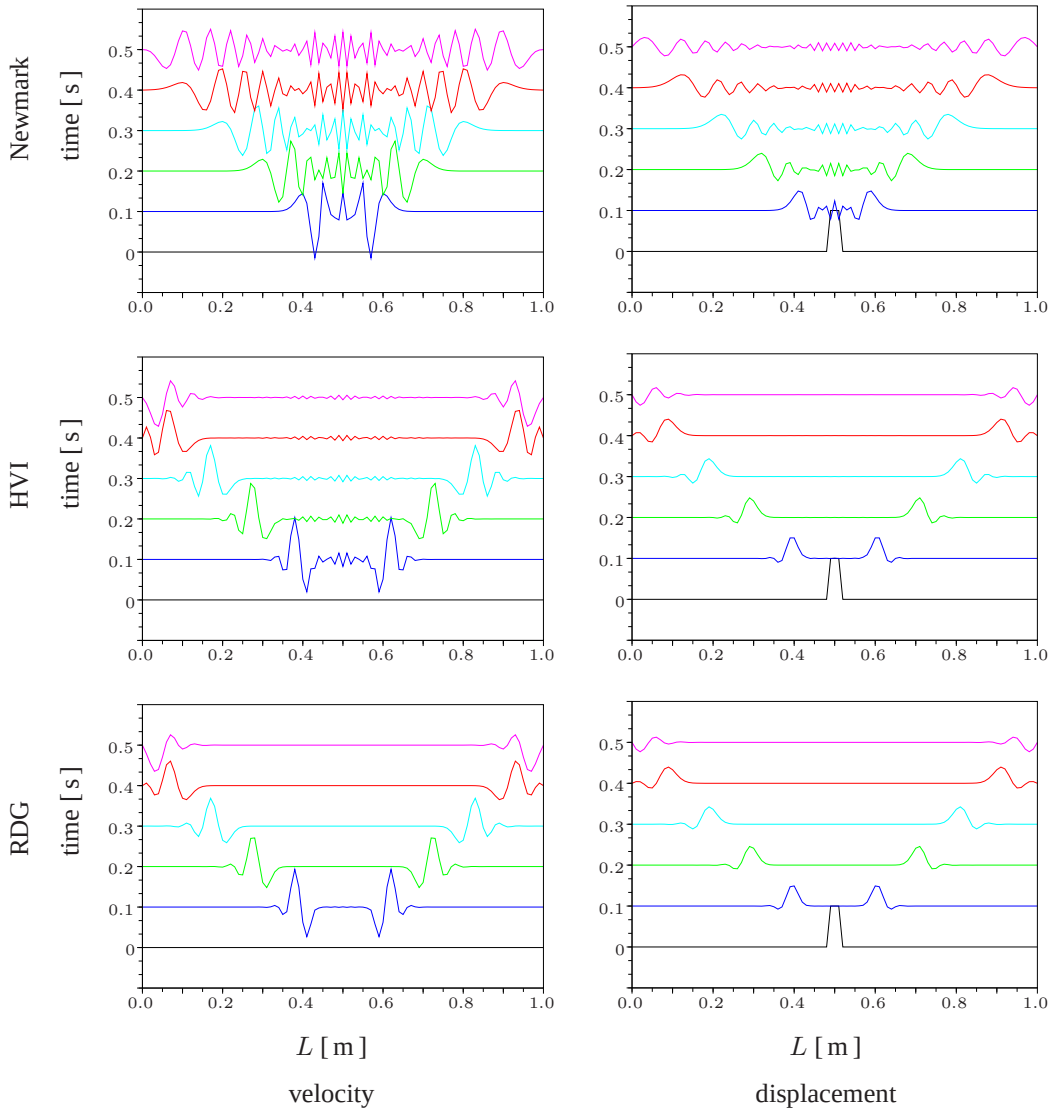

Figure 9. Propagation of discontinuous wave front computed with 100 element $\Delta t = 0.01$ [s] with Newmark method, HVI method and RDG method

4.3. Propagation of a compressional wave in two dimensions

Next, we focus on the wave propagation in a two-dimensional elastic medium. For the sake of simplicity, the propagation of the scalar compressional wave is considered. The governing equation of the compressional wave (see (17)) reads

$$\ddot{\phi}(\mathbf{x},t) - c^2 \operatorname{div}\operatorname{grad}\phi(\mathbf{x},t) = 0, \quad \text{in} \quad \Omega\times\mathcal{I}, \quad \text{with} \quad \Omega = [-5,-5]\times[5,5] \text{ and } \mathcal{I} = [0,3]\,\text{s}, \tag{45}$$

where $\phi(\mathbf{x},t)$ represents the displacement and c^2 is an elastic parameter with $c = \sqrt{\lambda + 2\mu}$ representing the speed of the wave propagation. Homogeneous Neumann (stress-free) boundary conditions are assumed. The initial condition is given for the displacement as

$$\phi(\mathbf{x},t_0) = \begin{cases} 10\,\cos(|\mathbf{x}|\,\pi), & |\mathbf{x}| < 1, \\ 0, & \text{otherwise}, \end{cases} \qquad \text{and} \quad \dot{\phi}(\mathbf{x},t_0) = 0, \quad \forall\,\mathbf{x}\in\Omega. \tag{46}$$

The computation is carried out by the HVI method on a quadrilateral mesh of 40×40 elements with bilinear trial- and test-functions in space and first order polynomials in time. Concerning the Courant-Friedrich-Lewy condition, c. f. [16], which ensures the stability of the numerical solution, a uniform time step length of $\Delta t = 0.25$ [s] is employed. Figure 10 shows the snapshots of both the velocity $\dot{\phi}_h(\mathbf{x},t)$ and the displacement $\phi_h(\mathbf{x},t)$ at time $t = 1$ [s], 2 [s] and 3 [s]. From these pictures we observe more or less isotropic wave forms in the media. We denote here, upon the current spatial discretization (40×40 elements), the anisotropy in the phase speed introduced by the orientation of the elements is rather small. Thus, we conclude that the numerical solutions agree well with the physical observation.
In order to study the applicability and generality of the proposed HVI method, we apply the method to quadrilateral and triangular finite element meshes with both regular and Delaunay grids. Hereby, the influence of mesh anisotropy on the numerical solution is considered. We computed the given problem upon four different grids (P1-P4) with comparable DOFs, as shown in Figure 11. The time step size is fixed to $\Delta t = 0.2$ [s]. Linear trial and test functions in space and time are employed. In Figure 11 we depicted contour plots of velocities and displacements at $t = 3.0$ [s]. Herein anisotropies in the wave forms are shown, which imply differences in the wave speeds with respect to different directions. Nevertheless the qualitative behavior of the propagating dilatational wave is less influenced. Next, we define the error norm e_v as

$$e_v = \frac{1}{L}\int_{-L/2}^{L/2} \sqrt{\left(v_h(x,t_1) - v(x,t_1)\right)^2}\,\mathrm{d}x, \quad \text{with} \quad t_1 = 3\,[\,\mathrm{s}\,] \quad \text{and} \quad L = 10\,[\,\mathrm{m}\,] \tag{47}$$

with v_h and v the finite element solution and the exact solution, respectively. Figure 12 shows the polar plot of the error e_v with respect to various cuts of the solution at angel ψ ($0 < \psi < 180°$). We observe a more or less isotropic wave form obtained on the unstructured triangular grid (P4). However, the smallest error occurs in the P2 grid along the direction with the highest grid density.
Next, we compute the above problem again with quadrilateral meshes of 20×20 and 80×80 elements. With respect to the mesh parameter introduced in Eq. (42), the time step lengths Δt are chosen to be 0.5 [s] and 0.125 [s], respectively. Bilinear polynomials in space and linear polynomials in time are employed. Figure 13 shows the profiles of the velocity $\dot{\phi}$ and the displacement ϕ at $x_2 = 0$, $t = 2$ [s]. Hereby we observe a convergence towards a (numerically computed) reference solution. Furthermore, we point out that for such a space-time coupled problem reducing the size of the time step Δt while holding the spatial discretization fixed cannot improve the accuracy of the numerical result extensively, since the temporal approximation procedure cannot compensate the error induced

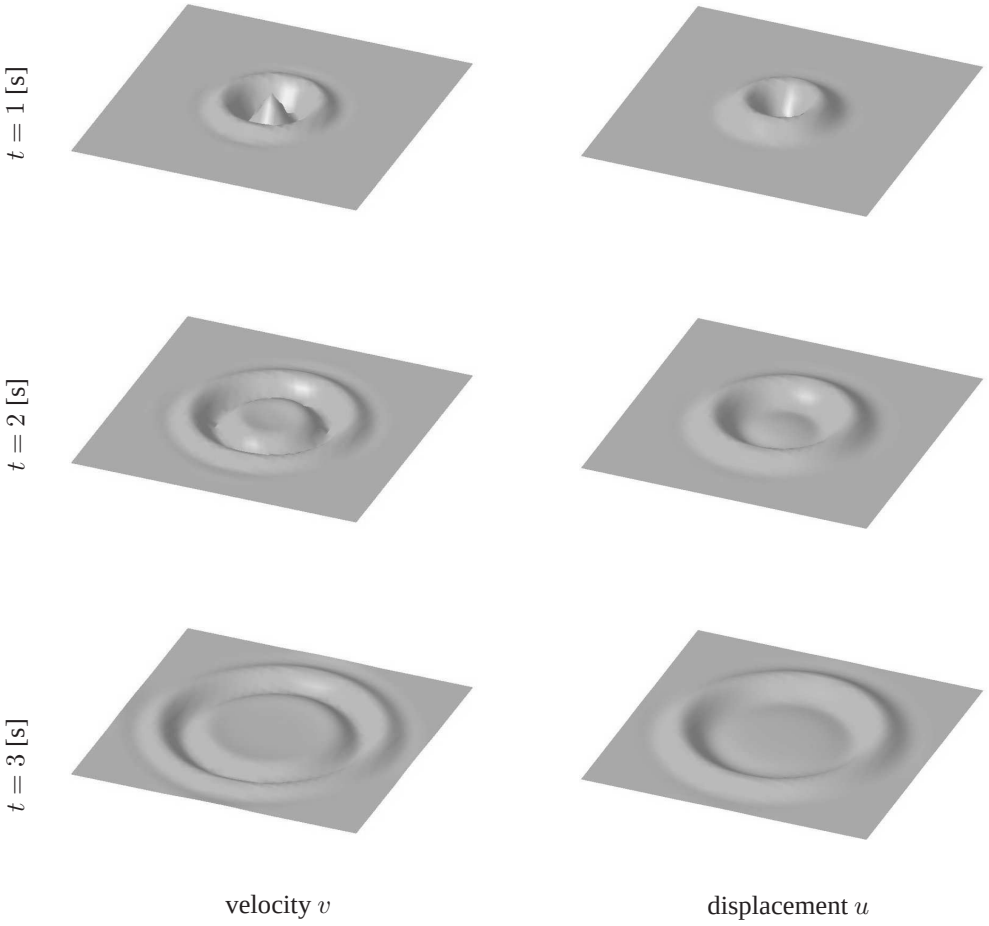

Figure 10. Wave propagation in a homogeneous media computed with 40×40 bilinear element with $\Delta t = 0.25$ [s]

by the spatial discretization [19].

4.4. Two-dimensional wave propagation in an elastic medium

In the last example, we compute the propagation of longitudinal and transversal waves in an elastic solid media. A square block of the size 50×50 [m^2] is subjected to an impulse load $\bar{\mathbf{t}}$, see Figure 14. The material parameters correspond to dry soil, with $\lambda = 1.447 \cdot 10^8$ [N/m^2], $\mu = 9.8 \cdot 10^7$ [N/m^2] and $\rho = 1884$ [kg/m^3], c. f. [30]. The governing equation is given by Eq. (18). For such a linear elastic material, we expect to observe a compressional and a shear wave propagating at different phase speeds c_P ($= \sqrt{(\lambda + 2\,\mu)/\rho}$) and c_S ($= \sqrt{\mu/\rho}$), respectively.
Figure 15 shows the vertical component of the velocity $\mathbf{v}_h$ and the displacement $\mathbf{u}_h$ (computed by 100×100 bilinear quadrilateral elements with $\Delta t = 0.001$ [s]) at time $t = 0.05$ [s] and $t = 0.10$ [s]. In these contour plots, we obviously observe two wave fronts traveling in the body which can be easily

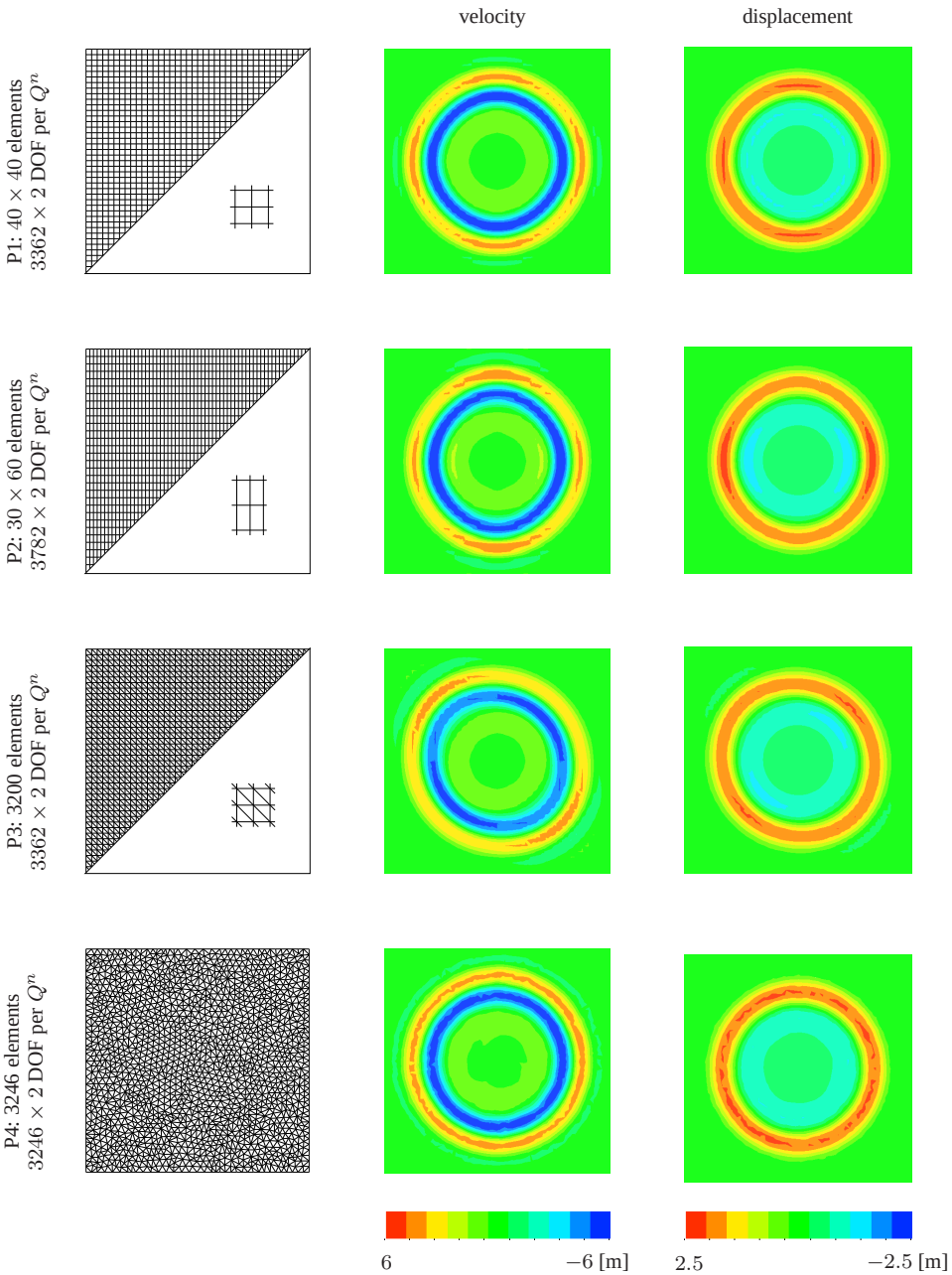

Figure 11. Contour plots of wave forms at t=3 [s], $\Delta t = 0.2$ [s], P1: regular square grid based on square quadrilaterals, P2: regular grids based on rectangular quadrilaterals, P3: regular gird based on triangular, P4: unstructured grid based on a Delaunay triangulars

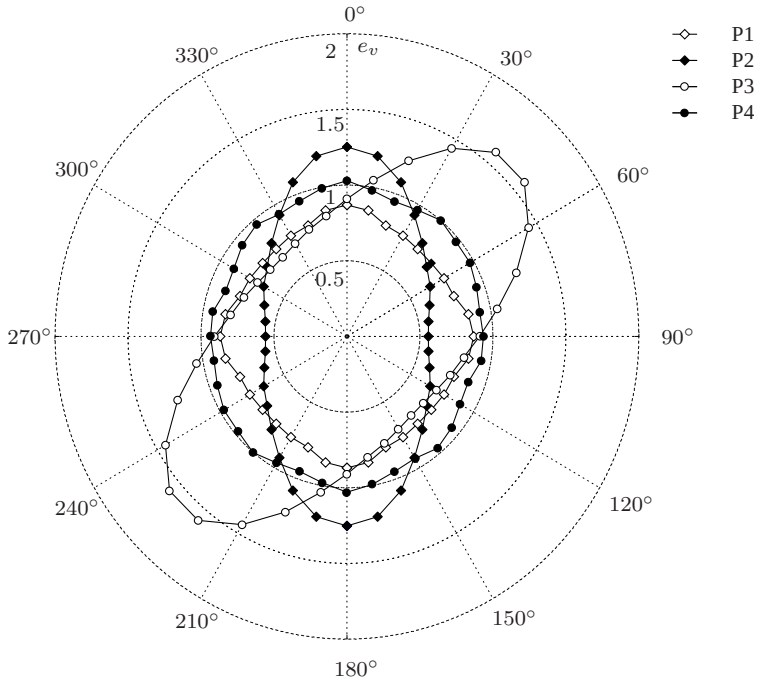

Figure 12. Polar plot of error e_v with respect to discrete "cut" of the discretizations (P1–P4)

identified as the compressional and the shear wave, respectively. Furthermore, the most significant property of the shear wave is the fact that it propagates at the direction 45° to the normal. According to our numerical simulation the compressional wave speed is 423.1 [m/s] and the shear wave speed reads 230.5 [m/s], corresponding to the analytical speeds 425.25 [m/s] and 228.07 [m/s], respectively. Thus, we conclude that the numerical simulation has a good agreement with the exact solution.

5. DISCUSSION AND CONCLUSIONS

In the present work, we studied a novel Hybrid Velocity Integration (HVI) scheme for second-order time-dependent problems. With an implicit embedment of the displacement-velocity relation, the governing equation is formulated in a one-field first-order problem in time with primary unknowns in the velocity field. A numerically consistent and exact integration scheme for the displacement field according to Gauss quadrature is proposed, which can be handled within a space-time finite element code. The resulting first-order equation is solved by the time-discontinuous Galerkin method on a space-time finite element mesh, whereby a natural *upwind* flux is employed to enforce the continuity between the time intervals. Convergence studies with respect to both p- and h- refinement are presented. Various numerical experiments demonstrate the efficiency and applicability of the proposed space-time finite element method. The introduced technique builds up a general framework to treat second-order problems in time in an efficient way. In a subsequent paper we intend to applied the method to coupled problems of wave propagation in a fluid-saturated porous media.

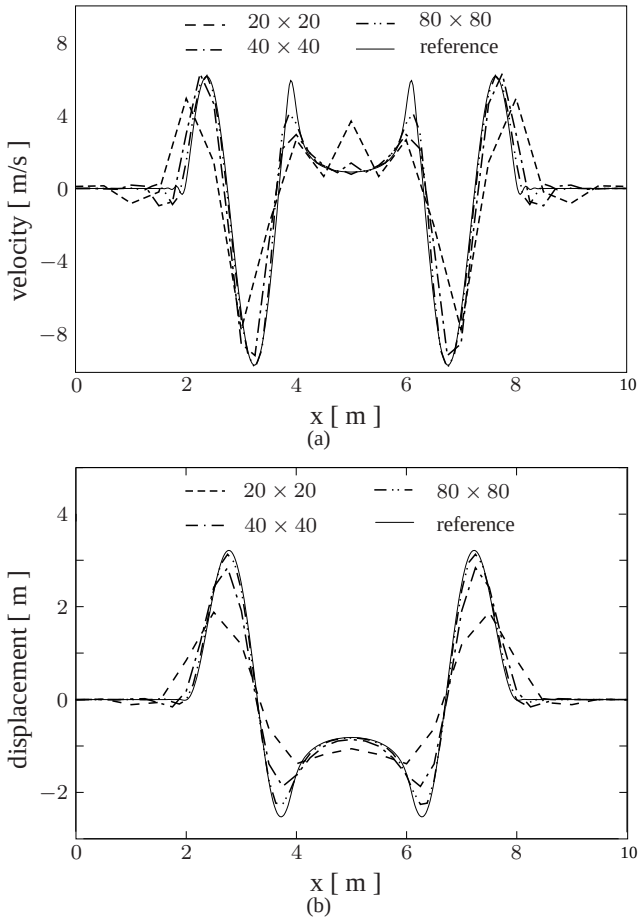

Figure 13. Profiles of velocity and displacement at $x_2 = 0$, $t = 2$ [s]

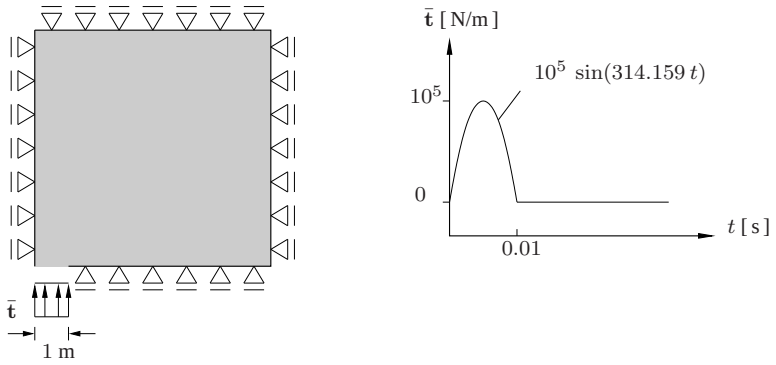

Figure 14. Geometry and boundary conditions of the problem of 2-dim linear elastic wave propagation

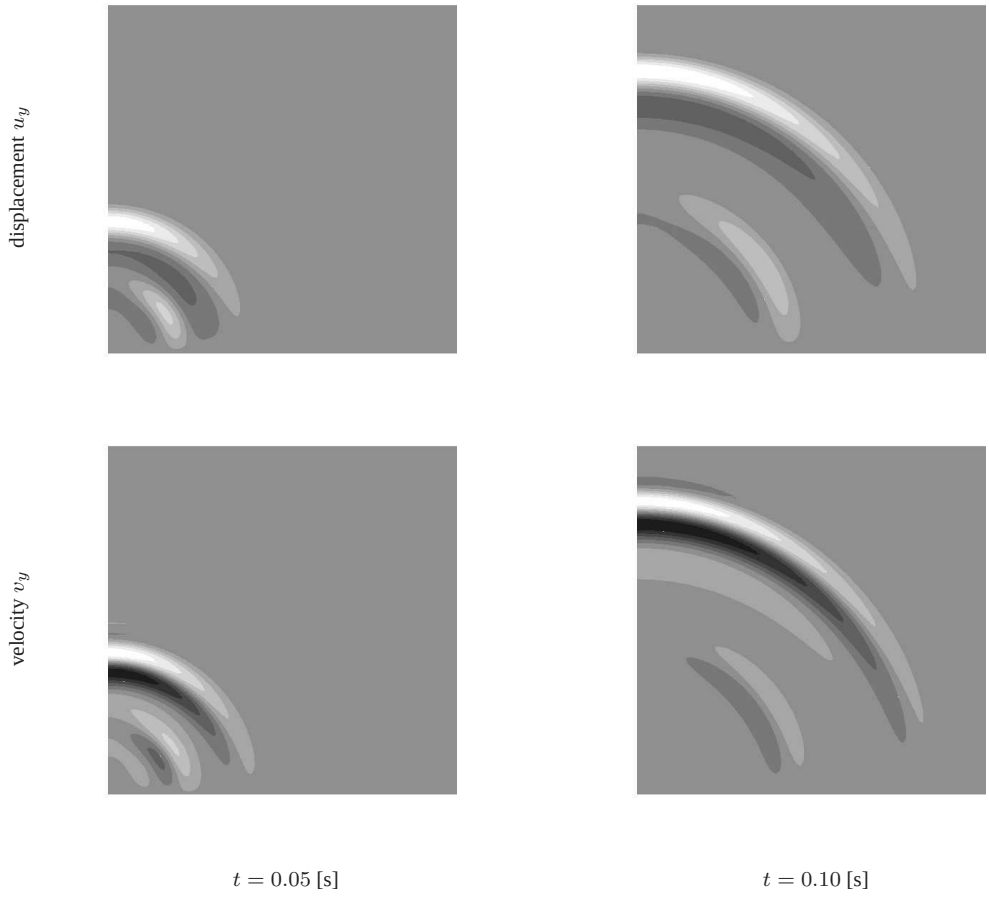

Figure 15. Contour plots of velocities and displacements

APPENDIX

I. Simple model equation

According to the weak form (10) we have to discuss the integration of the quantity

$$H = \int_{\mathcal{I}^n} g_{u_h}(t)\, \delta v_h \, \mathrm{d}t = J \int_{-1}^{+1} \left(J_\xi \int_{-1}^{\xi} v_h \, \mathrm{d}\tau \right) \delta v_h \, \mathrm{d}\xi. \tag{48}$$

Herein, the Jacobian s J and J_ξ are given as

$$J = \frac{t_{n+1} - t_n}{2} \quad \text{and} \quad J_\xi = \frac{t - t_n}{\xi + 1}. \tag{49}$$

Although J_ξ is function of ξ and t, its value can be determined uniquely with respect to a uniform mapping $[\,t_n, t_{n+1}\,] \to [\,-1, 1\,]$, cf. Figure 16. Thus we obtain

$$J_\xi = \frac{t - t_n}{\xi + 1} = \frac{t_{n+1} - t_n}{2} = J \tag{50}$$

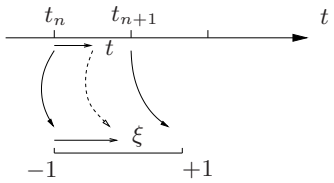

Figure 16. Uniform mapping $[\,t_n, t_{n+1}\,] \to [\,-1, 1\,]$

Applying the Gauss quadrature to (48) we get

$$H = J \sum_{GP} w_i \, g_{u_h}(\xi_i) \, \delta v_h(\xi_i) \tag{51}$$

with

$$g_{u_h}(\xi_i) = J \int_{-1}^{\xi_i} v_h \, \mathrm{d}\tau = J \, J_{\xi_i} \int_{-1}^{+1} v_h \, \mathrm{d}\eta = J \, J_{\xi_i} \sum_{GP} w_j \, v_h(\xi_i^j) \tag{52}$$

with GP the number of Gauss points, w_i and ξ_i the weight and the position of the corresponding Gauss point, respectively. In (52) we introduced the mapping $[\,-1, \xi_i\,] \to [\,-1, +1\,]$. The position ξ_i^j can be calculated by

$$\xi_i^j = \frac{1}{2}(\xi_i + 1)(\eta_i^j + 1) - 1 \quad \text{with} \quad \eta_i^j \in [\,-1, +1\,] \quad \text{and} \quad \xi_i \in [\,-1, +1\,], \tag{53}$$

where η_i^j is the local position of the Gauss points, see Figure 17.
Moreover, since ξ_i represents a fixed position of a Gauss point, the integral (52) can be determined uniquely. The Jacobian J_{ξ_i} is given as

$$J_{\xi_i} = \frac{\xi_i + 1}{2}. \tag{54}$$

Figure 17 shows examplarily the calculation of ξ_i^j of two Gauss points. Assume that the discrete trial- and test-functions are

$$v_h = \sum_{l=1}^{p+1} N_l \, \hat{v}_l \quad \text{and} \quad \delta v_h = \sum_{k=1}^{p+1} N_k \, \delta \hat{v}_k. \tag{55}$$

with the Lagrangian polynomials N_l and N_k of order p, $\hat{v}_l$ and $\delta \hat{v}_k$ the nodal values of the trial- and test-functions, respectively. By inserting equations (55) into (52) we obtain

$$g_{u_h}(\xi_i) = J \, J_{\xi_i} \sum_{GP} \left(w_j \sum_{l=1}^{p+1} N_l(\xi_i^j) \, \hat{v}_l \right) = J \sum_{l=1}^{p+1} N_l^{\xi_i} \, \hat{v}_l \tag{56}$$

with

$$N_l^{\xi_i} := J_{\xi_i} \sum_{GP} w_j \, N_l(\xi_i^j), \tag{57}$$

which ensures a consistent Gauss quadrature of $g_{u,h}(\xi_i)$ with GP Gauss points.

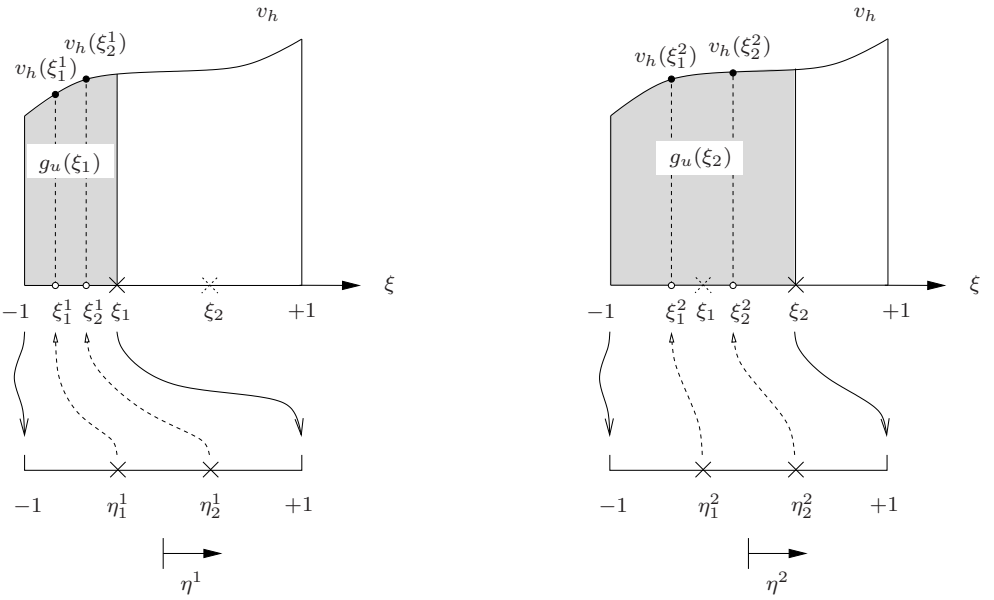

$$g_u(\xi_1) = J\, J_{\xi_1}\big(w_1\, v_h(\xi_1^1) + w_2\, v_h(\xi_2^1)\big) \qquad g_u(\xi_2) = J\, J_{\xi_2}\big(w_1\, v_h(\xi_1^2) + w_2\, v_h(\xi_2^2)\big)$$

Figure 17. Evaluation of $g_u(\xi_i)$ with a two Gauss points example

II. Space-time coupled formulation

The space-time trial- and test functions $\mathbf{v}_h$ and $\delta\mathbf{v}_h$ consist of tensor products of polynomials in space and time like

$$\mathbf{v}_h = \left(\sum_{m=1}^{q+1} M_m \sum_{l=1}^{p+1} N_l\right) \hat{\mathbf{v}}_\alpha \quad \text{and} \quad \delta\mathbf{v}_h = \left(\sum_{n=1}^{q+1} M_n \sum_{k=1}^{p+1} N_k\right) \delta\hat{\mathbf{v}}_\beta \tag{58}$$

with the spatial polynomials M_m and $M_n$of order q and the Lagrange polynomials N_l and N_k of order p. α and β are indices of the nodal values regarding the space-time domain. Bearing in mind the new type of temporal polynomials $N_l^{\xi_i}$, see (57), the integral $g_{\mathbf{u},h}$ at each Gauss point (η_j, ξ_i) can be written as

$$\mathbf{g}_{\mathbf{u},h}(\eta_j, \xi_i) = \left(\sum_{m=1}^{q+1} M_m(\eta_j) \sum_{l=1}^{p+1} J_{\Delta t} N_l^{\xi_i}\right) \hat{\mathbf{v}}_\alpha, \quad \text{with} \quad J_{\Delta t} = \frac{t_{n+1} - t_n}{2} \tag{59}$$

where η_j denotes the generalized Gauss point position in space while η_i represents the position in the time domain. Hereby we have obtained a similar structure for $\mathbf{g}_{\mathbf{u},h}$ and $\mathbf{v}_h$. Therefore the integral with respect to $\mathbf{g}_{\mathbf{u},h}$ and its associated quantity $\mathrm{grad}\,\mathbf{g}_{\mathbf{u},h}$ and $\mathrm{div}\, g_{\mathbf{u},h}$ can be evaluated according to the Gauss quadrature as familiar in the conventional FEM code.

ACKNOWLEDGEMENT

The authors are grateful to the DFG (German Science Foundation – Deutsche Forschungsgemeinschaft) for their financial support under the grant number Di 430/4-1 and Di 430/4-2.

references

[1] J. H. Argyris and D. W. Scharpf. Finite elements in space and time. *Nucl. Engrg. Des.*, 10:456–464, 1969.

[2] M. F. Wheeler B. Rivière and V. Girault. A priori error estiamates for finite methods based on discontinuous approximation spaces for elliptic problems. *SIAM J. Numer. Anal.*, 39:902–931, 2001.

[3] S. Shaw B. Rivière and M. F. Wheeler. Discontinuous Galerkin finite element methods for linear elasticity and quasistatic linear viscoelasticity. *Numer. Math.*, 95:347–376, 2003.

[4] F. Bassi and S. Rebay. A high-order accurate discontinuous finite element method for the numerical solution of the compressible navier-stokes equations. *J. Chem. Phys.*, 131:267–279, 1997.

[5] C. E. Baumann. *An hp-adaptive discontinuous finite element method for computational fluid dynamics*. PhD thesis, The University of Texas at Austin, 1997.

[6] C. E. Baumann and J. T. Oden. A discontinuous hp finite element method for convection-diffusion problems. *Comp. Meth. Appl. Mech. Eng.*, 175:311–341, 1999.

[7] C. E. Baumann and J. T. Oden. A discontinuous hp finite element method for the Euler and Navier-Stokes equations. *Int. J. Numer. Meth. Fluids*, 31:79–95, 1999.

[8] T. Belytschko and R. Mullen. On dispersive properties of finite element solutions. In J. Miklowitz and J. D. Achenback, editors, *Modern problems in wave propagation*, pages 67–82. Wiley, New York, 1978.

[9] Z. Chen, H. Steeb, and S. Diebels. A time-discontinuous Galerkin method for the dynamical analysis of porous media. *Int. J. Numer. Anal. Meth. Geomech.*, 30:1113–1134, 2006.

[10] B. Cockburn. Devising discontinuous Galerkin method for non-linear hyperbolic conservation laws. *J. Comput. Appl. Math.*, 128:187–204, 2001.

[11] B. Cockburn. Discontinuous Galerkin methods. *Z. Angew. Math. Mech.*, 11:731–754, 2003.

[12] B. Cockburn, S. Hou, and C. W. Shu. TVB Runge-Kutta local projection discontinuous Galerkin finite element methods for conservation laws. IV: The multidimensional case. *Math. Comp.*, 54:545–581, 1990.

[13] B. Cockburn, S. Y. Lin, and C. W. Shu. TVB Runge-Kutta local projection discontinuous Galerkin finite element methods for conservation laws III: One dimensional systems. *J. Comp. Phys.*, 84:90–113, 1989.

[14] B. Cockburn and C. W. Shu. TVB Runge-Kutta local projection discontinuous Galerkin finite element methods for conservation laws. II: General framework. *Math. Comp.*, 52:411–435, 1989.

[15] B. Cockburn and C. W. Shu. The local discontinuous Galerkin finite element method for convection-diffusion systems. *SIAM J. Numer. Anal.*, 35:2440–2463, 1998.

[16] R. Courant, K. Friedrichs, and H. Lewy. über die partiellen Differenzengleichungen der mathematischen Physik. *Mathematische Annalen*, 100:32–74, 1928.

[17] I. Fried. Finite element analysis of time-dependent phenomena. *AIAA Journal*, J.:1170–1173, 1969.

[18] E. Hairer, S. P. Nørsett, and G. Wanner. *Solving Ordinary Differential Equations I*. Springer-Verlag, Berlin, 1993.

[19] T. J. R. Hughes. *The Finite Element Method*. Prentice-Hall, Englewood Cliffs, New York, 1987.

[20] T. J. R. Hughes and G. M. Hulbert. Space-time finite element methods for elastodynamics: Formulations and error estimates. *Comp. Meth. Appl. Mech. Eng.*, 66:339–363, 1988.

[21] G. Hulbert. *Space-time finite element methods for second order hyperbolic equations*. PhD thesis, Department of Mechanical Engineering, Stanford University, Stanford, 1989.

[22] G. M. Hulbert and T. J. R. Hughes. Space-time finite element methods for second-order hyperbolic equations. *Comp. Meth. Appl. Mech. Eng.*, 84:327–348, 1990.

[23] C. Johnson. Discontinuous Galerkin finite element methods for second order hyperbolic problems. *Comp. Meth. Appl. Mech. Eng.*, 107:117–129, 1993.

[24] C. Johnson and J. Pitkäranta. An analysis of the discontinuous Galerkin method for a scalar hyperbolic equation. *Math. Comp.*, 46:1–26, 1986.

[25] P. Lesaint and P. A. Raviart. *On a finite element method for solving the neutron transport equation, in: C. de Boor (Ed), Mathematical Aspects of Finite Elements in Partial Differential Equations*. Academic Press, New York, 1974.

[26] X. Li, D. Yao, and R. W. Lewis. A discontinuous Galerkin finite element method for dynamic and wave propagation problems in non-linear solids and saturated porous media. *Int. J. Numer. Meth. Eng.*, 57:1775–1800, 2003.

[27] X. D. Li and N. E. Wiberg. Implementation and adaptivity of a space-time finite element method for structural dynamics. *Comp. Meth. Appl. Mech. Eng.*, 156:211–229, 1998.

[28] W. H. Reed and T. R. Hill. Triangular mesh methods for the neutron transport equation. *Los Alamos Scientific Laboratory Report LA-UR-73-479*, 1973.

[29] B. Rivière and M. F. Wheeler. Discontinuous galerkin methods for flow and transport problems in porous media. *Commun. Numer. Meth. En.*, 79:157–174, 2002.

[30] M. Schanz and A. H.-D. Cheng. Transient wave propagation in a one-dimensional poroelastic column. *Acta Mech.*, 145:1–18, 2000.

Paper C

A EVI-space-time Galerkin methods for dynamics at finite deformation in porous media

Computational Mechanics manuscript No.
(will be inserted by the editor)

Zhiyun Chen · Holger Steeb · Stefan Diebels

A EVI-space-time Galerkin method for dynamics at finite deformation in porous media

Received: date / Accepted: date

Abstract We present an EVI-space-time Galerkin method applied to dynamic analysis in fluid-saturated porous materials. The physical model is based on a materially incompressible solid skeleton saturated by a barotropic fluid. The deformation of the solid matrix is described by a compressible Neo-Hookean material law. The model equations are formulated in the Lagrangian description of the solid skeleton. In respect of the numerical modeling, by use of the Embedded Velocity Integration (EVI) technique, the governing set of second-order time-dependent equations is transformed to a first-order one, which is in turn solved by a time-discontinuous Galerkin method. In addition, a stability factor α, describing the embedded integration scheme of the displacement-velocity relation, is introduced. Depending on the chosen value of the α factor, the stability property of the overall solution can be enforced. Numerical experiments demonstrate the superior performance of the proposed method with respect to accuracy and low numerical damping in comparison with conventional time-stepping schemes.

Keywords Porous media · Finite deformation · Space-time FEM · Discontinuous Galerkin method · Embedded Velocity Integration method

1 Introduction

Fully-saturated porous materials consisting of a solid phase and a pore fluid phase have found lots of applications in our daily life, e. g. soils, rocks, polymer foams, human bones, biological tissues, etc. Since the pioneering work of Terzaghi [1], a great amount of works have been carried out to develop the theoretical foundation for the macroscopic modeling of porous media. Among others, Biot presented a three-dimensional consolidation model [2] and investigated systematically the propagating waves in biphasic mixtures [3; 4; 5]. The classical mixture theory was first investigated by Truesdell & Toupin [6]. In the following years, various works have been presented using continuum theories of the mixtures, [7; 8; 9; 10], etc. A historical survey is given in the monographic work by de Boer [11].

In seismological and petroleum engineering, propagating waves within saturated and unsaturated porous material are of great interest. Due to the small amplitudes of the elastic waves, it is sufficient to adopt the small-strain assumption, such that a linear theory taking into account the inertia forces of the solid and fluid phase is usually applied. However, for the modeling of bio-materials, e. g. soft tissues, or in the design of energy absorbing materials, e. g. cushion, where large deformations are usually present, a material model allowing for finite deformation is inevitable. Borja *et. al* [12] presented a framework for investigating elastoplastic consolidation at finite strains. Diebels & Ehlers [13] investigated the geometrically linear and nonlinear dynamic deformation of materially incompressible porous materials. Thermodynamically consistent formulations of non-linear deformation were studied by Advani *et. at* [14; 15] and Larsson & Larsson [16]. Therein, the general assumption that both constituents are materially incompressible with constant densities is adopted. More recently, Li *et. al* [17] proposed a complete model consisting of materially compressible solid and fluid constituents of porous media at finite strain, in which a Neo-Hooke material law combined with a Kelvin viscous mechanism was applied for the description of solid deformation. Nevertheless, in the presence of a highly compressible pore-fluid in a matrix with large porosity, the deformation of the mixture is strongly dependent on the deformation of the porous solid skeleton and the compressible response of the fluid, such that the compression of the solid grain itself can usually be neglected, cf. [11; 18]. In the current work,

Z. Chen, H. Steeb, S. Diebels
Saarland University, Chair of Applied Mechanics,
Im Stadtwald, Building A 4.2, D-66 123 Saarbrücken, Germany
Tel.: +49-681-302 2157
Fax: +49-681-302 2992
E-mail: s.diebels@mx.uni-saarland.de

we adopt a biphasic hybrid model consisting of materially incompressible solid phase and a compressible fluid phase [19; 20]. The deformation of the solid skeleton is described by a modified Neo-Hooke law [21; 22].
In respect of the numerical simulation technique, a space-time discontinuous Galerkin method is applied. Since the early work of Argyris & Scharpf [23] and Fried [24], in which they applied the Finite Element Method (FEM) in the temporal domain, the space-time Galerkin method has been developed rapidly. Years later, Hughes & Hulbert [25] proposed the so-called penalty time-discontinuous Galerkin method in which a Least Square term was introduced to enforce the continuity between the time intervals. Later on, this idea has been applied to hyperbolic equations [26; 27; 28]. A more innovative idea was to employ a so-called *upwind* flux treatment to enforce the continuity. Using the *upwind* flux instead of a penalty term to enforce the interelement continuity was originally a technique in the finite volume method, which was first introduced to the FEM community by Reed & Hill [29]. Cockburn and co-workers developed this idea to the more general Runge-Kutta Discontinuous Galerkin (RKDG) method, in which they applied the *upwind* flux treatment in the spatial domain and solved the resulting Ordinary Differential Equations (ODEs) in time with a Runge-Kutta approach [30; 31; 32].
In previous works [33; 34], we applied the *upwind* flux to the temporal domain, and developed a coupled Time-Discontinuous Galerkin method (DGT). The method has been successfully applied to the analysis of propagating waves in porous materials. However, due to the restriction of the *upwind* flux term to first-order systems, before being solved by the DGT method, the governing set of second-order equations in time had to be degenerated into a set of two first-order equations, cf. [33].
In the present work, we apply the DGT scheme for the solution strategy of coupled problems. By using the Embedded Velocity Integration (EVI)[1] technique [34], we circumvent the direct solution of the balance of momentum with respect to the solid displacement, and solve the resulting first-order equation for the velocity field with the DGT method. The solid displacement is subsequently computed according to a consistent integration of the velocities. Furthermore, beside the exact integration scheme proposed in [34; 35], a generalized EVI integration scheme complemented with a stabilization factor α is developed. The overall numerical stability of the solution can be enhanced by the proper choice of the stabilization parameter α.
The structure of the paper is as follows: In the next section, we introduce the balance equations of the biphase porous materials in the Lagrangian description of the solid phase. In section 3, after giving a brief introduction of the EVI technique, we derive the generalized EVI scheme with a stabilization factor α. In section 4, a coupled space-time finite element weak form is given. In section 5, we present some numerical experiments to demonstrate the performance of the model. In the last section we briefly discuss the proposed methods and mention related future work.

[1] Originally the method was named "Hybrid Velocity Integration (HVI)", but in the present work, the term "Embedded Velocity Integration (EVI)" was used for convenience.

2 Balance equations

We consider a two-phase fluid-saturated porous medium consisting of a solid phase $\varphi^{\mathfrak{s}}$ and a fluid phase $\varphi^{\mathfrak{f}}$. The model is based on the thermodynamically consistent Theory of Porous Media (TPM), cf. [9; 36; 37; 38; 39]. According to the idea of the mixture theory, different constituents at positions $\mathbf{X}_{\mathfrak{s}}$ and $\mathbf{X}_{\mathfrak{f}}$ in the reference configurations, are superimposed at position $\mathbf{x}$ in the current configuration. The partial density $\rho^{\mathfrak{i}} = n^{\mathfrak{i}}\,\rho^{\mathfrak{i}R}$ ($\mathfrak{i} \in \{\mathfrak{f}, \mathfrak{s}\}$) is defined as the mass of the constituent $\varphi^{\mathfrak{i}}$ with respect to the total volume of the mixture, i. e. $\rho^{i} = \mathrm{d}m^{i}/\mathrm{d}v$. The volume fraction is denoted as $n^{\mathfrak{i}} = \mathrm{d}v^{i}/\mathrm{d}v$ and $\rho^{\mathfrak{i}R}$ represents the so-called effective or true density of the constituent $\varphi^{\mathfrak{i}}$. As a consequence, the density of the mixture ρ equals the sum of the partial densities, i. e. $\rho = \rho^{\mathfrak{s}} + \rho^{\mathfrak{f}}$. The dynamic behavior of a mixture consisting of incompressible constituents, i. e. $\rho^{\mathfrak{s}R}$ =const and $\rho^{\mathfrak{f}R}$ =const, was studied in [13]. In the current work, we focus on a so-called biphasic hybrid model, in which only the solid phase $\varphi^{\mathfrak{s}}$ is considered as materially incompressible, i. e. $\rho^{\mathfrak{s}R}$ =const., while the fluid phase behaves like a barotropic fluid, i. e. $\rho^{\mathfrak{f}R} = f(p)$, [19; 20]. Assume that there exists no mass exchange between the solid and fluid phases, the mass balance of each constituent can be written as

$$(\rho^{\mathfrak{i}})'_{\mathfrak{i}} + \rho^{\mathfrak{i}}\,\mathrm{div}(\mathbf{x})'_{\mathfrak{i}} = 0, \quad \mathfrak{i} \in \{\mathfrak{s}, \mathfrak{f}\}. \tag{1}$$

Herein, $(\bullet)'_{\mathfrak{i}}$ represents the material time derivative following the motion of the constituent $\varphi^{\mathfrak{i}}$

$$(\bullet)'_{\mathfrak{i}} = \frac{\partial(\bullet)}{\partial t} + \mathrm{grad}(\bullet)\cdot\mathbf{v}_{\mathfrak{i}}, \tag{2}$$

in which $\mathbf{v}_{\mathfrak{i}}$ denotes the velocity of the phase $\varphi^{\mathfrak{i}}$, i. e. $\mathbf{v}_{\mathfrak{i}} = (\mathbf{x})'_{\mathfrak{i}}$. We define grad$(\bullet)$ and div$(\bullet)$ as the gradient and the divergence operator with respect to current configuration.
Since the solid constituent is assumed to be materially incompressible ($\rho^{\mathfrak{s}R}$ =const.), the mass balance of the solid constituent can be simplified to the volume balance as

$$(n^{\mathfrak{s}})'_{\mathfrak{s}} + n^{\mathfrak{s}}\ \mathrm{div}\,\mathbf{v}_{\mathfrak{s}} = 0. \tag{3}$$

Introducing the seepage velocity $\mathbf{w}_{\mathfrak{f}} = \mathbf{v}_{\mathfrak{f}} - \mathbf{v}_{\mathfrak{s}}$, which describs the relative velocity between the solid and fluid phases, we relate the material time derivate of the two constituents by

$$(\bullet)'_{\mathfrak{f}} = (\bullet)'_{\mathfrak{s}} + \mathrm{grad}(\bullet)\cdot\mathbf{w}_{\mathfrak{f}}. \tag{4}$$

Bearing in mind the definition of the partial density $\rho^{\mathfrak{f}} = n^{\mathfrak{f}}\,\rho^{\mathfrak{f}R}$, we obtain the mass balance of the fluid as

$$(n^{\mathfrak{f}}\,\rho^{\mathfrak{f}R})'_{\mathfrak{f}} + n^{\mathfrak{f}}\,\rho^{\mathfrak{f}R}(\operatorname{div}\mathbf{w}_{\mathfrak{f}} + \operatorname{div}\mathbf{v}_{\mathfrak{s}}) = 0. \tag{5}$$

Applying (4) to the material time derivative in (5), the mass balance of fluid phase yields

$$(n^{\mathfrak{f}}\rho^{\mathfrak{f}R})'_{\mathfrak{s}} + \operatorname{div}(n^{\mathfrak{f}}\rho^{\mathfrak{f}R}\mathbf{w}_{\mathfrak{f}}) + n^{\mathfrak{f}}\rho^{\mathfrak{f}R}\operatorname{div}\mathbf{v}_{\mathfrak{s}} = 0. \tag{6}$$

Multiplying (3) with the effective density of the fluid $\rho^{\mathfrak{f}R}$ and adding up to (6), we get the mass balance of the mixture in current configuration as

$$n^{\mathfrak{f}}(\rho^{\mathfrak{f}R})'_{\mathfrak{s}} + \rho^{\mathfrak{f}R}\operatorname{div}\mathbf{v}_{\mathfrak{s}} + \operatorname{div}(\rho^{\mathfrak{f}R}\,n^{\mathfrak{f}}\mathbf{w}_{\mathfrak{f}}) = 0. \tag{7}$$

Herein, we have taken into account the saturation condition $n^{\mathfrak{f}} + n^{\mathfrak{s}} = 1$. For the sake of simple notation, in the following context, we suppress the subscript in the material time derivative following the solid phase motion, i. e. $(\bullet)' = (\bullet)'_{\mathfrak{s}}$.
Assume that the bulk modulus of the fluid $K^{\mathfrak{f}}$ is constant, the equation of state for the fluid effective density may be chosen as [17]

$$\rho^{\mathfrak{f}R} = \rho_0^{\mathfrak{f}R}\exp\Big(\frac{p - p_0}{K^{\mathfrak{f}}}\Big), \tag{8}$$

in which $\rho_0^{\mathfrak{f}R}$ and p_0 denote the initial fluid effective density and the pore pressure, respectively. p denotes the pore fluid pressure at the current state. The material time derivative of the fluid density $(\rho^{\mathfrak{f}R})'$ in (7) can be further replaced by, [17]

$$(\rho^{\mathfrak{f}R})' = \frac{\rho^{\mathfrak{f}R}}{K^{\mathfrak{f}}}(p)'. \tag{9}$$

Finally, by inserting (9) into (7), we get the mass balance of the mixture in current configuration as

$$\frac{n^{\mathfrak{f}}\,\rho^{\mathfrak{f}R}}{K^{\mathfrak{f}}}(p)' + \rho^{\mathfrak{f}R}\operatorname{div}\mathbf{v}_{\mathfrak{s}} + \operatorname{div}(\rho^{\mathfrak{f}R}\,n^{\mathfrak{f}}\,\mathbf{w}_{\mathfrak{f}}) = 0. \tag{10}$$

It can be seen that the third term in (10) represents the mass flux of the fluid flowing through the unit area of the solid matrix. For future convenience, we introduce here the filter velocity, which is also known as the Darcy velocity, as $\mathbf{q} = n^{\mathfrak{f}}\,\mathbf{w}_{\mathfrak{f}}$.
Let $\mathbf{F}_{\mathfrak{s}}$ denote the deformation gradient of the solid skeleton and $J_{\mathfrak{s}} = \det\mathbf{F}_{\mathfrak{s}}$ be the Jacobian determinant. Moreover, since the solid phase is assumed to be materially incompressible, its volume change can be directly derived by

$$n^{\mathfrak{s}} = n_0^{\mathfrak{s}}J_{\mathfrak{s}}^{-1}, \quad n^{\mathfrak{f}} = 1 - n^{\mathfrak{s}}, \tag{11}$$

in which $n_0^{\mathfrak{s}}$ is the initial volume fraction of the solid. Next, we introduce the Piola transformation of the filter velocity $\mathbf{q}$, cf. [17]

$$\mathbf{Q} = J_{\mathfrak{s}}\,\mathbf{F}_{\mathfrak{s}}^{-1}\,\mathbf{q}. \tag{12}$$

For convenience, we define the vector

$$\mathbb{Q} = \mathbf{F}_{\mathfrak{s}}\,\mathbf{Q} = J_{\mathfrak{s}}\,\mathbf{q} = J_{\mathfrak{s}}\,n^{\mathfrak{f}}\,\mathbf{w}_{\mathfrak{f}}. \tag{13}$$

Moreover, let $\theta = J_{\mathfrak{s}}\,p$ be the intrinsic Kirchhoff pressure, by use of the chain rule of differentiation, we get

$$\theta' = J'_{\mathfrak{s}}\,p + J_{\mathfrak{s}}\,p' = p\,\operatorname{Div}\mathbf{v}_{\mathfrak{s}} + J_{\mathfrak{s}}\,p'. \tag{14}$$

In the above expression, we have made use of the Piola identity [40]

$$J'_{\mathfrak{s}} = J_{\mathfrak{s}}\,\operatorname{div}\mathbf{u}'_{\mathfrak{s}} = \operatorname{Div}\mathbf{v}_{\mathfrak{s}}. \tag{15}$$

Herein, $\operatorname{Grad}(\bullet)$ and $\operatorname{Div}(\bullet)$ represent the gradient and the divergence operator with respect to the reference configuration of the solid phase, i. e. with respect to $\mathbf{X}_{\mathfrak{s}}$. Multiplying (10) with the Jacobian determinant $J_{\mathfrak{s}}$, the mass balance of the mixture with respect to the reference configuration can be written as [2]

$$\frac{n^{\mathfrak{f}}\,\rho^{\mathfrak{f}R}}{K^{\mathfrak{f}}}\theta' + \rho^{\mathfrak{f}R}\Big(1 - \frac{n^{\mathfrak{f}}}{K^{\mathfrak{f}}}\frac{\theta}{J_{\mathfrak{s}}}\Big)\operatorname{Div}\mathbf{v}_{\mathfrak{s}} + \operatorname{Div}(\rho^{\mathfrak{f}R}\,\mathbf{F}_{\mathfrak{s}}^{-1}\,\mathbb{Q}) = 0. \tag{17}$$

The momentum balance of the mixture in current configuration is given by [13]

$$\begin{aligned}(n^{\mathfrak{s}}\rho^{\mathfrak{s}R} + n^{\mathfrak{f}}\,\rho^{\mathfrak{f}R})\,\mathbf{v}'_{\mathfrak{s}} + n^{\mathfrak{f}}\rho^{\mathfrak{f}R}\{\mathbf{w}'_{\mathfrak{f}} + [\operatorname{grad}(\mathbf{v}_{\mathfrak{s}} + \mathbf{w}_{\mathfrak{f}})]\,\mathbf{w}_{\mathfrak{f}}\}\\ = \operatorname{div}(\mathbf{T}_{\mathrm{E}}^{\mathfrak{s}} - p\,\mathbf{I}) + (\rho^{\mathfrak{f}} + \rho^{\mathfrak{s}})\,\mathbf{b},\end{aligned} \tag{18}$$

in which $\mathbf{b}$ is the body force. According to the Terzaghi's effective stress principle [41], the total stress within the mixture equals

$$\mathbf{T} = \mathbf{T}_{\mathrm{E}}^{\mathfrak{s}} - p\,\mathbf{I}, \tag{19}$$

in which $\mathbf{T}_{\mathrm{E}}^{\mathfrak{s}}$ is the extra stress of the solid phase.
Following the concept of effective stresses [41], we introduce the following total stresses

$$\mathbf{P} = \mathbf{P}_{\mathrm{E}}^{\mathfrak{s}} - \theta\,\mathbf{F}_{\mathfrak{s}}^{-\mathrm{T}}, \tag{20}$$

$$\mathbf{S} = \mathbf{S}_{\mathrm{E}}^{\mathfrak{s}} - \theta\,\mathbf{C}_{\mathfrak{s}}^{-1}, \tag{21}$$

[2] Let $\mathcal{B}_0$ and $\partial\mathcal{B}_0$ be an arbitrary domain and its boundary in the reference configuration, while $\mathcal{B}$ and $\partial\mathcal{B}$ are their counterparts in the current configuration, there exists the following transformation

$$\begin{aligned}&\int_{\mathcal{B}}\operatorname{div}(\rho^{\mathfrak{f}R}\,\mathbf{q})\,\mathrm{d}v = \int_{\partial\mathcal{B}}\rho^{\mathfrak{f}R}\,\mathbf{q}\cdot\mathbf{n}\,\mathrm{d}a\\ &= \int_{\partial\mathcal{B}_0} J\,\rho^{\mathfrak{f}R}\,\mathbf{q}\cdot(\mathbf{F}^{-T}\,\mathbf{N})\,\mathrm{d}A = \int_{\mathcal{B}_0}\operatorname{Div}(\rho^{\mathfrak{f}R}\,J\,\mathbf{F}^{-1}\,\mathbf{q})\,\mathrm{d}V\\ &= \int_{\mathcal{B}_0}\operatorname{Div}(\rho^{\mathfrak{f}R}\,\mathbf{F}^{-1}\,\mathbb{Q})\,\mathrm{d}V = \int_{\mathcal{B}_0}\operatorname{Div}(\rho^{\mathfrak{f}R}\,\mathbf{Q})\,\mathrm{d}V,\end{aligned} \tag{16}$$

where $\mathbf{n}$ and $\mathbf{N}$ are the unit outward normal on $\partial\mathcal{B}$ and $\partial\mathcal{B}_0$, respectively.

in which $\mathbf{P}$ and $\mathbf{S}$ are the first and second Piola-Kirchhoff stress, i. e. $\mathbf{P} = \mathbf{F}_{\mathfrak{s}} \cdot \mathbf{S}$. The corresponding extra stresses of the solid phase are denoted by $\mathbf{P}_{\mathrm{E}}^{\mathfrak{s}}$ and $\mathbf{S}_{\mathrm{E}}^{\mathfrak{s}}$. The right Cauchy-Green deformation tensor is denoted by $\mathbf{C}_{\mathfrak{s}}$, i. e. $\mathbf{C}_{\mathfrak{s}} = \mathbf{F}_{\mathfrak{s}}^{\mathrm{T}} \cdot \mathbf{F}_{\mathfrak{s}}$.
By constructing the constitutive law for the solid effective stress, we note that with respect to a hybrid model consisting of an incompressible solid phase and a compressible fluid phase, the Jacobian determinant $J_{\mathfrak{s}}$ must fulfill

$$n_0^{\mathfrak{s}} \leq J_{\mathfrak{s}} < \infty, \tag{22}$$

which means that there exists a compaction point when all fluid has been squeezed out of the matrix and pores are closed, i. e. $J_{\mathfrak{s}} = n_0^{\mathfrak{s}}$. After reaching this compaction point, no further volume change is possible and the solid material behaves like an incompressible material. In the current work, we employ the modified Neo-Hooke model [22] developed for the porous material

$$\mathbf{S}_{\mathrm{E}}^{\mathfrak{s}} = \mu\,(\mathbf{I} - \mathbf{C}_{\mathfrak{s}}^{-1}) + \lambda\,(1 - n_0^{\mathfrak{s}})^2 \Big[\frac{J_{\mathfrak{s}}}{1 - n_0^{\mathfrak{s}}} - \frac{J_{\mathfrak{s}}}{J_{\mathfrak{s}} - n_0^{\mathfrak{s}}}\Big]\mathbf{C}_{\mathfrak{s}}^{-1}, \tag{23}$$

in which λ and μ are the Lamé parameters of the solid skeleton. Note that μ and λ characterized the macroscopic properties of the porous matrix material.
The material time derivative of the vector $\mathbb{Q}$ reads

$$\mathbb{Q}' = J_{\mathfrak{s}}'\, n^{\mathfrak{f}}\, \mathbf{w}_{\mathfrak{f}} + J_{\mathfrak{s}}\, n^{\mathfrak{f}}\, \mathbf{w}_{\mathfrak{f}}' + J_{\mathfrak{s}}\, \mathbf{w}_{\mathfrak{f}}\, (n^{\mathfrak{f}})'. \tag{24}$$

By use of the saturation condition, we further obtain

$$\begin{aligned} J_{\mathfrak{s}}\,(n^{\mathfrak{f}})' &= J_{\mathfrak{s}}\,(1 - n^{\mathfrak{s}})' \\ &= -J_{\mathfrak{s}} \left(\frac{n_0^{\mathfrak{s}}}{J_{\mathfrak{s}}}\right)' = \frac{n_0^{\mathfrak{s}}}{J_{\mathfrak{s}}} J_{\mathfrak{s}}' = n^{\mathfrak{s}}\, J_{\mathfrak{s}}'. \end{aligned} \tag{25}$$

Inserting now (25) into (24), we can get

$$J_{\mathfrak{s}}\, n^{\mathfrak{f}}\, \mathbf{w}_{\mathfrak{f}}' = \mathbb{Q}' - J_{\mathfrak{s}}'\, \mathbf{w}_{\mathfrak{f}} = \mathbb{Q}' - \mathcal{J}\,\mathrm{Div}\,\mathbf{v}_{\mathfrak{s}}\,\mathbb{Q}, \tag{26}$$

in which $\mathcal{J} = 1/(J_{\mathfrak{s}}\, n^{\mathfrak{f}})$. Thus, we can rewrite the balance of momentum of the mixture (18) in reference configuration of the solid phase as

$$\begin{aligned} &(\rho_0^{\mathfrak{s}} + (J_{\mathfrak{s}} - n_0^{\mathfrak{s}})\rho^{\mathfrak{f}R})\,\mathbf{v}_{\mathfrak{s}}' + \rho^{\mathfrak{f}R}\,(\mathbb{Q}' - \mathcal{J}\,\mathrm{Div}\,\mathbf{v}_{\mathfrak{s}}\,\mathbb{Q}) \\ &+ \rho^{\mathfrak{f}R}\,\mathrm{Grad}\,(\mathbf{v}_{\mathfrak{s}} + \mathcal{J}\mathbb{Q})\;(\mathbf{F}_{\mathfrak{s}}^{-1}\,\mathbb{Q}) \\ &= \mathrm{Div}(\mathbf{P} - \theta\,\mathbf{F}_{\mathfrak{s}}^{-T}) + (\rho_0^{\mathfrak{s}} + (J_{\mathfrak{s}} - n_0^{\mathfrak{s}})\,\rho^{\mathfrak{f}R})\,\mathbf{b}, \end{aligned} \tag{27}$$

in which $\rho_0^{\mathfrak{s}} = n_0^{\mathfrak{s}}\rho^{\mathfrak{s}R}$ denotes the initial partial density of the solid constituent.
In the following, let us look at the momentum balance of the fluid constituent in current configuration, [13]

$$\begin{aligned} &\rho^{\mathfrak{f}}\{(\mathbf{w}_{\mathfrak{f}} + \mathbf{v}_{\mathfrak{s}})' + [\mathrm{grad}(\mathbf{v}_{\mathfrak{s}} + \mathbf{w}_{\mathfrak{f}})]\,\mathbf{w}_{\mathfrak{f}}\} \\ &\qquad = -\,\mathrm{grad}(n^{\mathfrak{f}}\,p) + \hat{\mathbf{p}}^{\mathfrak{f}} + \rho^{\mathfrak{f}}\,\mathbf{b}. \end{aligned} \tag{28}$$

Here, $\hat{\mathbf{p}}^{\mathfrak{f}}$ represents the interaction force describing the exchange of momentum between the solid and the fluid phase

$$\hat{\mathbf{p}}^{\mathfrak{f}} = p\,\mathrm{grad}\,n^{\mathfrak{f}} - \frac{(n^{\mathfrak{f}})^2\gamma^{\mathfrak{f}R}}{k^{\mathfrak{f}}}\mathbf{w}_{\mathfrak{f}}, \tag{29}$$

in which $\gamma^{\mathfrak{f}R}$ is the effective weight of the fluid, i. e. $\gamma^{\mathfrak{f}R} = \rho^{\mathfrak{f}R} g$ where g is the gravity constant, and $k^{\mathfrak{f}}$ is Darcy's permeability. Inserting (29) into (28), we get

$$\begin{aligned} &\rho^{\mathfrak{f}}\{(\mathbf{w}_{\mathfrak{f}} + \mathbf{v}_{\mathfrak{s}})' + [\mathrm{grad}(\mathbf{v}_{\mathfrak{s}} + \mathbf{w}_{\mathfrak{f}})]\,\mathbf{w}_{\mathfrak{f}}\} \\ &\qquad = -n^{\mathfrak{f}}\,\mathrm{grad}\;p - \frac{(n^{\mathfrak{f}})^2\,\gamma^{\mathfrak{f}R}}{k^{\mathfrak{f}}}\mathbf{w}_{\mathfrak{f}} + \rho^{\mathfrak{f}}\,\mathbf{b}. \end{aligned} \tag{30}$$

For the sake of simplicity, we restrict ourselves to isotropic and constant permeability. An evolution of the permeability depending on the deformation state of the solid matrix is not involved. Considering the develop of permeability depending on the deformation of the solid phase, the interested readers are referred to [42; 21].
In addition, the gradient operator in current configuration can be transported to reference configuration of the solid phase by

$$\mathrm{grad}\,p = (\mathrm{Grad}\,p)\,\mathbf{F}_{\mathfrak{s}}^{-1}. \tag{31}$$

By use of the relation (26), we get the balance of momentum of the fluid in the Lagrangian description of the solid phase

$$\begin{aligned} &\rho^{\mathfrak{f}R}\,(\mathbb{Q}' - \mathcal{J}\;\mathrm{Div}\,\mathbf{v}_{\mathfrak{s}}\,\mathbb{Q}) + (J_{\mathfrak{s}} - n_0^{\mathfrak{s}})\,\rho^{\mathfrak{f}R}\,\mathbf{v}_{\mathfrak{s}}' \\ &+ \rho^{\mathfrak{f}R}\,\mathrm{Grad}(\mathbf{v}_{\mathfrak{s}} + \mathcal{J}\,\mathbb{Q})\,(\mathbf{F}_{\mathfrak{s}}^{-1}\,\mathbb{Q}) \\ &= -(J_{\mathfrak{s}} - n_0^{\mathfrak{s}})\,\Big[\mathrm{Grad}\;\frac{\theta}{J_{\mathfrak{s}}}\Big]\,\mathbf{F}_{\mathfrak{s}}^{-1} - \frac{n^{\mathfrak{f}}\gamma^{\mathfrak{f}R}}{k^{\mathfrak{f}}}\mathbb{Q} \\ &+ (J_{\mathfrak{s}} - n_0^{\mathfrak{s}})\,\rho^{\mathfrak{f}R}\,\mathbf{b}. \end{aligned} \tag{32}$$

So far we have derived the balance equations of a two-phase hybrid model with the primary variables $\{\mathbf{v}_{\mathfrak{s}}, \mathbb{Q}, \theta\}$ in reference configuration of the solid phase. The model problem can be closed by a proper definition of boundary conditions and the associated initial values. Given the spatial domain $\Omega \in \mathbb{R}^k$ $(k = 1, 2, 3)$ in the undeformed state, the boundary of Ω is composed of a superposition of the solid and fluid part $\partial\Omega = \Gamma^{\mathfrak{s}} = \Gamma^{\mathfrak{f}}$. Each boundary is split into Neumann and Dirichlet parts, $\Gamma^{\mathfrak{i}} = \Gamma_N^{\mathfrak{i}} \cup \Gamma_D^{\mathfrak{i}}$ with $\Gamma_N^{\mathfrak{i}} \cap \Gamma_D^{\mathfrak{i}} = \emptyset$, i. e. $\mathfrak{i} \in \{\mathfrak{s}, \mathfrak{f}\}$. Let $\mathcal{I} = [t_0, T]$ be the temporal domain, the boundary conditions are given as

$$\begin{aligned} \mathbf{v}_{\mathfrak{s}} &= \bar{\mathbf{v}}_{\mathfrak{s}}, \quad \text{on } \Gamma_D^{\mathfrak{s}} \times \mathcal{I}, \\ \mathbf{P}\,\mathbf{N} &= \bar{\mathbf{P}}, \quad \text{on } \Gamma_N^{\mathfrak{s}} \times \mathcal{I}, \\ \mathbf{Q} \cdot \mathbf{N} &= \bar{Q}, \quad \text{on } \Gamma_N^{\mathfrak{f}} \times \mathcal{I}, \\ \theta &= \bar{p}, \quad \text{on } \Gamma_D^{\mathfrak{f}} \times \mathcal{I}, \end{aligned} \tag{33}$$

where $\mathbf{N}$ denotes the unit outward normal vector on the boundary. $\bar{\mathbf{v}}_{\mathfrak{s}}$ is boundary value the solid velocity defined on the reference configuration. $\bar{\mathbf{P}}$ and $\bar{Q}$ are the normal

traction applied on the mixture and the normal fluid flux through a unit surface of the undeformed solid matrix, respectively. $\bar{p}$ is fluid pressure function defined on the Dirichlet boundary of the fluid phase.
The associated initial conditions are given for

$$\begin{aligned} \mathbf{u}_{\mathfrak{s}}(\mathbf{X}_{\mathfrak{s}}, t_0) &= \mathbf{u}_{\mathfrak{s},0}(\mathbf{X}_{\mathfrak{s}}), \\ \mathbf{v}_{\mathfrak{s}}(\mathbf{X}_{\mathfrak{s}}, t_0) &= \mathbf{v}_{\mathfrak{s},0}(\mathbf{X}_{\mathfrak{s}}), \\ \theta(\mathbf{X}_{\mathfrak{s}}, t_0) &= \theta_0(\mathbf{X}_{\mathfrak{s}}). \end{aligned} \tag{34}$$

Further details concerning the model set-up and the derivation of the governing equations can be found in the literature [36; 37].
We denote that in the community of the TPM, it is usual to introduce the kinematic relation

$$\mathbf{v}_{\mathfrak{s}} = \mathbf{u}'_{\mathfrak{s}} \tag{35}$$

as an extra auxiliary equation to construct a four-field equation system with the primary variables $\{\mathbf{u}_{\mathfrak{s}}, \mathbf{v}_{\mathfrak{s}}, \mathbb{Q}, \theta\}$ and solved the resulting first-order system with an implicit numerical approach, e. g. the backward Euler method or others, [43]. Alternatively, it is also possible to solve a three-fields formulation with the primary variables $\{\mathbf{u}_{\mathfrak{s}}, \mathbb{Q}, \theta\}$ with the Newmark scheme [44]. However, both approaches are based on finite difference schemes, i. e. the Method of Lines (MOLs), which is often known as numerically inefficient.
In our previous work, we have investigated a space-time discontinuous Galerkin (DGT) approach for the solution strategy of incompressible porous mixtures with a four-field formulation [33]. However, due to the restriction of the flux treatment in the DGT method to time-dependent systems of first-order, a four-field formulation including the kinematic relation (35) as an extra governing equation is applied. It is obvious that by introducing the extra equation (35) in the governing set of equations, a larger system of algebraic equation is resulted, which increases the computational burden.
In the current work, we employ the so-called Embedded Velocity Integration (EVI) technique [34] to construct an equation system with the primary variables $\{\mathbf{v}_{\mathfrak{s}}, \mathbb{Q}, \theta\}$. The resulting equation system is composed of first-order equations, which can be solved by the flux based space-time discontinuous Galerkin method [33]. No extra auxiliary equation is introduced, which makes the approach very efficient for solving second-order time-dependent equations.

3 The EVI(α) formulation

We construct the space-time domain by adding the time axis orthogonal to the spatial domain, i. e. $Q = \Omega \times \mathcal{I}$. According to the discrete time interval $\mathcal{I}^n = [t_n, t_{n+1})$ $(0 \leq t_n < t_{n+1} \leq \mathcal{I}^n)$, we further define the space-time slab $Q^n = \Omega \times \mathcal{I}^n$. Analogical to conventional MOLs, the numerical solution is solved on each time-slab subsequently. Here, we apply the time-discontinuous Galerkin method [33] for the solution strategy, such that discontinuous approximations for the primary variables in time are employed. By use of the Embedded Velocity Integration (EVI) technique, the kinematic relation (35) is involved implicitly into the time-integration scheme. Hence, the second-order time-dependent problem with the unknown displacement field $\mathbf{u}_{\mathfrak{s}}(\mathbf{x}, t)$ can be transformed into a first-order one with the unknown velocities $\mathbf{v}_{\mathfrak{s}}(\mathbf{x}, t)$. After solving the first-order equation for the velocities, the displacement field is obtained explicitly in a post-processing step according to a consistent integration of the velocities. Analogical to the Newmark scheme, the computation starts with the given information, i. e. initial velocity and initial displacement. For each subsequent time step, the input information is the solution obtained at the end of the previous time slab. Note that the EVI technique is different to the conventional order-reduction one, where both the displacement and the velocity fields are solved as primary variables simultaneously. In a previous work, we proposed a high-order EVI method applied to elastic wave propagation problems [34]. Therein, an exact integration scheme for the displacement is proposed, such that no degeneration of the solutions was involved by the numerical integration. Convergence studies with respect to the simple model equation demonstrated the accuracy of the method. In the current work, a generalized EVI method is studied which allows for an implicit evaluation of the displacement. In comparison with the exact integration scheme, the implicit one implies more numerical dissipation, that contributes to the numerical stability of the overall solution. In addition, we introduce a stabilization factor α into the numerical integration scheme. Depending on the chosen values of the factor α, the stability of the overall solution can be enforced. This property is important in practical computations, such that without an extreme refinement of the discretization, the overall stability can be achieved by a simple modification of the integration scheme.
For the sake of completeness, we recall briefly the basic idea of the EVI method. The kinematic relation of a material point $\mathbf{X}_{\mathfrak{s}}$ reads

$$\mathbf{u}'_{\mathfrak{s}}(\mathbf{X}_{\mathfrak{s}}, t) = \mathbf{v}_{\mathfrak{s}}(\mathbf{X}_{\mathfrak{s}}, t), \quad t \in \mathcal{I}^n. \tag{36}$$

Integrating the above equation to an arbitrary time t, i. e. $t_n < t < t_{n+1}$, we obtain

$$\mathbf{u}_{\mathfrak{s}}(\mathbf{X}_{\mathfrak{s}}, t) = \tilde{\mathbf{u}}_{\mathfrak{s},n}(\mathbf{X}_{\mathfrak{s}}) + \mathbf{g}_{\mathbf{u},\mathfrak{s}}(\mathbf{X}_{\mathfrak{s}}, t), \tag{37}$$

where $\mathbf{g}_{\mathbf{u},\mathfrak{s}}(\mathbf{X}_{\mathfrak{s}}, t)$ denotes the time integral of the velocity from the lower bound of the interval t_n to the actual time t $(t < t_{n+1})$

$$\mathbf{g}_{\mathbf{u},\mathfrak{s}}(\mathbf{X}_{\mathfrak{s}}, t) = \int_{t_n}^{t} \mathbf{v}_{\mathfrak{s}}(\mathbf{X}_{\mathfrak{s}}, \tau)\, \mathrm{d}\tau, \qquad (t_n < t < t_{n+1}), \tag{38}$$

and $\tilde{\mathbf{u}}_{\mathfrak{s},n}$ represents the continuous distribution of the solid displacement at t_n

$$\tilde{\mathbf{u}}_{\mathfrak{s},n}(\mathbf{X}_{\mathfrak{s}}) = \begin{cases} \mathbf{u}_{\mathfrak{s},0}(\mathbf{X}_{\mathfrak{s}}), & n = 0, \\ \mathbf{u}_{\mathfrak{s}}(\mathbf{X}_{\mathfrak{s}}, t_n), \text{ otherwise.} \end{cases} \tag{39}$$

Herein, $\mathbf{u}_{\mathfrak{s},0}$ is the given initial condition of the solid displacement and $\mathbf{u}_{\mathfrak{s}}(\mathbf{X}_{\mathfrak{s}}, t_n)$ represents the discrete value of $\mathbf{u}_{\mathfrak{s}}$ at the time t_n. In practise, this value represents the numerical solution obtained at the end of the previous time-slab Q^{n-1}.
Next, the integral of $\mathbf{g}_{\mathbf{u},\mathfrak{s}}$ of the material point located at $\mathbf{X}_{\mathfrak{s}}$ over the time interval $\mathcal{I}^n$ can be evaluated by applying the Gauss quadrature

$$\int_{\mathcal{I}^n} \mathbf{g}_{\mathbf{u},\mathfrak{s}}(\mathbf{X}_{\mathfrak{s}}, t)\,\mathrm{d}t = J \sum_{i=1}^{\mathrm{GP}} w_i\, \mathbf{g}^*_{\mathbf{u},\mathfrak{s}}(\mathbf{X}_{\mathfrak{s}}, \xi_i), \tag{40}$$

in which GP is the number of Gaussian points, w_i and ξ_i are the corresponding weight and the position of the ith Gaussian point, respectively. $J = (t_{n+1} - t_n)/2$ denotes the Jacobian and $\mathbf{g}^*_{\mathbf{u},\mathfrak{s}}(\mathbf{X}_{\mathfrak{s}}, \xi_i)$ represents the integration of the velocity from -1 to a fixed position of a Gaussian point ξ_i, which can be again evaluated by the Gauss quadrature as

$$\begin{aligned} \mathbf{g}^*_{\mathbf{u},\mathfrak{s}}(\mathbf{X}_{\mathfrak{s}}, \xi_i) &= J \int_{-1}^{\xi_i} \mathbf{v}_{\mathfrak{s}}(\mathbf{X}_{\mathfrak{s}}, \xi)\,\mathrm{d}\xi \\ &= J\, J_{\xi_i} \sum_{j=1}^{\mathrm{GP}} w_j\, \mathbf{v}_{\mathfrak{s}}(\mathbf{X}_{\mathfrak{s}}, \xi_i^j). \end{aligned} \tag{41}$$

Herein, $J_{\xi_i} = (\xi_i + 1)/2$ denotes the Jacobian of the mapping from the interval $[-1, \xi_i]$ to the canonical interval $[-1, +1]$. ξ_i^j is the position of the jth Gaussian point in the interval $[-1, \xi_i]$, i. e. $\xi_i^j = J_{\xi_i}(\xi_j + 1) - 1$. Inserting Eq. (41) into Eq. (40), we obtain

$$\begin{aligned} &\int_{\mathcal{I}^n} \mathbf{g}_{\mathbf{u},\mathfrak{s}}(\mathbf{X}_{\mathfrak{s}}, t)\,\mathrm{d}t \\ &\qquad = J^2 \sum_{i=1}^{\mathrm{GP}} \left[w_i\, J_{\xi_i} \sum_{j=1}^{\mathrm{GP}} \left(w_j\, \mathbf{v}_{\mathfrak{s}}(\mathbf{X}_{\mathfrak{s}}, \xi_i^j) \right) \right]. \end{aligned} \tag{42}$$

Obviously, depending on the order of the temporal approximation of $\mathbf{v}_{\mathfrak{s}}$, as long as enough Gauss points are chosen, Eq. (42) can be evaluated exactly.
Note that (37) represents an exact expression of $\mathbf{u}_{\mathfrak{s}}$, such that the integral of $\mathbf{g}_{\mathbf{u},\mathfrak{s}}$ is evaluated at the actual time t. We remark, according to an implicit evaluation of $\mathbf{u}_{\mathfrak{s}}$, we have

$$\mathbf{u}_{\mathfrak{s}}(\mathbf{X}_{\mathfrak{s}}, t) = \tilde{\mathbf{u}}_{\mathfrak{s},n}(\mathbf{X}_{\mathfrak{s}}) + \mathbf{g}_{\mathbf{u},\mathfrak{s}}(\mathbf{X}_{\mathfrak{s}}, t_{n+1}). \tag{43}$$

Herein, $\mathbf{g}_{\mathbf{u},\mathfrak{s}}(\mathbf{X}_{\mathfrak{s}}, t_{n+1})$ represents the integral of velocity $\mathbf{v}_{\mathfrak{s}}(\mathbf{X}_{\mathfrak{s}})$ over the whole time interval $\mathcal{I}^n$. Thus, $\mathbf{g}_{\mathbf{u},\mathfrak{s}}(\mathbf{X}_{\mathfrak{s}})$ can be evaluated directly by the ansatz of the velocity $\mathbf{v}_{\mathfrak{s}}$

$$\mathbf{g}_{\mathbf{u},\mathfrak{s}}(\mathbf{X}_{\mathfrak{s}}, t_{n+1}) = J \sum_{j=1}^{\mathrm{GP}} w_j\, \mathbf{v}_{\mathfrak{s}}(\mathbf{X}_{\mathfrak{s}}, \xi_j). \tag{44}$$

According to the implicit approach, the integration of $\mathbf{g}_{\mathbf{u},\mathfrak{s}}(\mathbf{X}_{\mathfrak{s}}, t)$ over the interval $\mathcal{I}^n$ can be expressed in a similar way

$$\begin{aligned} \int_{\mathcal{I}^n} \mathbf{g}_{\mathbf{u},\mathfrak{s}}(\mathbf{X}_{\mathfrak{s}}, t)\,\mathrm{d}t &= \int_{\mathcal{I}^n} \mathbf{g}_{\mathbf{u},\mathfrak{s}}(\mathbf{X}_{\mathfrak{s}}, t_{n+1})\,\mathrm{d}t \\ &= J^2 \sum_{i=1}^{\mathrm{GP}} \left[w_i \sum_{j=1}^{\mathrm{GP}} \left(w_j\, \mathbf{v}_{\mathfrak{s}}(\mathbf{X}_{\mathfrak{s}}, \xi_j) \right) \right]. \end{aligned} \tag{45}$$

It has to be remarked, that the evaluation of Eq. (44) is formally identical to the evaluation of the primary variable $\mathbf{v}_{\mathfrak{s}}(\mathbf{X}_{\mathfrak{s}}, t)$ over the time interval $\mathcal{I}^n$. Implicit solutions are achieved by evaluating the displacement $\mathbf{u}_{\mathfrak{s}}(\mathbf{X}_{\mathfrak{s}}, t)$ at the end of the interval, rf. Eq. (43).
As it is well known, the inherent numerical dissipation of implicit approaches contributes to the stability of the overall solution. However, too strong numerical dissipation also affects the accuracy of the solution. Therefore, it is natural to introduce a α factor, which enables an easy control of the integration scheme, such that

$$\mathbf{u}_{\mathfrak{s}}(\mathbf{X}_{\mathfrak{s}}, t) = \tilde{\mathbf{u}}_{\mathfrak{s},n}(\mathbf{X}_{\mathfrak{s}}) + \mathbf{g}^{\alpha}_{\mathbf{u},\mathfrak{s}}(\mathbf{X}_{\mathfrak{s}}, t), \qquad (0 \le \alpha \le 1), \tag{46}$$

with

$$\mathbf{g}^{\alpha}_{\mathbf{u},\mathfrak{s}}(\mathbf{X}_{\mathfrak{s}}, t) = \begin{cases} \displaystyle\int_{t_n}^{t} \mathbf{v}_{\mathfrak{s}}(\mathbf{X}_{\mathfrak{s}}, \tau)\,\mathrm{d}\,\tau, & \text{if } \alpha = 0, \text{(exact)}, \\ \displaystyle\int_{t_n}^{t_{n+1}} \mathbf{v}_{\mathfrak{s}}(\mathbf{X}_{\mathfrak{s}}, \tau)\,\mathrm{d}\,\tau, & \text{if } \alpha = 1, \text{(implicit)}. \end{cases} \tag{47}$$

The choice of $0 < \alpha < 1$ leads to a method which lies between the implicit and the exact approach. Further details concerning the derivation of the stability parameter α are given in the appendix.
It is obvious that the construction of the deformation gradient $\mathbf{F}_{\mathfrak{s}}$ can be directly derived from the solid displacement $\mathbf{u}_{\mathfrak{s}}$. Therefore, analog to Eq. (46), we derive

$$\mathbf{F}_{\mathfrak{s}}(\mathbf{X}_{\mathfrak{s}}, t) = \tilde{\mathbf{F}}^n_{\mathfrak{s}}(\mathbf{X}_{\mathfrak{s}}) + \mathbf{F}^{\alpha}_{\mathbf{g}}(\mathbf{X}_{\mathfrak{s}}, t), \tag{48}$$

with

$$\tilde{\mathbf{F}}^n_{\mathfrak{s}}(\mathbf{X}_{\mathfrak{s}}) = \mathbf{I} + \mathrm{Grad}\, \tilde{\mathbf{u}}_{\mathfrak{s},n}(\mathbf{X}_{\mathfrak{s}}), \tag{49}$$

$$\mathbf{F}^{\alpha}_{\mathbf{g}}(\mathbf{X}_{\mathfrak{s}}, t) = \mathbf{I} + \mathrm{Grad}\, \mathbf{g}^{\alpha}_{\mathbf{u},\mathfrak{s}}(\mathbf{X}_{\mathfrak{s}}, t). \tag{50}$$

Analogically, the right Cauchy-Green tensor $\mathbf{C}_{\mathfrak{s}}$ as well as the second Piola Kirchhoff tensor of the solid phase $\mathbf{S}_{\mathrm{E}}^{\mathfrak{s}}$ (rf. (23)) can be computed correspondingly.
So far we have discussed the temporal integration of the displacement fields and its related quantities with respect to a single material point $\mathbf{X}_{\mathfrak{s}}$. As long as the complete approximation of the unknown quantities is available, the space-time integration can be solved straight forwardly by evaluating the Gauss quadrature values in the space-time domain.
In the next section, we proceed with the finite element variational form of the space-time discontinuous Galerkin method. As stated before, the resulting set of first-order time-dependent equations is solved for the primary unknowns $\{\mathbf{v}_{\mathfrak{s}}, \mathbb{Q}, \theta\}$. Nevertheless, it has to be mentioned, that the idea of embedding the displacement field as the integral of the velocity is independent of the chosen time-stepping approach. The EVI technique can be applied to other space-time Galerkin methods as long as a finite element approximation of the velocity in the time domain is available, e. g. [25; 45] etc. For a time-difference scheme, e. g. the Euler method or the Newmark method etc., since there exists no complete approximation of the velocity field in the time domain[3], it is not possible to apply a consistent integration of the velocity and displacement fields over the time interval. Thus, the MOL approaches are not suitable for the application of the EVI technique.

4 Weak form and Space-time finite element formulation

In the next, we discuss the weak form used in a space-time Galerkin formulation. According to the DGT method, discontinuous approximations in time are applied. The consistency over the time interval is enforced weakly by the flux treatment. The *upwind* flux at discrete time level t_n is defined as [33; 46]

$$[\breve{\bullet}]_n = \begin{cases} [\bullet]_0, \text{ if } \quad n = 0, \\ [\bullet]_n^-, \text{ otherwise,} \end{cases} \qquad [\bullet]_n^- = \lim_{\epsilon \to 0^+} [\bullet](\mathbf{X}_{\mathfrak{s}}, t_n - \epsilon), \tag{51}$$

where $[\bullet] = \{\mathbf{v}_{\mathfrak{s}}, \mathbb{Q}, \theta\}$.
The weak form of the mass balance is obtained by multiplying Eq. (17) with a test function $\delta\theta$ and integrating over Q^n

$$\begin{aligned} &\int_{Q^n} \Big\{ -\frac{n^{\mathfrak{f}}}{K^{\mathfrak{f}}}\theta\,\delta\theta' + \big(1 - \frac{n^{\mathfrak{f}}}{K^{\mathfrak{f}}}\frac{\theta}{J_{\mathfrak{s}}}\big)\,\mathrm{Div}\,\mathbf{v}_{\mathfrak{s}}\,\delta\theta \\ &- (\mathbf{F}_{\mathfrak{s}}^{-1}\,\mathbb{Q})\cdot\mathrm{Grad}\,\delta\theta\Big\}\,\mathrm{d}Q + \int_{\Omega_0}\frac{n^{\mathfrak{f}}}{K^{\mathfrak{f}}}\theta_{n+1}^-\,\delta\theta\,\mathrm{d}V \\ &= \int_{\Omega_0}\frac{n^{\mathfrak{f}}}{K^{\mathfrak{f}}}\breve{\theta}\,\delta\,\theta\,\mathrm{d}A + \int_{\Gamma_N\times\mathcal{I}^n}\bar{Q}\,\delta\theta\,\mathrm{d}A\,\mathrm{d}t. \end{aligned} \tag{52}$$

Herein, we have applied the integration by parts in time to achieve the terms that act only on the borders t_n and t_{n+1} of the time interval.
Analogically, by multiplying Eq. (27) with a test function $\delta\mathbf{v}_{\mathfrak{s}}$ and subsequently integrating over the time-slab Q^n, we get the weak form of the mass balance of the mixture as

$$\begin{aligned} &\int_{Q^n}\Big\{ -\big\{\big[\rho_0^{\mathfrak{s}} + (J_{\mathfrak{s}} - n_0^{\mathfrak{s}})\rho^{\mathfrak{f}R}\big]\,\mathbf{v}_{\mathfrak{s}} + \rho^{\mathfrak{f}R}\mathbb{Q}\big\}\cdot\delta\mathbf{v}_{\mathfrak{s}}' \\ &- \rho^{\mathfrak{f}R}\big\{\mathcal{J}\,\mathrm{Div}\,\mathbf{v}_{\mathfrak{s}}\,\mathbb{Q} - \mathrm{Grad}(\mathbf{v}_{\mathfrak{s}} + \mathcal{J}\,\mathbb{Q})\,(\mathbf{F}_{\mathfrak{s}}^{-1}\,\mathbb{Q})\big\}\cdot\delta\mathbf{v}_{\mathfrak{s}} \\ &+ (\mathbf{P} - \theta\,\mathbf{F}_{\mathfrak{s}}^{-T}) : \mathrm{Grad}\,\mathbf{v}_{\mathfrak{s}}\Big\}\,\mathrm{d}Q \\ &+ \int_{\Omega_0}\Big\{\,[\rho_0^{\mathfrak{s}} + (J_{\mathfrak{s}} - n_0^{\mathfrak{s}})]\,\mathbf{v}_{\mathfrak{s},n+1}^- + \rho^{\mathfrak{f}R}\,\mathbb{Q}_{n+1}^-\Big\}\cdot\delta\mathbf{v}_{\mathfrak{s}}\,\mathrm{d}V \\ &= \int_{\Omega_0}\Big\{\,[\rho_0^{\mathfrak{s}} + (J_{\mathfrak{s}} - n_0^{\mathfrak{s}})]\,\breve{\mathbf{v}}_{\mathfrak{s}} + \rho^{\mathfrak{f}R}\,\breve{\mathbb{Q}}\Big\}\cdot\delta\mathbf{v}_{\mathfrak{s}}\,\mathrm{d}V \\ &+ \int_{\Gamma_N\times\mathcal{I}^n}\bar{\mathbf{P}}\cdot\delta\mathbf{v}_{\mathfrak{s}}\,\mathrm{d}A\,\mathrm{d}t. \end{aligned} \tag{53}$$

Here, $\bar{\mathbf{P}}$ is the external force acting on the mixture.
The weak form of the momentum balance of the fluid phase is derived by multiplying (32) with the test function $\delta\mathbb{Q}$ and in turn integrating over Q^n

$$\begin{aligned} &\int_{Q^n}\Big\{ -[\mathbb{Q} + (J_{\mathfrak{s}} - n_0^{\mathfrak{s}})\,\mathbf{v}_{\mathfrak{s}}]\cdot\delta\mathbb{Q}' \\ &- \Big[\mathcal{J}\;\mathrm{Div}\,\mathbf{v}_{\mathfrak{s}}\,\mathbb{Q} - \mathrm{Grad}(\mathbf{v}_{\mathfrak{s}} + \mathcal{J}\mathbb{Q})\,(\mathbf{F}_{\mathfrak{s}}^{-1}\,\mathbb{Q})\Big]\cdot\delta\mathbb{Q} \\ &+ \frac{J_{\mathfrak{s}} - n_0^{\mathfrak{s}}}{\rho^{\mathfrak{f}R}}\Big[\mathrm{Grad}\,\frac{\theta}{J_{\mathfrak{s}}}\,\mathbf{F}_{\mathfrak{s}}^{-1} + \frac{n^{\mathfrak{f}}\gamma^{\mathfrak{f}R}}{k^{\mathfrak{f}}}\mathbb{Q}\Big]\cdot\delta\mathbb{Q}\Big\}\,\mathrm{d}Q \\ &+ \int_{\Omega_0}\Big[\mathbb{Q}_{n+1}^- + (J_{\mathfrak{s}} - n^{\mathfrak{f}})\,\mathbf{v}_{\mathfrak{s},n+1}^-\Big]\cdot\delta\mathbb{Q}\,\mathrm{d}V \\ &= \int_{\Omega_0}\Big[\breve{\mathbb{Q}} + (J_{\mathfrak{s}} - n_0^{\mathfrak{s}})\,\breve{\mathbf{v}}_{\mathfrak{s}}\Big]\cdot\delta\mathbb{Q}\,\mathrm{d}V \\ &+ \int_{Q^n}(J_{\mathfrak{s}} - n_0^{\mathfrak{s}})\,\mathbf{b}\cdot\delta\mathbb{Q}\,\mathrm{d}Q. \end{aligned} \tag{54}$$

[3] For the finite difference method, only quantities at discrete time level t_n are available.

Note that due to the mathematical character of the governing set of equations, cf. remarks in [47], quadratic shape functions are chosen for the spatial approximations of the solid phase variables $\mathbf{v}_{\mathfrak{s}}$, while linear ones are selected for fluid phase unknowns $\mathbb{Q}$ and θ.
After solving the set of equations for the primary variables $\{\mathbf{v}_{\mathfrak{s}}, \mathbb{Q}, \theta\}$, the solid displacement $\mathbf{u}_{\mathfrak{s}}$ is computed subsequently in a post-processing step

$$\mathbf{u}_{\mathfrak{s},n+1} = \tilde{\mathbf{u}}_{\mathfrak{s},n} + \mathbf{g}_{\mathbf{u},\mathfrak{s}}(\mathbf{x}, t_{n+1}). \tag{55}$$

The deformation gradient $\mathbf{F}_{\mathfrak{s}}^{n+1}$ must be updated accordingly

$$\mathbf{F}_{\mathfrak{s}}^{n+1} = \mathbf{I} + \operatorname{Grad} \mathbf{u}_{\mathfrak{s},n+1}. \tag{56}$$

In order to solve the set of equations efficiently, the linearization of the weak forms is inevitable. In the current work, the nonlinear set of equations is solved by a global Newton-Raphson scheme, which ensures quadratic convergence [40; 48]. In this context, it should be remarked that the consistent linearization of the EVI method with respect to the Lagrangian formulation presented in Sect. 2 is much simpler than the respective linearization with respect to the current configuration.

5 Numerical experiments

Next, we present one- and two-dimensional numerical experiments calculated by the EVI method. For the reason mentioned before, cf. [47], quadratic trial- and test-functions in space are chosen for $\mathbf{v}_{\mathfrak{s}}$ and linear ones are used for $\mathbb{Q}$ and θ. Different orders of polynomials in time for the different primary variables are possible, but not investigated here. The influence of the stabilization parameter α is investigated. A detailed convergence study with respect to a simple model equation was given in [34]. Therein, the numerical experiment of the simple elastic wave equation demonstrates a convergence rate of $O(p+1)$ for the velocities, and a slightly higher convergence rate for the displacement field if exact integration is applied for the velocity-displacement relation. Due to the complexity of the multiphase system, a direct determination of the wave velocity is not available. In the following examples, the size of the time step is chosen in such a way that the overall stability of the numerical solution is guaranteed.

5.1 Porous matrix under step load

In the first example, we perform a one-dimensional consolidation test. The geometry and the boundary conditions of the specimen are shown in Fig. 1. The soil tube is saturated by a fluid with the compressibility $K^{\mathfrak{f}} = 1.0 \times 10^9$ Pa, i. e. water. The effective density of the solid is $\rho^{\mathfrak{s}R} = 2000$ kg/m^3, and the initial effective

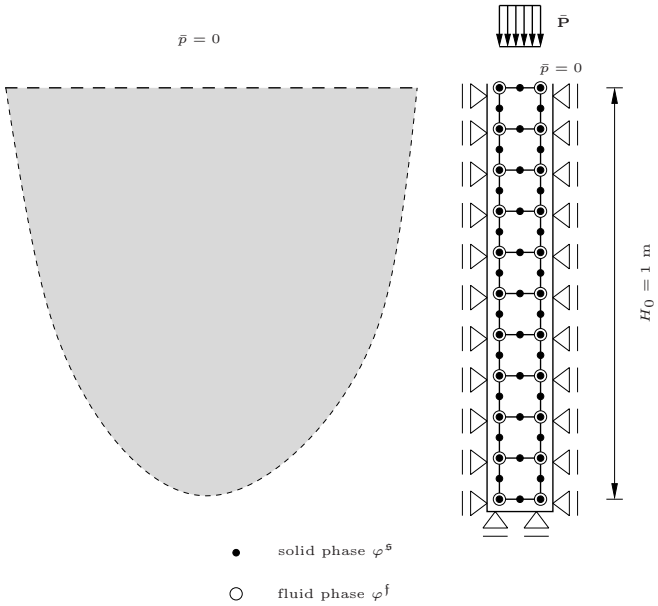

Fig. 1 Geometry of a one-dimensional column and the spatial discretization.

density of the fluid is $\rho_0^{\mathfrak{f}R} = 1000$ kg/m^3. Both Lamé constants of the solid skeleton are $\lambda = 8375$ kPa and $\mu = 5583$ kPa. The initial porosity of the specimen is $n_0^{\mathfrak{f}} = 0.33$ and the Darcy permeability is $k^{\mathfrak{f}} = 10^{-4}$ m/s. For the problem at hand, due to the fact that the fluid compressibility is much larger than the structural compressibility of the solid skeleton, the solid and the fluid constituents can be considered to be materially incompressible. A compression of the mixture is only possible due to a fluid flux moving relative to the deforming skeleton.
At first, a step load $\bar{\mathbf{P}}(t) = 3$ kPa is applied to the drained upper surface. Here, the deformation of the solid skeleton is within the linear regime, whereas the analytical settlement for the steady state, i. e. $t \to \infty$ can be directly achieved via, cf. [17].

$$\Delta H = \frac{\bar{\mathbf{P}}(t)\, H_0}{M_c}, \quad \text{and} \quad M_c = \lambda + 2\,\mu, \tag{57}$$

in which M_c is known as the constrained modulus of the solid skeleton. Fig. 2 show the numerical results computed via the exact EVI ($\alpha = 0$) method with different temporal discretizations Δt. We observe that even if the displacement fields of both computations, $\Delta t = 0.01$ s and $\Delta t = 0.001$ s, converge asymptotically to the analytical settlement, in the diagram of the corresponding velocities, strong oscillations are observed in both experiments, i. e. $\Delta t = 0.01$ s and $\Delta t = 0.001$ s. These unphysical oscillations diminish with the pass of time. We denote that a even larger time step, i. e. $\Delta t = 0.1$ s, leads to an unstable solution. such that the spurious oscillation becomes dominant.
We remark that these spurious oscillations are closely related to the physical characteristic of the consolidation

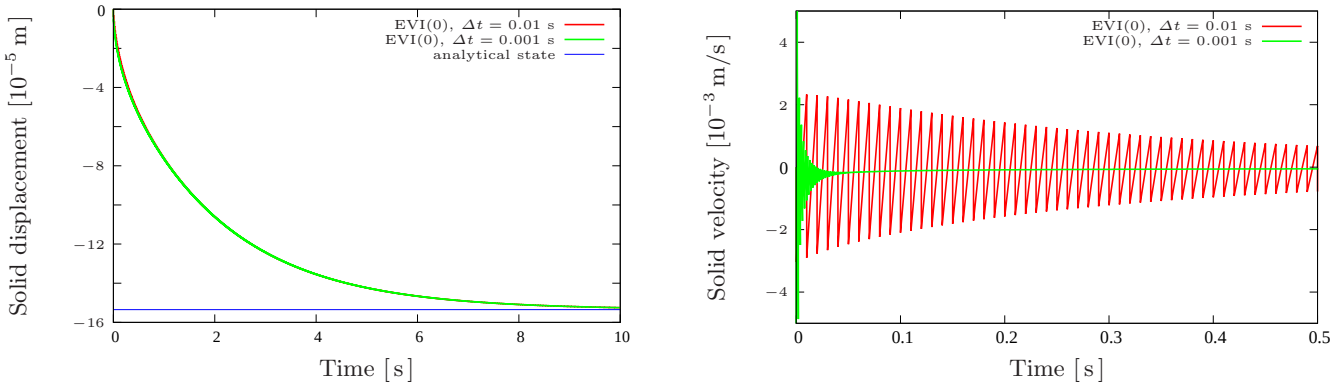

Fig. 2 Solid displacement (left) and solid velocity (right) at the top of the specimen computed by the EVI ($\alpha = 0$) method.

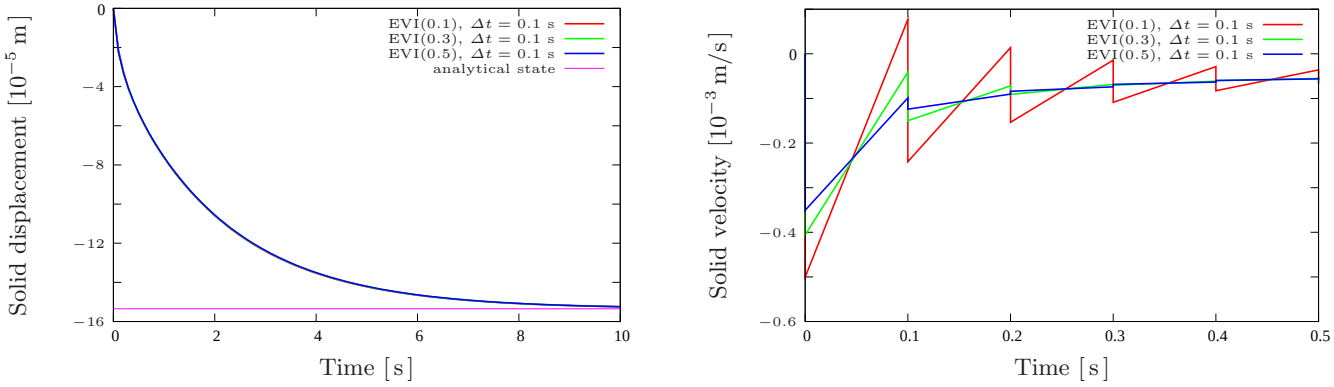

Fig. 3 Solid displacement (left) and solid velocity (right) at the top of the specimen computed by the EVI ($\alpha > 0$) methods.

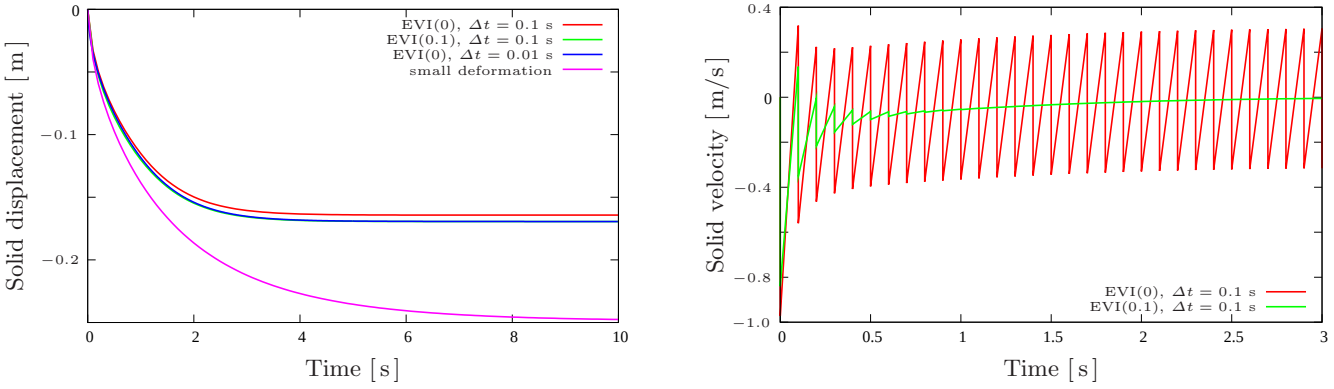

Fig. 4 Solid displacement (left) computed by the EVI(0) method at finite deformation and small deformation cases and velocity (right) at finite deformation.

process. Due to the drained condition $\bar{p} = 0$ on the upper boundary of the sample, the consolidation process begins with a extremely steep gradient in the pore pressure field close to this drained boundary, which results in steep increasement in the both velocity fields, i. e. solid velocity $\mathbf{v}_\mathfrak{s}$ and seepage velocity $\mathbf{w}_\mathfrak{f}$. Thus, an insufficient spatial mesh resolution in the vicinity of the drained boundary leads to spurious oscillation in the numerical results. Furthermore, depending on the accuracy of the time-stepping method, these unphysical oscillations may propagate in time and pollute the complete computational domain. Such phenomena is analogical to the boundary-layer effect occurring in convection-dominated flow problems, whereby very fine discretization in the vicinity of the boundary-layer must be used in order to avoid these unphysical oscillations, cf. [49; 50; 51; 52]. However, it is usually known as numerical inefficient to refine the mesh discretization only to eliminate the spurious oscillations in the boundary-layer, such that various stabilization approaches have been developed. Among others, there

are the streamline upwind Petrov Galerkin (SUPG)[53], Galerkin Least Square methods (GLS) [54; 55], etc.
Next, we compute the same problem by the stabilized EVI method with $\alpha > 0$. Here, by use of the stabilized integration scheme, we are able to compute the problem with a larger time step length $\Delta t = 0.1$ s. Fig. 3 shows the settlement and the solid velocity at the top of the specimen obtained with $\alpha = 0.1, 0.3, 0.5$. Despite different choices of the α parameter, there is no significant difference in the displacement diagram, see Fig. 3 (left). However, difference arises in the solid velocity diagram, Fig. 3 (right). Here, different α values lead to different damping characteristics of the solution. Obviously, increasing the value of α, we increase the amount of the numerical dissipation in the numerical scheme, which further contributes to eliminating the discontinuities, i. e. jumps in the solution.
Next, in order to exam the response in the finite deformation range, we increase the external load to $\bar{\mathbf{P}} = 5$ MPa. Fig. 4 (left) shows the surface displacement of the consolidation obtained by the finite deformation and by the small deformation model (linear model). Obviously, the finite deformation model predicts a much smaller deformation state than the linear model. As for the finite deformation case, solutions computed by EVI($\alpha = 0$) and EVI($\alpha = 0.1$) with $\Delta t = 0.1$ s at finite deformations are depicted. As a reference, we plot the solution computed by the EVI(0) with a finer temporal discretization $\Delta t = 0.01$ s in the same figure, i. e. Fig. 4. It is observed that the solution of the stabilized EVI with $\alpha = 0.1$ coincides with the reference solution even better than that of the exact EVI method ($\alpha = 0$). Fig. 4 (right) shows the diagrams of the solid velocity obtained by the exact EVI(0) and stabilized EVI(0.1) with $\Delta t = 0.1$ s. We observe that there are strong oscillations in the EVI(0) solution, while the EVI($\alpha = 0.1$) leads to more smooth solution. It is seen that even with a very small α factor, the stability of the overall solution can be enhanced significantly. In this case, the accuracy of the solution is improved by a stabilized approach.

5.2 Porous matrix under partial compression

Next, we consider a two-dimensional dynamic consolidation problem that has been investigated in various publications in the past, cf. [33; 13; 17]. An instantaneous load $\bar{\mathbf{P}} = 15$ kPa is applied to the right half of the upper surface of a soil block, see Fig. 5. The sample has the physical dimensions of 10×10 m^2. The side walls and the bottom of the specimen are assumed to be rigid and undrained. The spatial domain is covered by a coarse mesh of 10×10 grids. The solid matrix is saturated by a nearly incompressible fluid with $K^{\mathfrak{f}} = 22$ GPa. The Lamé parameters of the porous matrix are $\lambda = 8.27$ GPa, $\mu = 5.6$ GPa. The density of the solid is $\rho^{\mathfrak{s}R} = 2700$ kg/m^3 and the initial density of the fluid is $\rho_0^{\mathfrak{f}R} = 1000$ kg/m^3. The initial porosity of the solid matrix is $n_0^{\mathfrak{f}} = 0.42$. In the present example, the quality of a local result is considered, i. e. the vertical component of the solid displacement $\mathbf{u}_{\mathfrak{s}}$ and the solid velocity $\mathbf{v}_{\mathfrak{s}}$ at point A, see Fig. 5.

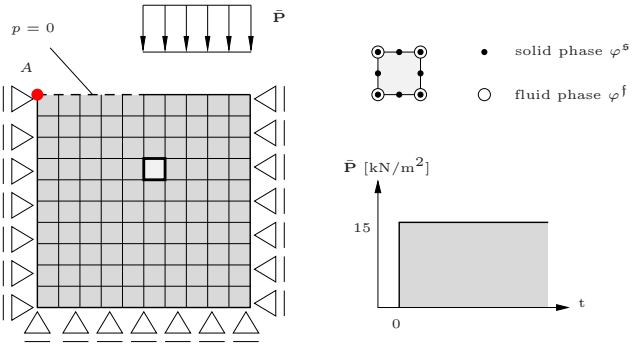

Fig. 5 Geometry and boundary conditions of the porous matrix as well as the spatial discretization and the external load

Fig. 6 shows results computed by the exact EVI($\alpha = 0$) method with linear polynomials in time. The solution is compared with the ones calculated by the three-stage implicit Runge-Kutta Method (Cash3(2))[56; 57] which is a second-order method. In Fig. 6, as for the coarse temporal discretization $\Delta t = 0.1$ s and $\Delta t = 0.05$ s, the EVI ($\alpha = 0$) leads to slightly better results than those obtained by the Cash3(2), in that less numerical damping in the amplitude is resulted. As for the fine discretization $\Delta t = 0.01$ s, both methods produce similar results. We denote that further refinements in Δt has also been tested but do not produce visible improvement in the plotted scale. It has to be mentioned, that the Cash3(2) approach is only suitable for the first-order time-dependent problem. Therefore, it requires the four-fields formulation with the primary variables $\{\mathbf{u}_{\mathfrak{s}}, \mathbf{v}_{\mathfrak{s}}, \mathbb{Q}, \theta\}$. The total number of Degree of Freedoms (DOFs) sums up to 1727 per time step. However, by embedding the kinematic relation implicitly, the EVI method is suitable for a three-field formulation with the EVI method. Despite the extra unknowns in the time domain introduced by the discontinuous approximation in time, the total DOFs of the EVI approach turns out to be 2090. Moreover, since there are several internal calculation stages involved in the Cash3(2) scheme, we found out that with the same spatial and temporal discretizations, the computation time of the Cash3(2) is even slightly longer than the EVI approach.
Next, we compare the numerical effort of the EVI(α) method with the Time-Discontinuous Galerkin method (DGT) [33]. Same as the Cash3(2) scheme, the DGT approach can only handle first-order equations, such that a four-field formulation with the primary unknowns $\{\mathbf{u}_{\mathfrak{s}}, \mathbf{v}_{\mathfrak{s}}, \mathbb{Q}, \theta\}$ is applied. For the current discretization, i. e. 10×10 elements, and linear polynomials in time, the DGT formulation leads to 3454 DOFs per time slab (the

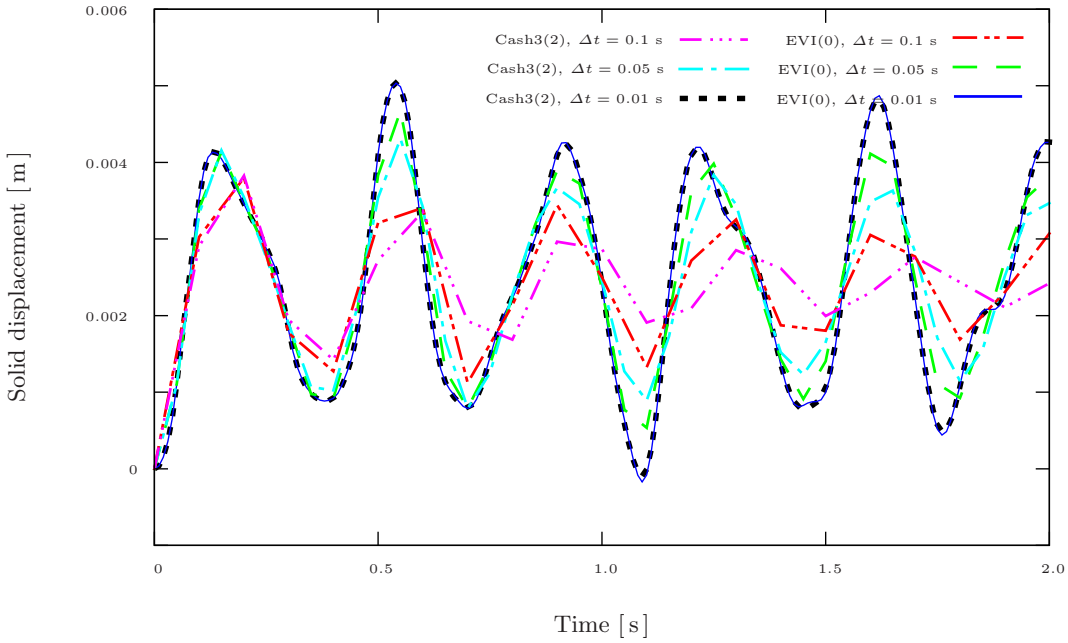

Fig. 6 Vertical solid displacement at point A obtained by the EVI($\alpha = 0$) and Cash3(2) methods.

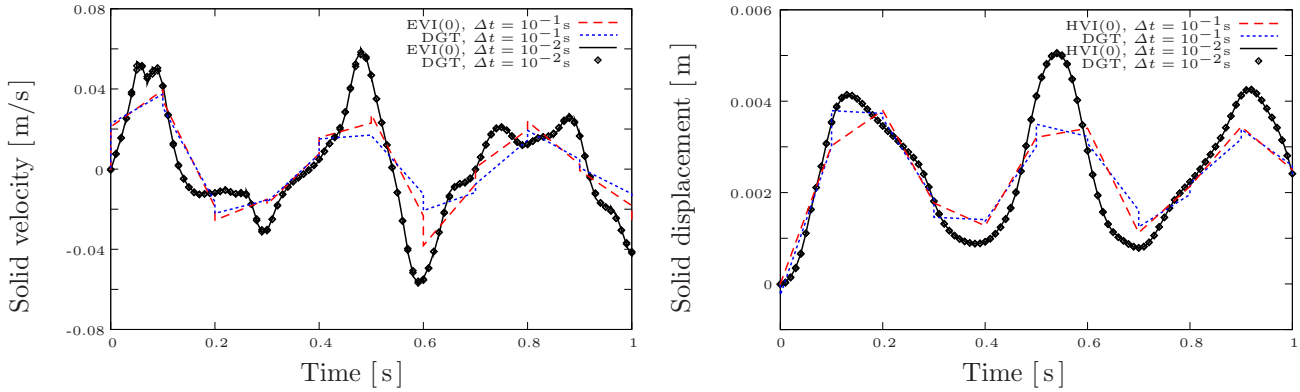

Fig. 7 Vertical solid velocity and displacement at point A, computed by the EVI($\alpha = 0$) method and the DGT method.

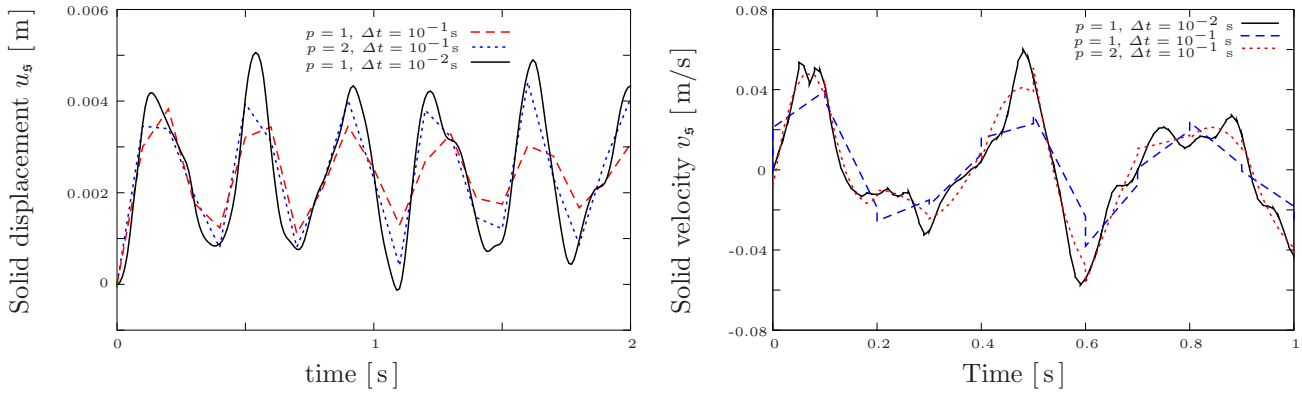

Fig. 8 Vertical solid displacement and velocity at point A, computed by the EVI($\alpha = 0$) method with linear ($p = 1$) and quadratic ($p = 2$) polynomials in time.

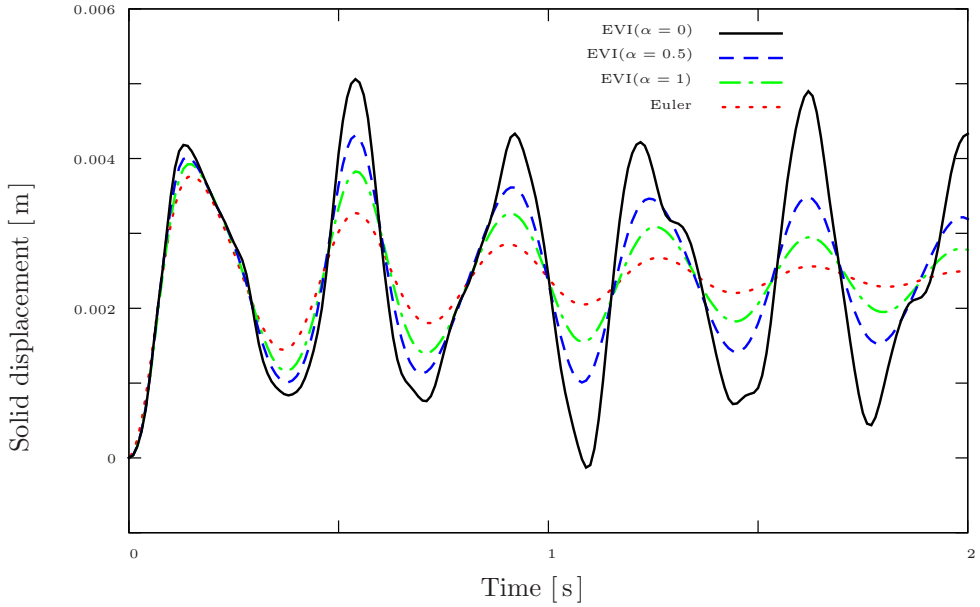

Fig. 9 Vertical solid displacement at point A, computed with the EVI(α) method. Different stabilization parameters α are investigated and the results are compared to those obtained by the backward Euler scheme at $\Delta t = 0.01$ s.

solid phase variables $\mathbf{u}_s$ and $\mathbf{v}_s$ are solved with quadratic polynomials in space while linear polynomials for the fluid phase variables $\mathbb{Q}$ and θ are employed). Fig. 7 shows the numerical solutions of the solid displacement and the velocity obtained by the DGT and by the exact EVI(0) method. In the results obtained with a coarse temporal discretization $\Delta t = 0.1$ s, obvious jumps are observed in the primary unknowns. Note that for the DGT method, both the solid displacement $\mathbf{u}_s$ and its velocity $\mathbf{v}_s$ are solved as primary variable, while for the EVI(0) method, only the solid velocity $\mathbf{v}_s$ is solved as primary unknown. Moreover, by use of the EVI method, since the displacement field is computed as integral of the velocity, its distribution is always continuous and smooth. In these diagrams, only the results at discrete time levels t_n are plotted. No interpolation concerning the integration of velocities in between the time levels t_n and t_{n+1} is concerned. With a refined time step size $\Delta t = 0.01$ s, both methods lead to similar results. No obvious jumps are observed on the plot scale. Moreover, we denote that the jumps shown in the numerical solutions can serve as an easy and reliable error indicator for an adaptive strategy [33].

In Fig. 8 we depict those results obtained by the exact EVI($\alpha = 0$) method with linear ($p = 1$) and quadratic ($p = 2$) polynomials in time. The size of the time step is fixed as $\Delta t = 0.1$ s. Again, as for the displacement, only the results at discrete time levels t_n are plotted, no interpolation within the time intervals is applied. Here, the advantage of the proposed space-time Galerkin method is highlighted. Increasing the polynomial order (p-refinement in time) or decreasing the size of the time-slab (h-refinement) leads to more accurate numerical solutions. Obviously, choosing quadratic polynomials in time results in a larger algebraic system of equations (3135 DOFs per time-slab) than those of linear polynomials in time (2090 DOFs per time-slab). However the extra effort caused by employing higher order polynomials in time can be compensated by allowing for a larger time step length without degenerate the accuracy of the solution.

At last, we investigate the influence of the stabilization parameter α. Fig. 9 shows the results computed by EVI(α) method with different values of the stabilization parameter α. Hereby, the spatial and temporal discretizations are kept fixed (10×10 elements in space and $\Delta t = 0.01$ s). To compare the effect of numerical damping, the solution calculated by the backward Euler scheme is depicted in the same figure. Comparing both implicit methods, the implicit EVI(1) method and the backward Euler scheme, the implicit EVI(α) method leads to even more accurate numerical results. Moreover, the choice of $\alpha = 0.5$ implies less numerical damping than the fully implicit approach ($\alpha = 1$), leading to less damped solution. According to this example, depending on the characteristics of the solution, the best results are achieved by the exact EVI(0) method. Nevertheless, according to the given numerical results, it is shown that the stabilization parameter α can serve as an effective quantity to adjust the effect of numerical damping in the EVI(α) method. Obviously, this property is essential for the applicability of the numerical approach in realistic applications.

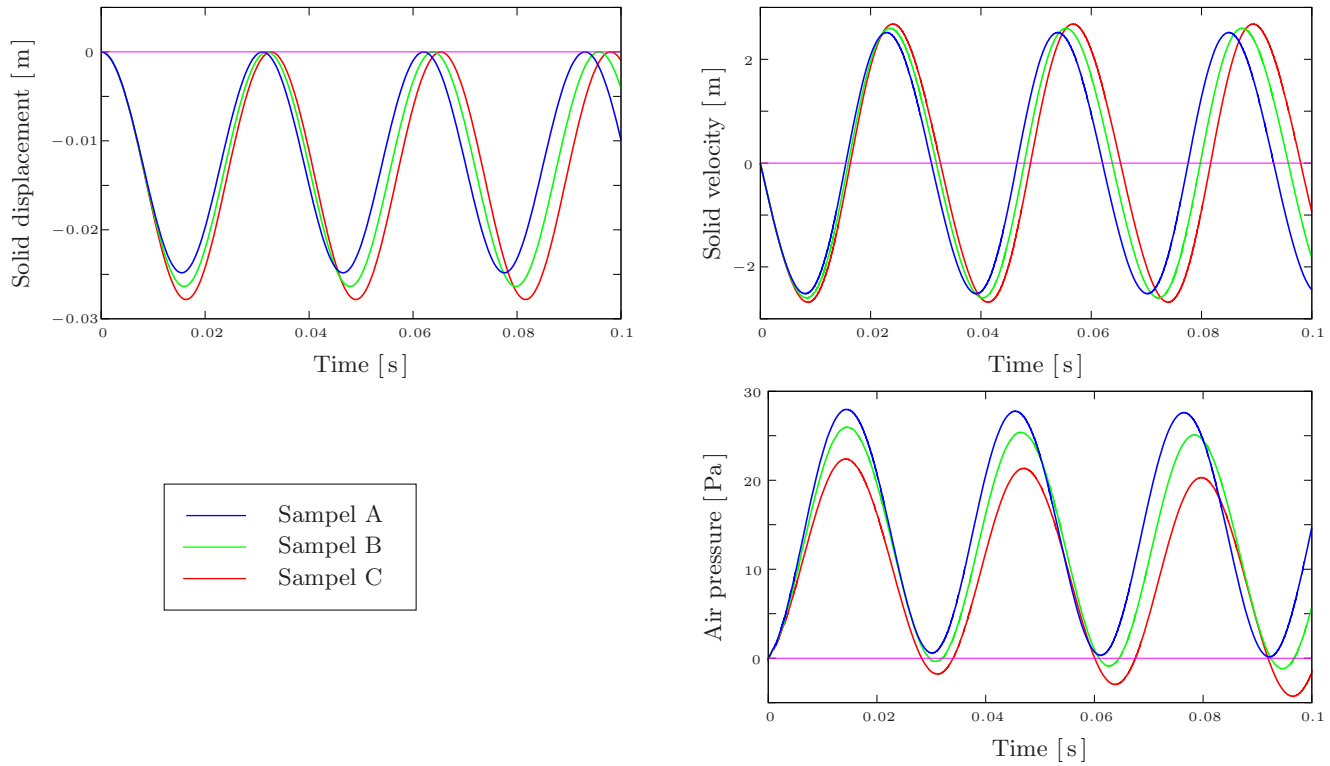

Fig. 11 Numerical solutions at the control point obtained for the sample A, B and C.

5.3 Two-dimensional impaction test on polyethylene foam

In the last example, we investigate impaction tests on air-filled polyethylene foams. The polyethylene foam is usually used as cushioning material in the crash test. A through understanding of the mechanical behavior of polyethylene foam under impact loading is important for the realistic design in practice. The effective density of the solid matrix is $\rho^{\mathfrak{s}R} = 910\ \mathrm{kg/m^3}$, with the both Lamé constants $\lambda = 375$ MPa, $\mu = 187.5$ MPa. The initial porosity of the foam is 0.95 and the Darcy permeability is $k^{\mathfrak{f}} = 6.722 \cdot 10^{-4}$ m/s, cf. [58]. The initial density of air is $\rho_0^{\mathfrak{f}R} = 1.21\ \mathrm{kg/m^3}$, with the compressibility $K^{\mathfrak{f}} = 0.133$ MPa. In order to simulate more realistic experiments, a rigid impervious plate with the line density $\tilde{m}$ is sticked to the foam, see Fig. 10. The rheological model of the current experiments can be considered as a nonlinear mass-spring-damper system. The deformation of the foam is modeled by the compressible Neo-Hooke material law [21; 22] together with the compressible air, while the energy dissipation is caused by the interaction force between the two phases. Moreover, in order to study the influence of the geometry of the specimen to the response of the transient load, we perform tests on samples of size $400 \times 100\ \mathrm{mm^2}$, $200 \times 100\ \mathrm{mm^2}$ and $100 \times 100\ \mathrm{mm^2}$ subsequently. By cutting the sample into small pieces, we increase the permeable surface of the sample with respect to the volume, which further influence the mechanical response of the sample. During the experiments, the bottom of the samples are undrained, while both side walls are assumed to be perfectly drained. A constant load $\bar{\mathbf{P}} = 0.1$ GPa is applied to the rigid plate of a line density $\tilde{m} = 7000\ \mathrm{kg/m}$. For the sake of simplicity, we don't consider the influence of the gravity force. We perform the numerical experiments with an uniform element size of $0.01 \times 0.0125 \times 0.0002$ [$\mathrm{m^2}$ s] in the space-time domain. Here, due to the fact that the matrix is highly compressible, according to the chosen discretization, no extra stability enforcement is necessary, such that we perform the computation with the exact EVI($\alpha = 0$) method. Furthermore, in order to reduce the size of the algebraic system, linear approximations in time are employed. Fig. 11 shows the development of solid displacements, solid velocity and pore pressure at the control point, see Fig. 10. It is observed that the amplitude in the solid phase variables (solid displacement and solid velocity) decreases with increase of the width of the sample. i. e. the amplitude of sample A is the largest, and that sample C is the smallest. In contract to the solid phase, in the fluid phase variable, i. e. pore pressure, we observe the complete inverse effect, such that the maximum pressure occurs in the largest sample, i. e. sample A, and the highest pressure of the sample B is greater than that of the sample C. Obviously, by increasing the width of the sample, we increase the length of the path way of the air flow to the per-

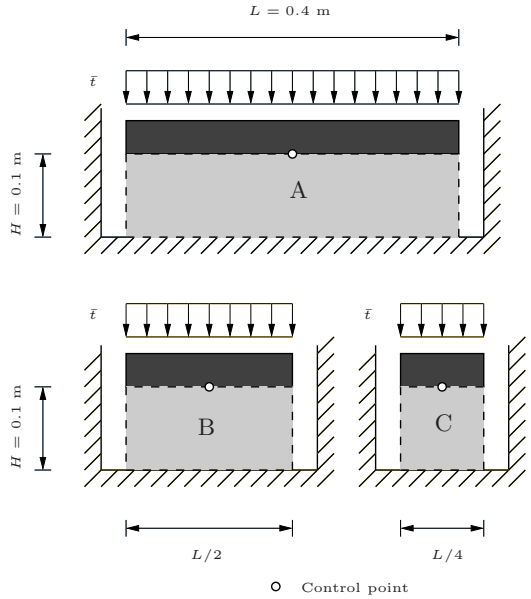

Fig. 10 Geometry and boundary conditions of sample A, B and C.

meable surface, which further results in a faster pore pressure development in the sample. As a consequence, the transient stiffness of the larger sample is greater than the smaller one, cf. [42]. In the present investigation, the evolution of the permeability depending on the porosity development, which is beyond the scope of this work, is not taken into account. Furthermore, within the short period of observation time, the decrease in the amplitude of the oscillations, as a consequence of the energy dissipation due to the interaction forces between the two phases, is not observed.

6 Conclusion

In the present work we investigate a three-fields formulation for the dynamics of multi-phase material at finite strains. The deformation of the solid skeleton is described by the modified Neo-Hooke material law [21]. The dynamical response of the porous material is modeled by the so-called EVI method introduced in [34]. The resulting three-fields equation system is solved on a coupled space-time finite element mesh with a Time Discontinuous Galerkin method (DGT), cf. [33]. The interelement consistency between the time-slabs is enforced weakly by an *upwind* flux treatment. Moreover, by introduction of the α parameter, we are able to control the numerical dissipation inherent to the EVI scheme, which further contribute to the stability of the overall solution. The feasibility of a stable Galerkin approach in the temporal domain is demonstrated by both p- and h-refinements. Furthermore, the efficiency of space-time Galerkin methods for coupled problems can be increased by adaptive strategies based on space-time error indicators. Obviously, such techniques have to be developed in the future.

Appendix

Without loss of generality, we consider a prototype equation like

$$\int_{Q^n} \mathbf{u}_\mathfrak{s} \cdot \delta\mathbf{v}_\mathfrak{s} \, \mathrm{d}Q = \int_{Q^n} \mathbf{g}^{\alpha}_{\mathbf{u},\mathfrak{s}} \cdot \delta\mathbf{v}_\mathfrak{s} \mathrm{d}Q + \Delta t \int_{\Omega} \tilde{\mathbf{u}}_{\mathfrak{s},n} \cdot \delta\mathbf{v}_\mathfrak{s} \, \mathrm{d}v. \quad (58)$$

Herein, we made use of the relation (46) and took into account that the value of $\tilde{\mathbf{u}}_{\mathfrak{s},n}$ was known with respect to the current interval $\mathcal{I}^n$. Next, for the sake of a simple notation, we consider Eq. (58) for spatially constant quantities. Therefore, only the temporal integration is investigated

$$\int_{\mathcal{I}^n} \mathbf{u}_\mathfrak{s} \cdot \delta\mathbf{v}_\mathfrak{s} \, \mathrm{d}t = \int_{\mathcal{I}^n} \mathbf{g}^{\alpha}_{\mathbf{u},\mathfrak{s}} \cdot \delta\mathbf{v}_\mathfrak{s} \, \mathrm{d}t + \Delta t \, \tilde{\mathbf{u}}_{\mathfrak{s},n} \cdot \delta\mathbf{v}_\mathfrak{s}. \quad (59)$$

According to the standard Gauss quadrature, the integral over $\mathcal{I}^n$ can be carried out as

$$\int_{\mathcal{I}^n} \mathbf{g}^{\alpha}_{\mathbf{u},\mathfrak{s}} \cdot \delta\mathbf{v}_\mathfrak{s} \, \mathrm{d}t = J \sum_{i=1}^{\mathrm{GP}} w_i \, \mathbf{g}^{*,\alpha}_{\mathbf{u},\mathfrak{s}}(\xi_i) \cdot \delta\mathbf{v}_\mathfrak{s}(\xi_i), \quad (60)$$

where GP denotes the number of Gaussian points, w_i is the weight and ξ_i is the position of the corresponding ith Gaussian point. J represents the Jacobian of the mapping from the time interval $[t_n, t_{n+1}]$ to the canonical interval $[-1, +1]$. Note that by employing the Gauss quadrature rule, only a discrete value of $\mathbf{g}^{*,\alpha}_{\mathbf{u},\mathfrak{s}}(\xi_i)$ regarding the individual Gaussian point ξ_i is considered

$$\mathbf{g}^{*,\alpha}_{\mathbf{u},\mathfrak{s}}(\xi_i) = J \int_{-1}^{\xi_i^\alpha} \mathbf{v}_\mathfrak{s}(\xi) \, \mathrm{d}\xi, \quad (1 \leq \alpha \leq 0). \quad (61)$$

We denote, as for an exact integration scheme ($\alpha = 0$), there exists $\xi_i^\alpha = \xi_i$, which is the position of ith Gaussian point, while for an implicit scheme, we have $\xi_i^\alpha = 1$, which is independent of the positions of the individual Gaussian points. Fig. 12 examplarily shows the exact and implicit integration scheme with a linear polynomial evaluated with one Gaussian point. It is obvious to see that the difference between an implicit and an exact integration of $\mathbf{g}^{*,\alpha}_{\mathbf{u},\mathfrak{s}}$ lies alone in the integration domain. With $\alpha = 1$ (implicit), the integration interval of $\mathbf{g}^{*,\alpha}_{\mathbf{u},\mathfrak{s}}$ covers the whole canonical interval $[-1, +1]$, while with $\alpha = 0$ only the integration from the lower bound of the canonical interval -1 to the current position of the Gaussian point ξ_i is involved. Taking the linear mapping, we further derive $\xi_i^\alpha = \alpha(1 - \xi_i) + \xi_i$, see Fig. 12.

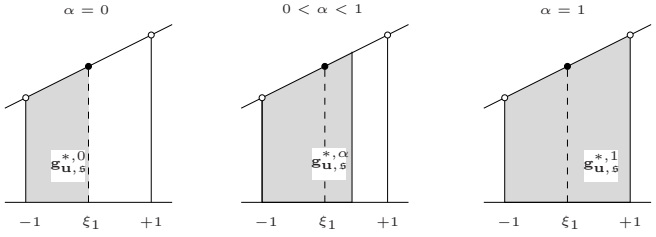

Fig. 12 Evaluation of $\mathbf{g}^1_{\mathbf{u},\mathfrak{s}}$, $\mathbf{g}^0_{\mathbf{u},\mathfrak{s}}$ and $\mathbf{g}^\alpha_{\mathbf{u},\mathfrak{s}}$ $(0 < \alpha < 1)$ with one Gaussian point example. ξ_1 is the position of Gaussian point.

Next, applying the Gauss quadrature rule for the evaluation of Eq. (61), we get rf. [34]

$$\mathbf{g}^{*,\alpha}_{\mathbf{u},\mathfrak{s}}(\xi_i) = J\, J^\alpha_i \sum_{j=1}^{\mathrm{GP}} w_j \mathbf{v}_\mathfrak{s}({}^\alpha\xi^j_i), \tag{62}$$

in which $J^\alpha_i = (\alpha(1-\xi_i)+\xi_i+1)/2$. ${}^\alpha\xi^j_i$ denotes the new position of the jth Gaussian point on the interval $[-1, \alpha(1-\xi_i)+\xi_i]$, i. e. ${}^\alpha\xi^j_i = J^\alpha_i(\xi_j+1)-1$.
Consequently, inserting Eq. (62) into Eq. (60), we get

$$\int_{\mathcal{I}^n} \mathbf{g}^\alpha_{\mathbf{u},\mathfrak{s}} \cdot \delta\mathbf{v}_\mathfrak{s}\, \mathrm{d}t = J^2 \sum_{i=1}^{\mathrm{GP}} \Big[w_i J^\alpha_i \sum_{j=1}^{\mathrm{GP}} \Big(w_j \mathbf{v}_\mathfrak{s}({}^\alpha\xi^j_i) \Big) \cdot \delta\mathbf{v}_\mathfrak{s}(\xi_i) \Big]. \tag{63}$$

Furthermore, we define the shape function $\mathbf{v}_\mathfrak{s}$ and the test function $\delta\mathbf{v}_\mathfrak{s}$ as

$$\mathbf{v}_\mathfrak{s}(\xi) = \sum_{l=1}^{p+1} N_l(\xi)\hat{\mathbf{v}}_l, \quad \delta\mathbf{v}_\mathfrak{s}(\xi) = \sum_{k=1}^{p+1} N_k(\xi)\, \delta\hat{\mathbf{v}}_k, \tag{64}$$

in which N_l denotes the polynomial of the highest order p. $\hat{\mathbf{v}}_l$ represents the nodal value of the velocities and $\delta\hat{\mathbf{v}}_l$ are the corresponding test values. Thus, the velocity $\mathbf{v}_\mathfrak{s}({}^\alpha\xi^j_i)$, cf. Eq. (63), can be expressed as

$$\mathbf{v}_\mathfrak{s}({}^\alpha\xi^j_i) = \sum_{l=1}^{p+1} N_l({}^\alpha\xi^j_i)\, \hat{\mathbf{v}}_l. \tag{65}$$

We observe that as long as the type of shape function N_l and the number of Gaussian points GP as well as the stabilization parameter α are fixed, the quantity $N_l({}^\alpha\xi^j_i)$ can be determined uniquely. From Eq. (65) we observe that $N_l({}^\alpha\xi^j_i)$ is independent of the nodal solution $\hat{\mathbf{v}}_l$.
Moreover, a new type of polynomial depending on the order of shape function and the integration scheme can be introduced as

$$N_l^{\xi^\alpha_i} = J\, J^\alpha_i \sum_{j=1}^{\mathrm{GP}} w_j\, N_l({}^\alpha\xi^i_j). \tag{66}$$

Note that the $N_l^{\xi^\alpha_i}$ is only given at the chosen Gaussian points. Inserting Eq. (66) into Eq. (63) and taking into account the communication property of summations, we further obtain

$$\int_{\mathcal{I}^n} \mathbf{g}^\alpha_{\mathbf{u},\mathfrak{s}} \cdot \delta\mathbf{v}_\mathfrak{s}\, \mathrm{d}t = J \sum_{i=1}^{\mathrm{GP}} \Big[w_i \big(\sum_{l=1}^{p+1} N_l^{\xi^\alpha_i} \hat{\mathbf{v}}_l \big) \cdot \big(\sum_{k=1}^{p+1} N_k(\xi_i)\, \delta\hat{\mathbf{v}}_k \big) \Big]. \tag{67}$$

We denote that this expression is identical to a conventional finite element approximation except for the approximation function $N_l^{\xi^\alpha_i}$. $N_l^{\xi^\alpha_i}$ is an integral of the approximation function N_l, cf. Eq. (66) at the Gaussian point ξ_i. However, we note that $N_l^{\xi^\alpha_i}$ is independent of the nodal solution $\hat{\mathbf{v}}_l$. This property simplifies the computation dramatically, since as long as the approximation function N_l and the integration Gaussian points ξ_i are chosen, the computation of $N_l^{\xi^\alpha_i}$ needs only to be carried out once.

Acknowledgements The authors are grateful to the DFG (German Science Foundation – Deutsche Forschungsgemeinschaft) for their financial support under the grant number Di 431/4-2.

References

1. K. Terzaghi, Die Berechnung der Durchlässigkeitsziffer des Tones aus dem Verlauf der hydromechanischen Spannungserscheinungen, Sitzungsberichte der Akademie der Wissenschaften in Wien, mathematisch-naturwissenschaftliche Klasse 132 (1923) 125–138.
2. M. A. Biot, General theory of three-dimensional consolidation, J. Appl. Phys. 12 (1941) 155–164.
3. M. A. Biot, Theory of propagation of elastic waves in a fluid-saturated porous solid. I. Low-frequency range, J. Acoust. Soc. Am. 29 (1956) 168–178.
4. M. A. Biot, Theory of propagation of elastic waves in a fluid-saturated porous solid. II. Higher frequency range, J. Acoust. Soc. Am. 29 (1956) 179–191.
5. M. A. Biot, Mechanics of deformation and acoustic propagation in porous media, J. Appl. Phys. 33 (1962) 1482–1498.
6. C. A. Truesdell, R. Toupin, The classical field theories, In S. Flügge (Herausgeber), Handbuch der Physik III/1, Springer-Verlag, Berlin, 1960.
7. R. J. Aktin, R. E. Craine, Continuum theories of mixtures: basic theory and historical developement, Quarterly J. Mech. Appl. Math. 29(2) (1976) 209–244.
8. R. M. Bowen, Theory of mixture, Continuum physics III (1976) 1–127.
9. R. M. Bowen, Compressible porous media models by use of the theory of mixtures, Int. J. Engng. Sci. 20 (1982) 697–735.
10. A. Bedford, D. S. Drumheller, Recent advances: theories of immiscible and structured mixtures, Int. J. Engng. Sci. 21 (1973) 863–960.
11. R. de Boer, Theory of porous media: Highlights in the historical development and current state, Springer Verlag, Berlin, 2000.

12. R. I. Borja, E. Alarcón, A mathematical framework for finite strain elastoplastic consolidation. part1: balance laws, variational formulation and linearization, Comp. Meth. Appl. Mech. Eng. 159 (1995) 145–171.
13. S. Diebels, W. Ehlers, Dynamic analysis of a fully saturated porous medium accounting for geometrical and material non-linearities, Int. J. Numer. Meth. Eng. 39 (1996) 81–97.
14. S. H. Advani, T. S. Lee, J. K. Lee, C. S.Kim, Hygrothermomechanical evaluation of porous media under finite deformation, part I– finite element formulations, Int. J. Numer. Meth. Eng. 36 (1993) 147–160.
15. C. S. Kim, T. S. Lee, S. H. Advani, J. K. Lee, Hygrothermomechanical evaluation of porous media under finite deformation: partII–model validations and field simulations, Int. J. Numer. Meth. Eng. 36 (1993) 161–179.
16. J. Larsson, R. Larsson, Non-linear analysis of nearly saturated porous media: theoretical and numerical formulation, Comp. Meth. Appl. Mech. Eng. 191 (2002) 3885–3907.
17. C. Li, R. Borja, R. Regueiro, Dynamics of porous media at finite strain, Comp. Meth. Appl. Mech. Eng. 193 (2004) 3837–3870.
18. W. Ehlers, Foundations of multiphasic and porous materials, in: W. Ehlers, J. Bluhm (Eds.), Porous Media: Theory, Experiments and Numerical Applications, Springer-Verlag, Berlin, 2002, pp. 3–86.
19. S. Diebels, Mikropolare Zweiphasenmodelle: Modellierung auf der Basis der Theorie Poröser Medien, Habilitationsschrift, Institut für Mechanik (Bauwesen), Nr. II-4, Universität Stuttgart, 2000.
20. W. Ehlers, S. Diebels, Dynamic deformations in the theory of fluid-saturated porous solid materials, in: D. F. Parker, A. H. England (Eds.), Proc. of IUTAM Symp.: Anisotropy, Inhomogeneity and Nonlinearity in Solid Mechanics, Kluwer Academic Publishers, Dordrecht, 1995, pp. 241–246.
21. W. Ehlers, G. Eipper, Finite elastic deformations in liquid-saturated and empty porous solids, Transport Porous Med. 34 (1999) 179–191.
22. G. Eipper, Theorie und Numerik finiter elastischer Deformationen in fluidgesättigten porösen Festkörpern, Dissertation, Institut für Mechanik (Bauwesen), Lehrstuhl II, Universität Stuttgart, 1998.
23. J. H. Argyris, D. W. Scharpf, Finite elements in space and time, Nucl. Engrg. Des. 10 (1969) 456–464.
24. I. Fried, Finite element analysis of time-dependent phenomena, AIAA Journal J.7 (1969) 1170–1173.
25. T. J. R. Hughes, G. M. Hulbert, Space-time finite element methods for elastodynamics: Formulations and error estimates, Comp. Meth. Appl. Mech. Eng. 66 (1988) 339–363.
26. G. Hulbert, Space-time finite element methods for second order hyperbolic equations, Ph.D. thesis, Department of Mechanical Engineering, Stanford University, Stanford (1989).
27. G. M. Hulbert, T. J. R. Hughes, Space-time finite element methods for second-order hyperbolic equations, Comp. Meth. Appl. Mech. Eng. 84 (1990) 327–348.
28. C. Johnson, Adaptive finite element methods for diffusion and convection problems, Comp. Meth. Appl. Mech. Eng. 82 (1990) 301–322.
29. W. H. Reed, T. R. Hill, Triangular mesh methods for the neutron transport equation, Los Alamos Scientific Laboratory Report LA-UR-73-479.
30. B. Cockburn, C. W. Shu, TVB Runge-Kutta local projection discontinuous Galerkin finite element methods for conservation laws. II: General framework, Math. Comp. 52 (1989) 411–435.
31. B. Cockburn, S. Y. Lin, C. W. Shu, TVB Runge-Kutta local projection discontinuous Galerkin finite element methods for conservation laws III: One dimensional systems, J. Comp. Phys. 84 (1989) 90–113.
32. B. Cockburn, S. Hou, C. W. Shu, TVB Runge-Kutta local projection discontinuous Galerkin finite element methods for conservation laws. IV: The multidimensional case, Math. Comp. 54 (1990) 545–581.
33. Z. Chen, H. Steeb, S. Diebels, A time-discontinuous Galerkin method for the dynamical analysis of porous media, Int. J. Numer. Anal. Meth. Geomech. 30 (2006) 1113–1134.
34. Z. Chen, H. Steeb, S. Diebels, A new hybrid velocity integration method applied to elastic wave propagation, Int. J. Numer. Meth. Eng. 74(1) (2008) 56–79.
35. Z. Chen, H. Steeb, S. Diebels, Dynamic analysis of porous materials: Numerical modeling with a space-time FEM, Proc. Appl. Math. Mech.Submitted for publication.
36. E. by W. Ehlers, J. Bluhm, Porous media, Springer-Verlag, Berlin, 2002.
37. R. de Boer, Theory of porous media, Springer-Verlag, Berlin, 2000.
38. R. M. Bowen, Incompressible porous media models by use of the theory of mixtures, Int. J. Engng. Sci. 18 (1980) 1129–1148.
39. R. de Boer, W. Ehlers, Theorie der Mehrkomponentenkontinua mit Anwendung auf bodenmechanische Probleme, in: Forschungsberichte aus dem Fachbereich Bauwesen, Vol. 40, Universität-GH-Essen, 1986.
40. J. E. Marsden, T. J. R. Hughes, Mathematical Foundations of Elasticity, Dover Publications, Inc., New York, 1983.
41. K. Terzaghi, Theoretical soil mechanics, Wiley, New York, 1943.
42. B. Markert, A constitutive approach to 3-d nonlinear fluid flow through finite deformable porous continua, with application to a high-porosity polyurethane foam, Transport Porous Med.
43. P. Ellsiepen, Zeit- und Ortsadaptive Verfahren angewandt auf Mehrphasenprobleme poröser Medien, PhD-thesis, Institute of Applied Mechanics (CE), Chair II, University of Stuttgart, 1999.
44. S. Breuer, Quasi-static and dynamic behavior of saturated porous media with incompressible constituents, Transport Porous Med. 34 (1999) 285–303.
45. A. Masud, T. J. R. Hughes, A space-time Galerkin/least-squares finite element formulation of the navier-stokes equations for moving domain problems, Comp. Meth. Appl. Mech. Eng. 146 (1997) 91–126.
46. B. Cockburn, Discontinuous Galerkin methods, Z. Angew. Math. Mech. 11 (2003) 731–754.
47. O. C. Zienkiewicz, Coupled problems and their numerical solution, in: R. W. Lewis, P. Bettess, E. Hinton (Eds.), Numerical methods in coupled systems, Wiley, New York, 1984, pp. 35–68.
48. P. Wriggers, Konsistente Lineariserung in der Kontinuumsmechanik und ihre Anwendung auf die Finite-Element-Methode, Bericht Nr. F88/4 (1999) Institut für Baustatik und Numerische Mechanik, Univerität Honnover, 1988.
49. K. Eriksson, D. Estep, P. Hansbo, C. Johnson, Computational Differential Equations, Cambridge University Press, Cambridge, 1996.
50. C. Gresho, R. L. Lee, Don't suppress the wiggles-they're telling you something, Finite Element Methods in Convection dominated Flows, ASME AME 34 (1979) 27–61.
51. W. A. Wall, Fluid-Struktur-Interaktion mit stabilisierten Finiten Elementen, Bericht Nr. 31 (1999), Institut für Baustatik der Universität Stuttgart, 1999.

52. H. Steeb, F. Cirak, E. Ramm, On local error estimators for non-self-adjoint boundary value problems, Z. Angew. Math. Mech. (2000) 507–508.
53. A. N. Brooks, T. J. R. Hughes, Streamline upwind/petrov-Galerkin formulations for convection dominated flows with particular emphasis on the incompressible Navier-Stokes equations, Comp. Meth. Appl. Mech. Eng. 32 (1982) 199–259.
54. T. J. R. Hughes, L. P. Franca, M. Hulbert, A new finite element formulation for computational fluid dynamics: Viii. the Galerkin/Least-squares method for advective-diffusive equations, Comp. Meth. Appl. Mech. Eng. 73 (1989) 173–189.
55. L. P. Franca, S. L. Frey, T. J. R. Hughes, Stabilized finite element methods: I. application to the advective-diffusive model, Comp. Meth. Appl. Mech. Eng. 95 (1992) 253–276.
56. J. R. Cash, Diagonally implicit Runge-Kutta formulae with error estimates, J.Inst.Maths Applics 24 (1979) 293–301.
57. P. Bogacki, L. F. Shampine, A 3(2) pair of Runge-Kutta formulas, Appl. Math. Lett. 2 (1989) 321–325.
58. L. J. Gibson, M. F. Ashby, Cellular solids. Structure and properties, Cambridge Solid State Science Series, Cambridge University Press, Cambridge, 1997.

Paper D

A space-time discontinuous Galerkin method for single-phase flow in porous media

A space-time discontinuous Galerkin method applied to single-phase flow in porous media

Zhiyun Chen*, Holger Steeb, Stefan Diebels
Saarland University, Chair of Applied Mechanics,
Campus Saarbrücken, Building A 4.2, D-66 123 Saarbrücken, Germany

May 6, 2008

Abstract. A space-time discontinuous Galerkin finite element method is proposed and applied to a convection-dominant single-phase flow problem in porous media. The numerical scheme is based on a coupled space-time finite element discretization allowing for discontinuous approximations in space and in time. The continuities on the element interfaces are weakly enforced by the flux treatments, so that no extra penalty factor has to been determined. The resulting space-time formulation possesses the advantage of capturing the steep concentration front with sharp gradients efficiently. The stability and reliability of the proposed approach is demonstrated by numerical experiments.

Keywords: discontinuous Galerkin methods, convection-dominant flow, porous media

1. Introduction

The objective of this paper is to study an efficient numerical method for the simulation of miscible flow in porous media. The numerical investigation of such problems can be dated back to [1, 2, 3]. However, the traditional approaches such as finite difference, finite volume and continuous finite element methods usually fail to capture the steep concentration fronts in heterogeneous porous materials. Since the last decade, more and more attention has been focused on the use of the spatial discontinuous Galerkin (DGS) methods to model convection-dominant flows in porous media, [4, 5, 6, 7]. The advantage of using such DGS approaches lies in the fact that these methods are locally mass conservative and that they are able to capture the steep concentration front without extreme refinement in the discretization. Among the variety of different DGS formulations, there are some most popular ones, such as the Oden-Baumann-Babuska (OBB) scheme [8], the Nonsymmetric Interior Penalty Galerkin method (NIPG) [9], the Symmetric Interior Penalty Galerkin method (SIPG) [10, 11] and the Incomplete

* The author is grateful to the DFG (German Science Foundation - Deutsche Forschungsgemeinschaft) for the financial support under the grant number Di 430/4-2.

Interior Penalty Galerkin method (IIPG) [12, 13]. We mention that except the OBB formulation, the other three can be classified to the penalty method with a penalty factor σ. However, with a proper choice of the penalty factor, all the four formulations lead to very similar numerical results [4, 14].

With respect to the dynamic modeling, it is common to solve the time-dependent problem, e. g. transport phenomena, in a semi-discrete manner, i. e. by means of the Method of Lines (MOL), such that the governing set of Partial Differential Equations (PDE) is first evaluated in space according to a finite element discretization to produce an Ordinary Differential Equation system (ODE) in time, which can be in turn solved by a time difference approach, e. g. the Euler method, the Newmark method, etc. However, these time-stepping schemes are often known as low efficient suffering from strong numerical dissipation and dispersion [15, 16]. Besides the time difference approaches, studies of using finite element method in time can be dated back to 1960s, [17, 18, 19]. Using finite element discontinuous approximation in time was first proposed by Hughes & Hulbert [20]. Therein, they proposed a decoupled space-time Galerkin method, in which a continuous Galerkin approximation is applied in space to produce an ODE system, which is in turn evaluated by a discontinuous Galerkin method in time, cf. [21, 22, 23]. This method is also known as semi-discrete approach, in that the spatial and temporal integrations are evaluated subsequently. In the previous work of the authors, we investigate a space-time coupled discontinuous Galerkin formulation. By use of finite element shape function consisting of tensor products of polynomials in space and in time, we are able to evaluate the spatial and temporal integration simultaneously. As the finite element approximation is continuous in space but discontinuous in time, the method is called Time-discontinuous Galerkin method (DGT) [24]. In contrast to decoupled methods, i. e. semi-discrete methods, a coupled formulation has advantage in less numerical dispersion and dissipation. Moreover, it is easy to develop a simple efficient space-time discretization scheme based on the coupled formulation. Higher order methods can be achieved straight forwardly by employing higher order polynomials in space and in time.

In the current work, we combined the DGT approach in time with the OBB formulation [25] in space to construct a coupled numerical formulation that is neither continuous in space nor in time. We remark that as the treatment of enforcing the continuity in time and in space are decoupled, such a combination of the DGT with the DGS approach is generally allowed. In addition, other popular DGS formulations, i. e. NIPG, SIPG and IIPG, combined with the DGT method in time have also been tested. It has to be mentioned, with the proper choice of

the penalty factor, no significant difference has been observed in the numerical solutions.
The structure of the current work is as follows, in the next section, we discuss briefly about the modeling aspect of the miscible flow through porous materials. After that, a coupled space-time discontinuous Galerkin (DGST) formulation for the solution of model equations is proposed. In the next section, some numerical experiments are performed in order to demonstrate the behavior of the new space-time coupled scheme. We close our discussion with a short conclusion.

2. Physical modeling

The physical model describes the procedure of a liquid mixture through a rigid porous skeleton with a constant porosity $\phi(\mathbf{x}, t)$. The liquid mixture $\varphi^{\mathfrak{l}}$ consists of a resident fluid $\varphi^{\mathfrak{f}}$ and a solvent fluid $\varphi^{\mathfrak{a}}$, i. e. $\varphi^{\mathfrak{l}} = \varphi^{\mathfrak{f}} \cup \varphi^{\mathfrak{a}}$. The partial density of the liquid mixture ρ is given by $\rho = \rho^{\mathfrak{a}} + \rho^{\mathfrak{f}}$, in which $\rho^{\mathfrak{a}}$ and $\rho^{\mathfrak{f}}$ are the partial density of the solvent and the resident fluid, respectively. The *mass-specific* concentration c of the solvent is defined as $c := \rho^{\mathfrak{a}}/\rho$. For the sake of simplicity, we assume that the density ρ of the liquid mixture is a constant. Next, we introduce the *barotropic velocity* of the liquid mixture as $\mathbf{v} = (\rho^{\mathfrak{f}}\mathbf{v}_{\mathfrak{f}} + \rho^{\mathfrak{a}}\mathbf{v}_{\mathfrak{a}})/\rho$, in which $\mathbf{v}_{\mathfrak{f}}$ and $\mathbf{v}_{\mathfrak{a}}$ represent the velocity of the resident and the solvent fluid, respectively. Note that this *barotropic velocity* can be further related to the *filter velocity* or Darcy's velocity $\mathbf{q}$ through $\mathbf{q} := \phi\,\mathbf{v}$. The *diffusion velocity* $\mathbf{d}_{\mathfrak{a}}$ is introduced as $\mathbf{d}_{\mathfrak{a}} = \mathbf{v}_{\mathfrak{a}} - \mathbf{v}$.
Taken into consideration that the porous skeleton is rigid, the field equations of the system can be obtained by evaluating the continuity equation and the momentum balance of the liquid mixture $\varphi^{\mathfrak{l}}$, as well as the mass balance of the solvent fluid $\varphi^{\mathfrak{a}}$ as

$$\operatorname{div}\mathbf{v} = 0, \tag{1}$$

$$\rho\,\mathbf{a}_{\mathfrak{l}} - \operatorname{div}\mathbf{T}^{\mathfrak{l}} = \hat{\mathbf{p}}^{\mathfrak{l}} + \rho\,\mathbf{b}, \tag{2}$$

$$\phi\,\rho\,\partial_t(c) + \operatorname{div}(\mathbf{j}_{\mathfrak{a}} + \phi\,c\,\rho\,\mathbf{v}) = 0. \tag{3}$$

In eq. (2), $\mathbf{T}^{\mathfrak{l}}$ denotes the Cauchy stress tensor, $\rho\mathbf{b}$ is the volume force and $\mathbf{a}_{\mathfrak{l}}$ is the acceleration of the liquid mixture. $\hat{\mathbf{p}}^{\mathfrak{l}}$ represents the momentum exchange between the liquid mixture $\varphi^{\mathfrak{l}}$ and solid phase $\varphi^{\mathfrak{s}}$. The stress tensor of the liquid mixture can be further written as $\mathbf{T}^{\mathfrak{l}} = -\phi\,p\,\mathbf{I} + \mathbf{T}^{\mathfrak{l}}_{\mathrm{E}}$. An order-of-magnitude analysis [26, 27] shows that for standard conditions of liquid-flow in porous media, the so-called extra stress $\mathbf{T}^{\mathfrak{l}}_{\mathrm{E}}$ of the liquid is of higher order, which is not counted here. The momentum exchange $\hat{\mathbf{p}}^{\mathfrak{l}}$ can be expressed as the sum of an equilibrium part $\hat{\mathbf{p}}^{\mathfrak{l}}_{\mathrm{eq}}$ and a non-equilibrium part $\hat{\mathbf{p}}^{\mathfrak{l}}_{\mathrm{neq}}$, i. e. $\hat{\mathbf{p}}^{\mathfrak{l}} = \hat{\mathbf{p}}^{\mathfrak{l}}_{\mathrm{eq}} + \hat{\mathbf{p}}^{\mathfrak{l}}_{\mathrm{neq}}$, cf.

[28]. Usually, the equilibrium part $\hat{\mathbf{p}}_{\mathrm{eq}}$ is proportional to the gradient of the porosity ϕ and the pore pressure p, i. e. $\hat{\mathbf{p}}^{\mathfrak{l}}_{\mathrm{eq}} = p \operatorname{grad} \phi$, while the non-equilibrium part $\hat{\mathbf{p}}_{\mathrm{neq}}$ is an isotropic vector-valued function of the non-equilibrium process variable $\mathbf{v}$. In the simplest case, it is a linear function of $\mathbf{v}$, i. e. $\hat{\mathbf{p}}^{\mathfrak{l}}_{\mathrm{neq}} = -[(\phi^2 \mu^{\mathfrak{l}})/k^{\mathfrak{s}}]\, \mathbf{v}$, in which $\mu^{\mathfrak{l}}$ and $k^{\mathfrak{s}}$ are the dynamic viscosity of the liquid mixture and the so-called intrinsic permeability, respectively. Generally, the dynamic viscosity of the liquid mixture $\mu^{\mathfrak{l}}$ is a function of the concentration c, i. e. $\mu = \mu^{\mathfrak{l}}(c)$. Since the liquid acceleration $\mathbf{a}_{\mathfrak{l}}$ is mostly very small, it is common to neglect this term, i. e. $\mathbf{a}_{\mathfrak{l}} = \mathbf{0}$ in eq. (2). Thus, eq. (2) boils down to Darcy's equation

$$\mathbf{q} = \frac{k^{\mathfrak{s}}}{\mu^{\mathfrak{l}}} \operatorname{grad} p. \tag{4}$$

In eq. (3), the diffusion flux $\mathbf{j}_{\mathfrak{a}}$ can be modeled by the Fick's law given by $\mathbf{j}_{\mathfrak{a}} = -\mathbf{D} \cdot \operatorname{grad} \rho^{\mathfrak{a}}$, in which $\mathbf{D}$ denotes the second-order diffusion tensor. Note that in the current work, we do not consider mass exchanges, e. g. chemical reactions between the solvent and the resident fluid. Inserting the Fick's law into eq. (3) and eq. (4) into the continuity equation eq. (1), we obtain the set of field equations on the spatial domain $\Omega \in \mathbb{R}^2$ over the time $\mathcal{I} = [t_0, T]$ as

$$\phi\, \partial_t(c) + \operatorname{div}(c\, \mathbf{q} - \mathbf{D} \operatorname{grad} c) = \quad 0, \quad \text{in} \quad \Omega \times \mathcal{I}, \tag{5}$$

$$\operatorname{div}\left[\frac{k^{\mathfrak{s}}}{\mu^{\mathfrak{l}}} \operatorname{grad} p\right] = 0 \equiv \operatorname{div} \mathbf{q}, \ \text{in} \quad \Omega \times \mathcal{I}. \tag{6}$$

The boundary $\partial\Omega$ consists of non-overlapping Dirichlet part $\Gamma^{\mathfrak{a}/\mathfrak{l}}_{\mathrm{D}}$ and the Neumann part $\Gamma^{\mathfrak{a}/\mathfrak{l}}_{\mathrm{N}}$ of the liquid mixture $\varphi^{\mathfrak{l}}$ and the solvent fluid $\varphi^{\mathfrak{a}}$, respectively, i. e. $\partial\Omega = \Gamma^{\mathfrak{l}/\mathfrak{a}}_{\mathrm{D}} \cup \Gamma^{\mathfrak{l}/\mathfrak{a}}_{\mathrm{N}}$ and $\Gamma^{\mathfrak{l}/\mathfrak{a}}_{\mathrm{D}} \cap \Gamma^{\mathfrak{l}/\mathfrak{a}}_{\mathrm{N}} = \emptyset$. The boundary conditions are given for the pressure p and for the concentration c as

$$\begin{aligned} p &= \bar{p} \quad \text{on} \quad \Gamma^{\mathfrak{l}}_{\mathrm{D}} \times \mathcal{I}, \\ c &= \bar{c} \quad \text{on} \quad \Gamma^{\mathfrak{a}}_{\mathrm{D}} \times \mathcal{I}, \\ \mathbf{q} \cdot \mathbf{n} &= \bar{q} \quad \text{on} \quad \Gamma^{\mathfrak{l}}_{\mathrm{N}} \times \mathcal{I}, \\ (c\, \mathbf{q} - \mathbf{D} \cdot \operatorname{grad} c) \cdot \mathbf{n} &= c_{\mathrm{in}} \quad \text{on} \quad \Gamma^{\mathfrak{a}}_{\mathrm{N}} \times \mathcal{I}, \end{aligned} \tag{7}$$

in which $\bar{p}$ and $\bar{c}$ are the pressure and concentration prescribed on the Dirichlet boundaries. The inflow flux of the liquid mixture is denoted by $\bar{q}$. c_{in} represents the concentration of the inflow fluid.
The associated initial conditions at $t = 0$ are given for the fluid pressure p and the concentration c as

$$p = p_0 \quad \text{at} \quad \Omega \times t_0, \qquad \text{and} \qquad c = c_0 \quad \text{at} \quad \Omega \times t_0. \tag{8}$$

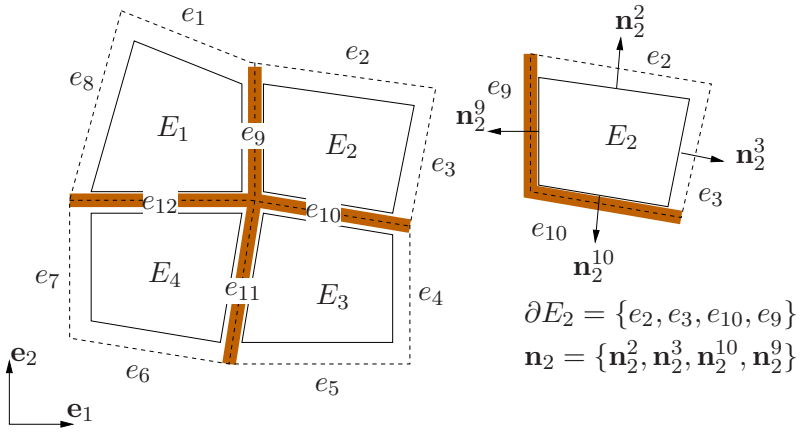

Figure 1. A finite element patch of four quadrilaterals $\mathcal{E}_h = \{E_1 \sim E_4\}$ with the boundaries $\mathcal{K}_h = \{e_1 \sim e_{12}\}$, among which $\{e_9 \sim e_{12}\}$ are interior edges.

3. Finite element weak form

In the current work, we investigate a coupled space-time discontinuous Galerkin method (DGST) for the solution strategy of single-phase flow problems. The space-time domain Q is constructed by adding the time axis orthogonal to the spatial domain Ω, i. e. $Q = \Omega \times \mathcal{I}$. The temporal domain $\mathcal{I}$ is discretized into a sequence of time intervals $\mathcal{I}^n = [t_n, t_{n+1})$, with $t_n < t_{n+1}$. As a consequence, we introduce the discrete space-time slab as $Q^n = \Omega \times \mathcal{I}^n$, rf. [24]. Let $\mathcal{E}_h = \{E_1, E_2, \ldots, E_{N_E}\}$ be subdivisions of the discrete spatial domain $\Omega_h \in \Omega$ consisting of triangles or quadrilaterals. The edges of each subdivision E_i are denoted by ∂E_i $(i < N_E)$. $\mathcal{K}_h = \{e_1, e_2, \ldots, e_{N_K}\}$ represents the union of all edges in $\mathcal{E}_h$. Furthermore, $\mathbf{n}_i^k$ represents the the outward normal vector on ∂E_i that coincides with the edge e_k and $\mathbf{n}_i$ stands for the union of all outward normal vectors on ∂E_i. *Figure* 1 shows examplarily one of such a finite element patch with four quadrilaterals.
Moreover, according to the direction of the flows over the edges, we can further divide the edge $\mathcal{K}_h$ into an inflow part $\mathcal{K}_h^-$ and an outflow part $\mathcal{K}_h^+$,

$$\mathcal{K}_h^- = \{\mathbf{x} \in (e_k \cap \partial E_i) : (\tilde{\mathbf{q}}_h(\mathbf{x}) \cdot \mathbf{n}_i^k(\mathbf{x})) > 0\}, \quad \mathcal{K}_h^+ = \mathcal{K}_h \setminus \mathcal{K}_h^-. \quad (9)$$

Note that due to a discontinuous approximation of the pressure p_h, different values of the filter velocities $\mathbf{q}_h^{\mathrm{DG}} = (k^{\mathfrak{s}}/\mu^{\mathfrak{l}})\ \mathrm{grad}\, p_h$ are evaluated from both sides of the edge. In eq. (9), $\tilde{\mathbf{q}}_h$ stands for the continuous projection of the filter velocity $\mathbf{q}_h^{\mathrm{DG}}$ on the edge. More details concerning the projection approach will be mentioned later. We denote the normal vector as $\mathbf{n}_j^k = \sum_d (n_d\, \mathbf{e}_d)$, $(d = 1, 2)$, in which $\mathbf{e}_d$ represents the basis

vector. The operator $\{\mathbf{n}_j^k\}$ is defined as $\{\mathbf{n}_j^k\} = \sum_d (n_d\, \mathbf{e}_d \cdot \mathbf{e}_d)$, $(d = 1, 2)$. The vector $\mathbf{n}_i^k$ is considered as positive if $\{\mathbf{n}_i^k\} > 0$. According to the direction of the positive normal vector, we can uniquely define the jump on this edge. Assume that e_k is the interior edge shared by the two finite elements E_i and E_j, i. e. $e_k = \partial E_i \cap \partial E_j$. For $\{\mathbf{n}_i^k\} > 0$, we define the jump of a function ψ as

$$[\![\, \psi(\mathbf{x}, t) \,]\!]_{e_k} = \psi_j(\mathbf{x}, t) - \psi_i(\mathbf{x}, t), \quad \mathbf{x} \in e_k, \quad \{\mathbf{n}_i^k\} > 0, \tag{10}$$

where $\psi_l = \{\psi(\mathbf{x}, t) : \mathbf{x} \in (e_k \cap \partial E_l)\}$. The jumps may be defined for the concentration and the pressure, i. e. $\psi \in \{c, p\}$. Analogically, the average of a vector Ψ on the boundary e_k is given by

$$\langle \Psi(\mathbf{x}, t) \cdot \mathbf{n} \rangle|_{e_k} \;=\; \tfrac{1}{2}\Big(\Psi_i(\mathbf{x}, t) \cdot \mathbf{n}_i^k + \Psi_j(\mathbf{x}, t) \cdot \mathbf{n}_i^k \Big), \quad \{\mathbf{n}_i^k\} > 0, \tag{11}$$

with $\Psi_l(\mathbf{x}, t) = \{\Psi(\mathbf{x}, t) : \mathbf{x} \in (e_k \cap \partial E_l)\}$. This operation is required for the flux terms, i. e. $\Psi = \{(\mathbf{D} \cdot \operatorname{grad} c), (k^{\mathfrak{s}}/\mu^{\mathfrak{l}}) \operatorname{grad} p\}$. In addition, according to the direction of the flow, the spatial *upwind* flux ψ^{in} on the edge e_k is given by

$$\psi^{\text{in}}(\mathbf{x}, t)|_{e_k} = \begin{cases} \psi_i(\mathbf{x}, t), & \text{if} \quad (\tilde{\mathbf{q}} \cdot \mathbf{n}_i^k) > 0, \\ \psi_j(\mathbf{x}, t), & \text{otherwise.} \end{cases} \tag{12}$$

Obviously, if inconsistent values of ψ occur on the interior edges, the flux ψ^{in} on the edge e_k equals the value on the inflow part $e_k \in \mathcal{K}_h^-$. In *Figure* 2a, we depict examplarily the spatial *upwind* flux ψ^{in} on a finite element patch of four quadrilaterals. We remark that, due to the introduction of the flux treatment on the boundaries, the Dirichlet boundary conditions are assigned as inflow flux rather than strict assignments, i. e. $\Gamma_D^{\mathfrak{l}/\mathfrak{a}} \in \mathcal{K}_h^-$, cf. [29].

Analog to the spatial *upwind* flux definition, we define the temporal *upwind* flux $\breve{\psi}_n$ at time t_n as, cf. [24, 30]

$$\breve{\psi}_n(\mathbf{x}) = \begin{cases} \psi_0(\mathbf{x}), & \text{if} \quad n = 0 \\ \psi^-(\mathbf{x}, t_n), & \text{otherwise,} \end{cases} \tag{13}$$

with

$$\psi^-(\mathbf{x}, t_n) = \lim_{\varepsilon \to 0^+} \psi(\mathbf{x}, t_n - \epsilon), \tag{14}$$

where ε is an infinitely small positive number. The temporal *upwind* definition $\breve{\psi}_n$ implies that the value of ψ at the discrete time level t_n equals its immediate previous value $\psi^-(t_n)$. For $n > 0$, the immediate previous value $\psi^-(t_n)$ results from the previous computation on the time-slab Q^{n-1} at time t_n, while for the initial step $n = 0$, $\breve{\psi}_0$ stands

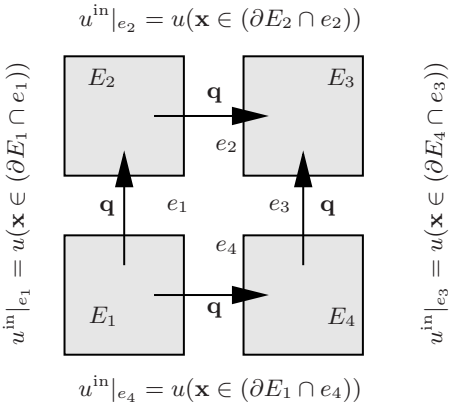

a. *upwind* flux $\psi^{\text{in}}|_{e_i}$ in space

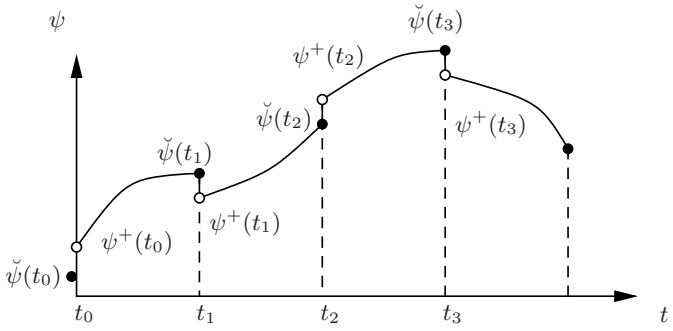

b. *upwind* flux $\breve{\psi}(t_n)$ in time

Figure 2. Upwind fluxes in space and in time

for the initial condition, see *Figure* 2b. Obviously, such a definition fulfills the causality condition that the information travels "*from the past to the future*". Moreover, we denote that the algebraic solution schemes on each time-slab are decoupled, so that $\breve{\psi}_n$ serves as the initial condition for the current time-slab Q^n. Such a sequential solution scheme is favorable as it avoids huge algebraic system consisting of the total number of Degree of Freedoms (DOFs) on the space-time domain Q. Nevertheless, adopting larger time step sizes without degenerating numerical accuracy can be easily achieved by employing higher order polynomials in time. A further discussion of the temporal *upwind* flux technique can be found in [24, 30].

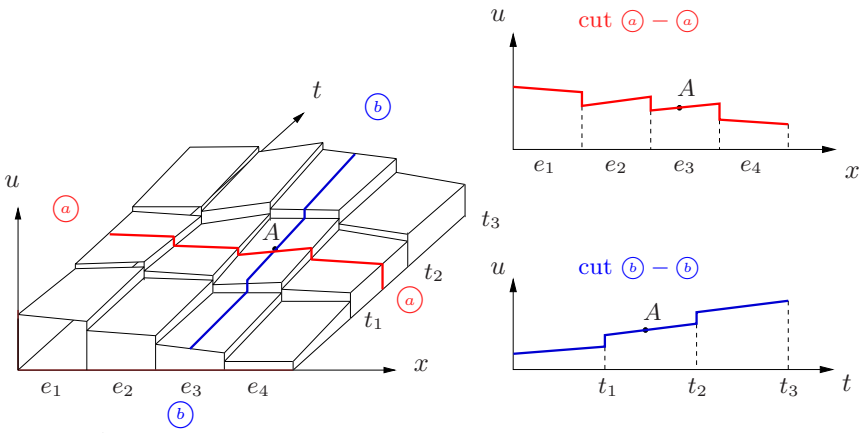

Figure 3. Approximation of a 1-dim spatial problem with the DGST formulation

Let $\mathcal{W}$ be the finite dimensional functional space consisting of tensor products in space and in time. $\mathcal{W}$ consists of discontinuous piecewise polynomials over the subdomains E_j and the time intervals $\mathcal{I}^n$. *Figure* 3 examplarily shows a one-dimensional spatial problem with four finite elements in space and three time-slabs in the temporal domain. Herein, linear polynomials in space and in time are employed. Noting that since the flux treatments in space and in time are decoupled, we construct the finite element weak form by combining the spatial discontinuous Galerkin scheme with the time-discontinuous Galerkin scheme [24] independently. In the current work, we construct the spatial discretization of the pressure equation (eq. (6)) with the OBB scheme [31], while the concentration equation (eq. (5)) is formulated either by the OBB scheme, the NIPG scheme [9], the SIPG scheme [10, 11] or the IIPG scheme [12, 13]. It has to been mentioned, all these four spatial formulations are very similar, which can be identified by a pair of parameters ϵ and σ (cf. [4]). The resulting space-time finite element problem can be formulated as follows:
Find $\mathbf{u}_h = [c_h, p_h]^T \in \mathcal{W}$, *such that* $\forall \delta\mathbf{u}_h = [\delta c_h, \delta p_h]^T \in \mathcal{W}$ *there exists*

$$B(\mathbf{u}_h, \delta\mathbf{u}_h) = L(\delta\mathbf{u}_h). \tag{15}$$

The discrete bilinear form $B(\mathbf{u}_h, \delta\mathbf{u}_h)$ and the linear form $L(\mathbf{u}_h)$ are given as

$$
\begin{aligned}
&B(\mathbf{u}_h, \delta\mathbf{u}_h) \\
&= \sum_{j=1}^{N_E} \Big\{ \int\limits_{E_j \times \mathcal{I}^n} \{ -\phi\, c_h\, \partial_t \delta c_h + \frac{k^{\mathfrak{s}}}{\mu^{\mathfrak{l}}} \operatorname{grad} p_h \cdot \operatorname{grad} \delta p_h \\
&\qquad\qquad + \mathbf{D}\, \operatorname{grad} c_h \cdot \operatorname{grad} \delta c_h - c_h (\mathbf{q}_h \cdot \operatorname{grad} \delta c_h) \}\, \mathrm{d}v\, \mathrm{d}t \\
&\qquad + \int\limits_{(\partial E_j \setminus \Gamma_D^{\mathfrak{a}}) \times \mathcal{I}^n} (\tilde{\mathbf{q}}_h \cdot \mathbf{n}_j)\, c_h^{\mathrm{in}}\, \delta c_h\, \mathrm{d}a\, \mathrm{d}t + \int\limits_{E_j} \phi\, c_{h,n+1}^{-}\, \delta c_h\, \mathrm{d}v \Big\} \\
&+ \sum_{k=1}^{P_e} \Big\{ \int\limits_{e_k \times \mathcal{I}^n} \{ \langle \frac{k^{\mathfrak{s}}}{\mu^{\mathfrak{l}}} \operatorname{grad} \delta p_h \cdot \mathbf{n} \rangle [\![\, p_h \,]\!] - \langle \frac{k^{\mathfrak{s}}}{\mu^{\mathfrak{l}}} \operatorname{grad} p_h \cdot \mathbf{n} \rangle [\![\, \delta p_h \,]\!] \\
&\qquad\qquad + \epsilon \langle \mathbf{D}\, \operatorname{grad} \delta c_h \cdot \mathbf{n} \rangle [\![\, c_h \,]\!] - \langle \mathbf{D}\, \operatorname{grad} c_h \cdot \mathbf{n} \rangle [\![\, \delta c_h \,]\!] \\
&\qquad\qquad + \sigma\, [\![\, c_h \,]\!]\, [\![\delta c_h]\!] \}\, \mathrm{d}a\, \mathrm{d}t \Big\} \\
&+ \sum_{e_k \in \Gamma_D^{\mathfrak{l}}} \Big\{ \int\limits_{e_k \times \mathcal{I}^n} \{ (\frac{k^{\mathfrak{s}}}{\mu^{\mathfrak{l}}} \operatorname{grad} \delta p_h \cdot \mathbf{n})\, p_h - (\frac{k^{\mathfrak{s}}}{\mu^{\mathfrak{l}}} \operatorname{grad} p_h \cdot \mathbf{n})\, \delta p_h \}\, \mathrm{d}a\, \mathrm{d}t \Big\} \\
&+ \sum_{e_k \in \Gamma_D^{\mathfrak{a}}} \Big\{ \int\limits_{e_k \times \mathcal{I}^n} \{ \epsilon\, (\mathbf{D}\, \operatorname{grad} \delta c_h \cdot \mathbf{n})\, c_h - (\mathbf{D}\, \operatorname{grad} c_h \cdot \mathbf{n})\, \delta c_h \\
&\qquad\qquad + \sigma\, c_h\, \delta c_h \}\, \mathrm{d}a\, \mathrm{d}t \Big\},
\end{aligned}
\tag{16}
$$

$$
\begin{aligned}
L(\delta\mathbf{u}_h) \;=\; & \sum_{e_k \in \Gamma_D^{\mathfrak{l}}} \Big\{ \int\limits_{e_k \times \mathcal{I}^n} \{ (\frac{k^{\mathfrak{s}}}{\mu^{\mathfrak{l}}} \operatorname{grad} \delta p_h \cdot \mathbf{n})\, \bar{p} \}\, \mathrm{d}a\, \mathrm{d}t \Big\} \\
& + \sum_{e_k \in \Gamma_N^{\mathfrak{l}}} \Big\{ \int\limits_{e_k \times \mathcal{I}^n} \bar{q}\, \delta p\, \mathrm{d}a\, \mathrm{d}t \Big\} \\
& + \sum_{e_k \in \Gamma_D^{\mathfrak{a}}} \Big\{ \int\limits_{e_k \times \mathcal{I}^n} \{ \epsilon\, (\mathbf{D}\, \operatorname{grad} \delta c_h \cdot \mathbf{n})\, \bar{c} - (\tilde{\mathbf{q}}_h \cdot \mathbf{n})\, \bar{c}\, \delta c_h \\
& \qquad\qquad + \sigma\, \bar{c}\, \delta c_h \}\, \mathrm{d}a\, \mathrm{d}t \Big\} \\
& + \sum_{e_k \in \Gamma_N^{\mathfrak{a}}} \Big\{ \int\limits_{e_k \times \mathcal{I}^n} c_{\mathrm{in}}\, \delta c_h\, \mathrm{d}a\, \mathrm{d}t \Big\} + \sum_{j=1}^{N_E} \Big\{ \int\limits_{E_j} \phi\, \breve{c}_{h,n}\, \delta c_h\, \mathrm{d}v \Big\}.
\end{aligned}
\tag{17}
$$

Herein, P_e denotes the total number of the interior edges. In eq. (16), the filter velocity $\mathbf{q}_h = (k^{\mathfrak{s}}/\mu^{\mathfrak{l}})\, \operatorname{grad} p_h$, which introduce the nonlinear coupling into the governing set of equations. In the current work, the nonlinear set of equations is linearized and solved by a global Newton-Raphson scheme [32, 33]. The integral $\int_{E_j}(\cdot)\, \mathrm{d}v$ has to be

evaluated at the borders of the time-slab t_n and t_{n+1}. Since the quantity of the *upwind* flux $\check{c}_{h,n}$ is known on the current time-slab Q^n, the integral $\{\int_{E_j} \phi\, \check{c}_{h,n}\, \delta c_h \,\mathrm{d}v\}$ can be evaluated explicitly in the linear form $L(\delta \mathbf{u}_h)$. The parameters ϵ and σ designate the various spatial schemes for the concentration equation (eq. (5)), in particular OBB: $\epsilon = 1$ and $\sigma = 0$; SIPG: $\epsilon = -1$ and $\sigma > 0$; NIPG: $\epsilon = 1$ and $\sigma > 0$; IIPG: $\epsilon = 0$ and $\sigma > 0$. It can be observed that in the above expressions, the parameter σ is a purely penalty factor that controls the amount of jumps, i. e. $[\![c_h]\!]$, on edges. However, it has also to be mentioned, according to a proper choice of the penalty factor σ, all these four approaches lead to very similar numerical solutions. In the latter context, without special notification, the system of equations (eq. (5) and eq. (6)) is solved by the OBB-OBB formulation, i. e. OBB scheme for both the pressure and concentration equations.

Recall that $\tilde{\mathbf{q}}_h$ represents the continuous projection of the discontinuous filter velocity $\mathbf{q}_h^{\mathrm{DG}}$ on the edges. As we now apply discontinuous approximations in space, different quantities of the filter velocity $\mathbf{q}_h^{\mathrm{DG}} = (k^{\mathfrak{s}}/\mu)\,\mathrm{grad}\, p_h$ are evaluated from the adjacent elements on both sides of the edge. Such an inconsistency on the interior edges raises spurious oscillations which may further spoils the overall solution [14, 34]. Thus, a conservative projection resulting in continuous normal components of the filter velocities $\tilde{\mathbf{q}}_h$ over the element boundaries is necessary. In the present work, for the sake of simplicity, we apply the $H(\mathrm{div})$ projection for the computation of $\tilde{\mathbf{q}}_h$ in a post-processing step. Therefore, for the computation of the current time-slab Q^n $(n > 0)$, the quantity of $\tilde{\mathbf{q}}$ is results of the projected velocity at the end of previous time slab t_n. As for the initial step i. e. Q^0, as there is no previous computation available, we assume that $\tilde{\mathbf{q}}_h = \mathbf{q}_h$, and solve the nonlinear set of equations by a global Newton-Raphson scheme [32, 33].

It is well known that in the DGS formulations, for linear or higher-order polynomials in space, it is usually necessary to apply a slope limiting procedure to avoid over- and undershoot in the neighborhood of concentration fronts, cf. [36, 4]. In the present work, by using the DGT formulation in time, $\check{c}_{h,n}$ serves as the only input information for the computation on the current time-slab Q^n. Note that this is either a result $c_{h,n}^-$ obtained from the previous time-slab Q^{n-1} $(n > 1)$, or the initial condition c_0 given at $t = t_0$. Here, we apply the slope limiting procedure to $c_{h,n}^-$ $(n > 0)$ in a post-processing step. So that, only regular quantities of $\check{c}_{h,n} = c_{h,n}^-$ occur in the input data for the computation on the current time-slab Q^n. We denote that with respect to the numerical experiments performed in our work, it is sufficient to

apply the slope limiting procedure to $c^-_{h,n}$ to ensure the stability of the solution. A stabilization procedure of the pressure p_h is not necessary. We denote that this procedure is different to the most semi-discrete methods. In usual, depending on the chosen finite difference procedure in time, a consistent slope limiting procedure for the primary unknown and its rate term must be developed, see e. g. [36]. In the current work, we apply the quadratic slope limiter [37] for the limiting procedure of the concentration $c^-_{h,n}$.

4. Numerical experiments

Table I. Material parameters

porosity	ϕ	0.1	[-]
molecular diffusion coefficient	d_m	1.16e-9	[m^2/s]
longitudinal dispersion coefficient	α_l	0.1	[m]
transversal dispersion coefficient	α_t	0.01	[m]
mobility factor	M	$1,5$	[-]
concentration of injected flow	c_{in}	1	[-]

In the following numerical experiments, we consider a square domain of the geophysical size 1600×1600 m^2, which is subjected to a pressure difference on the left side $p_l = 0.1$ GPa and on the right side $p_r = 0$. A fluid with the concentration $c_{\text{in}} = 1$ is injected from the left side into the domain, see *Figure* 4. Here, we apply quadratic shape functions in space combined with linear polynomials in time for the pressure p_h and the concentration c_h.
According to [38], for the two-dimensional case, the diffusion tensor $\mathbf{D}(\mathbf{q})$ depending on the filter velocities $\mathbf{q} = [q_1, q_2]^T$ is given by

$$\mathbf{D}(\mathbf{q}) = \phi\, d_m\, \mathbf{I} + \frac{\alpha_l}{|\mathbf{q}|} \begin{pmatrix} q_1^2 & q_1\, q_2 \\ q_1\, q_2 & q_2^2 \end{pmatrix} \mathbf{e}_1 \otimes \mathbf{e}_2 + \frac{\alpha_t}{|\mathbf{q}|} \begin{pmatrix} q_1^2 & -q_1\, q_2 \\ -q_1\, q_2 & q_2^2 \end{pmatrix} \mathbf{e}_1 \otimes \mathbf{e}_2 \tag{18}$$

in which d_m is the molecular diffusion coefficient, and α_l and α_t are the longitudinal and transversal dispersion coefficients, respectively. $\mathbf{e}_1$ and $\mathbf{e}_2$ represent the basis vectors. The quantities of these parameters are given in Table I. The concentration-dependent viscosity $\mu^{\text{l}}(c)$ of the

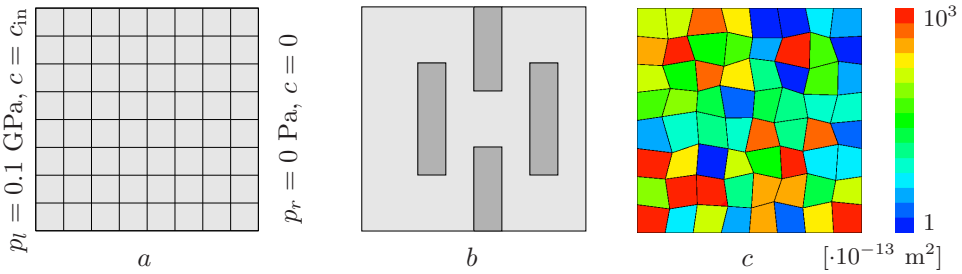

Figure 4. Geometry and boundary condition for problem a , band c.

liquid mixture reads [3, 5],

$$\mu^{\mathfrak{l}}(c) = \mu^{\mathfrak{a}R}\left(c + (1-c)\left[\frac{\mu^{\mathfrak{f}R}}{\mu^{\mathfrak{a}R}}\right]^{-0.25}\right)^{-4}, \tag{19}$$

in which $\mu^{\mathfrak{a}R}$ and $\mu^{\mathfrak{f}R}$ are the viscosities of the solvent fluid and the resident fluid, respectively. The stability of the flow is characterized by the mobility factor M, which describes the ratio of the viscosity of the resident fluid to that of the solvent one, i. e. $M = \mu^{\mathfrak{f}R}/\mu^{\mathfrak{a}R}$. The flow may be instable if the mobility factor is greater than unity, when viscous fingering effects tends to occur. For more detail concerning the evolution of viscous fingering effects, we refer to the review work [39].

4.1. Homogeneous domain

In the first example, we consider a homogeneous domain, see *Figure* 4a. The intrinsic permeability of the matrix is $k^{\mathfrak{s}} = 10^{-11}$ m^{-2}. We first compute the problem with the mobility factor $M = 1$, which means a constant viscosity distribution, i. e. $\mu^{\mathfrak{l}} \equiv 0.001$ Pa s. Since the computational domain is homogeneous, the pressure distribution is linear and remains constant throughout the whole process. Thus, the quantity of the filter velocity $\mathbf{q}$ can be computed analytically, i. e. $\mathbf{q} = 6.25 \cdot 10^{-4}$ m/s. Note that the seepage velocity $\mathbf{v}$ equals $\mathbf{v} = \mathbf{q}/\phi = 6.25 \cdot 10^{-3}$ m/s, which is the true propagation velocity of the solvent fluid.
The sufficient but not necessary condition for the stability of the numerical scheme is the Courant-Friedrich-Levy (CFL) condition. Given the representative element size h in space and the time step size Δt, the Courant number C_r can be calculated by

$$C_r = \frac{|v|\,\Delta t}{h} \tag{20}$$

where $|v|$ is the maximum wave speed within an element. Generally speaking, the Courant number has to be smaller than one, i. e. $C_r \leq 1$, to ensure numerical stability. Beside the stability criterion, the choice of an *optimal* time step size Δt for a given finite element discretization is an important aspect in a coupled space-time finite element analysis. It is well known, that the quality of the numerical solution can not be improved extensively by simply reducing the size of time steps while holding the spatial discretization fixed [40]. In the 1-dim case, for a three-node (quadratic) element with first order time-stepping algorithm the critical time step is [40]

$$\Delta t = \frac{h}{\sqrt{6}\,|v|}. \tag{21}$$

According to the problem at hand, quadratic polynomials in space and linear ones in time are chosen for the concentration c_h and the pressure p_h. We conclude that the critical time step corresponds to the Courant number $C_r \approx 0.4$.

Figure 5 shows the concentration front at $t = 1.4 \cdot 10^5$ s obtained by the DGST method, the spatial conforming Finite Element method combined with a backward Euler scheme in time (EUL) and the Spatial Discontinuous Galerkin method with the backward Euler scheme in time (DGS) [5]. The choice of spatial grids and the corresponding time step sizes are listed in Table II. The sizes of the time steps are chosen according to $C_r = 0.4$. For a qualitative comparison, we generate a ref-

Table II. Choice of time step sizes Δt of various grids $h_0, \ldots, h_3$ on homogeneous/inhomogeneous domains

Δt [s]		h_0	h_1	h_2	h_3
homogeneous domain	M=1	12800	6400	3200	1600
inhomogeneous domain	M=1	-	3200	1600	800
	M=5	-	1600	800	400
number of elements		8×8	16×16	32×32	64×64

erence solution by the EUL with an overkill discretization. In *Figure* 5, we observe that with respect to all four grids $h_0, \ldots, h_3$, under the same spatial and temporal discretization, the DGST method leads to the best solution in that the steep concentration front is much better resolved than the other approaches, i. e. the EUL and the DGS approaches. Moreover, with respect to the numerical results obtained by the DGST method on relatively coarse grids h_0 and h_1, inconsistent quantities,

i. e. jumps, occur nearby the steep concentration front. Obviously, we also observe that the jumps do not spoil the numerical results, but contribute to the accuracy of the overall solutions. The amount of the jumps decreases in the numerical solutions of the finer discretizations h_2 and h_3. Note in passing that the jumps that occur in the solution of discontinuous Galerkin methods can be used as a simple but reliable error indicator for further adaptive strategies, cf. [30].

In *Figure* 5, we also observe that there is no significant difference between the quantity of the numerical results obtained by the EUL and the DGS method. Yet, the DGS method is well known for capturing sharp gradients and for contributing to the stability of the overall numerical solution scheme, cf. [25, 6, 5]. According to the knowledge of the authors, so far the DGS method is always implemented by means of semi-discrete numerical techniques, such that a discontinuous approximations in space is applied to produce an ODE system, which is in turn solved by the backward Euler scheme, cf. [41, 5]. However, according to our numerical experiments, we conclude that a discontinuous Galerkin approximation in space alone does not always ensure more accurate solutions, see *Figure* 5. In these cases, the error introduced by the time-stepping method, i. e. the backward Euler scheme, is dominant. Thus, an advanced DGS formulation in space can not rescue the overall quality of the numerical solution. However, we remark that due to the employment of the discontinuous approximations in space, the number of DOFs for the solution scheme of the DGS scheme is almost four times larger than that of the spatially conforming FE method.

Next, we compute the same problem on the coarse discretization h_0 by the EUL and DGS method with a much smaller time step, i. e. $\Delta t = 320$ s. For comparison, the numerical solution obtained by the DGST scheme on the same spatial mesh h_0 with the time step $\Delta t = 12800$ s is depicted in the same figure, see *Figure* 6. Herein, due to the much refined temporal discretization, slight difference in the solutions of the EUL and the DGS are observed. Herein, the concentration c_h obtained by the EUL is continuous, while jumps are observed in the solution of DGS method nearby the concentration front. In spite of the slight difference, no significant improvement is obtained than that of the DGST method with a much larger time step. Further refinements of the time step size have also been tested, but they produce no significant improvements. We conclude that in this case the error introduced by the spatial discretization is dominant, such that a further refinement of the time step can not improve the quality of the solution. However, we denote that in achieving those comparable solutions, the size of the time step of the DGST method is 40 times larger than those used in the DGS and the FE methods.

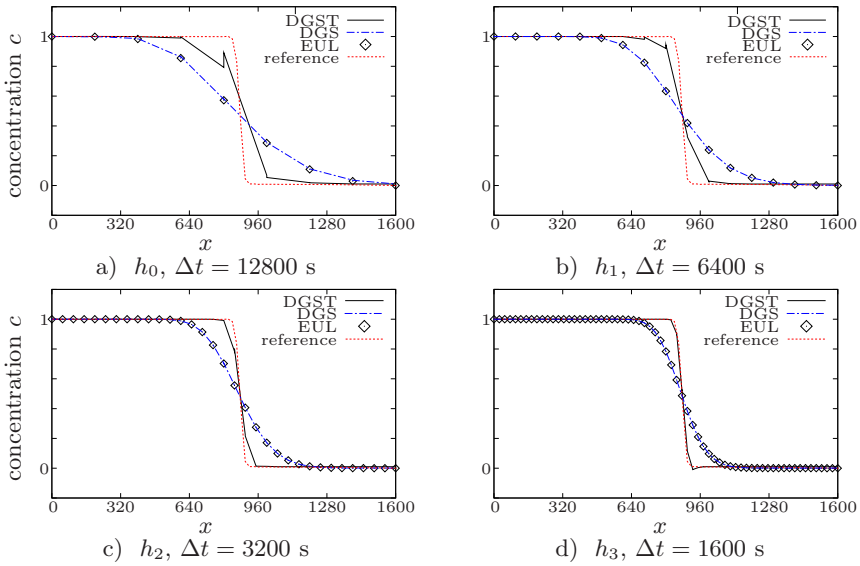

Figure 5. Concentration profile at $t = 1.4e5$ s with the mobility ratio $M = 1$.

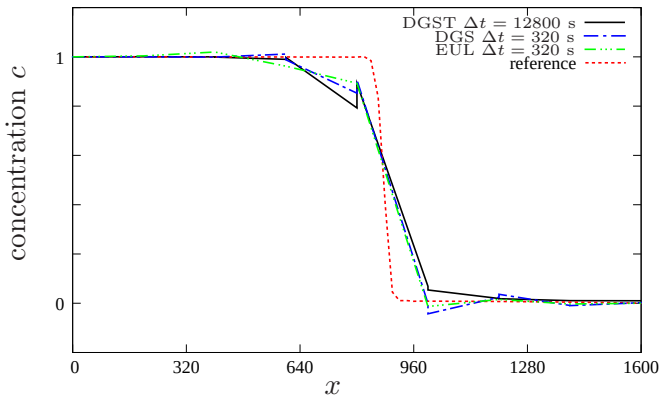

Figure 6. Concentration front

4.2. Inhomogeneous domain

Next, we consider the flow propagation in an inhomogeneous domain as depicted in *Figure* 4b. The patches with dark gray color represent the less permeable material with the intrinsic permeability $k^{\mathfrak{s}} = 10^{-14}$ m^{-2} which is 1000 times smaller than the rest of the domain ($k^{\mathfrak{s}} = 10^{-11}$ m^{-2}). Since it is natural to choose a mesh whose grids are smaller than the obstacles, we perform the computations on the meshes $h_1, \ldots, h_3$.

We first consider the stable case ($M = 1$) with a constant viscosity $\mu^{\mathfrak{l}} = 0.001$ Pa s. Due to the inhomogeneity of the computational do-

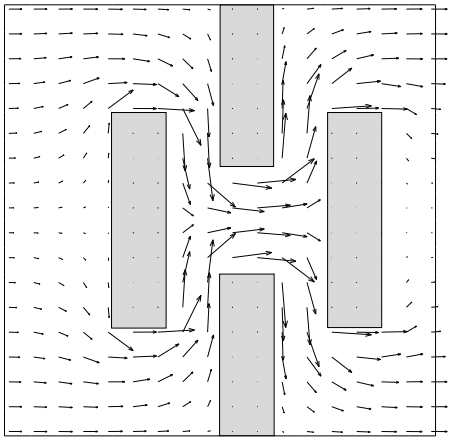

Figure 7. Filter velocity distribution $\tilde{\mathbf{q}}_h$ of the inhomogeneous domain for the mobility ratio $M = 1$.

main, the filter velocity $\mathbf{q}_h$ can not be determined directly. However, we conclude that the highest velocity occurs between the two parallel patches. The distribution of the fluid pressure $p_h(\mathbf{x}, t)$ is constant over time. Moreover, it is easy to observe that the highest pressure gradient occurs between the two parallel patches. Hence, we can derive that the highest filter velocity $\mathbf{q}_h$ in this case is almost twice as large as in the previous example. The time steps are chosen as one half of those used in the previous example, see Table II.

Figure 7 shows the $H(\mathrm{div})$ projection of the filter velocity $\tilde{\mathbf{q}}_h$ obtained on the mesh h_1. We observe that there is no spurious sinks or source terms in the computational domain. The necessity and quality of this $H(\mathrm{div})$ projection were discussed extensively in [34]. Since the distribution of the pressure field $p_h(\mathbf{x}, t)$ is relatively smooth, no significant improvement in the $\tilde{\mathbf{q}}_h$ on h_2 and h_3 grids can be achieved.

Figure 8 shows the concentration profiles at different time levels, i. e. $t = 1.5e5$, $3.0e5$, $4.5e5$, $6.0e5$ s. Herein, we observe that the injected fluid circumvents the less permeable patches. Steep concentration fronts around these patches are well resolved, even on the coarse discretization h_1. The slope limiting procedure is applied to the concentration field $c^-_{h,n}$ $(n > 0)$ in a post processing step on each time-slab Q^n, i. e. $c^-_{h,n} = S(c_{h,n})$ whereby $S(c_n)$ denotes the function of the slope limiting procedure. Despite slight over- and undershoots around the less permeable patches, the numerical solutions are stable and reflect the propagation phenomena of the flow. It is necessary to mention that all three meshes, i. e. h_1, h_2 and h_3, produce qualitatively similar solutions. More accurate numerical solutions are obtained by a finer discretization, i. e. h_2 and h_3. As the mobility factor equals one, no

fingering effects result in the computational domain.
Next, we consider a physically more sophisticated case with a small mobility factor $M = 5$, i. e. $\mu_0 = 0.001$ Pa s and $\mu_{\mathfrak{a}} = 0.0002$ Pa s. Thus, the viscosity $\mu^{\mathfrak{l}}$ is no more a constant but decreases with the increase of the concentration level, cf. eq. (19). The viscosity $\mu^{\mathfrak{l}}$ is computed by

$$\mu^{\mathfrak{l}}(\mathbf{x}) = \begin{cases} \mu^{\mathfrak{l}}(c_0(\mathbf{x})) & \text{if} \quad n = 0, \\ \mu^{\mathfrak{l}}(\tilde{c}_n(\mathbf{x})), & \text{otherwise.} \end{cases} \quad \mathbf{x} \in \Omega \tag{22}$$

Since the viscosity $\mu^{\mathfrak{l}}$ varies with the concentration field, the pressure distribution evolves over time. However, we denote that due to the small mobility factor $M = 5$, the filter velocity $\mathbf{q}_h(\mathbf{x}, t)$ grows slowly as the concentration level increases. The choice of the time step sizes according to different discretizations are given in Table II.
Figure 9 shows the simulation results obtained at different time levels. As the liquid viscosity $\mu^{\mathfrak{l}}$ decreases as the concentration level increases, the propagation of the solvent is much faster than in the previous test, such that the solvent fluid takes almost one half of the time to reach the right side of the computational domain than in the stable case, cf. *Figure* 8 and *Figure* 9. Since in the current experiment the mobility factor is larger than one, the propagation of the flow tends to be instable. However, in the results obtained by the coarse discretizations of h_1 and h_2, such effects are not significant. In the solution of the finest discretization h_3, we observe that the solvent fluid tends to penetrate through the more viscous resident fluid, leaving out vacancy around the less permeabile patches with very low concentration.

5. Heterogeneous domain

In the last example, we consider a heterogeneous domain (1600×1600 m^2) with randomly distributed permeabilities k^s in the range of $[10^{-11}, 10^{-14}]$ m^2, see *Figure* 4c. The remaining problem-relevant material parameters are listed in Table I. The boundary and initial conditions are the same as before. We compute the problem on three non-conforming meshes $g_0, \ldots, g_2$ with different mesh densities, see *Figure* 10. Since a direct determinant of the filter velocity is not available, the time step sizes are chosen empirically, such that the stability of the overall solution is ensured. More details with respect to the computational effort of the meshes are given in Tab. III.
We start with the computation of the stable case with the mobility factor $M = 1$, i. e. the liquid viscosity equals $\mu^{\mathfrak{l}} = 0.001$ Pa s. Here, by choosing different pairs of parameters σ and ϵ, we perform the

Table III. Computational effort of non-conforming meshes.

mesh	g_0	g_1	g_2
number of elements	332	1260	7704
number of DOFs/step	10624	40320	246528
Δt [s]	200	100	50

computation with different DGS formulations, i. e. NIPG, SIPG and IIPG, rf. eq. (16) and eq. (17). It is well known that the choice of the penalty parameter σ is essential for the accuracy of the solution. For the problem at hand, it is known that the penalty factor must not be "*sufficiently large*", rf. [14], so that we set $\sigma = 1/h$, whereas h is the representative element size in space. In *Figure* 11, we depicted the concentration state at $t = 1.8e5$ s obtained by the four different spatial formulations. It can be observed that with the proper choice of the σ factor, the penalty methods, i. e. SIPG, NIPG and IIPG, produce very similar solutions as those of the OBB methods. In this sense, we conclude that these penalty methods are as good as the OBB formulations in modeling the propagation flow through the porous materials.
Next, we compute the same problem with a mobility factor $M = 10$, i. e. $\mu^{\mathfrak{f}R} = 0.001$ Pa s and $\mu^{\mathfrak{a}R} = 0.0001$ Pa s. *Figure* 12 shows the concentrations state obtained on meshes g_2 by OBB formulation at different time levels $t = 0.6e5$, $1.2e5$, $1.8e5$ s. Here, it is obvious to observe that fingers grow in the computational domain. Within the same period of time, i. e. $t = 1.8e5$ s, in the stable case, i. e. $M = 1$, the solvent fluid penetrates nearly one third of the domain, see *Figure* 11. However, in the current test, i. e. $M = 10$, the solvent fluid has almost finger through the whole domain. Local over- and undershoots nearby the steep concentration fronts are observed. However, the overall solution is stable and no degeneration of the numerical solution through local oscillations, i. e. over- and undershoots, are obtained.

6. Conclusions

We present an efficient coupled space-time discontinuous Galerkin method to model transport phenomena in porous media. Discontinuous approximations in space as well as in time are employed. Due to the employment of discontinuous approximations in the spatial and the

temporal domains, with the same spatial and temporal discretization the total number of DOFs of the DGST method is much larger than that of the conventional approaches. However the extra costs of the computational effort can be well compensated by using larger discretization either in space or in time. Moreover, various formulations of Spatial Discontinuous Galerkin methods have been tested. According to a proper choice of the penalty factor, all methods produce very similar solutions. The proposed new coupled solution scheme is able to capture steep gradients in the solution very well and is suitable for modeling more complex phenomena, i. e. viscous fingering effects.

References

1. R. E. Ewing, U. Wyoming, T. F. Russell, M. F. Wheeler, Simulation of miscible displacement using mixed methods and a modified method of characteristics, Soc. Pet. Eng. J. (1983) 12241.
2. J. Douglas, The numerical simulation of miscible displacement in porous media, in: J. T. Oden (Ed.), Computational methods in nonlinear mechanics, North-Holland, Amsterdam, 1980, pp. 225–237.
3. E. J. Koval, A method for predicting the performance of unstable miscible displacement in heterogeneous media, Soc. Pet. Eng. J. 3 (1963) 145–154.
4. W. Klieber, B. Rivière, Adaptive simulations of two-phase flow by discontinuous Galerkin methods, Comp. Meth. Appl. Mech. Eng. 196 (2006) 404–419.
5. B. Rivière, M. F. Wheeler, Discontinuous Galerkin methods for flow and transport problems in porous media, Commun. Numer. Meth. En. 79 (2002) 157–174.
6. B. Rivière, M. F. Wheeler, K. Banaś, Part II: Discontinuous Galerkin methods applied to a single phase flow in porous media, Comp. Geosciences 4 (2000) 337–349.
7. D. Nayagum, G. Schäfer, R. Mosé, Modelling two-phase incompressible flow in porous media using mixed hybrid and discontinuous finite elements, Computers and Geotechnics 8 (2004) 49–73.
8. J. T. Oden, I. Babuška, C. E. Baumann, A discontinuous *hp* finite element method for diffusion problems, J. Chem. Phys. 146 (1998) 491–519.
9. B. Rivière, M. F. Wheeler, V. Girault, Improved energy estimates for interior penalty, constrained and discontinuous Galerkin methods for elliptic problems.Part I, Comp. Geosciences 3 (1999) 337–360.
10. M. F. Wheeler, An elliptic collocation-finite element method with interior penalties, SIAM J. Numer. Anal. 15 (1978) 152–161.
11. D. N. Arnold, An interior penalty finite element method with discontinuous elements, SIAM J. Numer. Anal. 19 (1982) 742–760.
12. C. Dawson, J. Proft, Coupled discontinuous and continuous Galerkin finite element methods for the depth-integrated shallow water equations, Comp. Meth. Appl. Mech. Eng. 193 (2004) 289–318.
13. S. Sun, M. F. Wheeler, Symmetric and nonsymmetric discontinuous Galerkin methods for reactive transport in porous media, SIAM J. Numer. Anal. 43(1) (2005) 195–219.

14. C. Dawson, S. Sun, M. Wheeler, Compatible algorithms for coupled flow and transport, Comp. Meth. Appl. Mech. Eng. 193 (2004) 2565–2680.
15. W. F. Ames, Numerical Methods for Partial Differential Equations,Second Edition, Academic Press, Boston-New York, 1977.
16. K. Eriksson, D. Estep, P. Hansbo, C. Johnson, Computational Differential Equations, Cambridge University Press, Cambridge, 1996.
17. J. H. Argyris, D. W. Scharpf, Finite elements in space and time, Nucl. Engrg. Des. 10 (1969) 456–464.
18. I. Fried, Finite element analysis of time-dependent phenomena, AIAA Journal J.7 (1969) 1170–1173.
19. J. T. Oden, A general theory of finite elements ii. applications, Int. J. Numer. Meth. Eng. 1 (1969) 247–259.
20. T. J. R. Hughes, G. M. Hulbert, Space-time finite element methods for elastodynamics: Formulations and error estimates, Comp. Meth. Appl. Mech. Eng. 66 (1988) 339–363.
21. G. Hulbert, Space-time finite element methods for second order hyperbolic equations, Ph.D. thesis, Department of Mechanical Engineering, Stanford University, Stanford (1989).
22. G. M. Hulbert, Time finite element methods for structural dynamics, Int. J. Numer. Meth. Eng. 33 (1992) 307–331.
23. G. M. Hulbert, T. J. R. Hughes, Space-time finite element methods for second-order hyperbolic equations, Comp. Meth. Appl. Mech. Eng. 84 (1990) 327–348.
24. Z. Chen, H. Steeb, S. Diebels, A time-discontinuous Galerkin method for the dynamical analysis of porous media, Int. J. Numer. Anal. Meth. Geomech. 30 (2006) 1113–1134.
25. C. E. Baumann, An *hp*-adaptive discontinuous finite element method for computational fluid dynamics, Ph.D. thesis, The University of Texas at Austin (1997).
26. S. M. Hassanizadeh, W. G. Gray, High velocity flow in porous media, Transport Porous Med. 2 (1987) 521–531.
27. S. Diebels, W. Ehlers, B. Markert, Neglect of the fluid-extra stresses in volumetrically coupled solid-fluid problems, Z. Angew. Math. Mech. 81 (2001) S521–S522.
28. W. Ehlers, Foundations of multiphasic and porous materials, in: W. Ehlers, J. Bluhm (Eds.), Porous Media: Theory, Experiments and Numerical Applications, Springer-Verlag, Berlin, 2002, pp. 3–86.
29. C. E. Baumann, J. T. Oden, A discontinuous *hp* finite element method for convection-diffusion problems, Comp. Meth. Appl. Mech. Eng. 175 (1999) 311–341.
30. B. Cockburn, Discontinuous Galerkin methods, Z. Angew. Math. Mech. 11 (2003) 731–754.
31. J. T. Oden, I. Babuška, C. E. Baumann, A discontinuous *hp* finite element method for diffusion problems, J. Comp. Phys. 146 (1998) 491–519.
32. J. E. Marsden, T. J. R. Hughes, Mathematical Foundations of Elasticity, Dover Publications, Inc., New York, 1983.
33. P. Wriggers, Konsistente Lineariserung in der Kontinuumsmechanik und ihre Anwendung auf die Finite-Element-Methode, Bericht Nr. F88/4 (1999) Institut für Baustatik und Numerische Mechanik, Univerität Honnover, 1988.
34. P. Bastian, B. Rivière, Superconvergence and $h(div)$-projectin for discontinuous Galerkin methods, Int. J. Numer. Meth. Fluids 42 (2003) 1043–1057.

35. F. Brezzi, J. Douglas, L. Marini, Two families of mixed finite elements for second order elliptic problems, Numerische Mathematik 47 (1985) 217–235.
36. B. Cockburn, C. W. Shu, The Runge-Kutta discontinuous Galerkin method for conservation laws V, J. Chem. Phys. 141 (1998) 199–224.
37. H. Hoteit, P. Ackerer, R. Mosé, J. Erhel, B. Philippe, New two-dimensional slope limiters for discontinuous galerkin methods on arbitrary meshes, Int. J. Numer. Meth. Eng. 61 (2004) 2566–2593.
38. R. E. Ewing (Ed.), The mathematics of reservoir simulation, SIAM, 1983.
39. G. M. Homsy, Viscous fingering in porous media, Ann. Rev. Fluid Mech 19 (1987) 271–311.
40. T. J. R. Hughes, The Finite Element Method, Prentice-Hall, Englewood Cliffs, New York, 1987.
41. C. E. Baumann, J. T. Oden, An adaptive-order discontinuous Galerkin method for the solution of the Euler equations of gas dynamics, Int. J. Numer. Meth. Eng. 47(1-3) (2000) 61–73.

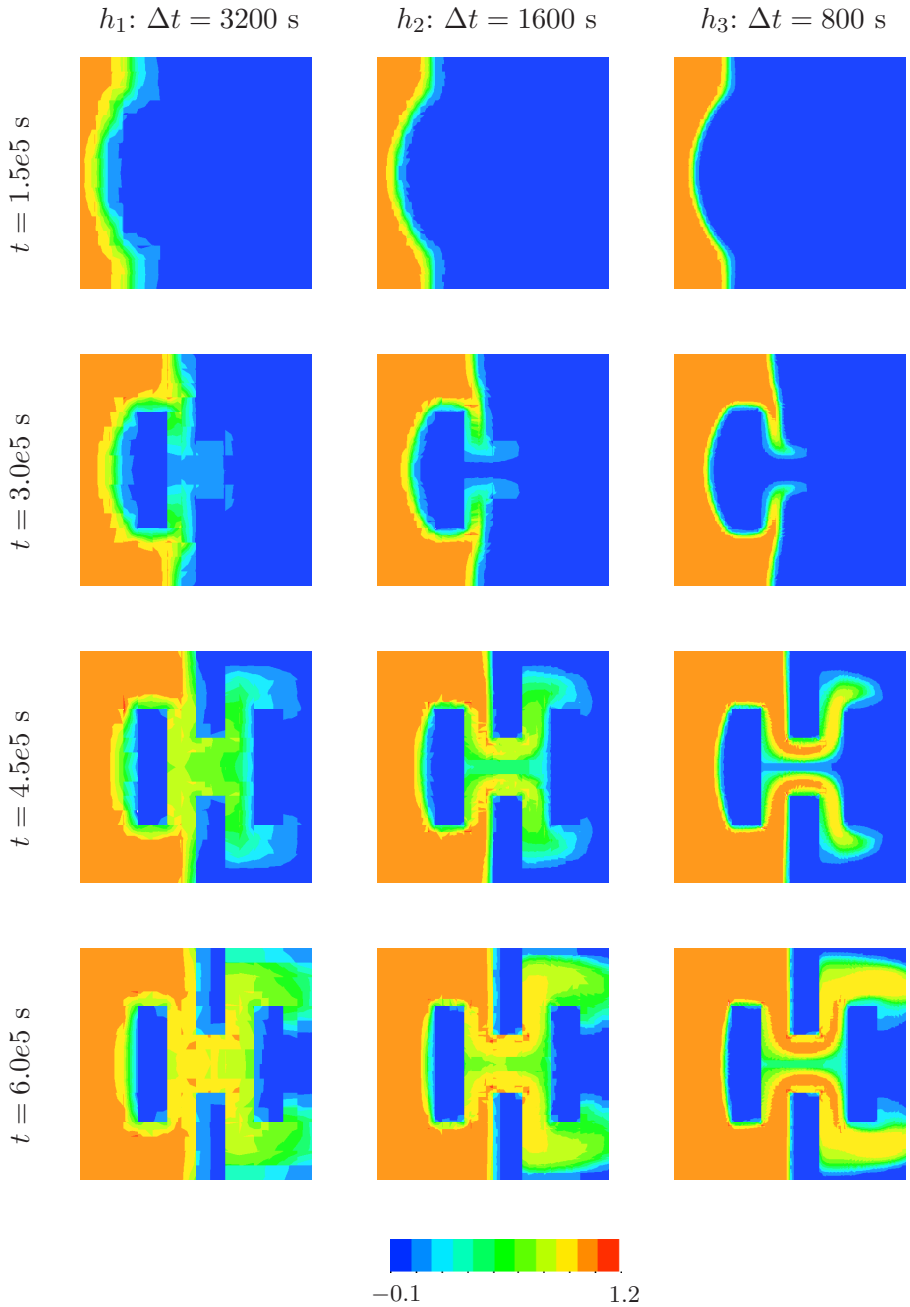

Figure 8. Concentration c_h at various time levels $t = 1.5e5$, $3.0e5$, $4.5e5$, $6.0e5$ s in the inhomogeneous domain with mobility factor $M = 1$.

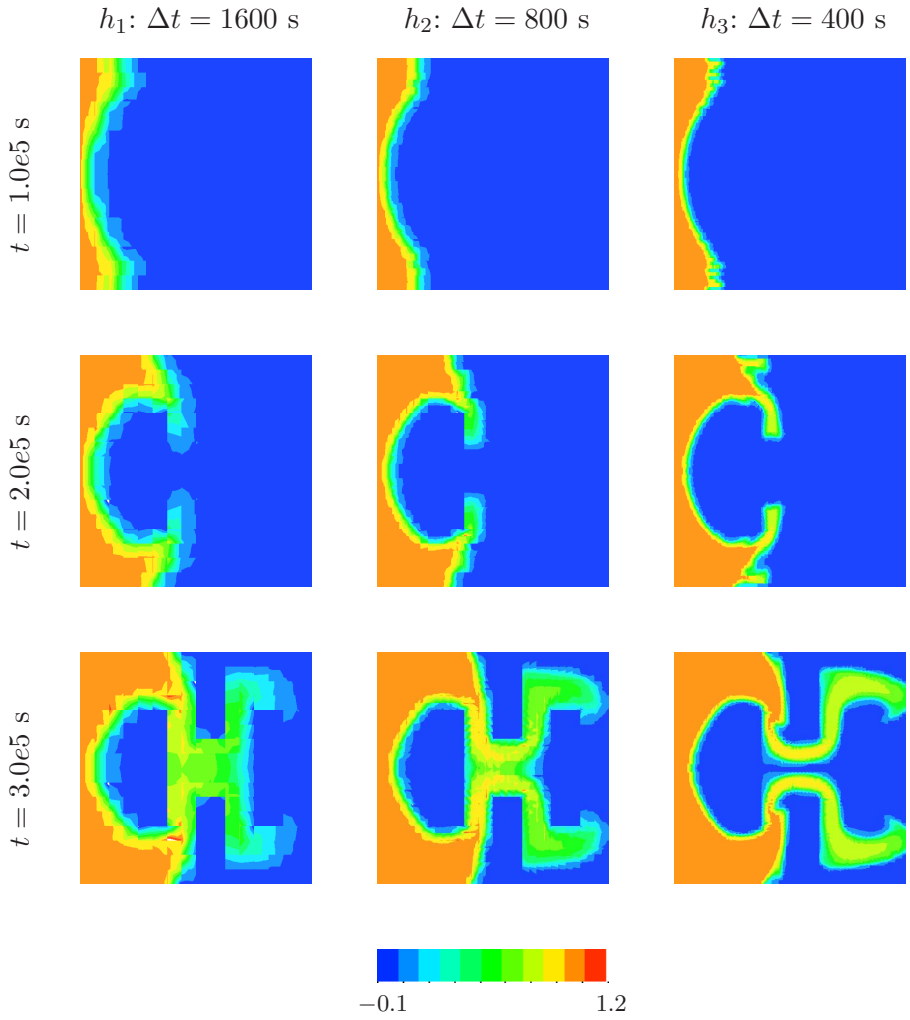

Figure 9. Concentration c_h at various time levels $t = 1.0e5, 2.0e5, 3.0e5$ s in the inhomogeneous domain with mobility factor $M = 5$.

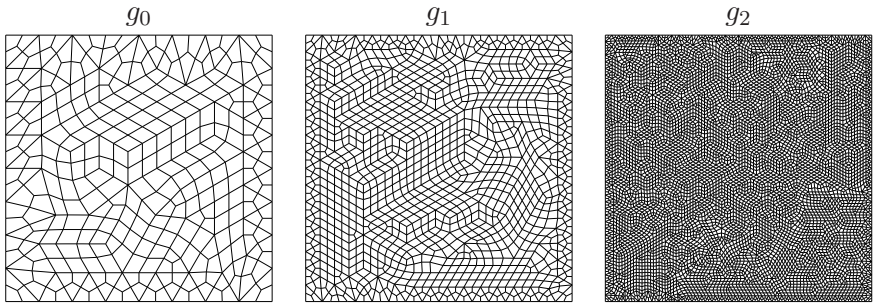

Figure 10. Non-conforming meshes with different mesh densities.

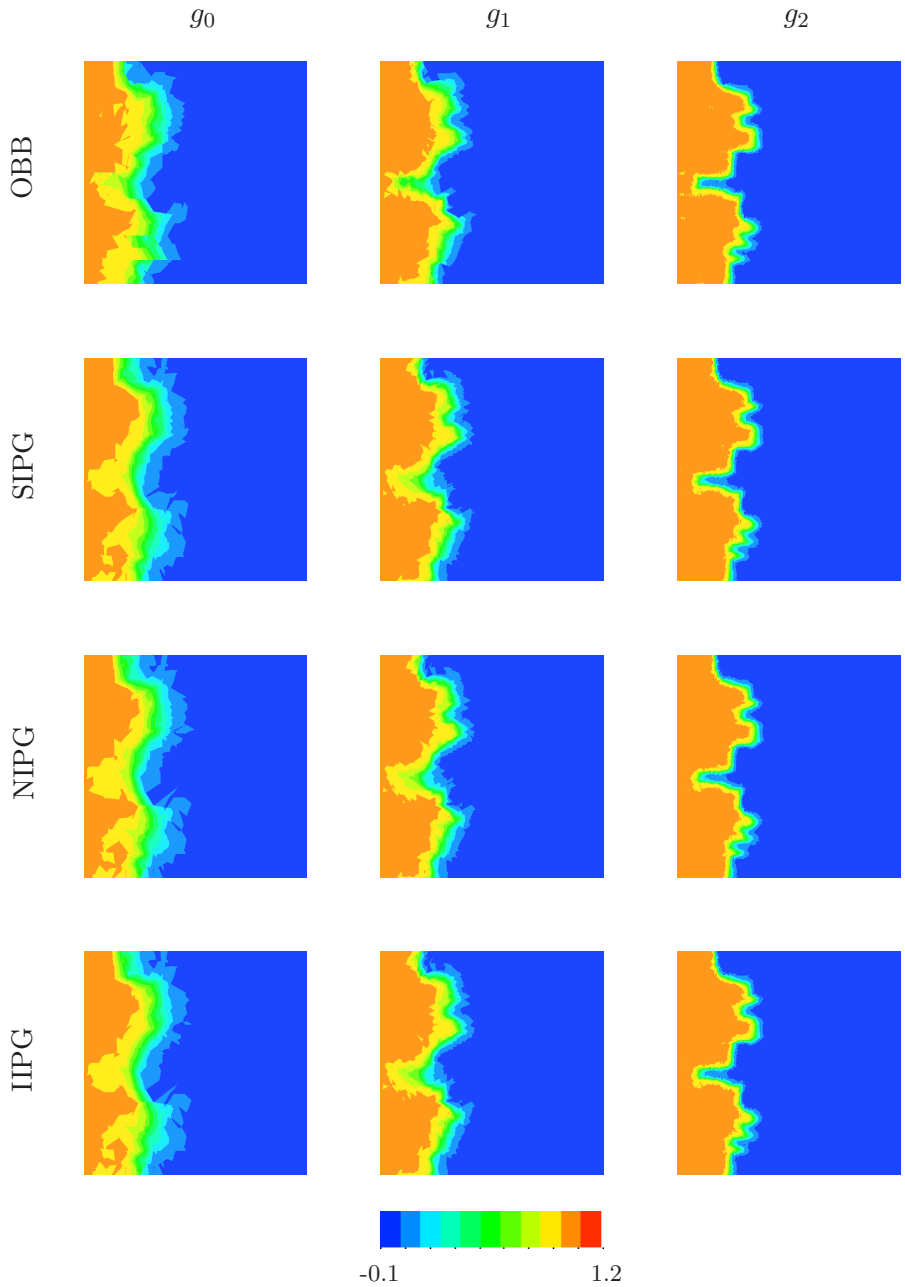

Figure 11. Concentration c_h at $t = 1.8e5$ s in the heterogeneous domain computed by various DGS formulations with $M = 1$

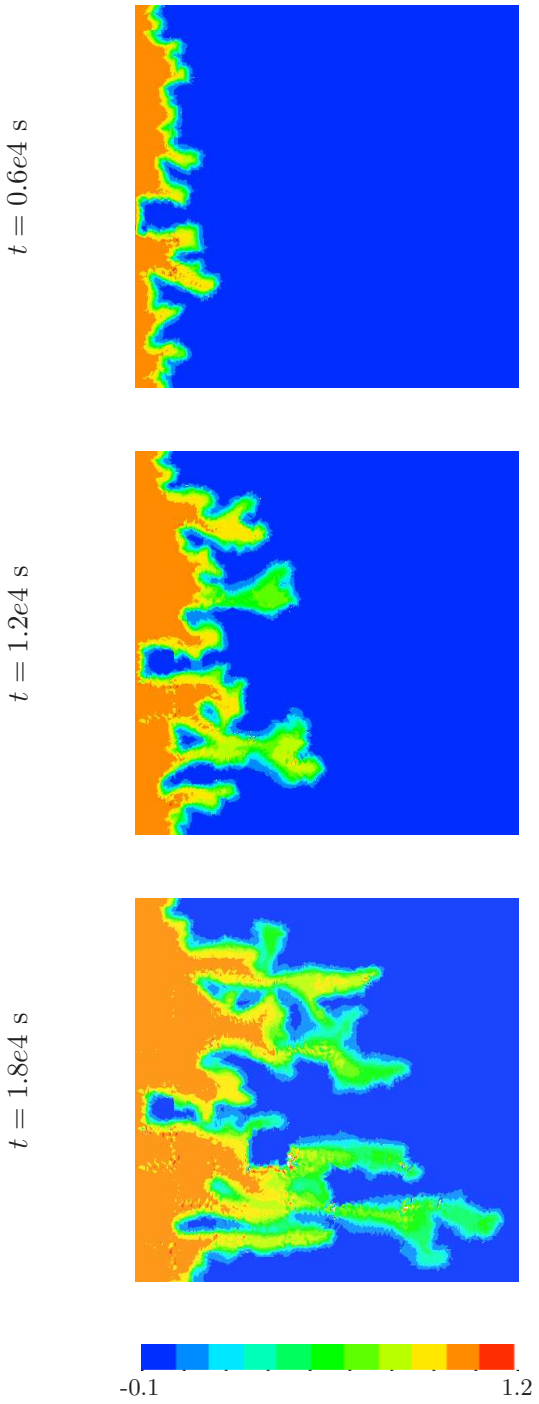

Figure 12. Concentration c_h at various time levels $t = 0.6e5, 1.2e5, 1.8e5$ s in the heterogeneous domain computed by OBB formulation with $M = 10$ on g_2 mesh.